CAPITAL UNIVERSITY OF SCIENCE AND TECHNOLOGY, ISLAMABAD

Flow and Heat Transfer Characteristics of non-Newtonian Nanofluids

by

Wasim Jamshed

A thesis submitted in partial fulfillment for the degree of Doctor of Philosophy

in the

Faculty of Computing
Department of Mathematics

2020

Flow and Heat Transfer Characteristics of non-Newtonian Nanofluids

By

Wasim Jamshed

(DMT 143-004)

Dr. Anuar Mohd Ishak, Professor

Universiti Kebangsaan Malaysia, Malaysia

(Foreign Evaluator 1)

Dr. Mustafa Turkyilmazoglu, Professor

Hacettepe University Ankara, Turkey

(Foreign Evaluator 2)

Dr. Asim Aziz

(Thesis Supervisor)

Dr. Muhammad Sagheer

(Head, Department of Mathematics)

Dr. Muhammad Abdul Qadir

(Dean, Faculty of Computing)

DEPARTMENT OF MATHEMATICS

CAPITAL UNIVERSITY OF SCIENCE AND TECHNOLOGY

ISLAMABAD

2020

This dissertation is dedicated to my loving parents and family for their endless love, prayers and support especially to my mother **Mrs. Meer Werjana**

CAPITAL UNIVERSITY OF SCIENCE & TECHNOLOGY
ISLAMABAD
Expressway, Kahuta Road, Zone-V, Islamabad
Phone:+92-51-111-555-666 Fax: +92-51-4486705
Email: info@cust.edu.pk Website: https://www.cust.edu.pk

CERTIFICATE OF APPROVAL

This is to certify that the research work presented in the thesis, entitled "**Flow and Heat Transfer Characteristics of non-Newtonian Nanofluids**" was conducted under the supervision of **Dr. Asim Aziz**. No part of this thesis has been submitted anywhere else for any other degree. This thesis is submitted to the **Department of Mathematics, Capital University of Science and Technology** in partial fulfillment of the requirements for the degree of Doctor in Philosophy in the field of **Mathematics**. The open defence of the thesis was conducted on **June 17, 2020**.

Student Name : Mr. Wasim Jamshed (DMT143004) ______________________

The Examining Committee unanimously agrees to award PhD degree in the mentioned field.

Examination Committee :

(a) External Examiner 1: Prof. Dr. Sohail Nadeem
Professor
QAU, Islamabad ______________________

(b) External Examiner 2: Dr. Rehmat Elahi
Associate Professor
IIU, Islamabad ______________________

(c) Internal Examiner : Dr. Shafqat Hussain
Associate Professor
CUST, Islamabad ______________________ 17/06/2020

Supervisor Name : Dr. Asim Aziz
Assistant Professor
NUST, Islamabad ______________________ 17/6/2020

Name of HoD : Prof. Dr. Muhammad Sagheer
Professor
CUST, Islamabad ______________________

Name of Dean : Prof. Dr. Muhammad Abdul Qadir
Professor
CUST, Islamabad ______________________

<u>AUTHOR'S DECLARATION</u>

I, **Mr. Wasim Jamshed (Registration No. DMT-143004)**, hereby state that my PhD thesis titled, '**Flow and Heat Transfer Characteristics of non-Newtonian Nanofluids**' is my own work and has not been submitted previously by me for taking any degree from Capital University of Science and Technology, Islamabad or anywhere else in the country/ world.

At any time, if my statement is found to be incorrect even after my graduation, the University has the right to withdraw my PhD Degree.

(Mr. Wasim Jamshed)

Registration No : DMT-143004

Dated: June, 2020

PLAGIARISM UNDERTAKING

I solemnly declare that research work presented in the thesis titled "**Flow and Heat Transfer Characteristics of non-Newtonian Nanofluids**" is solely my research work with no significant contribution from any other person. Small contribution/ help wherever taken has been duly acknowledged and that complete thesis has been written by me.

I understand the zero tolerance policy of the HEC and Capital University of Science and Technology towards plagiarism. Therefore, I as an author of the above titled thesis declare that no portion of my thesis has been plagiarized and any material used as reference is properly referred/ cited.

I undertake that if I am found guilty of any formal plagiarism in the above titled thesis even after award of PhD Degree, the University reserves the right to withdraw/ revoke my PhD degree and that HEC and the University have the right to publish my name on the HEC/ University Website on which names of students are placed who submitted plagiarized thesis.

(Mr. Wasim Jamshed)

Dated: June, 2020

Registration No : DMT-143004

Acknowledgements

All the appreciations and praises are for the most omnipotent **ALMIGHTY ALLAH**, the lord of the world, the most Generous and Merciful that knows the hidden truth of this universe and the **Holy Prophet Muhammad (PBUH)** who declared "Acquire Knowledge, learn tranquility and dignity"

First and foremost I would like to express my sincerest gratitude and deep regards to my supervisor **Dr. Asim Aziz**, for providing precious time, encouragement and guidance. I am extremely grateful to him for his constant support throughout my research phase with his patience and knowledge which enabled me to complete my thesis work.

This segment would be incomplete without referring to very generous and noble person **Dr. Muhammad Sagheer**, (Head department of Mathematics), Capital University of Science and Technology, for his continuous encouragement, motivation and moral assistance.

In March 2018, I was awarded six months scholarship by Higher Education Commission of Pakistan under International Research Support Initiative Program for Pennsylvania State University, York United State of America for advance research work. I am very grateful to Dr. Javed I. Siddque (Associate Professor) as foreign supervisor for his precious time, hospitality and collaboration in my thesis and research work during my stay in USA.

My heartiest and sincere salutations to my parents, who put their greater effort in making me a good human being. I also feel grateful to my dearest brother and my sisters, who never let me down and always fortified me throughout the hard period of my research work.

List of Publications

It is certified that following publications have been made out of the research work that has been carried out for this thesis:-

1. **W. Jamshed** and A. Aziz, "Cattaneo-Christov based study of TiO_2-CuO/EG Casson hybrid nanofluid flow over a stretching surface with entropy generation," Applied Nanoscience, vol. 08, pp. 01-14, 2018.
2. M. Asif, **W. Jamshed** and A. Aziz " Entropy and heat transfer analysis using Cattaneo-Christov heat flux model for a boundary layer flow of Casson nanofluid," Result in Physics, vol. 10, pp. 640-649, 2018.
3. **W. Jamshed** and A. Aziz, "A comparative entropy based analysis of Cu and Fe_3O_4 /methanol Powell-Eyring nanofluid in solar thermal collectors subjected to thermal radiation, variable thermal conductivity and impact of different nanoparticles shape," Result in Physics, vol. 09, pp. 195-205, 2018.
4. A. Aziz, **W. Jamshed** and T. Aziz, "Mathematical model for thermal and entropy analysis of thermal solar collectors by using Maxwell nanofluids with slip conditions, thermal radiation and variable thermal conductivity," Open Physics, vol. 16, pp. 123-136, 2018.

(Wasim Jamshed)

Registration No: DMT 143-004

Abstract

The aim of this thesis is to investigate the flow, heat transfer and entropy generation characteristics of thermal systems containing non-Newtonian nanofluids. Extensive research is carried out to study the flow and heat transfer characteristics of nanofluids considering different flow geometries, boundary conditions, external effects and surface motion etc. However limited attention is given towards study of non-Newtonian nanofluids. In real situation nanofluids do not have characteristics of Newtonian fluids, hence it is more appropriate to consider them as non-Newtonian fluids. Keeping above in view the present research is devoted to the study of flow, heat transfer and entropy generation of non-Newtonian nanofluid including effects of applied magnetic field, thermal radiation and variable thermophysical properties. Three non-Newtonian fluid models namely, Maxwell, Powell-Eyring and Casson are considered for the nanofluids. The mathematical model include electrically conducting nanofluid occupies the space over a porous stretching surface and the flow is generated due to the non-uniform stretching of the surface. The fundamental equations are obtained from the laws of conservation of mass, momentum and energy. These partial differential equations are transformed into a system of coupled nonlinear ordinary differential equations by means of suitable similarity transformation and then solved by an efficient numerical finite difference scheme known as Keller box method. The numerical results are presented in the form of graphs and tables for variation in parameters, for example, non-Newtonian parameter, material parameter, porous medium parameter, nanoparticle volume concentration parameter, velocity slip parameter, thermal radiation parameter, suction/injection parameter, Biot number, Reynolds number and Brinkman number. The impact of these parameters has been observed on the velocity, temperature and entropy generation profiles of the nanofluid.

Contents

List of Figures

List of Tables

Abbreviations

BC	Boundary Condition
BVP	Boundary Value Problem
FDM	Finite Difference Method
IVP	Initial Value Problem
MHD	Magnetohydrodynamics
ODEs	Ordinary Differential Equations
PDEs	Partial Differential Equations
KBM	Keller Box Method

Symbols

A	unsteadiness parameter
A_1	Rivlin-Erickson tensor
A^*	surface area
b	initial stretching rate
B	total magnetic field
B_0	magnetic constant
B_i	Biot number
B_r	Brinkman number
C_f	skin friction coefficient
C_p	specific heat $(J\ kg^{-1}\ K^{-1})$
E_G	dimensional entropy (J/K)
e_{ij}	deformation direction component rate
h	heat transfer coefficient
J	current density
k	thermal conductivity $(W\ m^{-1}\ K^{-1})$
k_0	thermal conductivity of surface
k^*	absorption coefficient
K	porous media parameter
K^*	variable thermal conductivity
L	characteristic length
m	particle shape factor
M	magnetic parameter
N_r	radiation parameter

N_G	dimensionless entropy generation
Nu_x	local Nusselt number
p	column vectors of order $J \times 1$
P	pressure
P_r	Prandtl number (ν/α)
P_y	yield stress of the fluid
Q	heat flux
q_r	radiative heat flux
q_w	wall heat flux
R_e	Reynolds number
S	suction/injection parameter
S^*	extra stress tensor
t	dimensional time (s)
u, v	velocity component in x, y direction $(m\ s^{-1})$
U_w	velocity of the stretching sheet
V	reference velocity
V_w	vertical velocity
x, y	dimensional space coordinates (m)

Greek symbols

τ	Cauchy stress tensor
τ_{xy}	shear stress $(m^2\ s^{-1})$
τ_w	wall shear stress
ξ	effective stretching rate
λ	fluid relaxation parameter
μ_a	apparent viscosity
μ_B	plastic dynamic viscosity
ϕ,	volume fraction of the nanoparticles
ρ	density $Kg\ m^{-3}$
σ	electrical conductivity $(\Omega\ m)^{-1}$
σ^*	Stefan Boltzmann constant
ψ	stream function

η	Independent similarity variable
γ	Maxwell nanofluid parameter
β	Casson nanofluid parameter
θ	dimensionless temperature
Θ	fluid temperature
Θ_w	fluid temperature of the surface
Θ_∞	ambient temperature
ϵ	variable thermal conductivity parameter
ε	unknown vector
Δ	Powell-Eyring nanofluid parameter
ω	Powell-Eyring nanofluid parameter
Λ	velocity slip parameter
π	product of the component of rate of deformation with itself
π_c	critical value of the product of the component (strain tensor rate)
ν	kinematic viscosity $(m^2\ s^{-1})$
α	thermal diffusivity $(m^2\ s^{-1})$
Ω	dimensionless temperature gradient

Subscripts

f	base fluid
p	nanoparticles
nf	nanofluid
hnf	hybrid nanofluid
s	particles

Chapter 1

Introduction

The need to enhance the thermal capabilities of heat transfer fluids in thermal transport processes, scientists and engineers are looking to device mechanisms those can achieve this purpose. One efficient way is the use of specially engineered heat transfer fluids called nanofluids. The present work is carried out in the light of already existing study with the intentions of getting fruitful addition to it. The present chapter throws light on the research carried out in the field of heat transfer by nanofluids. The chapter highlights the models and numerical methods that are used to achieve the desired results.

1.1 Literature Survey

Fluid is a continuously deforming substance under the action of applied shear stress. Flow of fluid has all kinds of aspects, uniform and non-uniform, compressible and incompressible, viscous and inviscid, rotational and irrotational, steady and unsteady etc. A boundary layer is the thin region of fluid flow in which flow is influenced by the friction between the solid surface and the fluid. The flow of boundary layer have been extensively studied in the literature and plays a vital role in the field of fluid dynamics. The study of boundary layer flows over a horizontal surface had countless industrial applications, for example, food manufacturing, production of glass fibers, manufacturing of rubber sheets, extrusion, metal spinning, wire drawing and cooling of huge metallic plates such as an electrolyte [1–3]. The first to introduce the theory of the boundary layer was Ludwig Prandtl [4]. Makinde and Onyejekwe [5] presented the numerical computations for the boundary layer flow model due to the stretching sheet with variable electrical conductivity and variable viscosity using shooting technique together with a sixth-order RK integration algorithm. They concluded that, when electrical conductivity parameter is increased the rate of convective heat transfer and skin friction coefficient decreases within the boundary surface. Moreover rise in the variable viscosity parameter results in an increase in viscous force and makes viscous forces dominant over the applied magnetic field. Ibrahim and Makinde [6] used the numerical shooting technique and examine the boundary layer flow pass a vertical moving flat sheet with Joule heating and chemical reaction effects. Moreover, in a chain of research articles, Makinde [7] and Makinde *et al.* [8] explored the fluid flow and thermal boundary layer passing over a flat sheet. They evaluated the impact of viscous dissipation and Newtonian heating on fluid flow for many types of geometries containing permeable boundary surface. The key purpose of their research is to investigate mathematical models of Newtonian and non-Newtonian fluid flow over a stretching surface. Some significant studies on boundary layer fluid flow past a stretching sheet are presented in [9–19].

Heat transfer is the thermal energy movement from one system to another system due to variation in temperatures. Phenomenon of heat transfer occurs between two bodies (or a similar body) because of the difference of temperature. The research of fluid flow and heat transfer generated by means of stretching medium has plenty of significance in numerous industrial developments for example, manufacturing of composite materials, geothermal reservoirs, drying of porous solids, thermal insulation, oil recovery and underground species transport. In the above cases heat transfer and flow investigation are of significant importance because the final product quality be determined on the basis of coefficient of velocity gradient (skin friction) and the rate of convective heat exchange. Elbashbeshy [20] numerically studied flow of viscous fluid and heat transfer by assuming the exponentially continuous stretching sheet. In his work fluid occupies the space over an infinite horizontal surface and the flow is induced by the non-linear stretching of the surface. Here numerical technique is used to solve the modelled equations. The results indicated that the suction parameter can be used as means for cooling the continuous moving stretching surface and the thickening level of thermal boundary layer reduces for larger values of suction parameter. After that Sanjayanand and Khan [21] extended the work of Elbashbeshy [20] to include heat and mass transfer of second order viscoelastic fluid across an exponentially stretching surface. Their work include the effects of elastic deformation and viscous dissipation. The main conclusion presented by the authors was, the velocity gradient and convective heat exchange (Nusselt number) drops at the boundary surface as the local viscoelastic parameter increases. The numerical results for mass and transfer of viscous fluid due to stretching sheet were developed by Magyari and Keller [22]. To further understand the boundary layer fluid flow along with heat transfer characteristics over a moving surface the readers are recommended to study [23–33].

Keeping in view of importance of heat transfer phenomena due to fluid flow in thermal systems, Choi [34] introduced the concept of nanofluids, by including solid additive (nanoparticles) having size of less than 100 nm in the conventional fluids. The nanoparticles are usually made of made of oxide ceramics CuO (Copper Oxide), Al_2O_3 (Aluminium Oxide) and metal nitrides SiN (Silicon Nitride), AlN (Aluminium Nitride) etc. The metallic particles change the heat conduction characteristics and transport properties of base fluids like water (H_2O), methanol (meth) and ethylene glycol (EG) etc. The enhanced thermal properties of nanofluids are the main features of nanofluids. Nanofluids tends to increase the heat transfer rate and because of this they have applications in industrial processes like the coolant in nuclear reactors, heat flow controller in heat valves, radiators of cars and vehicles temperature of frontal can be reduced by using nanofluids. The cooling and heating of water with nanofluids has power to preserve trillion Btu of energy [35]. The ability of nanofluids to conduct heat rapidly can be used to cool down the computer processors. In medical sciences, cancer patients can be treated with the help of drugs and radiations with iron base nanofluids [36–38]. Eastman *et al.* [39] investigated the thermal conductivity enhancement in Cu-Ethylene glycol (EG) nanofluids. After the Cu nanoparticles dispersed in ethylene glycol about 0.3 vol % of average diameter, 10 nm, they noted that the thermal conductivity of ethylene glycol has been increased by up to 40%. Further they compared Copper-Ethylene glycol $Cu-EG$ with Copper-oxide Ethylene glycol $CuO - EG$ and concluded that $Cu - EG$ is better thermal conductor then $CuO - EG$. There are numerous work and studies carried out on the physical characteristics of nanofluids particularly on heat transfer and boundary layer flow. The detailed review of literature can be found in the review research papers of Wang *et al.* [40] and Keblinski *et al.* [41]. Buongiorno [42] concluded nanofluids have better stability with better wetting, spreading and dispersion capabilities on the surface of solid when compared with ordinary fluids. Recent additions considering nanofluids with heat and mass transfer in various physical situations are given by [43–49]

Solar thermal system is one of key area where use of nanofluids improved the performance of thermal systems. Solar thermal systems consists of three main parts, the solar energy collection system, the heat storage medium and the heat circulation system. Most popular types of thermal solar systems are power tower systems, parabolic dish and trough collectors [50]. The latest research of solar energy emphasized on improvement of efficiency of solar thermal collector systems. The efficiency of any solar thermal system depends on the thermophysical characteristics of operating fluid, volume fraction of nanoparticles, shape of the nanoparticles and the geometry of fluid flowing system. The properties of operating fluids include viscosity, density, thermal conductivity, specific heat at high temperature as well as the velocity of the flow [51, 52]. Chaji *et al.* [53] experimented on flat thermal solar collectors using TiO_2-water nanofluid with the aim to study the collectors efficiency corresponding to nanoparticles concentration and the flow rate. They found that by adding the nanoparticles to water, the collector's efficiency increases between 2.6% to 7% relative to the base fluid. Ghasemi and Ahangar [54] numerically investigated the thermal field and thermal efficiency of parabolic trough collectors with Cu-water nanofluid and conclude that the solar collector with nanofluid is more efficient when compared with conventional collector. The inclusion of copper nanoparticles considerably increase the heat gain capacity of solar collector. Sharma and Kundan [55] in their experimental setup for parabolic solar collector compare the efficiency of ordinary fluid with aluminum-water nanofluid and copper oxide nanofluid. It is concluded that the aluminum water nanofluid improve the efficiency of solar collector between 1% to 2.55%. Whereas the use of copper oxide nanofluid improve the efficiency by 0.95% to 3.05%. Bellos *et al.* [52] presented that the efficiency of parabolic trough collectors with sine geometry improved by 4.25% if nanofluids are used as operating fluids instead of thermal oil or pressurized water. Recently [56, 57] independently used carbon nanotube nanofluids as working fluids to examine the efficiency of U-tube thermal solar collectors. The use of carbon nanotube nanofluids not only improve the efficiency of solar collectors they also reduced the CO_2 emissions. Kim *et al.* [57] also compared the efficiency of carbon nanotube nanofluids with Al_2O_3, CuO, SiO_2 and TiO_2 nanofluids. Their results indicated that the greatest efficiency is obtained at 62.8% when carbon nanotube nanofluids are used. Finally the review article of Muhammad *et. al* [58] covered almost all the literature of past ten years on use of nanofluids and enhancement in thermal efficiency of solar collectors. Recent survey on nanofluid flows in solar thermal collector are presented in [59–68].

Magnetohydrodynamics (MHD) is the study of electrically conducting fluid in the existence of magnetic field. MHD was first exposed by Micheal Faraday in 1832. Whereas the MHD fluid flow was introduced by Swedish physicist, Alfven [69]. The MHD flow and heat transfer characteristics of nanofluids past a stretching surface have significant industrial applications such as liquid metal flow, optical switches, geothermal energy extraction, plasma flow, MHD generators, and MHD flow meters, etc. It plays an important role to control the velocity and heat transfer rate of the thermal systems. Many researchers tend to discuss MHD flow into their models. Hakeem *et al.* [70] examined the impact of MHD on the second order partial slip flow of nanofluids over a stretching/ shrinking sheets with thermal radiation. They used the analytical hyper-geometric function and numerical shooting techniques and concluded that the skin friction factor is higher for $Al - H_2O$ and lowest for $Au - H_2O$ in both cases of stretching and shrinking sheets. Further, they observed that the growing values of magnetic field parameter vanishes the lower branch solution of shrinking sheet. Hsiao [71] scrutinized the influence of Lorentz forces and viscous dissipation of micropolar nanofluid passing a stretching surface by using Buongiorno's mathematical model. It was noticed the temperature profiles rises with increase in Eckert and Prandtle numbers. Furthermore, the rate of heat transfer is also increased for increasing the values of these numbers. Qayyum *et al.* [72] investigated analytically the magneto flow of $3rd$ grade nanofluid past a stretching surface with variable thickness and convective boundary conditions. They exhibited the velocity and temperature distributions rises with raising values of third grade fluid and thermal conjugate parameters respectively. Khan *et al.* [73] used the shooting technique to obtain the numerical solutions of inclined magnetohydrodynamic Williamson fluid flow over a nonlinear stretching sheet with cumulative effects of variable viscosity in the presence of nanoparticles. They concluded that increasing values of angle of inclination, Hartmann number and variable viscosity showed the reduction in velocity profile. On the other hand velocity gradient rises with higher values of Harmann number. Eid *et al.* [74] analyzed two-dimensional MHD flow of Carreau nanofluid passing a permeable stretching surface with thermal radiation. They utilized the shooting scheme for the numerical results and discussed the effects of different physical parameters effecting flow and heat transfer. They found the thickening of thermal boundary layer as concentration of nanoparticle volume fraction is increased in the base fluid. Kho *et al.* [75] used the numerical shooting technique to solve the Casson nanofluid flow induced by the stretching sheet with the impact of Lorentz forces, permeability and thermal radiation. They determined that the velocity gradient and heat transfer rate drops at the boundary surface as Casson and magnetic parameters increases in the fluid. For other studies regarding MHD nanofluid flows one can consult [76–83].

It is well known, the particles used in the preparation of nanofluids have impact on heat transfer of the system. However little attention is given to study the effect of nanoparticles shapes on heat transfer characteristics of nanofluids. Choi [34] observed that the heat transfer is maximized when nanoparticles are spherical shaped. The reason he described for greater heat transfer is the greater surface area of spherical particles when compared with non-spherical particles. The effect of nanoparticles shape on thermodynamic efficiency of tube and shell shaped heat exchangers are exhibited by Elias *et al.* [84]. They observed the better heat transfer rate for the cylindrical shaped nanoparticles. On the other hand, entropy generation rate is also higher for cylindrical shaped nanoparticle. Mahian *et al.* [85] scrutinized the influence of nanoparticles shape and tube material on the performance of flat plate mini-channel thermal solar system. Nanoparticles of platelet, blade, cylinder, and brick shapes were considered for the study. The findings include the lowest rate of temperature increase for platelet shaped nanoparticles. Whereas, the entropy generation analysis indicate the minimum rate for the cylindrical shaped nanoparticles. Ellahi *et al.* [86] considered the Brinkman nanofluid model to investigate the impact of $HFE - 7100$ fluid over a wedge. The influence of porous medium, entropy generation and nanoparticles shapes of needle, disk and sphere are taken into consideration. They concluded that needle–shaped nanoparticles results is the maximum temperature in the boundary layer while the minimum temperature are observed in the case of sphere-shaped nanoparticles. It is also concluded when one choose disk-shaped particles the $HFE - 7500$ fluid showed greater heat transfer ability. The entropy is highest for the needle-shaped nanoparticles as well. Sheikholeslami and Bhatti [87] used spherical, brick, cylinder and platelet shaped nanopartices in their numerical study of nanofluid forced convective heat exchange in a permeable annulus. They observed the highest rate of heat transfer for the platelet shaped nanoparticles. Xu and Chen [88] presented the heat exchange of Marangoni boundary layer flow for Cattaneo-Christov heat flux theory. In their results, spherical shaped nanoparticles provide the greatest performance for heat exchange enhancement. The reason for this behavior is that spherical particles have a larger surface area than non-spherical particles. The analysis is based on sphere, hexahedron, tetrahedron, cylinder and lamina shaped nanoparticles and $Cu - H_2O$ nanofluid. Sheikholeslami [89] used the control volume finite element method (CVFEM) and scrutinized the impact of Lorentz forces on $Cu - H_2O$ nanofluid convective flow in a porous cavity considering common geometrical shapes for nanoparticles. The observation was that the platelet shaped particles lead to greatest heat transfer rate. Tausif *et al.* [90] used the Brinkman nanofluid model to examine the impact of Lorentz force on the Casson fluid with Zirconium dioxide (ZrO_2) nanoparticles. Their model include study of four dissimilar shapes of nanoparticles (i.e. cylinder, platelet, brick and blade). In their research, they concluded that cylindrical-shaped nanoparticles show extreme temperature when compared to the other shaped particles due to its maximum thermal conductivity. Recently, Shen *et al.* [91] introduced the Cattaneo heat flux model for Maxwell viscoelastic nanofluid over a vertical sheet with natural convection and considered the five different types of nanoparticle shapes containing sphere, hexahedron, tetrahedron, column and lamina. They adopted the numerical finite difference scheme with $L1$-algorithm to get the solution. The results clearly indicated that the sphere shaped nanoparticles have the greatest rate of heat transfer and the lowest convective heat exchange rate. The skin friction factor and convective heat exchange reduces with increase in magnetic parameter and the temperature fractional parameter have opposite impact. Recent contributions regarding wall slip condition and nanoparticle shapes are presented in [92–97].

Hybrid nanofluids were introduced by Suresh [98] to further enhance the positive features of nanofluids. Hybrid nanofluids are constructed by the mixture of two different types of nanoparticles. The recent research in the field of nanofluids is focused towards thermal systems using hybrid nanofluids. However it is imperative to comprehend the impacts of different types of the nanoparticles, nanoparticles shapes, nanoparticles concentration in the base fluid and the nanofluid's thermophysical properties. Devi and Anjali [99] used RK-Fehlberg integration method to study the three-dimensional flow of Copper-Alumina/water ($Cu -$

$Al_2O_3/water$) hybrid nanofluid. The flow is induced by the unidirectional linear stretching of surface with consideration of Lorentz forces. The Numerical results gave the impression that heat exchange rate of $Cu - Al_2O_3/water$ hybrid nanofluid is greater than the $Cu - water$ nanofluid. Afrand *et al.* [100] examined the impact of temperature distribution and nanoparticles concentration on rheological behavior of magnetite ferrofluid-Silver/Ethylene glycol ($Fe_3O_4 - Ag/EG$) hybrid nanofluid. Hayat and Nadeem [101] considered the three dimensional Brinkman hybrid nanofluid model to investigate the heat transfer characteristics of Copper-oxide/water ($CuO/water$) and Silver-Copper-oxide/water ($Ag - CuO/water$) nanofluids over a linearly stretching, rotating surface with thermal radiation and homogeneous-heterogeneous reactive flow. Their results deducted that the hybridity enhanced the temperature profile along with the rate of heat transfer at the boundary of the surface. Ghadikolaei *et al.* [102] scrutinized the thermophysical properties of MHD Titanium-Copper/water ($TiO_2 - Cu/H_2O$) hybrid nanofluid with common geometrical shapes factor for nanoparticles. Hussian *et al.* [103] pondered at the flow of a hybrid nanofluid containing Alumina-Copper/water ($Al_2O_3 - Cu/water$) flowing through an open cavity with an adiabatic square obstacle inside the cavity. They used the finite element method for the numerical solutions and discussed the impact of different physical parameters on hybrid nanofluid. Further detail regarding the flow and heat transfer characteristics of hybrid nanofluids can be found in [104–109].

Literally speaking the entropy of a system refers to the disorder of the system. This means that the system is unable to use 100% of useful energy. In an ideal system where we are able to conserve the energy contained in the system perfectly, the entropy of that system is zero but in actual world this is not the case. There is a loss of energy in one form or the other thus, entropy is enhanced all the time. Here aim is to find ways to minimize this loss in the form of entropy. This makes entropy minimization an important task in any industrial setup. The researchers have been analyzing the entropy generation and looking for methods of reducing it. Entropy generation emphasized the importance of irreversible factors associated to heat transfer, friction, and other non ideal processes within a system (for details see Bejan [110]). Qing *et al.* [111] examined the volumetric total entropy generation on Casson nanofluid flow passing through a permeable stretching sheet with magnetic effects. They used the numerical successive linearization method and found that the increase in Hartmann number, permeability parameter, Reynolds and Brinkman numbers causes an increase in the entropy generation. Bhatti *et al.* [112] used the numerical scheme of Chebyshev spectral collocation and investigate the entropy generation of MHD Powell-Eyring nanofluid over a porous stretching sheet. They concluded that the entropy distribution rises by raising values of Hartmann number and the radiation parameter. Akbarzadeh *et al.* [113] applied the finite volume approach to investigate the entropy generation and thermohydraulic performance of a wavy channel with three corrugation profiles i.e. sinusoidal, trapezoidal, and triangular shapes. Mehrali *et al.* [114] synthesized graphene oxide-magnetite-ferro ($GO - Fe_3O_4$) hybrid nanofluid using graphene oxide, iron salts and tannic acid for the process of redundancy and stabilization. It was observed, the use of hybrid nanofluid increases the overall thermal conductivity of the system by 11%. They also observed that heat transfer performance of $GO - Fe_3O_4$ hybrid nanofluid improve with the application of magnetic field and the entropy is reduced by upto 41% on the use of graphene instead of distilled water. Recently, Sithole *et al.* [115] examined the entropy and chemical reaction effects on $2nd$ grade nanofluid over a heated stretching surface considering MHD and non-linear thermal radiation. The results showed the entropy of the system increases for higher values of Hartmann, Reynolds and Brinkmann numbers and decreases with greater values of temperature difference ratio parameter. Similar analysis of entropy generation on nanofluid with stretching surface taking different geometries are carried out in [116–124].

Emphasis in the past on the heat exchange has been on the use of the Fourier's law [125] of heat conduction. Fourier's law of heat conduction produces parabolic equation. This means that any initial change is felt promptly throughout the complete substance. To address this issue, Cattaneo [126] extended the Fourier law of heat conduction by including the thermal relaxation time in which the heat is transferred by the propagation of thermal waves at low speed. Later, Christov [127] extended the Cattaneo model by the application of Oldroyd's upper-convective derivatives for time in order to have the material-invariant formulation. A comprehensive research survey on Cattaneo-Christov heat flux model of nanofluids are presented in [128–135].

In most of the aforementioned studies Newtonian fluid models are considered for convective transport of nanofluids. However nanofluids donot behave as Newtonian fluids in real situation. Therefore it is more suitable to consider non-Newtonian fluids model for nanofluids. Ellahi *et al.* [136] used optimal homotopy asymptotic method (OHAM) to find the exact solution of Power-law nanofluid with copper nanoparticles by using the Brinkman nanofluid model. They found that the velocity profile of shear thinning fluids falls when nanoparticle volume fraction is increased. Furthermore, the temperature and heat flux of shear thinning fluid enlarged by improvement of particle volume concentration (PVC) while enhancement in temperature with small size of particle is detected. Eid *et al.* [137] analyzed two dimensional MHD flow of a Carreau nanofluid passing a permeable nonlinear surface with thermal radiation. They utilized the shooting scheme and explored the influence of different physical parameters on nanofluid flow and heat transfer. Their efforts concluded that the rate of heat transfer reduces with increasing thermal radiation and the opposite behaviour is seen with increasing values of magnetic parameter. Sravanthi *et al.* [138] computationally analyzed the Maxwell nanofluid flow including the Lorentz force effect over a porous exponentially stretching surface in the existence of homogeneous-heterogeneous heat source. For raising values of heat source rate the temperature profile increases and reduces the convection heat exchange capacity. The increase in heat sink increases the strength of convective heat exchange and lowers the nanofluid temperature. Kho *et al.* [139] used shooting technique to solve the Casson nanofluid flow induced by the stretching sheet with porous media and thermal radiation effects. Khan *et al.* [140] analytically solved the electrically conducting mixed convective flow of Powell-eyring nanofluid over an inclined sheet. More recently, discussions on non-Newtonian nanofluids can be found in [141–148] and in references therein.

It is well known fact that the viscosity and thermal conductivity are not constants when the temperature of the nanofluid is very high. Irfan *et al.* [149] numerically investigated the problem of 3-dimensional convective flow of Carreau nanofluid over a bidirectional stretching sheet in the existence of heat absorption and temperature dependent thermal conductivity. In their research, influence of variable thermal conductivity parameter was opposite to unsteadiness parameter on concentration and temperature profiles for both $n < 1$ and $n > 1$ (n is power law index). Reddy *et al.* [150] presented the effects of Lorentz forces on the Williamson nanofluid over a non-flat stretching surface with thermal radiation, variable thickness and temperature dependent thermal conductivity. They used the spectral quasilinearization method (SQLM) and found that the influence of variable thermal conductivity parameter reduces the temperature gradient at the boundary surface. Furthermore, they noticed thats velocity distribution reduces for higher values of Williamson parameter and its also deceases the thinking level of momentum boundary layer. Khan *et al.* [151] discussed 3-dimensional flow of Sisko magneto-nanofluid past a stretching sheet with the impact of heat source and variable thermal conductivity. They used the Buongiorno nanofluid model and detected that for increasing values of temperature dependent thermal conductivity the local Nusselt number increases for both shear thickening and thinning fluids. A few recent contributions on variable thermophysical properties of nanofluids can be seen in [152–155].

In the light of aforementioned studies and the detailed survey of literature on nanofluids flow and heat transfer, authors believe that the limited work is carried out to study non-Newtonian model for nanofluids along with the variable thermophysical properties. Keeping above in view this thesis present the flow, heat transfer and volumetric entropy generation analysis for thermal system involving non-Newtonian nanofluids e.g. (Maxwell, Powell-Eyring and Casson nanofluids). The interest lies in the numerical aspect of the heat transfer phenomena. The solution to the mathematical model have been achieved via finite difference scheme named Keller box method. Graphical interpretations have been used to study the numerical solution.

1.2 Thesis Contribution

In the present work, we consider two-dimensional unsteady, laminar, incompressible flow of non-Newtonian nanofluids over a porous stretching sheet. The flow is generated due to the stretching of the sheet. The following four models are considered for the non-Newtonian nanofluids.

- Maxwell nanofluid model.
- Powell-Eyring nanofluid model.
- Casson nanofluid model.
- Casson hybrid nanofluid model.

The governing equations of flow, heat transfer and volumetric entropy generation analysis are modeled under boundary layer approximations using Tiwari and Das model [156] for non-Newtonian nanofluids. The slip interface conditions are assumed at the interface of fluid-solid boundary. The analysis are presented considering the effect of

- Uniform applied magnetic field (MHD).
- Porous medium.
- Variable thermal physical properties.
- Thermal radiation.
- Cattaneo-Christov heat flux model.
- Different types of nanopartciles.
- Nanoparticle shape factor.
- Single phase model.

1.3 Objectives

The objective of thesis/research is to develop and understand non-Newtonian nanofluids based on Tiwari and Das model [156]. The model is applied to different problems in different flow patterns and are solved numerically for flow, heat transfer and entropy generation of non-Newtonian nanofluids, influenced by the applied magnetic field, slip condition, thermal radiation, variable thermal physical properties, porous medium, Cattaneo-Christov heat flux model, nanoparticle shape effects and hybrid models of nanofluids etc.

1.4 Thesis Outline

The present thesis aims to numerically study the thermal systems containing non-Newtonian nanofluids. The nanofluids occupies the space over the porous flat surface and the flow is induced by the non-uniform stretching of the surface. The mathematical models presented here also includes the impact of variable viscosity, variable thermal conductivity, MHD, thermal radiation, particle shape, entropy generation and the hybrid nanofluid. This thesis is organized in the following chapters.

- A brief literature survey in **Chapter 1** relating nanofluids, types of nanofluids methods of its synthesis and effect of external forces have been discussed. The recent trends in nanofluid research have also been cited.

- In **Chapter 2**, basic definitions related to flow heat transfer in nanofluids are presented. The thermophysical properties of various nanomaterial have been given. The mathematical models that are used in present research have been discussed in detail as well as the solution methodology.

- Entropy generation analysis due to magnetohydrodynamic Maxwell nanofluid flow across a stretching sheet with thermal radiation and variable thermal conductivity is presented in **Chapter 3**. This chapter's contents are published in the journal **Open Physics**.

- **Chapter 4** consists of entropy analysis of Powell-Eyring nanofluid past a stretching surface with temperature dependent thermal conductivity and thermal radiation. The mathematical model also includes the effects of different nanoparticles shape. This chapter's contents are published in the journal **Results in Physics**.

- In **Chapter 5** mathematical model presented in the previous chapters is extended to include the heat transfer and entropy analysis using the Cattaneo-Christov heat flux model for the Casson nanofluid flow. The contents of this chapter are published in journal **Results in Physics**.

- Finally the Cattaneo-Christov based study of Casson hybrid nanofluid flow past a stretching sheet with entropy generation is carried out in **Chapter 6**. The contents of this chapter are published in **Applied Nanoscience**.

- Conclusion and the future directions of the present research are presented in **Chapter 7**.

Chapter 2

Definitions and Governing Equations

In this chapter, basic definitions of fluid mechanics, nanofluids and conservation laws to obtain differential forms of fundamental governing equations are discussed. Furthermore, a brief description of Keller box method is also given in the last section.

2.1 Boundary layer

The idea of boundary layer was first introduced by Ludwig Prandtl in 1904. Ludwig Prandtl gave the basic idea of the boundary layer for moving fluid over a surface (see for example, Prandtl [4]). It is the close layer of fluid flow near solid region where the viscosity effects are significant. The flow in this layer is usually laminar. The boundary layer thickness is the measure of the distance apart from the surface. There are two types of boundary layers:

- Hydrodynamic boundary layer.
- Thermal boundary layer.

2.2 Newton's Law of Viscosity

The relationship in which shear stress is directly and linearly proportional to the rate of deformation is known as Newton law of viscosity (see for details, George and Qureshi [157]). Mathematically, it is expressed as

$$\tau_{xy} \propto \left(\frac{du}{dy}\right), \tag{2.1}$$

$$\tau_{xy} = \mu\left(\frac{du}{dy}\right). \tag{2.2}$$

In the above expression, τ_{yx} is the shear stress, x and y represents horizontal and vertical coordinates, u is the horizontal component of velocity, $\frac{du}{dy}$ is the deformation rate. Fluids in which viscous stresses that arises from flow are linearly proportional to the local strain rate are known as Newtonian fluids. When shear stress is not directly proportional to the velocity gradient are defined as non-Newtonian fluid. Mathematically, it can be written as

$$\tau_{xy} \propto \left(\frac{du}{dy}\right)^{n}, \ n \neq 1 \tag{2.3}$$

$$\tau_{xy} = \mu_a\left(\frac{du}{dy}\right), \ \mu_a = j\left(\frac{du}{dy}\right)^{n-1}, \tag{2.4}$$

where n and j represents the index of flow behaviour and consistency, respectively. Paints, toothpaste, shampoo, blood, ketchup, drilling muds and biological fluids are good examples of non-Newtonian fluids.

2.3 Heat Transfer Mechanism

Heat transfer (see for example, Incropera *et al.* [158]) is a process in which transfer of thermal energy occurs due to temperature difference between the physical system. There are three elementary modes of heat transfer i.e. conduction, convection and radiation.

2.3.1 Conduction

The process of heat transfer which occurs because of the molecular collisions is known as conduction. Fourier developed a law known as Fourier's law of heat conduction. Mathematical form of the law is

$$Q = -kA^* \left(\frac{d\Theta}{dx} \right). \tag{2.5}$$

Here $\frac{d\Theta}{dx}$ represents the temperature gradient. This is called the Fourier law.

2.3.2 Convection

It is defined as heat transfer in fluids from a part with high temperature to a part where temperature is comparatively low. In convection, Newton's law of cooling governs heat transfer rate with the expression

$$Q = hA^* \left(\Theta_w - \Theta_\infty \right). \tag{2.6}$$

2.3.3 Radiation

Radiation occurs by photons of light or waves emitted from a surface volume. Radiation can happen in vacuum also. Stefan-Boltzmann law is used to calculate the amount transfer through radiation. Mathematically

$$Q = \sigma^* \cdot \Theta^4. \tag{2.7}$$

2.4 Maxwell Fluid

A Maxwell fluid is a viscoelastic fluid with characteristic features of elasticity as well as viscosity. It is famous after the name of James Clerk Maxwell, who introduced the model in 1867. The rheology of Maxwell fluid is given by the following mathematical relation

$$\left(1+\lambda\frac{D}{Dt}\right)S^{*}=\mu A_{1}. \tag{2.8}$$

Here λ is a fluid relaxation time, $\frac{D}{Dt}$ is a upper convected derivative, S^{*} is a extra stress tensor and A_1 is a Rivlin-Erickson tensor. The boundary layer for 2-dimensional flow of upper-convected Maxwell fluid was first derived by Harris [159]. The modeled boundary layer equations for continuity, momentum and energy for the two-dimensional flow in the cartesian coordinate systems for Maxwell fluid are as follows (see for example, Mukhopadhyay *et al.* [160]).

2.4.1 Law of Conservation of Mass

The law of conservation of mass i.e. continuity equation (see for example, Papanastasiou *et al.* [161]) is given by

$$\frac{\partial\rho}{\partial t}+\nabla.(\rho\mathbf{V})=0, \tag{2.9}$$

where

$$\nabla=\left(\frac{\partial}{\partial x},\frac{\partial}{\partial y}\right)=0. \tag{2.10}$$

The unsteady velocity field for two-dimensional flow given this

$$\mathbf{V}=\left(u(x,y,t),v(x,y,t)\right). \tag{2.11}$$

For incompressible fluid equation (2.9) expressed as

$$\nabla.\mathbf{V}=0, \tag{2.12}$$

$$\left(\frac{\partial}{\partial x},\frac{\partial}{\partial y}\right).\left(u(x,y,t),v(x,y,t)\right)=0, \tag{2.13}$$

$$\frac{\partial u}{\partial x}+\frac{\partial v}{\partial y}=0. \tag{2.14}$$

2.4.2 Momentum Equation for Maxwell Fluid

The law of conservation of momentum (for example, Ruban and Gajjar [162]) is given by

$$\rho a_i = \nabla.\tau, \tag{2.15}$$

where

$$a_i = \left(\frac{d\mathbf{V}}{dt}\right) \qquad \text{and} \qquad \tau = -PI + S^*. \tag{2.16}$$

In equation (2.15)-(2.16), τ is a cauchy stress tensor, $\frac{d}{dt}$ is a material time derivative, P is a pressure, I is a unit tensor and S^* is defined in equation (2.8)

$$\rho\left(\frac{d\mathbf{V}}{dt}\right) = -\nabla.P + \nabla.S^*. \tag{2.17}$$

Eliminating S^* in equation (2.8) and (2.17), we obtained the following equation

$$\rho\left(1 + \lambda\frac{D}{Dt}\right) a_i = -\nabla P + \mu(\nabla.A_1), \tag{2.18}$$

$$\left(1 + \lambda\frac{D}{Dt}\right) a_i = -\nabla P + \nu(\nabla.A_1), \tag{2.19}$$

where

$$A_1 = L_1 + L_1^T \qquad \text{with} \qquad L_1 = grad\ \mathbf{V}. \tag{2.20}$$

Defined in general

$$L_1 = \begin{bmatrix} \frac{\partial u}{\partial x} & \frac{\partial u}{\partial y} & \frac{\partial u}{\partial z} \\ \frac{\partial v}{\partial x} & \frac{\partial v}{\partial y} & \frac{\partial v}{\partial z} \\ \frac{\partial w}{\partial x} & \frac{\partial w}{\partial y} & \frac{\partial w}{\partial z} \end{bmatrix}. \tag{2.21}$$

For two-dimensional case

$$L_1 = \begin{bmatrix} \frac{\partial u}{\partial x} & \frac{\partial u}{\partial y} & 0 \\ \frac{\partial v}{\partial x} & \frac{\partial v}{\partial y} & 0 \\ 0 & 0 & 0 \end{bmatrix}, \qquad L_1^T = \begin{bmatrix} \frac{\partial u}{\partial x} & \frac{\partial v}{\partial y} & 0 \\ \frac{\partial u}{\partial y} & \frac{\partial v}{\partial y} & 0 \\ 0 & 0 & 0 \end{bmatrix}. \tag{2.22}$$

Substitution (2.22) into (2.20) gives

$$A_1 = \begin{bmatrix} 2\frac{\partial u}{\partial x} & \frac{\partial u}{\partial y} + \frac{\partial v}{\partial y} & 0 \\ \frac{\partial v}{\partial x} + \frac{\partial u}{\partial y} & 2\frac{\partial v}{\partial y} & 0 \\ 0 & 0 & 0 \end{bmatrix}. \tag{2.23}$$

The upper convected derivative a_i are defined as

$$\frac{Da_i}{Dt} = (\mathbf{V}.\nabla)a_i - L_1 a_i \quad \text{for} \quad i = 1, 2 \tag{2.24}$$

$$\frac{Da_1}{Dt} = u\frac{\partial a_1}{\partial x} + v\frac{\partial a_1}{\partial y} - a_1\frac{\partial u}{\partial x} - a_1\frac{\partial u}{\partial y}, \tag{2.25}$$

$$\frac{Da_2}{Dt} = u\frac{\partial a_2}{\partial x} + v\frac{\partial a_2}{\partial y} - a_2\frac{\partial v}{\partial x} - a_2\frac{\partial v}{\partial y}. \tag{2.26}$$

From equations (2.25) and (2.26)

$$a_1 = \frac{\partial u}{\partial t} + u\frac{\partial u}{\partial x} + v\frac{\partial u}{\partial y}, \tag{2.27}$$

$$a_2 = \frac{\partial v}{\partial t} + u\frac{\partial v}{\partial x} + v\frac{\partial v}{\partial y}. \tag{2.28}$$

Using (2.27) and (2.28) in (2.25) and (2.26)

$$\begin{aligned} \frac{Da_1}{Dt} = {} & u\frac{\partial}{\partial x}\left(\frac{\partial u}{\partial t} + u\frac{\partial u}{\partial x} + v\frac{\partial u}{\partial y}\right) + v\frac{\partial}{\partial y}\left(\frac{\partial u}{\partial t} + u\frac{\partial u}{\partial x} + v\frac{\partial u}{\partial y}\right) \\ & - \left(\frac{\partial u}{\partial t} + u\frac{\partial u}{\partial x} + v\frac{\partial u}{\partial y}\right)\frac{\partial u}{\partial x} - \left(\frac{\partial u}{\partial t} + u\frac{\partial v}{\partial x} + v\frac{\partial v}{\partial y}\right)\frac{\partial u}{\partial y}, \end{aligned} \tag{2.29}$$

$$\begin{aligned} \frac{Da_2}{Dt} = {} & u\frac{\partial}{\partial x}\left(\frac{\partial v}{\partial t} + u\frac{\partial v}{\partial x} + v\frac{\partial v}{\partial y}\right) + v\frac{\partial}{\partial y}\left(\frac{\partial v}{\partial t} + u\frac{\partial v}{\partial x} + v\frac{\partial v}{\partial y}\right) \\ & - \left(\frac{\partial v}{\partial t} + u\frac{\partial u}{\partial x} + v\frac{\partial u}{\partial y}\right)\frac{\partial v}{\partial x} - \left(\frac{\partial v}{\partial t} + u\frac{\partial v}{\partial x} + v\frac{\partial v}{\partial y}\right)\frac{\partial v}{\partial y}. \end{aligned} \tag{2.30}$$

x-component of $(\nabla.A_1)$ is

$$(\nabla.A_1)_x = \left(\frac{\partial}{\partial x}, \frac{\partial}{\partial y}, 0\right)\left(2\frac{\partial u}{\partial x}, \left(\frac{\partial u}{\partial y} + \frac{\partial v}{\partial x}\right), 0\right), \tag{2.31}$$

$$(\nabla.A_1)_x = \left(2\frac{\partial^2 u}{\partial x^2} + \frac{\partial^2 u}{\partial y^2} + \frac{\partial^2 v}{\partial x \partial y} + 0\right). \tag{2.32}$$

y-component of $(\nabla.A_1)$ is

$$(\nabla.A_1)_y = \left(\frac{\partial}{\partial x}, \frac{\partial}{\partial y}, 0\right)\left(\left(\frac{\partial v}{\partial x} + \frac{\partial u}{\partial y}\right), 2\frac{\partial v}{\partial y}, 0\right), \tag{2.33}$$

$$(\nabla.A_1)_y = \left(\frac{\partial^2 v}{\partial x^2} + 2\frac{\partial^2 v}{\partial y^2} + \frac{\partial^2 u}{\partial x \partial y} + 0\right). \tag{2.34}$$

Using equation (2.32) and(2.34) into (2.19), the x-component will be

$$\begin{aligned} \frac{\partial u}{\partial t} + u\frac{\partial u}{\partial x} + v\frac{\partial u}{\partial y} + \lambda\left(u^2\frac{\partial^2 u}{\partial x^2} + 2uv\frac{\partial^2 u}{\partial x \partial y} + v^2\frac{\partial^2 u}{\partial y^2}\right) \\ = -\frac{\partial P}{\partial x} + \nu\left(2\frac{\partial^2 u}{\partial x^2} + \frac{\partial^2 u}{\partial y^2} + \frac{\partial^2 v}{\partial x \partial y}\right). \end{aligned} \tag{2.35}$$

Using equation (2.32) and(2.34) into (2.19), the y-component will be

$$\begin{aligned} \frac{\partial v}{\partial t} + u\frac{\partial v}{\partial x} + v\frac{\partial v}{\partial y} + \lambda\left(u^2\frac{\partial^2 v}{\partial x^2} + 2uv\frac{\partial^2 v}{\partial x \partial y} + v^2\frac{\partial^2 v}{\partial y^2}\right) \\ = -\frac{\partial P}{\partial y} + \nu\left(\frac{\partial^2 v}{\partial x^2} + 2\frac{\partial^2 v}{\partial y^2} + \frac{\partial^2 u}{\partial x \partial y}\right). \end{aligned} \tag{2.36}$$

Considering the following assumptions of boundary layer approximations in (2.35) and (2.36),

$$\nu = o(\delta^2), \quad u = x = o(1), \quad v = y = o(\delta), \quad \lambda_1 = o(1), \quad \Theta = o(1). \tag{2.37}$$

The expression of momentum equation takes the form,

$$\frac{\partial u}{\partial t} + u\frac{\partial u}{\partial x} + v\frac{\partial u}{\partial y} = \nu\left(\frac{\partial^2 u}{\partial y^2}\right) - \lambda\left(u^2\frac{\partial^2 u}{\partial x^2} + v^2\frac{\partial^2 u}{\partial y^2} + 2uv\frac{\partial^2 u}{\partial x \partial y}\right). \tag{2.38}$$

2.5 Powell-Eyring Fluid

The Powell-Eyring fluid model is one of many non-Newtonian model. The constitutive equations of the Powell-Eyring model are derived from the theory of liquids and not from the empirical relationship as in the power-law model. It can correctly reduce at low and high shear rates to Newtonian flow behavior, while the power-law model describes an infinite effective viscosity at low shear rate and thus limits its range of applicability. The stress tensor for Powell-Eyring fluid is given by (see for example, Powell and Eyring *et al.* [163])

$$\tau_{ij} = \mu\left(\frac{\partial u_i}{\partial x_j}\right) + \frac{1}{\tilde{\beta}}\sinh^{-1}\left(\frac{1}{\varsigma^*}\frac{\partial u_i}{\partial x_j}\right), \tag{2.39}$$

where $\tilde{\beta}$, ς^* are the material constants.

2.5.1 Momentum Equation for Powell-Eyring Fluid

The law of conservation of momentum equation is defined in equation (2.15), where

$$a_i = \left(\frac{d\mathbf{V}}{dt}\right) \qquad and \qquad \tau = -PI + \tau_{ij}. \tag{2.40}$$

Here τ_{ij} is defined in (2.39) and further using (2.40) in (2.15), gives

$$\rho\left(\frac{d\mathbf{V}}{dt}\right) = -\nabla P + \nabla.\tau_{ij}. \tag{2.41}$$

Now consider

$$\sinh^{-1}\left(\frac{1}{\varsigma^*}\frac{\partial u_i}{\partial x_j}\right) \cong \left(\frac{1}{\varsigma^*}\frac{\partial u_i}{\partial x_j}\right) - \frac{1}{6}\left(\frac{1}{\varsigma^*}\frac{\partial u_i}{\partial x_j}\right)^3, \quad \left|\left(\frac{1}{\varsigma^*}\frac{\partial u_i}{\partial x_j}\right)\right| \leq 1. \tag{2.42}$$

Using (2.42) in (2.39), gives

$$\tau_{11} = \mu\left(\frac{\partial u_1}{\partial x_1}\right) + \frac{1}{\tilde{\beta}\varsigma^*}\frac{\partial u_1}{\partial x_1} - \frac{1}{6\tilde{\beta}\varsigma^{*3}}\left(\frac{\partial u_1}{\partial x_1}\right)^3, \tag{2.43}$$

where

$$(u_1, u_2, u_3) = (u, v, w) \tag{2.44}$$

are the velocity components,

$$(x_1, x_2, x_3) = (x, y, z) \tag{2.45}$$

are the cartesian coordinates.

$$\tau_{12} = \left(\mu + \frac{1}{\tilde{\beta}\varsigma^*}\right)\frac{\partial u}{\partial y} - \frac{1}{6\tilde{\beta}\varsigma^{*3}}\left(\frac{\partial u}{\partial y}\right)^3, \tag{2.46}$$

$$\tau_{21} = \left(\mu + \frac{1}{\tilde{\beta}\varsigma^*}\right)\frac{\partial v}{\partial x} - \frac{1}{6\tilde{\beta}\varsigma^{*3}}\left(\frac{\partial v}{\partial x}\right)^3, \tag{2.47}$$

$$\tau_{22} = \left(\mu + \frac{1}{\tilde{\beta}\varsigma^*}\right)\frac{\partial v}{\partial y} - \frac{1}{6\tilde{\beta}\varsigma^{*3}}\left(\frac{\partial v}{\partial y}\right)^3, \tag{2.48}$$

$$\tau_{13} = 0, \qquad \tau_{23} = 0, \qquad \tau_{31} = 0, \qquad \tau_{32} = 0, \qquad \tau_{33} = 0. \tag{2.49}$$

From (2.41) the x-component of the momentum equation is given by

$$\frac{\partial u}{\partial t} + u\frac{\partial u}{\partial x} + v\frac{\partial u}{\partial y} = -\frac{\partial P}{\partial x} + \left(\frac{\partial \tau_{11}}{\partial x} + \frac{\partial \tau_{12}}{\partial y}\right), \tag{2.50}$$

Using equation (2.43) and (2.46) in equation (2.50), we get

$$\begin{aligned}\rho\left(\frac{\partial u}{\partial t} + u\frac{\partial u}{\partial x} + v\frac{\partial u}{\partial y}\right) = -\frac{\partial P}{\partial x} + \frac{\partial}{\partial x}\left(\left(\mu + \frac{1}{\tilde{\beta}\varsigma^*}\right)\frac{\partial u}{\partial x} - \frac{1}{6\tilde{\beta}\varsigma^{*3}}\left(\frac{\partial u}{\partial x}\right)^3\right)\\ +\frac{\partial}{\partial y}\left(\left(\mu + \frac{1}{\tilde{\beta}\varsigma^*}\right)\frac{\partial u}{\partial y} - \frac{1}{6\tilde{\beta}\varsigma^{*3}}\left(\frac{\partial u}{\partial y}\right)^3\right),\end{aligned} \tag{2.51}$$

$$\begin{aligned}\rho\left(\frac{\partial u}{\partial t} + u\frac{\partial u}{\partial x} + v\frac{\partial u}{\partial y}\right) = -\frac{\partial P}{\partial x} + \left(\mu + \frac{1}{\tilde{\beta}\varsigma^*}\right)\frac{\partial^2 u}{\partial x^2} - \frac{3}{6\tilde{\beta}\varsigma^{*3}}\left(\frac{\partial u}{\partial x}\right)^2\frac{\partial^2 u}{\partial x^2},\\ +\left(\mu + \frac{1}{\tilde{\beta}\varsigma^*}\right)\frac{\partial^2 u}{\partial y^2} - \frac{3}{6\tilde{\beta}\varsigma^{*2}}\left(\frac{\partial u}{\partial y}\right)^2\frac{\partial^2 u}{\partial y^2}.\end{aligned} \tag{2.52}$$

Similarly from (2.41) the y-component of the momentum equation is given by

$$\frac{\partial v}{\partial t} + u\frac{\partial v}{\partial x} + v\frac{\partial v}{\partial y} = -\frac{\partial P}{\partial y} + \left(\frac{\partial \tau_{21}}{\partial x} + \frac{\partial \tau_{22}}{\partial y}\right), \tag{2.53}$$

Using equation (2.47) and (2.48) in equation (2.53), we get

$$\begin{aligned}\rho\left(\frac{\partial v}{\partial t} + u\frac{\partial v}{\partial x} + v\frac{\partial v}{\partial y}\right) = -\frac{\partial P}{\partial y} + \frac{\partial}{\partial x}\left(\left(\mu + \frac{1}{\tilde{\beta}\varsigma^*}\right)\frac{\partial v}{\partial x} - \frac{1}{6\tilde{\beta}\varsigma^{*3}}\left(\frac{\partial v}{\partial x}\right)^3\right)\\ +\frac{\partial}{\partial y}\left(\left(\mu + \frac{1}{\tilde{\beta}\varsigma^*}\right)\frac{\partial v}{\partial y} - \frac{1}{6\tilde{\beta}\varsigma^{*3}}\left(\frac{\partial v}{\partial y}\right)^3\right),\end{aligned} \tag{2.54}$$

$$\rho\left(\frac{\partial v}{\partial t}+u\frac{\partial v}{\partial x}+v\frac{\partial v}{\partial y}\right)=-\frac{\partial P}{\partial y}+\left(\mu+\frac{1}{\tilde{\beta}\varsigma^{*}}\right)\frac{\partial^2 v}{\partial x^2}-\frac{3}{6\tilde{\beta}\varsigma^{*^3}}\left(\frac{\partial v}{\partial x}\right)^2\frac{\partial^2 v}{\partial x^2},$$
$$+\left(\mu+\frac{1}{\tilde{\beta}\varsigma^{*}}\right)\frac{\partial^2 v}{\partial y^2}-\frac{3}{6\tilde{\beta}\varsigma^{*^2}}\left(\frac{\partial v}{\partial y}\right)^2\frac{\partial^2 v}{\partial y^2}. \tag{2.55}$$

Applying boundary layer approximation on (2.52) and (2.55), we obtain the following ODE

$$\frac{\partial u}{\partial t}+u\frac{\partial u}{\partial x}+v\frac{\partial u}{\partial y}=\left(\nu+\frac{1}{\rho\tilde{\beta}\varsigma^{*}}\right)\frac{\partial^2 u}{\partial y^2}-\frac{1}{2\tilde{\beta}\varsigma^{*^3}\rho}\left(\frac{\partial u}{\partial y}\right)^2\frac{\partial^2 u}{\partial y^2}. \tag{2.56}$$

2.6 Casson Fluid

Casson fluid is a kind of shear thinning fluid with an infinite viscosity at zero shear stress. The equations representing the basic form of incompressible Casson fluid with isotropic properties are given as (see for example, [164, 165])

$$\tau_{ij}=\begin{cases}2\left(\mu_B+\dfrac{p_y}{\sqrt{2\pi}}\right)e_{ij}, & \pi>\pi_c,\\[2em] 2\left(\mu_B+\dfrac{p_y}{\sqrt{2\pi_c}}\right)e_{ij}, & \pi<\pi_c.\end{cases} \tag{2.57}$$

Here μ_B, p_y, e_{ij}, $\pi=e_{ij}e_{ij}$ and π_c represents the plastic dynamic viscosity, yield stress, deformation direction component rate, the product of the component of rate of deformation with itself and the critical value of the product of the component of the strain tensor rate with itself, respectively.

2.6.1 Momentum Equation for Casson Fluid

The law of conservation of momentum equation and Cauchy stress tensor are defined in (2.15) and (2.40), respectively. And further using (2.15) in (2.40), gives

$$\rho\left(\frac{d\mathbf{V}}{dt}\right)=-\nabla P+\nabla.\tau_{ij}, \tag{2.58}$$

From equation (2.57)

$$\tau_{ij} = \mu_B \left(1 + \frac{1}{\beta}\right)(2e_{ij}). \tag{2.59}$$

In above equation $\beta = \frac{\mu_B\sqrt{2\pi_c}}{p_y}$ is the Casson parameter.

$$e_{ij} = \frac{1}{2}(L_1 + L_1^t). \tag{2.60}$$

Using (2.22) in above, we obtain

$$e_{ij} = \frac{1}{2}\begin{bmatrix} 2\frac{\partial u}{\partial x} & \frac{\partial u}{\partial y} + \frac{\partial v}{\partial y} & 0 \\ \frac{\partial v}{\partial x} + \frac{\partial u}{\partial y} & 2\frac{\partial v}{\partial y} & 0 \\ 0 & 0 & 0 \end{bmatrix}. \tag{2.61}$$

$$\tau_{11} = \mu_B \left(1 + \frac{1}{\beta}\right)\left(2\frac{\partial u}{\partial x}\right), \tag{2.62}$$

$$\tau_{12} = \mu_B \left(1 + \frac{1}{\beta}\right)\left(\frac{\partial u}{\partial x} + \frac{\partial v}{\partial x}\right), \tag{2.63}$$

$$\tau_{21} = \mu_B \left(1 + \frac{1}{\beta}\right)\left(\frac{\partial u}{\partial x} + \frac{\partial v}{\partial x}\right), \tag{2.64}$$

$$\tau_{22} = \mu_B \left(1 + \frac{1}{\beta}\right)\left(2\frac{\partial u}{\partial x}\right), \tag{2.65}$$

$$\tau_{13} = 0, \quad \tau_{23} = 0, \quad \tau_{31} = 0, \tag{2.66}$$

$$\tau_{32} = 0, \quad \tau_{33} = 0. \tag{2.67}$$

From (2.58) the x-component of the momentum equation is given by

$$\frac{\partial u}{\partial t} + u\frac{\partial u}{\partial x} + v\frac{\partial u}{\partial y} = -\frac{\partial P}{\partial x} + \left(\frac{\partial \tau_{11}}{\partial x} + \frac{\partial \tau_{12}}{\partial y}\right). \tag{2.68}$$

Using equation (2.62) and (2.63) in equation (2.68), we get

$$\begin{aligned} \rho\left(\frac{\partial u}{\partial t} + u\frac{\partial u}{\partial x} + v\frac{\partial u}{\partial y}\right) = -\frac{\partial P}{\partial x} &+ \frac{\partial}{\partial x}\left(\mu_B\left(1 + \frac{1}{\beta}\right)\left(2\frac{\partial u}{\partial x}\right)\right) \\ &+ \frac{\partial}{\partial y}\left(\mu_B\left(1 + \frac{1}{\beta}\right)\left(\frac{\partial u}{\partial x} + \frac{\partial v}{\partial x}\right)\right), \end{aligned} \tag{2.69}$$

$$\rho\left(\frac{\partial u}{\partial t}+u\frac{\partial u}{\partial x}+v\frac{\partial u}{\partial y}\right)=-\frac{\partial P}{\partial x}+2\mu_B\left(1+\frac{1}{\beta}\right)\left(\frac{\partial^2 u}{\partial x^2}\right)+\mu_B\left(1+\frac{1}{\beta}\right)\left(\frac{\partial^2 u}{\partial y^2}+\frac{\partial^2 v}{\partial x\partial y}\right). \tag{2.70}$$

From (2.58) the y-component of the momentum equation is given by

$$\frac{\partial v}{\partial t}+u\frac{\partial v}{\partial x}+v\frac{\partial v}{\partial y}=-\frac{\partial P}{\partial y}+\left(\frac{\partial \tau_{21}}{\partial x}+\frac{\partial \tau_{22}}{\partial y}\right), \tag{2.71}$$

Using equation (2.64) and (2.65) in equation (2.71), we get

$$\rho\left(\frac{\partial v}{\partial t}+u\frac{\partial v}{\partial x}+v\frac{\partial v}{\partial y}\right)=-\frac{\partial P}{\partial y}+\frac{\partial}{\partial x}\left(\mu_B\left(1+\frac{1}{\beta}\right)\left(\frac{\partial u}{\partial x}+\frac{\partial v}{\partial x}\right)\right)+\frac{\partial}{\partial y}\left(\mu_B\left(1+\frac{1}{\beta}\right)\left(2\frac{\partial u}{\partial x}\right)\right), \tag{2.72}$$

$$\rho\left(\frac{\partial v}{\partial t}+u\frac{\partial v}{\partial x}+v\frac{\partial v}{\partial y}\right)=-\frac{\partial P}{\partial y}+2\mu_B\left(1+\frac{1}{\beta}\right)\left(\frac{\partial^2 v}{\partial y^2}\right)+\mu_B\left(1+\frac{1}{\beta}\right)\left(\frac{\partial^2 v}{\partial x^2}+\frac{\partial^2 u}{\partial x\partial y}\right). \tag{2.73}$$

Applying boundary layer approximation on (2.70) and (2.73), we obtain the following ODE

$$\frac{\partial u}{\partial t}+u\frac{\partial u}{\partial x}+v\frac{\partial u}{\partial y}=\frac{\mu_B}{\rho}\left(1+\frac{1}{\beta}\right)\frac{\partial^2 u}{\partial y^2}, \tag{2.74}$$

2.7 Energy Equation

The energy equation (for example, Ruban and Gajjar [162]) for the fluid flow is defined as

$$\rho C_p\left(\frac{d\Theta}{dt}\right)=-\nabla .q. \tag{2.75}$$

Here q is defined by Fourier law

$$q=-k\nabla\Theta. \tag{2.76}$$

Here q is defined by Cattaneo-Christov heat flux model

$$q+\lambda^{*}\left[\frac{\partial q}{\partial t}+\mathbf{V}.\nabla .q-q.\nabla \mathbf{V}+(\nabla .\mathbf{V})q\right]=-k\nabla \Theta . \tag{2.77}$$

Using (2.12) the above equation becomes,

$$q+\lambda^{*}\left[\frac{\partial q}{\partial t}+\mathbf{V}.\nabla .q-q.\nabla \mathbf{V}\right]=-k\nabla \Theta . \tag{2.78}$$

Using (2.76) in (2.75), we get

$$\rho C_p\left(\frac{d\Theta}{dt}\right)=k\nabla^2\Theta , \tag{2.79}$$

where the time derivative $\frac{d}{dt}$ is defined as

$$\frac{d\Theta}{dt}=\frac{\partial \Theta}{\partial t}+(\mathbf{V}.\nabla)\Theta . \tag{2.80}$$

Using (2.80) in (2.79), we get

$$\rho C_p\left(\frac{\partial \Theta}{\partial t}+(\mathbf{V}.\nabla)\Theta\right)=k\nabla^2\Theta , \tag{2.81}$$

$$\rho C_p\left(\frac{\partial \Theta}{\partial t}+u\frac{\partial \Theta}{\partial x}+v\frac{\partial \Theta}{\partial y}\right)=k\left(\frac{\partial^2\Theta}{\partial x^2}+\frac{\partial^2\Theta}{\partial y^2}\right). \tag{2.82}$$

Eliminating q between (2.75) and (2.78), we get

$$\frac{\partial \Theta}{\partial t}+u\frac{\partial \Theta}{\partial x}+v\frac{\partial \Theta}{\partial y}=\frac{k}{(\rho C_p)}\left[\frac{\partial^2\Theta}{\partial x^2}+\frac{\partial^2\Theta}{\partial y^2}\right]$$
$$-\lambda^{*}\left[u\frac{\partial u}{\partial x}\frac{\partial \Theta}{\partial x}+v\frac{\partial v}{\partial y}\frac{\partial \Theta}{\partial y}+u\frac{\partial v}{\partial x}\frac{\partial \Theta}{\partial y}+v\frac{\partial u}{\partial y}\frac{\partial \Theta}{\partial x}+u^2\frac{\partial^2\Theta}{\partial x^2}+v^2\frac{\partial^2\Theta}{\partial y^2}+2uv\frac{\partial^2\Theta}{\partial x\partial y}\right] \tag{2.83}$$

After applying the boundary layer approximation on (2.82) in (2.83)

$$k=o(\delta^2),\quad u=x=o(1),\quad v=y=o(\delta),\quad \Theta=o(1). \tag{2.84}$$

We obtain the following final expressions

$$\frac{\partial \Theta}{\partial t} + u\frac{\partial \Theta}{\partial x} + v\frac{\partial \Theta}{\partial y} = \frac{k}{(\rho C_p)}\left[\frac{\partial^2 \Theta}{\partial y^2}\right]. \tag{2.85}$$

$$\frac{\partial \Theta}{\partial t} + u\frac{\partial \Theta}{\partial x} + v\frac{\partial \Theta}{\partial y} = \frac{k}{(\rho C_p)}\left[\frac{\partial^2 \Theta}{\partial y^2}\right]$$
$$-\lambda^*\left[u\frac{\partial u}{\partial x}\frac{\partial \Theta}{\partial x} + v\frac{\partial v}{\partial y}\frac{\partial \Theta}{\partial y} + u\frac{\partial v}{\partial x}\frac{\partial \Theta}{\partial y} + v\frac{\partial u}{\partial y}\frac{\partial \Theta}{\partial x} + u^2\frac{\partial^2 \Theta}{\partial x^2} + v^2\frac{\partial^2 \Theta}{\partial y^2} + 2uv\frac{\partial^2 \Theta}{\partial x \partial y}\right] \tag{2.86}$$

2.8 Entropy Generation

Entropy (see for details, Shiner [166]) of a system refers to the disorder of the system. This means that the system is unable to use 100% of useful energy. In an ideal system where we are able to conserve the energy contained in the system perfectly, the entropy of that system is zero but in actual world this is not the case. There is a loss of energy in one form or the other thus, entropy is enhanced all the time. Here aim is to find ways to minimize this loss in the form of entropy. This makes entropy minimization an important task in any industrial setup. The researchers have been analyzing the entropy generation and looking for methods of reducing it. The local entropy generation for the fluid flow are as follows (see for example, Das *et al.* [167])

$$E_G = \frac{k}{\Theta_\infty^2}\left\{\left(\frac{\partial \Theta}{\partial y}\right)^2 + \frac{16}{3}\frac{\sigma^*\Theta_\infty^3}{\kappa^*\nu_f(\rho C_p)_f}\left(\frac{\partial \Theta}{\partial y}\right)^2\right\} + \frac{\mu}{\Theta_\infty}\left(\frac{\partial u}{\partial y}\right)^2. \tag{2.87}$$

2.9 Magnetohydrodynamics

Branch of engineering in which behavior of magnetic field in electrically conducting fields is studied is known as Magnetohydrodynamics (MHD) (see for example, Alfven [69]). The basic concept of MHD is that magnetic fields can induce current in a moving conductive fluid, which create forces on the fluid and the magnetic field itself. Combination of equations of motion and Maxwells equation of electromagnetism results in the set of equations which represents MHD flow. The momentum equation which electromagnetic force term is given by Ligere [168]

$$\rho\left(\frac{d\mathbf{V}}{dt}\right) = (\nabla.\tau) + (J \times \mathbf{B}). \tag{2.88}$$

Where J , $B = B + B_1$, B_1 and $J \times \mathbf{B}$ represents the current density, total magnetic field, induced magnetic field and electromagnetic force term respectively. By Ohms law [169], we have

$$J = \sigma(\mathbf{E} + \mathbf{V} \times \mathbf{B}). \tag{2.89}$$

Here $\mathbf{E}$ and $\mathbf{V}$ represents the electric field and fluid velocity, respectively.

$$J = \sigma(\mathbf{V} \times \mathbf{B}). \tag{2.90}$$

Where $\mathbf{E}$ is neglected due to low Reynolds number and $\mathbf{V}$ and $\mathbf{B}$ is defined as

$$\mathbf{V} = [u, v, 0], \tag{2.91}$$

$$\mathbf{B} = [0, \mathbf{B_0}, 0], \tag{2.92}$$

$$J = \sigma \begin{vmatrix} i & j & k \\ u & v & 0 \\ 0 & \mathbf{B_0} & 0 \end{vmatrix}, \tag{2.93}$$

$$J = \sigma [0, 0, \mathbf{B_0} u], \tag{2.94}$$

$$J \times \mathbf{B} = \sigma \begin{vmatrix} i & j & k \\ 0 & 0 & \sigma \mathbf{B_0} u \\ 0 & \mathbf{B_0} & 0 \end{vmatrix}, \tag{2.95}$$

$$J \times \mathbf{B} = \sigma \left[0, 0, -\mathbf{B_o^2} u\right], \tag{2.96}$$

$$J \times \mathbf{B} = -\sigma \left[0, 0, \mathbf{B_o^2} u\right], \tag{2.97}$$

$$J \times \mathbf{B} = -\sigma {\mathbf{B_0}}^2 u. \tag{2.98}$$

Substituting equation (2.98) momentum equation (2.88) becomes,

$$\rho\left(\frac{d\mathbf{V}}{dt}\right) = (\nabla.\tau) - \sigma\mathbf{B_0}^2 u. \tag{2.99}$$

2.10 Nanofluids

The inclusion of solid nanoparicles having size of less than 100 nm in the ordinary fluid makes it nanofluid (see for details, Das *et al.* [170]). The nanoparticles are typically made of oxide ceramics CuO (Copper Oxide), Al_2O_3 (Aluminium Oxide) and metal nitrides SiN (Silicon Nitride), AlN (Aluminium Nitride) etc. The metallic particles change the heat conduction characteristics and transport properties of the base fluids like water, methanol, ethylene glycol etc. The enhanced thermal properties of nanofluids are the main features of the nanofluids. The Table 2.1 shows the thermophysical properties of nanofluids (for details, see for example, [171, 172]).

Properties	Nanofluid
Dynamic viscosity (μ)	$\mu_{nf} = \mu_f(1-\phi)^{-2.5}$
Density (ρ)	$\rho_{nf} = (1-\phi)\rho_f + \phi\rho_s$
Heat capacity (ρC_p)	$(\rho C_p)_{nf} = (1-\phi)(\rho C_p)_f + \phi(\rho C_p)_s$
Thermal Conductivity (κ)	$\frac{\kappa_{nf}}{\kappa_f} = \left[\frac{(\kappa_s+(m-1)\kappa_f)-(m-1)\phi(\kappa_f-\kappa_s)}{(\kappa_s+(m-1)\kappa_f)+\phi(\kappa_f-\kappa_s)}\right]$
Electrical Conductivity (σ)	$\frac{\sigma_{nf}}{\sigma_f} = \left[1 + \frac{3(\frac{\sigma_s}{\sigma_f}-1)\phi}{(\frac{\sigma_s}{\sigma_f}+2)-(\frac{\sigma_s}{\sigma_f}-1)\phi}\right]$

TABLE 2.1: Thermophysical Properties for Nanofluids

2.11 Material Properties of Nanofluids

The material properties of the base fluid water and various nanoparticles used in this thesis are given in the following table (for details, ([173–176]))

Thermophysical	$\rho(kg/m^3)$	$c_p(J/kgK)$	$k(W/mK)$	$\sigma(S/m)$
Ethylene glycol (EG)	1114	2415	0.252	5.5×10^{-6}
Water (H_2O)	997.1	4179	0.6130	0.5×10^{-6}
Methanol $(MeOH)$	792	2545	0.2035	0.5×10^{-6}
Ferro (Fe_3O_4)	5180	670	9.7	0.74×10^{6}
Copper (Cu)	8933	385.0	401.00	5.96×10^{7}
Copper oxide (CuO)	6510	540	18	5.96×10^{7}
Alumina (Al_2O_3)	3970	765.0	40.000	3.5×10^{7}
Titanium oxide (T_iO_2)	4250	686.2	8.9538	2.38×10^{6}

Table 2.2: Material Properties of Base fluid and Nanoparticles at 293K

2.11.1 Hybrid Nanofluids

The working principle of hybrid nanofluids (see for example, Ali [177]) is the suspension of two different types of nanoparticles in the base fluid. This enhances the heat transfer capabilities of the ordinary fluids and prove to better heat exponent as compare to the nanofluids. The Table 2.3 indicates the thermophysical properties of hybrid nanofluids (see for example, Hayat and Nadeem [101]).

Properties	Hybrid Nanofliud
Vicosity (μ)	$\mu_{hnf} = \mu_f(1-\phi_w)^{-2.5}(1-\phi_z)^{-2.5}$
Density (ρ)	$\rho_{hnf} = [(1-\phi_z)\{(1-\phi_w)\rho_f + \phi_w\rho_{p_1}\}] + \phi_z\rho_{p_2}$
Heat Capacity (ρC_p)	$(\rho C_p)_{hnf} = [(1-\phi_z)\{(1-\phi_w)(\rho C_p)_f + \phi_w(\rho C_p)_{p_1}\}] + \phi_z(\rho C_p)_{p_2}$
Thermal Conductivity (κ)	$\frac{\kappa_{hnf}}{\kappa_{gf}} = \left[\frac{(\kappa_{p_2}+(m-1)\kappa_{gf})-(m-1)\phi_z(\kappa_{gf}-\kappa_{p_2})}{(\kappa_{p_2}+(m-1)\kappa_{gf})+\phi_z(\kappa_{gf}-\kappa_{p_2})}\right]$; $\frac{\kappa_{gf}}{\kappa_f} = \left[\frac{(\kappa_{p_1}+(m-1)\kappa_f)-(m-1)\phi_w(\kappa_f-\kappa_{p_1})}{(\kappa_{p_1}+(m-1)\kappa_f)+\phi_w(\kappa_f-\kappa_{p_1})}\right]$
Electrical Conductivity (σ)	$\frac{\sigma_{hnf}}{\sigma_f} = \left[1 + \frac{3(\frac{\phi_w\sigma_{p_1}+\phi_z\sigma_{p_2}}{\sigma_f} - (\phi_w+\phi_z))}{(\frac{\phi_w\sigma_{p_1}+\phi_2\sigma_{p_2}}{(\phi_w+\phi_z)\sigma_f}+2) - (\frac{\phi_w\sigma_{p_1}+\phi_z\sigma_{p_2}}{\sigma_f} - (\phi_w+\phi_z))}\right]$

Table 2.3: Thermophysical Properties of Hybrid Nanofluids

2.12 Tiwari and Das Model

There are two types of model that are used mathematically solve problems relating to nanofluids. One is a single phase model and the other is a phase model. Tiwari and Das model [156] is one example of single phase model. In single phase model the fluid, velocity and temperature they are taken as the same. Where in two phase model the velocity of the fluid and the nanoparticle is taken as different and also the temperature of the fluid and the nanoparticles they taken as different. The advantage of the single phase model is that because we ignore the slip mechanisms so the model is simplified one and it is easily to solve numerically. But the disadvantage of this method is that in some cases the numerical results differ from that obtained by experiments. In Tiwari and Das model volume concentration of nanoparticles ranges between 3% - 20%.

2.13 Prandtl Number

The quantitative relation between the momentum diffusivity and thermal diffusivity is known as the Prandtl number (see for example, Favre and Tardu [178]). It is denoted by P_r. Mathematically, it is expressed by

$$P_r = \frac{\nu}{\alpha} = \frac{\frac{\mu}{\rho}}{\frac{\kappa}{(\rho C_p)}} = \frac{\mu(C_p)}{\kappa}. \tag{2.100}$$

2.14 Nusselt Number

Nusselt number is a dimensionless parameter used in numerical analysis of heat transfer at the boundary between a solid body and a moving fluid. Nusselt number is close to conduction and convection of same magnitude and is also characterized as laminar flow. It was firstly introduced by the German mathematician Nusselt, expressed by Nu_x is the dimensionless number. Mathematically, Nusselt number is denoted by

$$Nu_x = \frac{h\nabla\Theta}{\frac{\kappa\nabla\Theta}{L}}, \tag{2.101}$$

$$Nu_x = \frac{hL}{\kappa}, \tag{2.102}$$

and the local Nusselt number (see for example, Abolbashari *et al.* [179]) is defined as

$$Nu_x = \frac{xq_w}{k_f(\Theta_w - \Theta_\infty)}. \tag{2.103}$$

here, $h_f\nabla\Theta$, $\frac{\kappa_f\nabla T}{L}$, L, h_f and κ_f represents the heat transfer by convection, the heat transfer by conduction, the characteristic length, the convective heat transfer and the thermal conductivity of the base fluid, respectively.

2.15 Biot Number

The resistance of heat transfer is different inside of the material and at the surface. Their ratio is called Biot number (see for example, Kamran *et al.* [180]). It was introduced by the French physicist Jean-Baptiste Biot and is denoted by B_i. Mathematically, It is expressed by

$$B_i = \frac{hL}{\kappa}. \tag{2.104}$$

2.16 Reynolds Number

Reynolds number (see for example, Kamran *et al.* [180]) is the ratio of inertial forces to viscous forces. It is used to clarify the different flow behaviours like turbulent or laminar flow. It is denoted by R_e and mathematically it can be written as.

$$R_e = \frac{\rho VL}{\mu}. \tag{2.105}$$

2.17 Skin Friction Coefficient

Skin friction coefficient (see for example, Abbas *et al.* [181]) is a measures of the retardation in fluid due to friction. It is denoted by C_f and is mathematically defined as

$$C_f = \frac{\tau_w}{\rho_f U_w^2}. \tag{2.106}$$

2.18 Keller Box Method (KBM)

Keller box method [182] is a widely used numerical technique for solving BVPs of complex nature, This method has used in the present study to solve complex BVPs. Keller box method subdivides a large domain into collection of smaller, simpler domain using mesh points. The numerical scheme is inherently stable and is second order convergent. It is one of the implicit finite difference method.

The flow chart of the KBM is as follows

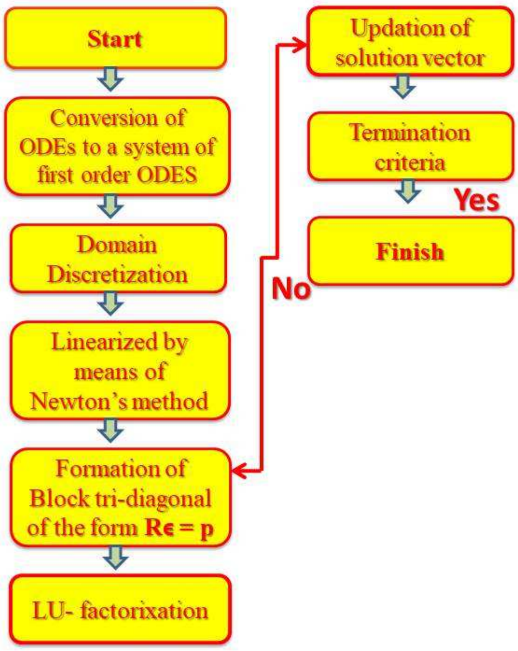

FIGURE 2.1: Flow Chart of KBM

Furthers features of KBM are given below as discussed in [183].

- The most useful feature of this method is to show accurate by handling of problem related to complexed geometry.

- The design of the scheme is simple and easy.

- Flexible for dealing with the nonlinear problem.

- Comprehensively used for parabolic differential equations.

Chapter 3

Flow and Heat Transfer of MHD Maxwell Nanofluid Flow over a Stretching Sheet with Variable Properties

3.1 Introduction

In this chapter numerical investigation is carried out to study the flow and heat transfer of electrically conducting Maxwell nanofluid. The nanofluid occupies the space over a flat, porous surface and the flow is generated by the stretching of the surface. The mathematical results are presented for considering velocity slip at the boundary and inducing the effect of thermal radiation for optically thick nanofluid. A uniformly distributed transverse magnetic field of strength is also assumed in the present model. Similarity transformations simplifications are carried to reduce governing PDEs to ODEs and then numerical simulations are performed using Keller box technique to approximate solutions for the velocity, temperature and entropy profiles. Furthermore, the velocity gradient and the heat exchange rate at the boundary have been computed and explored graphically. The numerical simulations are performed for Copper-water ($Cu - H_2O$) and Titanium-water ($TiO_2 - H_2O$) nanofluids. The significant findings of the study are the negative impact of Lorentz forces on the nanofluid motion within the boundary layer and the increase in temperature due to rise in non-Newtonian parameter, thermal radiation parameter and the sheet convection parameter. Moreover $Cu - H_2O$ nanofluid is detected as superior thermal conductor than $TiO_2 - H_2O$ nanofluid.

3.2 Mathematical Formulation

Assume an incompressible non-Newtonian Maxwell nanofluid which covers the space over a permeable stretching surface. The fluid is electrically conducting and the flow is generated due to the stretching of surface with non-uniform velocity (see for details, Hayat *et al.* [184])

$$U_w(x,t) = \frac{bx}{1-\xi t}, \tag{3.1}$$

where b and $\frac{1}{1-\xi t}$ (with $\xi t < 1$) are the initial and effective stretching rate and t is the time. A uniformly distributed transverse magnetic field of strength $B(t) = \frac{B_0}{\sqrt{1-\xi t}}$ is assumed in the present model and the temperature of the convective surface is $\Theta_w(x,t) = \Theta_\infty + \frac{bx}{1-\xi t}$, where Θ_∞ is the temperature outside of the boundary layer. Thermal conductivity of the nanofluid is assumed to vary as a linear function of temperature Θ. This assumption is valid because thermal properties of nanofluid changes significantly with rise in temperature, type of nanoparticles, pressure etc. Finally, the non-Newtonian Maxwell nanofluid is considered optically thick and radiation only travel a short distance within the fluid. Here radiative heat transfer is taken into account and Rosseland approximation is utilized for the radiation effects.

The schematic diagram of the mathematical model under consideration is presented in Figure 3.1.

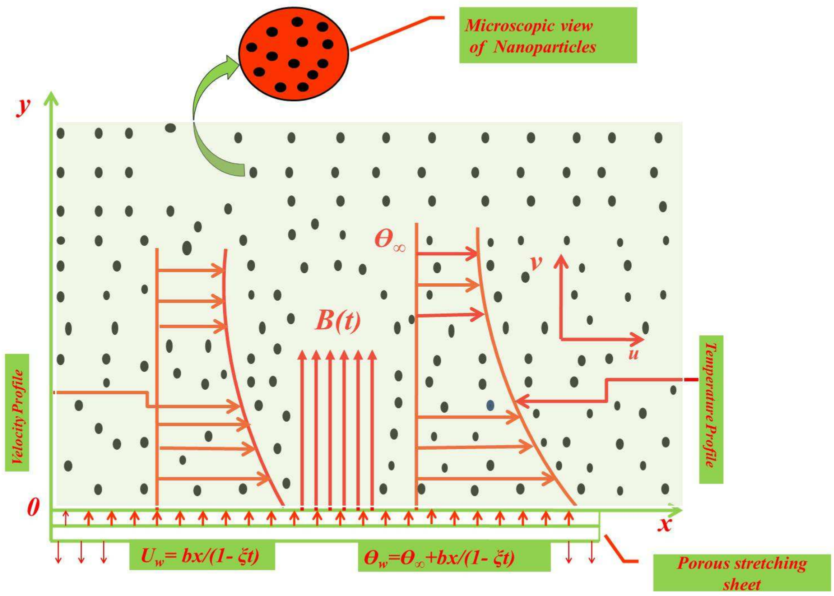

Figure 3.1: Physical Model of Schematic Diagram

The constitutive equations for conservation of mass, momentum and energy under boundary layer assumptions along with suitable boundary conditions for the Maxwell nanofluid are given in equations (2.14), (2.38) and (2.85). These equations for the Maxwell nanofluid reduced to the form (see for example, Mukhopadhyay [160])

$$\frac{\partial u}{\partial x} + \frac{\partial v}{\partial y} = 0, \tag{3.2}$$

$$\begin{aligned} \frac{\partial u}{\partial t} + u\frac{\partial u}{\partial x} + v\frac{\partial u}{\partial y} = -\lambda\left[u^2\frac{\partial^2 u}{\partial x^2} + v^2\frac{\partial^2 u}{\partial y^2} + 2uv\frac{\partial^2 u}{\partial x \partial y}\right] + \frac{\mu_{nf}}{\rho_{nf}}\left(\frac{\partial^2 u}{\partial y^2}\right) \\ -\frac{\sigma_{nf}B^2(t)u}{\rho_{nf}} - \frac{\mu_{nf}}{\rho_{nf}k}u, \end{aligned} \tag{3.3}$$

$$\frac{\partial \Theta}{\partial t} + u\frac{\partial \Theta}{\partial x} + v\frac{\partial \Theta}{\partial y} = \frac{1}{(\rho C_p)_{nf}}\left[\frac{\partial}{\partial y}(\kappa^*_{nf}(\Theta)\frac{\partial \Theta}{\partial y})\right] - \frac{1}{(\rho C_p)_{nf}}\left[\frac{\partial q_r}{\partial y}\right]. \tag{3.4}$$

The BCs for the modeled problem are

$$u(x,0) = U_w + \mu_{nf}\left(\frac{\partial u}{\partial y}\right), \quad v(x,0) = V_w, \quad -k_0\left(\frac{\partial \Theta}{\partial y}\right) = h_f(\Theta_w - \Theta), \tag{3.5}$$

$$u \to 0, \quad \Theta \to \Theta_\infty \quad \text{as} \quad y \to \infty. \tag{3.6}$$

The thermal conductivity and thermal radiation are assumed as (for details see for example, [153, 185, 186])

$$\kappa^*_{nf}(\Theta) = k_{nf}\left[1 + \epsilon\frac{\Theta - \Theta_\infty}{\Theta_w - \Theta_\infty}\right], \tag{3.7}$$

$$q_r = -\frac{4\sigma^*}{3k^*}\frac{\partial \Theta^4}{\partial y}. \tag{3.8}$$

The Taylor series expansion of temperature Θ about Θ_∞ and ignoring the terms of higher order gives

$$\Theta^4 \cong 4\Theta^3_\infty \Theta - 3\Theta^4_\infty. \tag{3.9}$$

Equation (3.8) after using equation (3.9) converted to

$$\frac{\partial q_r}{\partial y} = -\frac{16\Theta^3_\infty \sigma^*}{3k^*}\frac{\partial^2 \Theta}{\partial y^2}. \tag{3.10}$$

Equation (3.10) together with (3.4) gives

$$\begin{aligned}(\rho C_p)_{nf}\left(\frac{\partial \Theta}{\partial t} + u\frac{\partial \Theta}{\partial x} + v\frac{\partial \Theta}{\partial y}\right) = \left[\frac{\partial}{\partial y}k_{nf}\left(1 + \epsilon\frac{\Theta - \Theta_\infty}{\Theta_w - \Theta_\infty}\right)\left(\frac{\partial \Theta}{\partial y}\right)\right] \\ + \left[\frac{16\Theta^3_\infty \sigma^*}{3k^*}\frac{\partial^2 \Theta}{\partial y^2}\right].\end{aligned} \tag{3.11}$$

3.3 Solution of the Problem

In order to obtain the solution of the problem, first of all the system of equations (3.2), (3.3) and (3.11) along with boundary conditions (3.5)-(3.6) are converted into the system of ODEs. Here the following stream functions ψ and θ and the similarity variable η are introduced (see for example, Hayat *et al.* [184])

$$u = \frac{\partial \psi}{\partial y}, \qquad v = -\frac{\partial \psi}{\partial x}. \tag{3.12}$$

where

$$\psi(x, y) = \sqrt{\frac{\nu_f b}{(1 - \xi t)}}\, x f(\eta) \quad \text{and} \quad \eta(x, y) = \sqrt{\frac{b}{\nu_f(1 - \xi t)}}\, y, \qquad \theta(\eta) = \frac{\Theta - \Theta_\infty}{\Theta_w - \Theta_\infty}. \tag{3.13}$$

Using equations (3.13) in (3.12),

$$u = \frac{bx}{(1-\xi t)} f'(\eta), \tag{3.14}$$

$$v = -\sqrt{\frac{\nu_f b}{(1-\xi t)}} f(\eta). \tag{3.15}$$

In order to utilize (3.14)-(3.15) in (3.2), (3.3) and (3.11), gives

$$\frac{\partial u}{\partial x} = \frac{b}{(1-\xi t)} f'(\eta), \tag{3.16}$$

$$\frac{\partial v}{\partial y} = -\frac{b}{(1-\xi t)} f'(\eta), \tag{3.17}$$

$$u\frac{\partial u}{\partial x} = \frac{b^2 x}{(1-\xi t)^2} f'^2(\eta), \tag{3.18}$$

$$\frac{\partial u}{\partial y} = \frac{bxf''(\eta)}{(1-\xi t)} \sqrt{\frac{b}{\nu_f(1-\xi t)}}, \tag{3.19}$$

$$v\frac{\partial u}{\partial y} = -\frac{b^2 x f(\eta) f''(\eta)}{(1-\xi t)^2}, \tag{3.20}$$

$$u^2 = \frac{b^2 x^2 f'^2(\eta)}{(1-\xi t)^2}, \tag{3.21}$$

$$\frac{\partial^2 u}{\partial x^2} = 0, \tag{3.22}$$

$$u^2\left(\frac{\partial^2 u}{\partial x^2}\right) = 0, \tag{3.23}$$

$$v^2 = \frac{\nu_f b f^2(\eta)}{(1-\xi t)}, \tag{3.24}$$

$$\frac{\partial^2 u}{\partial y^2} = \left(\frac{b^2 x f'''(\eta)}{(1-\xi t)^2 \nu_f}\right), \tag{3.25}$$

$$v^2\frac{\partial^2 u}{\partial y^2} = \frac{xb^3 f^2(\eta) f'''(\eta)}{(1-\xi t)^3}, \tag{3.26}$$

$$2uv = 2\left(\frac{bx}{(1-\xi t)} f'(\eta)\right)\left(-\sqrt{\frac{\nu_f b}{(1-\xi t)}} f(\eta)\right), \tag{3.27}$$

$$2uv\left(\frac{\partial^2 u}{\partial x \partial y}\right) = \frac{-2c^3 f f' f'' x}{(1-\xi t)^3}, \tag{3.28}$$

$$\frac{\partial u}{\partial t} = \frac{bx}{(1-\xi t)^2}\left[\xi f' + \frac{\xi f''}{2}\right], \tag{3.29}$$

$$\frac{\partial \Theta}{\partial t} = \frac{b^2 x}{(1-\xi t)^2} A\left(\theta(\eta) + \frac{\eta}{2}\theta'(\eta)\right), \tag{3.30}$$

$$\frac{\partial \Theta}{\partial x} = \frac{b}{(1-\xi t)}\theta(\eta), \tag{3.31}$$

$$u\left(\frac{\partial \Theta}{\partial x}\right) = \left(\frac{bx}{(1-\xi t)}f'(\eta)\right)\frac{b}{(1-\xi t)}\theta(\eta), \tag{3.32}$$

$$\frac{\partial \Theta}{\partial y} = \frac{bx}{(1-\xi t)}\theta'(\eta)\sqrt{\frac{b}{\nu_f(1-\xi t)}}, \tag{3.33}$$

$$v\left(\frac{\partial \Theta}{\partial y}\right) = \left(-\sqrt{\frac{\nu_f b}{(1-\xi t)}}f(\eta)\right)\frac{bx}{(1-\xi t)}\theta'(\eta)\sqrt{\frac{b}{\nu_f(1-\xi t)}}. \tag{3.34}$$

Use (3.16) and (3.17) in (2.14) identically satisfies the continuity equation, that is

$$\frac{\partial u}{\partial x} + \frac{\partial v}{\partial y} = \frac{b}{(1-\xi t)}f'(\eta) - \frac{b}{(1-\xi t)}f'(\eta) = 0. \tag{3.35}$$

Now using appropriate equations from (3.16)- (3.34) into (3.2)-(3.3) and (3.11), following ODEs are obtained

$$\begin{aligned} A\left(\frac{\eta}{2}f'' + f'\right) + f'^2 - ff'' - \frac{f'''}{\phi_1\phi_2} + \gamma\left(f^2 f''' - 2ff'f''\right) + \frac{\phi_4}{\phi_2}Mf' \\ + \frac{1}{\phi_1\phi_2}Kf' = 0. \end{aligned} \tag{3.36}$$

$$\theta''\left(1 + \epsilon\theta + \frac{1}{\phi_5}P_r N_r\right) + \epsilon\theta'^2 + P_r\frac{\phi_3}{\phi_5}\left[f\theta' - f'\theta - A(\theta + \frac{\eta}{2}\theta')\right] = 0. \tag{3.37}$$

The boundary conditions (3.5) and (3.6) are transformed to the following form

$$u(x,0) = U_w + \mu_{nf}\left(\frac{\partial u}{\partial y}\right), \tag{3.38}$$

Using (3.1) and (3.19) in above equation, gives

$$u(x,0) = \frac{bx}{1-\xi t} + \frac{\mu_f}{\phi_1}\left(\frac{bxf''(0)}{(1-\xi t)}\sqrt{\frac{b}{\nu_f(1-\xi t)}}\right), \tag{3.39}$$

using equation (3.14) in equation (3.39)

$$\frac{bx}{(1-\xi t)}f'(0)=\frac{bx}{1-\xi t}+\frac{\mu_f}{\phi_1}\left(\frac{bxf''(0)}{(1-\xi t)}\sqrt{\frac{b}{\nu_f(1-\xi t)}}\right), \tag{3.40}$$

$$\frac{bx}{(1-\xi t)}f'(0)=\frac{bx}{1-\xi t}\left(1+\frac{\mu_f}{\phi_1}f''(0)\sqrt{\frac{b}{\nu_f(1-\xi t)}}\right), \tag{3.41}$$

$$f'(0)=1+\left(\sqrt{\frac{b}{\nu_f(1-\xi t)}}\right)\frac{\mu_f}{\phi_1}f''(0), \tag{3.42}$$

$$f'(0)=1+\frac{\Lambda}{\phi_1}f''(0). \tag{3.43}$$

$$v(x,0)=V_w. \tag{3.44}$$

Use of (3.15) in above equation, we get

$$-\sqrt{\frac{\nu_f b}{(1-\xi t)}}f(0)=V_w, \tag{3.45}$$

$$f(0))=S. \tag{3.46}$$

$$-k_0\left(\frac{\partial\Theta}{\partial y}\right)=h_f(\Theta_w-\Theta), \tag{3.47}$$

$$\theta(\eta)=\frac{\Theta-\Theta_\infty}{\Theta_w-\Theta_\infty}, \tag{3.48}$$

where

$$\Theta_w-\Theta_\infty=\frac{bx}{(1-\xi t)}, \tag{3.49}$$

$$\theta(\eta)=\frac{\frac{\Theta-\Theta_\infty}{bx}}{(1-\xi t)}, \tag{3.50}$$

$$\theta(\eta)\frac{bx}{(1-\xi t)}=(\Theta-\Theta_\infty), \tag{3.51}$$

$$\Theta=\Theta_\infty+\frac{bx}{(1-\xi t)}\theta(\eta). \tag{3.52}$$

Equations (3.49),(3.52) and (3.33) together with equation (3.47), gives

$$\frac{bx}{(1-\xi t)}\theta'(0)\sqrt{\frac{b}{\nu_f(1-\xi t)}}=-\frac{h_f}{k_0}\left(\Theta_\infty+\frac{bx}{1-\xi t}-\Theta_\infty-\frac{bx}{1-\xi t}\theta\right), \tag{3.53}$$

$$\sqrt{\frac{b}{\nu_f(1-\xi t)}}\theta'(0) = -\frac{h_f}{k_0}(1-\theta(0)), \tag{3.54}$$

$$\theta'(0) = -\frac{h_f}{k_0}(1-\theta(0))\left(\sqrt{\frac{\nu(1-\xi t)}{b}}\right), \tag{3.55}$$

$$\theta'(0) = -B_i(1-\theta(0)). \tag{3.56}$$

Using (3.14) and (3.52) in (3.6), we get

$$\frac{bx}{(1-\xi t)}f'(\eta) \to 0, \qquad \text{as} \;\; y \to \infty, \tag{3.57}$$

$$f'(\eta) \to 0, \qquad \text{as} \;\; \eta \to \infty, \tag{3.58}$$

$$\Theta_\infty + \frac{bx}{(1-\xi t)}\theta(\eta) \to \Theta_\infty \;\; \text{as} \;\; y \to \infty, \tag{3.59}$$

$$\theta(\eta) \to 0 \;\; \text{as} \;\; \eta \to \infty. \tag{3.60}$$

Here

$$\phi_1 = (1-\phi)^{2.5}, \quad \phi_2 = \left(1-\phi+\phi\frac{\rho_s}{\rho_f}\right), \quad \phi_3 = \left(1-\phi+\phi\frac{(\rho C_p)_s}{(\rho C_p)_f}\right), \tag{3.61}$$

$$\phi_4 = \left(1+\frac{3(\frac{\sigma_s}{\sigma_f}-1)\phi}{(\frac{\sigma_s}{\sigma_f}+2)-(\frac{\sigma_s}{\sigma_f}-1)\phi}\right), \quad \phi_5 = \left(\frac{(k_s+2k_f)-2\phi(k_f-k_s)}{(k_s+2k_f)+\phi(k_f-k_s)}\right). \tag{3.62}$$

In above equations primes stand for the differentiation of the function with respect to η. $A = \frac{\xi}{b}$ is the unsteady flow parameter, $\gamma = b\lambda_0$ is the Maxwell parameter, $M = \frac{\sigma_f B_0^2}{b\rho_f}$ is the magnetic parameter, $K = \frac{\nu_f(1-\xi t)}{bk}$ is the porous medium parameter, $P_r = \frac{\nu_f}{\alpha_f}$ is the Prandtl number, $\alpha_f = \frac{\kappa_f}{(\rho C_p)_f}$ is the thermal diffusivity parameter, $N_r = \frac{16}{3}\frac{\sigma^*\Theta_\infty^3}{\kappa^*\nu_f(\rho C_p)_f}$ is the thermal radiation parameter, $S = -V_w\sqrt{\frac{1-\xi t}{\nu_f \; b}}$ is the mass transfer parameter, $\Lambda = \sqrt{\frac{b}{\nu_f(1-\xi t)}}\mu_f$ is the velocity slip parameter and $B_i = \frac{h_f}{k_0}\sqrt{\frac{\nu_f(1-\xi t)}{b}}$ is the sheet convection parameter or so-called Biot number. It is observed some parameters depend on ξ and is time dependent. Therefore to obtain non-similar solutions for the proposed problem numerical results are computed for locally similar parameters.

The nonlinear system of ordinary differential equations (3.36)-(3.37), arising from mathematical modeling of physical system of nanofluid flow are difficult to solve analytically. Therefore Keller box method [182] scheme is employed to find the approximate solutions. The numerical scheme is inherently stable and is second order convergent and also known as implicit finite difference method.

The initial step of this scheme is to reduce the equations (3.36)-(3.37) into a system of five first ODEs, that is

$$z_1 = f', \tag{3.63}$$

$$z_2 = z_1', \tag{3.64}$$

$$z_3 = \theta', \tag{3.65}$$

$$A\left(\frac{\eta}{2}z_2 + z_1\right) + z_1^2 - fz_2 - \frac{z_2'}{\phi_1\phi_2} + \gamma\left(f^2 z_2' - 2fz_1z_2\right) + \frac{\phi_4}{\phi_2}Mz_1 + \frac{1}{\phi_1\phi_2}Kz_1 = 0, \tag{3.66}$$

$$z_3'\left(1 + \epsilon\theta + \frac{1}{\phi_5}P_rN_r\right) + \epsilon z_3^2 + P_r\frac{\phi_3}{\phi_5}\left[fz_3 - z_1\theta - A(\theta + \frac{\eta}{2}z_3)\right] = 0. \tag{3.67}$$

The boundary conditions (3.43),(3.46), (3.56), (3.58) and (3.60) are similarly transformed into

$$f(0) = S, z_1(0) = 1 + \frac{\Lambda}{\phi_1}z_2(0), z_3(0) = -B_i(1-\theta(0)), z_1(\infty) \to 0, \theta(\infty) \to 0. \tag{3.68}$$

The derivatives appeared in the above system are then approximated by the central differences and averages are centered at the midpoints of the mesh and are expressed by

$$\eta_0 = 0, \quad \eta_j = \eta_{j-1} + h, \quad j = 1, 2, 3, ..., J-1, \quad \eta_J = \eta_\infty. \tag{3.69}$$

The system of first order ODEs (3.63)-(3.67) is then reduced to the following set of algebraic nonlinear equations.

$$\frac{(z_1)_j + (z_1)_{j-1}}{2} = \frac{f_j - f_{j-1}}{h}, \tag{3.70}$$

$$\frac{(z_2)_j + (z_2)_{j-1}}{2} = \frac{(z_1)_j - (z_1)_{j-1}}{h}, \tag{3.71}$$

$$\frac{(z_3)_j+(z_3)_{j-1}}{2}=\frac{\theta_j-\theta_{j-1}}{h}, \tag{3.72}$$

$$\begin{aligned}
A\left\{\left(\frac{(z_1)_j+(z_1)_{j-1}}{2}\right)+\frac{\eta}{2}\left(\frac{(z_2)_j+(z_2)_{j-1}}{2}\right)\right\}+\left(\frac{(z_1)_j+(z_1)_{j-1}}{2}\right)^2 \\
-\left[\left(\frac{f_j+f_{j-1}}{2}\right)\left(\frac{(z_2)_j+(z_2)_{j-1}}{2}\right)\right]-\frac{1}{\phi_1\phi_2}\left(\frac{(z_2)_j-(z_2)_{j-1}}{h}\right) \\
+\gamma\left[-2\left(\frac{f_j+f_{j-1}}{2}\right)\left(\frac{(z_1)_j+(z_1)_{j-1}}{2}\right)\left(\frac{(z_2)_j+(z_2)_{j-1}}{2}\right)\right] \\
+\gamma\left[\left(\frac{f_j+f_{j-1}}{2}\right)^2\left(\frac{(z_2)_j-(z_2)_{j-1}}{h}\right)\right]+\frac{\phi_4}{\phi_2}M\left(\frac{(z_1)_j+(z_1)_{j-1}}{2}\right) \\
+\frac{1}{\phi_1\phi_2}K\left(\frac{(z_1)_j+(z_1)_{j-1}}{2}\right)=0,
\end{aligned} \tag{3.73}$$

$$\begin{aligned}
\left(\frac{(z_3)_j-(z_3)_{j-1}}{h}\right)\left(1+\epsilon\left(\frac{\theta_j+\theta_{j-1}}{2}\right)+\frac{1}{\phi_5}P_rN_r\right) \\
+\epsilon\left(\frac{(z_3)_j+(z_3)_{j-1}}{2}\right)^2+P_r\frac{\phi_3}{\phi_5}\left[\left(\frac{f_j+f_{j-1}}{2}\right)\left(\frac{(z_3)_j+(z_3)_{j-1}}{2}\right)\right] \\
-P_r\frac{\phi_3}{\phi_5}\left[\left(\frac{(z_1)_j+(z_1)_{j-1}}{2}\right)\left(\frac{\theta_j+\theta_{j-1}}{2}\right)\right] \\
-P_r\frac{\phi_3}{\phi_5}\left[A\left\{\left(\frac{\theta_j+\theta_{j-1}}{2}\right)+\frac{\eta}{2}\left(\frac{(z_3)_j+(z_3)_{j-1}}{2}\right)\right\}\right]=0.
\end{aligned} \tag{3.74}$$

In the above discussion, we write for the $(i+1)-th$ iterate as

$$()_j^{(i+1)}=()_j^{(i)}+\varepsilon()_j^{(i)}. \tag{3.75}$$

The substitution of above in equations (3.70)-(3.74) and ignoring the quadratic and higher terms of ε_j^i, a linear tri-diagonal system is achieved

$$\varepsilon f_j-\varepsilon f_{j-1}-\frac{1}{2}h(\varepsilon(z_1)_j+\varepsilon(z_1)_{j-1})=(r_1)_{j-\frac{1}{2}}, \tag{3.76}$$

$$\varepsilon(z_1)_j-\varepsilon(z_1)_{j-1}-\frac{1}{2}h(\varepsilon(z_2)_j+\varepsilon(z_2)_{j-1})=(r_2)_{j-\frac{1}{2}}, \tag{3.77}$$

$$\varepsilon\theta_j-\varepsilon\theta_{j-1}-\frac{1}{2}h(\varepsilon(z_3)_j+\varepsilon(z_3)_{j-1})=(r_3)_{j-\frac{1}{2}}, \tag{3.78}$$

$$
\begin{aligned}
&(a_1)_j\varepsilon f_j + (a_2)_j\varepsilon f_{j-1} + (a_3)_j\varepsilon (z_1)_j + (a_4)_j\varepsilon (z_1)_{j-1} + (a_4)_j\varepsilon (z_1)_{j-1} \\
&+(a_5)_j\varepsilon (z_2)_j + (a_6)_j\varepsilon (z_2)_{j-1} + (a_7)_j\varepsilon\theta_j + (a_8)_j\varepsilon\theta_{j-1} + (a_9)_j\varepsilon (z_3)_j \\
&\qquad +(a_{10})_j\varepsilon (z_3)_{j-1} = (r_4)_{j-\frac{1}{2}},
\end{aligned} \tag{3.79}
$$

$$
\begin{aligned}
&(b_1)_j\varepsilon f_j + (b_2)_j\varepsilon f_{j-1} + (b_3)_j\varepsilon (z_1)_j + (b_4)_j\varepsilon (z_1)_{j-1} + (b_4)_j\varepsilon (z_1)_{j-1} \\
&+(b_5)_j\varepsilon (z_2)_j + (b_6)_j\varepsilon (z_2)_{j-1} + (b_7)_j\varepsilon\theta_j + (b_8)_j\varepsilon\theta_{j-1} + (b_9)_j\varepsilon (z_3)_j \\
&\qquad +(b_{10})_j\varepsilon (z_3)_{j-1} = (r_5)_{j-\frac{1}{2}}.
\end{aligned} \tag{3.80}
$$

Where

$$
(r_1)_{j-\frac{1}{2}} = -f_j + f_{j-1} + \frac{h}{2}(z_1)_j + ((z_1)_{j-1}), \tag{3.81}
$$

$$
(r_2)_{j-\frac{1}{2}} = -(z_1)_j + (z_1)_{j-1} + \frac{h}{2}((z_2)_j + (z_2)_{j-1}), \tag{3.82}
$$

$$
(r_3)_{j-\frac{1}{2}} = -\theta_j + \theta_{j-1} + \frac{h}{2}((z_3)_j + (z_3)_{j-1}), \tag{3.83}
$$

$$
\begin{aligned}
(r_4)_{j-\frac{1}{2}} = &-h\left[-A\left(\frac{(z_1)_j + (z_1)_{j-1}}{2} + \eta\frac{(z_2)_j - (z_2)_{j-1}}{4}\right)\right] \\
&- h\left[\left(\frac{(z_1)_j + (z_1)_{j-1}}{2}\right)^2 - \frac{1}{\phi_1\phi_2}\left(\frac{(z_2)_j - (z_2)_{j-1}}{h}\right)\right] \\
&- h\left[-\left(\frac{f_j + f_{j-1}}{2}\right)\left(\frac{(z_2)_j + (z_2)_{j-1}}{2}\right)\right] \\
&- h\left[-\gamma\left(2\left(\frac{f_j + f_{j-1}}{2}\right)\left(\frac{(z_1)_j + (z_1)_{j-1}}{2}\right)\left(\frac{(z_2)_j + (z_2)_{j-1}}{2}\right)\right)\right] \\
&- h\left[\gamma\left(\left(\frac{f_j + f_{j-1}}{2}\right)^2\left(\frac{(z_2)_j - (z_2)_{j-1}}{h}\right)\right)\right] \\
&- h\left[\frac{\phi_4}{\phi_2}M\left(\frac{(z_1)_j + (z_1)_{j-1}}{2}\right) + \frac{1}{\phi_1\phi_2}K\left(\frac{(z_1)_j + (z_1)_{j-1}}{2}\right)\right],
\end{aligned} \tag{3.84}
$$

$$
\begin{aligned}
(r_5)_{j-\frac{1}{2}} = &-h\left[\frac{\left((z_3)_j - (z_3)_{j-1}\right)\left(1 + \epsilon\left(\frac{\theta_j + \theta_{j-1}}{2}\right) + \frac{1}{\phi_5}P_rN_r\right)}{h}\right] \\
&- h\left[\epsilon\left(\frac{(z_3)_j + (z_3)_{j-1}}{2}\right)^2\right]
\end{aligned} \tag{3.85}
$$

$$-h\frac{\phi_3}{\phi_5}P_rA\left[\left(\frac{\theta_j+\theta_{j-1}}{2}+\eta\frac{(z_3)_j+(z_3)_{j-1}}{2}\right)\right]$$
$$-h\frac{\phi_3}{\phi_5}P_rA\left[\left(\frac{(f_j+f_{j-1})((z_3)_j+(z_3)_{j-1})}{4}\right)\right]$$
$$+h\frac{\phi_3}{\phi_5}P_r\left[\left(\frac{(\theta_j+\theta_{j-1})((z_1)_j+(z_1)_{j-1})}{4}\right)\right]. \tag{3.86}$$

Using the similarity process the boundary conditions becomes

$$\varepsilon f_0=0, \varepsilon(z_1)_0=0, \varepsilon(z_3)_0=0, \varepsilon(z_1)_J=0, \varepsilon\theta_J=0. \tag{3.87}$$

The linear equations (3.76)-(3.80) can be written in the matrix form

$$R\varepsilon=p, \tag{3.88}$$

where

$$R=\begin{bmatrix} A_1 & C_1 & & & & \\ B_2 & A_2 & C_2 & & & \\ & \ddots & \ddots & \ddots & & \\ & & \ddots & \ddots & \ddots & \\ & & & B_{J-1} & A_{J-1} & C_{J-1} \\ & & & & B_J & A_J \end{bmatrix}, \varepsilon=\begin{bmatrix}\varepsilon_1\\ \varepsilon_2\\ \vdots\\ \varepsilon_{j-1}\\ \varepsilon_j\end{bmatrix}, p=\begin{bmatrix}(r_1)_{j-\frac{1}{2}}\\ (r_2)_{j-\frac{1}{2}}\\ \vdots\\ (r_{J-1})_{j-\frac{1}{2}}\\ (r_J)_{j-\frac{1}{2}}\end{bmatrix}. \tag{3.89}$$

Here R represents the $J\times J$ block tridiagonal matrix with each block size of 5×5, whereas, ε and p are column vectors of order $J\times 1$. The LU factorization method is now applied to find the solution of ε.

The desired physical quantities for the present model are the skin-friction coefficient (C_f) and the local Nusselt number (Nu_x) are defined in (2.106) and (2.103).

$$C_f=\frac{\tau_w}{\rho_f U_w^2}, \qquad Nu_x=\frac{xq_w}{k_f(\Theta_w-\Theta_\infty)}. \tag{3.90}$$

The τ_w and q_w are wall shear stress and wall heat flux for the present model are given as (see for example, Abel *et al.* [187])

$$\tau_w = \mu_{nf}\left(\frac{\partial u}{\partial y}\right)_{y=0}, \qquad q_w = -k_{nf}\left(1+\frac{16}{3}\frac{\sigma^*\Theta_\infty^3}{\kappa^*\nu_f(\rho C_p)_f}\right)\left(\frac{\partial \Theta}{\partial y}\right)_{y=0}, \tag{3.91}$$

using τ_w in (3.90) for C_f,

$$C_f = \frac{\mu_{nf}\left(\frac{\partial u}{\partial y}\right)_{y=0}}{\rho_f U_w^2}, \tag{3.92}$$

using (3.19) in

$$C_f = \frac{\mu_f}{\rho_f\phi_1}\frac{xf''(0)b^{3/2}}{\nu_f(1-\xi t)^{3/2}}\frac{(1-\xi t)^{3/2}\,^2}{bx}, \tag{3.93}$$

$$C_f = \frac{\sqrt{\nu_f}}{\phi_1}\sqrt{\frac{1}{U_w x}}f''(0), \tag{3.94}$$

$$C_f = \frac{1}{\sqrt{Re_x}}f''(0)\frac{1}{\phi_1}, \tag{3.95}$$

$$C_f = \frac{1}{\phi_1}\frac{1}{\sqrt{Re_x}}f''(0), \tag{3.96}$$

$$C_f\sqrt{Re_x} = \frac{f''(0)}{\phi_1}, \tag{3.97}$$

$$C_f Re_x^{\frac{1}{2}} = \frac{f''(0)}{(1-\phi)^{2.5}}. \tag{3.98}$$

Using q_w in equation (3.90) for Nu_x,

$$Nu_x = \frac{x}{k_f(\Theta_w-\Theta_\infty)}\left(-k_{nf}\left(1+\frac{16}{3}\frac{\sigma^*\Theta_\infty^3}{\kappa^*\nu_f(\rho C_p)_f}\right)\left(\frac{\partial \Theta}{\partial y}\right)_{y=0}\right), \tag{3.99}$$

using equation (3.33) in equation (3.99), we get

$$Nu_x = -\frac{k_{nf}}{k_f}(1+N_r)\left(\frac{bx}{(1-\xi t)}\theta'(0)\sqrt{\frac{b}{\nu_f(1-\xi t)}}\right), \tag{3.100}$$

$$Nu_x = -\frac{k_{nf}}{k_f}(1+N_r)\left(\sqrt{Re_x}\right)\theta'(0), \tag{3.101}$$

$$Nu_x Re_x^{-\frac{1}{2}} = -\frac{k_{nf}}{k_f}(1+N_r)\theta'(0). \tag{3.102}$$

3.4 Code Validation

To check the validity of our numerical scheme we compare our results to those already available in the literature [188–191] as the especial case for our study. The test case is the natural convection boundary layer flow of fluid across a flat plate in the presence Newtonian slip. Results have been obtained for $A = 0$, $\phi = 0$, $\Lambda = 0$, $\epsilon = 0$, $S = 0$, $N_r = 0$ and $B_i = 0$. In Table 3.1 the comparison is presented with acceptable level of accuracy. Therefore, it is assumed that the results presented through present numerical scheme are very much accurate.

P_r	*Grubka* [188]	*Ali* [189]	*Ishak* [190]	*Nazar* [191]	*Present* Results
0.72	0.8086	0.8058	0.8086	0.8086	0.8086
1.0	1.0000	0.9961	1.0000	1.0000	1.0000
3.0	1.9237	1.9144	1.9236	1.9237	1.9237
7.0	-	-	3.0722	3.0723	3.0723
10	3.7207	3.7006	3.7206	3.7207	3.7207

Table 3.1: Values of Nusselt Number for Newtonian Slip Flow

3.5 Entropy Generation Analysis

Entropy is measure of the loss of useful energy in any heat transfer process. The lose of energy is an irreversible process. It becomes important to analyze the entropy generation in the system those involves irreversibility of useful energy. Magnetohydrodynamics is one of the non-ideal effects which responsible for increasing the entropy of the system. In our case the actual entropy generation in the nanofluids is given by (see for example, Das *et al.* [167])

$$E_G = \frac{k_{nf}}{\Theta_\infty^2}\left\{\left(\frac{\partial\Theta}{\partial y}\right)^2 + \frac{16}{3}\frac{\sigma^*\Theta_\infty^3}{\kappa^*\nu_f(\rho C_p)_f}\left(\frac{\partial\Theta}{\partial y}\right)^2\right\} + \frac{\mu_{nf}}{\Theta_\infty}\left(\frac{\partial u}{\partial y}\right)^2 + \frac{\sigma_{nf}B^2(t)u^2}{\Theta_\infty} + \frac{\mu_{nf}u^2}{k\Theta_\infty}. \tag{3.103}$$

The first term in the above equation represents irreversibility of heat transfer, the second term is because of fluid friction, and the third and fourth term is because of magnetohydrodynamic and porous medium effects, respectively. The dimensionless entropy generation is represented by N_G and is given as (Das *et al.* [167])

$$N_G = \frac{\Theta_\infty^2 b^2 E_G}{k_f\left(\Theta_w - \Theta_\infty\right)^2}. \tag{3.104}$$

Now putting (3.103) in (3.104), we get

$$N_G = \frac{\Theta_\infty^2 b^2}{k_f\left(\Theta_w - \Theta_\infty\right)^2}\frac{k_{nf}}{\Theta_\infty^2}\left\{\left(\frac{\partial\Theta}{\partial y}\right)^2 + \frac{16}{3}\frac{\sigma^*\Theta_\infty^3}{\kappa^*\nu_f(\rho C_p)_f}\left(\frac{\partial\Theta}{\partial y}\right)^2\right\} + \frac{\mu_{nf}}{\Theta_\infty}\left(\frac{\partial u}{\partial y}\right)^2 + \frac{\sigma_{nf}B^2(t)u^2}{\Theta_\infty} + \frac{\mu_{nf}u^2}{k\Theta_\infty}. \tag{3.105}$$

Consider first term of equation (3.105),

$$\frac{\Theta_\infty^2 b^2}{k_f\left(\Theta_w - \Theta_\infty\right)^2}\frac{k_{nf}}{\Theta_\infty^2}\left\{(1+N_r)\left(\frac{\partial\Theta}{\partial y}\right)^2\right\}, \tag{3.106}$$

using equation (3.33) and (3.62), we get

$$= \frac{\Theta_\infty^2 b^2}{k_f\left(\Theta_w - \Theta_\infty\right)^2}\frac{k_f\phi_5}{\Theta_\infty^2}\left\{(1+N_r)\left(\frac{(bx)^2}{(1-\xi t)}^2\theta'(\eta)^2\frac{b}{\nu_f(1-\xi t)}\right)\right\}, \tag{3.107}$$

$$\frac{\Theta_\infty^2 b^2}{k_f\left(\Theta_w - \Theta_\infty\right)^2}\frac{k_{nf}}{\Theta_\infty^2}\left\{(1+N_r)\left(\frac{\partial\Theta}{\partial y}\right)^2\right\} = \frac{b^2}{k_f x}\left(\frac{bx}{(1-\xi t)}\right)\frac{\theta'^2}{\nu_f}\phi_5, \tag{3.108}$$

$$\frac{\Theta_\infty^2 b^2}{k_f\left(\Theta_w - \Theta_\infty\right)^2}\frac{k_{nf}}{\Theta_\infty^2}\left\{(1+N_r)\left(\frac{\partial\Theta}{\partial y}\right)^2\right\} = \frac{b^2}{\nu_f x}U_w\left(1+N_r\right)\frac{\theta'^2}{\phi_5}, \tag{3.109}$$

$$\frac{\Theta_\infty^2 b^2}{k_f\left(\Theta_w - \Theta_\infty\right)^2}\frac{k_{nf}}{\Theta_\infty^2}\left\{(1+N_r)\left(\frac{\partial\Theta}{\partial y}\right)^2\right\} = R_e\left(1+N_r\right)\frac{\theta'^2}{\phi_5}. \tag{3.110}$$

Consider second term of equation (3.105),

$$\frac{\mu_{nf}}{\Theta_\infty}\left(\frac{\partial u}{\partial y}\right)^2, \tag{3.111}$$

using equation (3.19) and (3.61), we get

$$\frac{\mu_{nf}}{\Theta_\infty}\left(\frac{\partial u}{\partial y}\right)^2=\frac{\mu_{nf}}{\Theta_\infty}\left(\frac{bxf''(\eta)}{(1-\xi t)}\sqrt{\frac{b}{\nu_f(1-\xi t)}}\right)^2, \tag{3.112}$$

$$\frac{\mu_{nf}}{\Theta_\infty}\left(\frac{\partial u}{\partial y}\right)^2=R_e\left(\frac{B_r}{\Omega\phi_1}\right)f''^2. \tag{3.113}$$

Consider third term of equation (3.105),

$$\frac{\sigma_{nf}B^2(t)u^2}{\Theta_\infty}, \tag{3.114}$$

$$\frac{\sigma_{nf}B^2(t)u^2}{\Theta_\infty}=\frac{\Theta_\infty^2 b^2}{k_f\left(\Theta_w-\Theta_\infty\right)^2}\left(\frac{\sigma_{nf}B^2(t)u^2}{\Theta_\infty}\right), \tag{3.115}$$

using equation (3.14) and (3.62), we get

$$\frac{\sigma_{nf}B^2(t)u^2}{\Theta_\infty}=\frac{\Theta_\infty^2 b^2}{k_f\left(\Theta_w-\Theta_\infty\right)^2}\left(\left(\frac{\sigma_f\phi_4}{\Theta_\infty}\right)\left(\frac{B_o^2}{1-\xi t}\right)\left(\frac{bx}{1-\xi t}\right)^2 f'^2\right), \tag{3.116}$$

$$\frac{\sigma_{nf}B^2(t)u^2}{\Theta_\infty}=\frac{\phi_4 Br}{\Omega}M^2Ref'^2. \tag{3.117}$$

Consider forth term of equation (3.103),

$$\frac{\mu_{nf}u^2}{k\Theta_\infty}, \tag{3.118}$$

$$\frac{\mu_{nf}u^2}{k\Theta_\infty}=\frac{\Theta_\infty^2 b^2}{k_f\left(\Theta_w-\Theta_\infty\right)^2}\left(\frac{\mu_{nf}u^2}{\Theta_\infty k}\right), \tag{3.119}$$

using equation (3.14) and (3.61), we get

$$\frac{\mu_{nf}u^2}{k\Theta_\infty}=\frac{\Theta_\infty^2 b^2}{k_f\left(\Theta_w-\Theta_\infty\right)^2}\left(\frac{\mu_f}{\phi_1\Theta_\infty k}\left(\left(\frac{bx}{1-\xi t}\right)^2\right)f'2\right), \tag{3.120}$$

$$\frac{\mu_{nf}u^2}{k\Theta_\infty} = \frac{\Theta_\infty^2 b^2 \mu_f}{k_f}\left(\frac{1}{\Theta_\infty k} f'2\right), \tag{3.121}$$

$$\frac{\mu_{nf}u^2}{k\Theta_\infty} = R_e\left(\frac{Brk}{\phi_2\Omega}\right) f'^2. \tag{3.122}$$

Substituting the equation (3.110), (3.113), (3.117) and (3.122) in (3.105), we get

$$N_G = R_e\left(1+N_r\right)\frac{\theta'^2}{\phi_{\ 5}} + R_e\left(\frac{Br}{\Omega\phi_1}\right) f''^2 + R_e\frac{\phi_4 Br}{\Omega} M^2 f'^2 + R_e\left(\frac{B_r K}{\phi_2\Omega}\right) f'^2, \tag{3.123}$$

$$N_G = R_e\left[\phi_5(1+N_r)\theta'^2 + \frac{1}{\phi_1}\frac{B_r}{\Omega}\left(f''^2 + \phi_1\phi_4 M f'^2 + K f'^2\right)\right], \tag{3.124}$$

here

$$R_e = \frac{U_w b^2}{\nu_f x}, \qquad B_r = \frac{\mu_f U_w^2}{k_f\left(\Theta_w - \Theta_\infty\right)}, \qquad \Omega = \frac{\Theta_w - \Theta_\infty}{\Theta_\infty}. \tag{3.125}$$

3.6 Numerical Results and Discussion

The main objective of this section is to analyze the numerical results displayed in the graphical and tabular form. The results are produced for the Cu-water and TiO_2-water non-Newtonian Maxwell nanofluids. The numerical results are presented in Figures 3.2-3.23 and in Table 3.2.

3.6.1 Effect of Maxwell Parameter γ

The influence of Maxwell parameter γ on velocity, temperature and entropy generation profiles of Cu-water and TiO_2-water non-Newtonian Maxwell nanofluids are presented in Figures 3.2-3.4. Computations are performed for $\gamma = 0.01, 0.3, 0.5$ at uniform nanoparticle concentration of 0.2. The velocity profiles in Figure 3.2 decreases with an increasing values of γ and hence declines the thickness of momentum boundary layer. Moreover, for the fixed value of $\gamma = 0.3$ the boundary layer thickness of TiO_2-water nanofluid is relatively more than the Cu-water nanofluid.

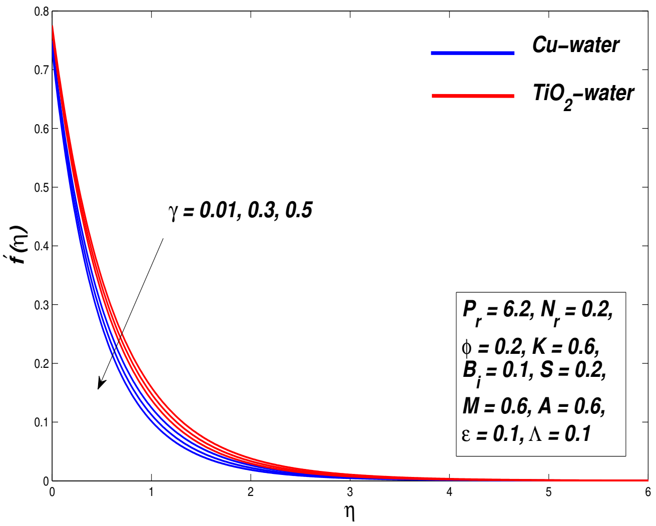

FIGURE 3.2: Velocity Distribution against the Parameter γ

The decreasing trend in velocity profiles is due to increase of resistance in fluid and also corresponds to increase in skin friction coefficient (velocity gradient) at the boundary.

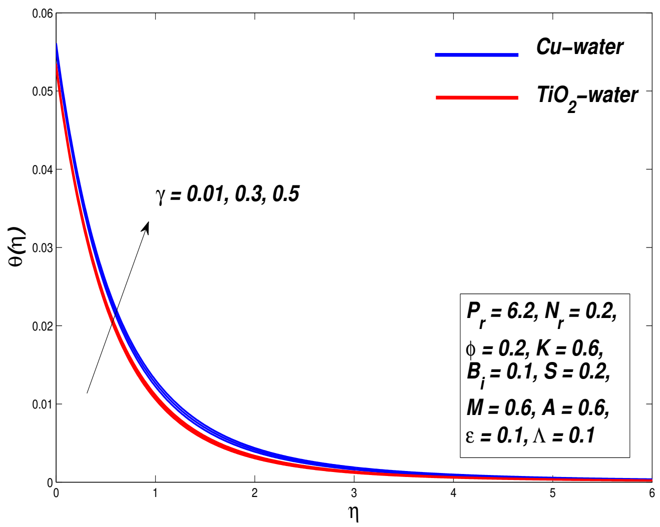

FIGURE 3.3: Temperature Distribution against the Parameter γ

It can be observed from Figure 3.3 that the temperature of nanofluids rises with the increasing values of parameter γ. This increasing trend indicate the enhancement in the thickness of thermal boundary layer and reduction in the rate of heat transfer. The reason behind this behaviour of temperature profiles is the increase in the elasticity stress parameter. Figure 3.4 showed the impact of Maxwell parameter γ on the entropy of the system.

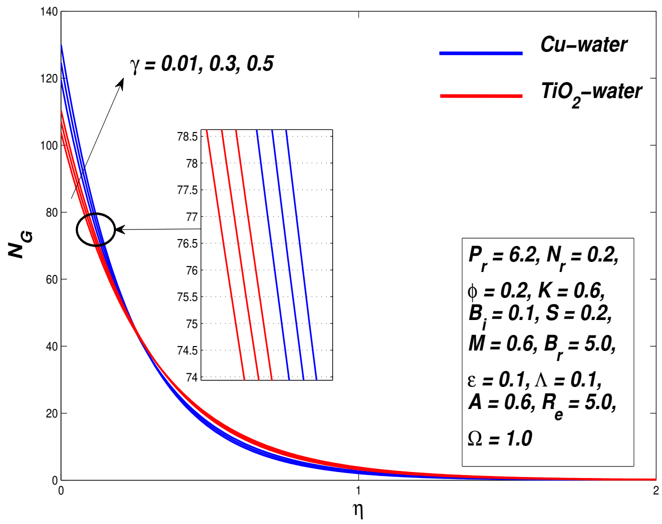

FIGURE 3.4: Entropy Generation Distribution against the Parameter γ

It is noticed, that raising Maxwell parameter increases the entropy of the system. Finally, it is observed from Table 3.2, the rate of heat transfer at the boundary (Nusselt number) decreases for both Cu and TiO_2 water based nanofluids.

3.6.2 Effect of Unsteadiness Parameter A

Figures 3.5-3.7 depicted the impact of unsteady parameter A on velocity, temperature and entropy generation profiles of Maxwell nanofluid. It is noted that the fluid flow slowly Figure 3.5 and its temperature decrease within boundary layer with ascending values of parameter A Figure 3.6. This due to the fact that unsteadiness parameter A is inversely proportional to stretching rate, so increasing A reduces the stretching of the surface and less stretching means less velocity. The impact of increasing values of parameter A is to decrease the thickness of both momentum and thermal boundary layer. Figure 3.7 displayed the influence of variation of unsteadiness parameter A on the entropy generation. The changeover point for the entropy profile is estimated at about

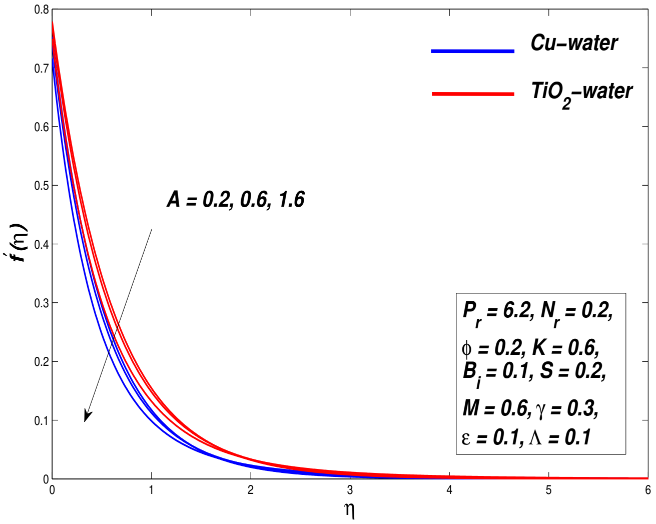

FIGURE 3.5: Velocity Distribution against the Parameter A

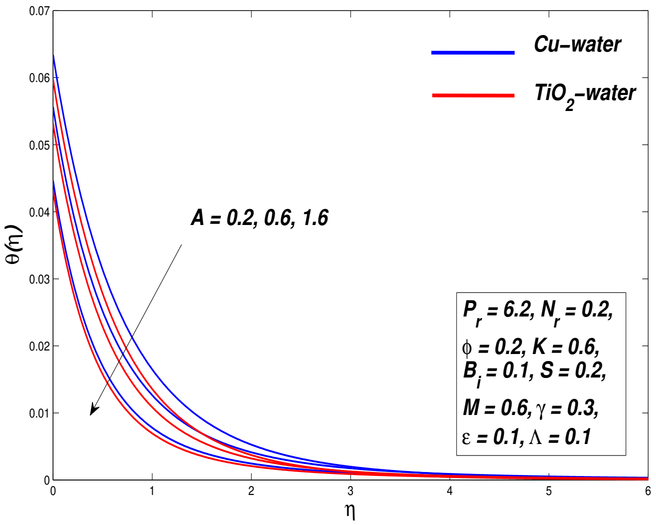

FIGURE 3.6: Temperature Distribution against the Parameter A

$\eta = 0.3$. In other words, the thermal process is converging towards the case of reversible process. From Table 3.2, the increasing trends are observed for the velocity and temperature gradients at the boundary. The boundary layer energy is absorbed due to unsteadiness resulting the increase in the rate of heat transfer at the boundary surface.

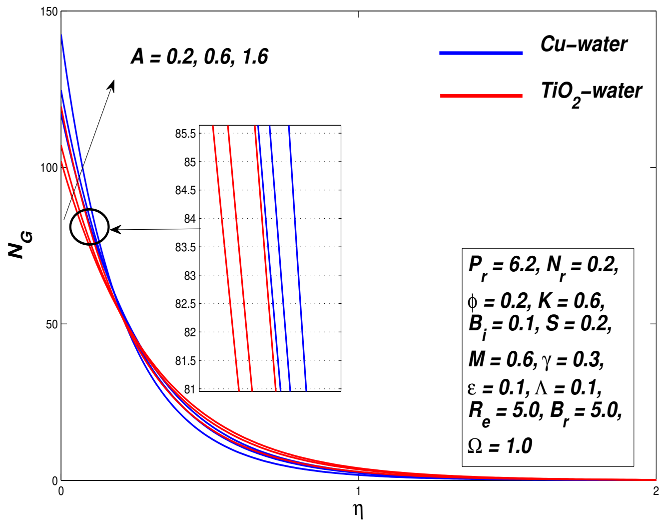

FIGURE 3.7: Entropy Generation Distribution against the Parameter A

3.6.3 Effect of Magnetic Parameter M and Porous Medium Parameter K

Figures 3.8-3.13 exhibited the behaviours of nanofluids motion, temperature distribution and entropy generation with increasing strength of applied transverse magnetic field and the porosity of the medium, respectively.

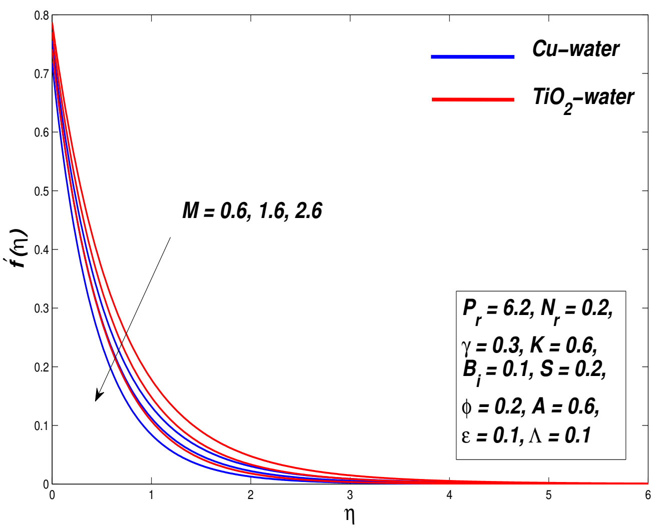

FIGURE 3.8: Velocity Distribution against the Parameter M

Similar behaviours are observed in profiles of velocity, temperature and entropy with increasing values of parameter M and K.

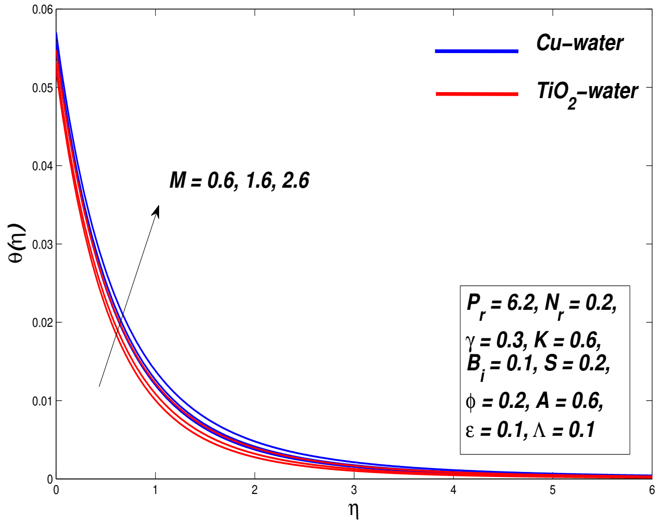

FIGURE 3.9: Temperature Distribution against the Parameter M

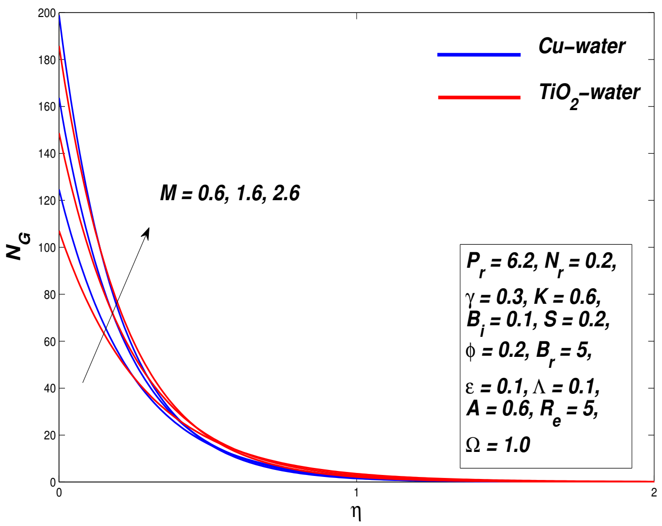

FIGURE 3.10: Entropy Generation Distribution against the Parameter M

The magnetic field applied normal to the flow direction, produces a resistive force known as Lorentz force that reduces fluid movement within the boundary layer. The Lorentz force impact in the form of decreasing trend in velocity profiles are clearly visible in Figure 3.8. Whereas, the increase in permeability is to decrease the magnitude of the resistive Darcian body force, therefore a continuous less drag is experienced by the fluid and flow reduces thereby declines the velocity within boundary layer Figure 3.11.

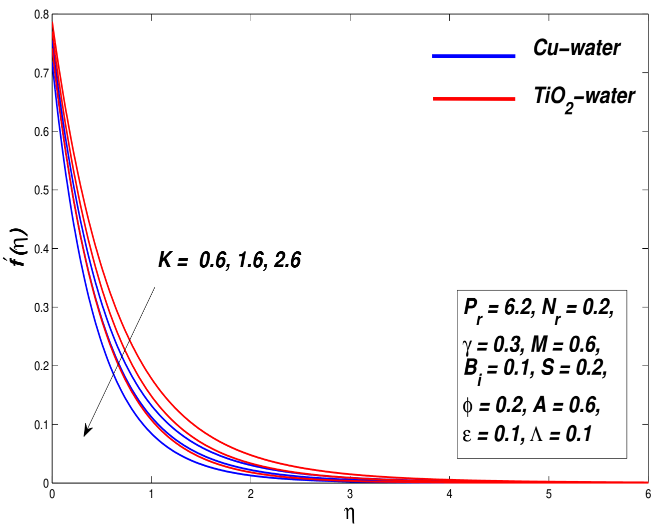

FIGURE 3.11: Velocity Distribution against the Parameter K

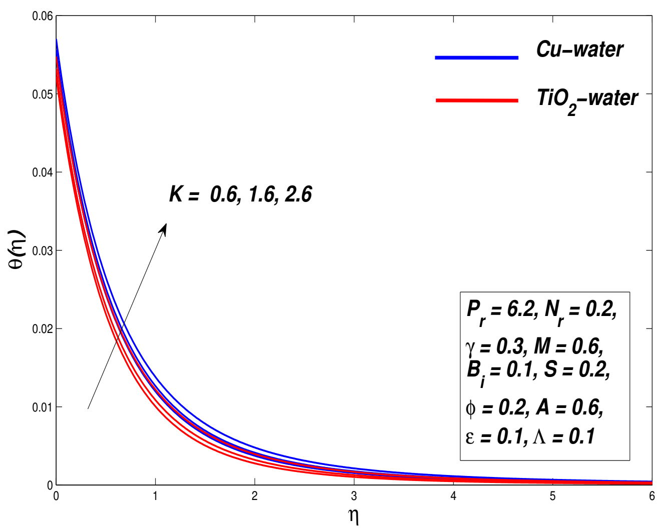

FIGURE 3.12: Temperature Distribution against the Parameter K

The parameters M and K are inversely proportional to the density of nanofluid hence the rise in applied magnetic field or the porosity of the medium decreases the density and as a result the temperature profile rises within boundary layer Figures 3.9, 3.12. This will increase the thickening level of thermal boundary layer and reduces the Nusselt number. The influence of Lorentz or the Darcian body force at the boundary is presented in Table 3.2. The velocity gradient increases but the rate of heat transfer declines with increasing strength of parameters M and K. Figure 3.10, 3.13 demonstrated that the entropy of the system increases with rise in magnetic field and the permeability of the medium.

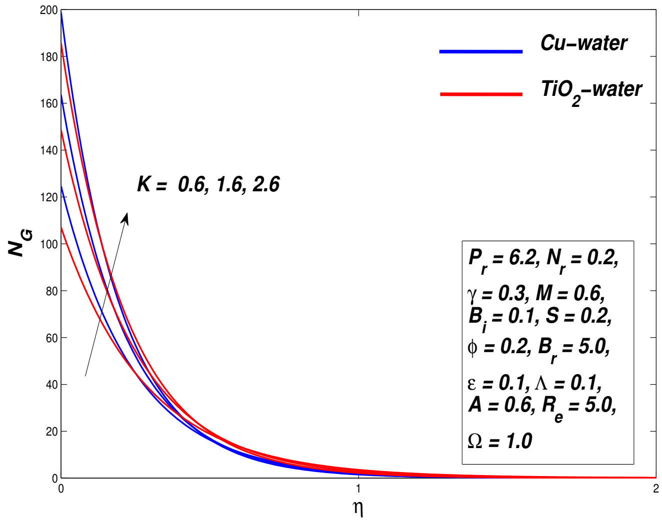

FIGURE 3.13: Entropy Generation Distribution against the Parameter K

3.6.4 Effect of Nanoparticle Volume Fraction Parameter ϕ

Figures 3.14-3.16 exhibited the nature of fluid motion, temperature distribution

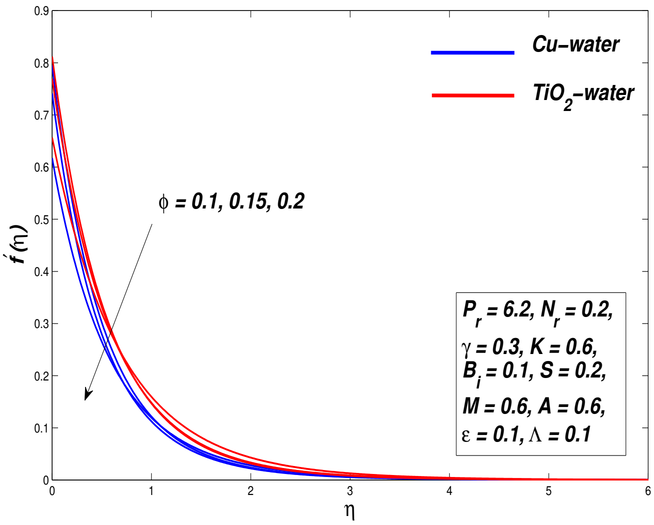

FIGURE 3.14: Velocity Distribution against the Parameter ϕ

and entropy generation within boundary layer for Maxwell nanofluids due to variation in nanoparticle volume concentration parameter ϕ. The parameter ϕ correspond to volume of solid particles in the basefluid.

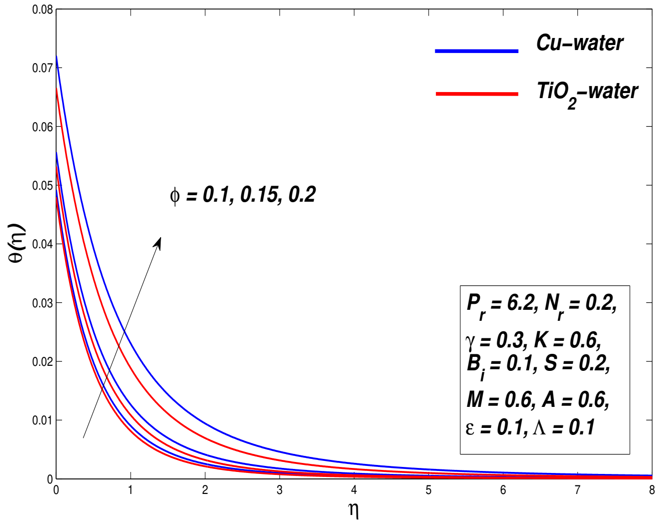

FIGURE 3.15: Temperature Distribution against the Parameter ϕ

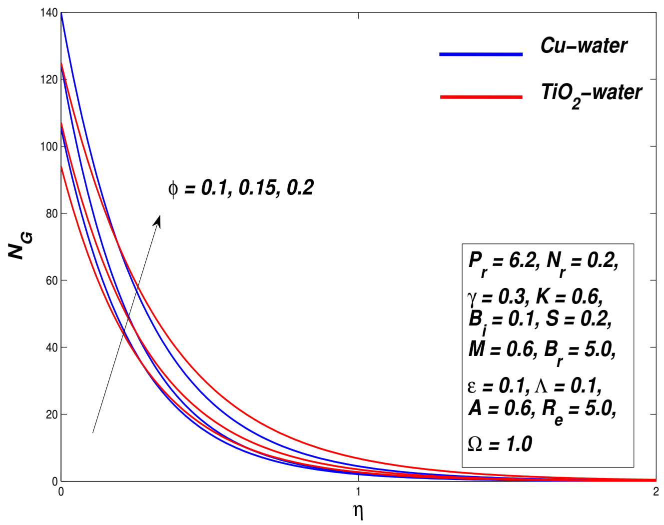

FIGURE 3.16: Entropy Generation Distribution against the Parameter ϕ

It is well known solid particles have higher thermal conductivity than fluids, therefore increase in ϕ reduces fluid velocity as observed from Figure 3.14 and enhances its temperature in the boundary layer region. Whereas, this fact is very much evident in Figure 3.15 that the increase in the total thermal conductivity of nanofluids increases the temperature and the thickness of thermal boundary layer. The increasing and decreasing trend of the velocity gradient and Nusselt number is observed with the increase of parameter ϕ see Table 3.2. Figure 3.16 illustrates that the entropy profile increases with the increasing nanoparticle volume fraction parameter. The entropy generation rate is higher for Cu-water nanofluids as compared to TiO_2-water nanofluids.

3.6.5 Effect of Velocity Slip Parameter Λ

Figures 3.17-3.19 illustrated that the positive values of slip parameter γ reduces fluid movement and entropy generation of Maxwell nanofluids. Whereas the temperature of Maxwell nanofluids increases with increasing values of parameter Λ. In Figure 3.17 the decrease in velocity is consistent with the fact that slip velocity retards the motion of the boundary surface. In other words, velocity slip act opposite to stretching pull of the surface and resists its transmission to the fluid. As a result, momentum boundary layer decreases with rise in parameter Λ.

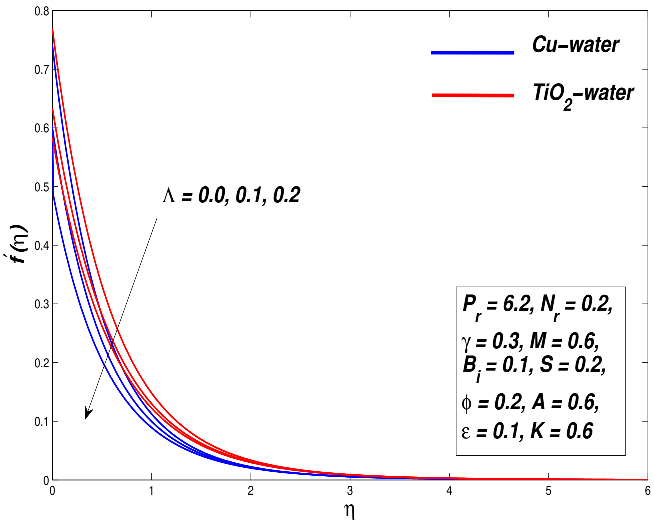

FIGURE 3.17: Velocity Distribution against the Parameter Λ

Figure 3.18 depicted the temperature distribution within the boundary layer against the parameter Λ.

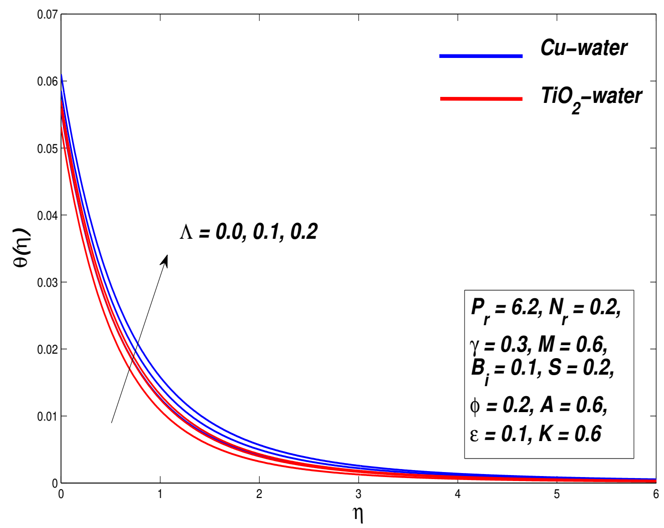

FIGURE 3.18: Temperature Distribution against the Parameter Λ

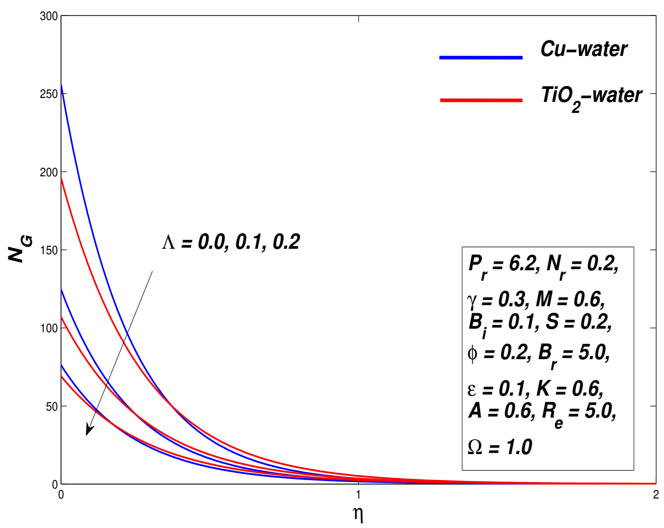

FIGURE 3.19: Entropy Generation Distribution against the Parameter Λ

It is noted that the temperature of nanofluids raises with the increase in velocity slip at the boundary. The velocity slip is inversely proportional to the temperature distribution and an increase in the parameter Λ increases the thermal boundary layer thickness and reduces the Nusselt number. Table 3.2 shows that positive increase in velocity slip leads to decrease in velocity gradient and heat transfer rate for both $Cu - H_2O$ and $TiO_2 - H_2O$ nanofluids. This expected behaviour is due to the fact that the boundary slip reduces the friction at the solid-fluid interface and consequently the rate of heat transfer. From Figure 3.19 it can be observed easily that the entropy decreases with increasing values of Λ. The decrease in entropy indicates that the system is cooling down. If the entropy in the boundary layer decreases, it must increase by the same amount outside the boundary layer.

3.6.6 Effect of Reynolds Number R_e and the Brinkman Number B_r

The effects of Reynolds number R_e and Brinkman number B_r on entropy generation profiles are presented in this section. Numerical computations showed the higher values of R_e increases entropy which physically means that the inertial forces dominate the viscous effects see Figure 3.20.

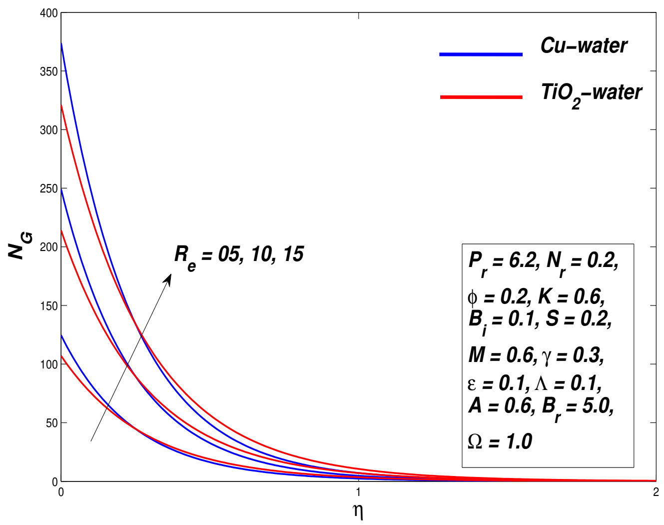

FIGURE 3.20: Entropy Generation Distribution against the Parameter R_e

Figure 3.21 discussed the influence of B_r on the entropy. It is found that the Brinkman number augmentation increases the entropy generation. This is due to the fact that Brinkman number is the ratio of heat dissipation to the conduction at the surface so increasing the values of B_r means more heat is dissipated compared with the conduction of heat at the surface, which results in an increase in the entropy.

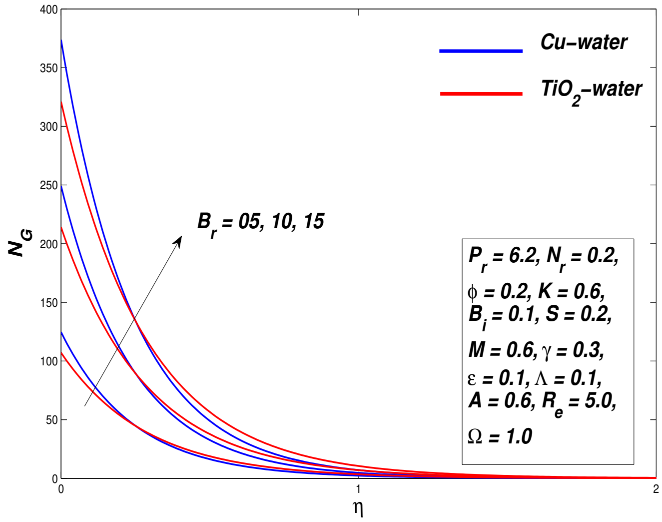

FIGURE 3.21: Entropy Generation Distribution against the Parameter B_r

3.6.7 Effect of Magnetic Parameter M and Radiation Parameter N_r on Skin Friction C_f and the Nusselt Number Nu_x, Respectively

The influence of magnetic parameter M and radiation parameter N_r on skin friction coefficient C_f and Nusselt number Nu_x profiles of Cu-water and TiO_2-water non-Newtonian nanofluids are presented in Figures 3.22-3.23, respectively. In 3.22 computations are performed for $M = 0.6, 0.8, 1.2$ whereas the parameter γ takes the values $0.01, 0.3, 0.5$. It is noted when we increase the magnetic parameter M the skin friction coefficient C_f increases. The physical reason behind this is that greater M is responsible for greater friction between the surface and the fluid as a result skin friction increases. In 3.23 computations are performed for $N_r = 0.2, 0.4, 0.9$ whereas the Prandtl number P_r is fixed on $1.0, 6.2, 7.38$. It is observed when we increase the radiation parameter Nr the rate of convective heat transfer (Nusselt number) increases. This is due to the fact that a greater heat flux is generated, which results in a greater heat transfer rate.

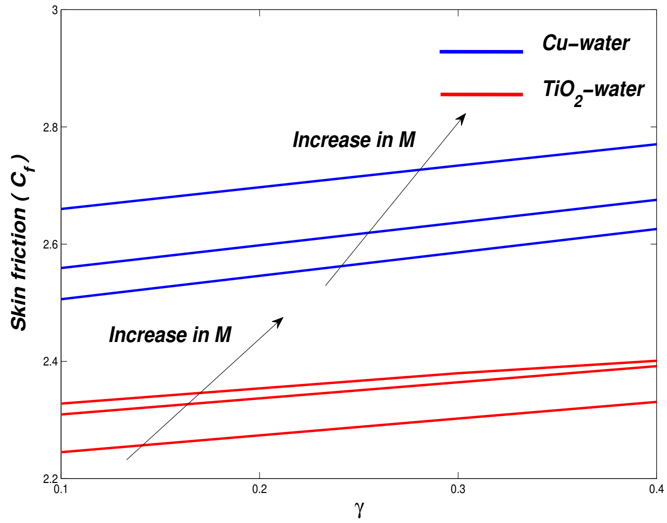

FIGURE 3.22: Skin Friction C_f against the Parameter γ

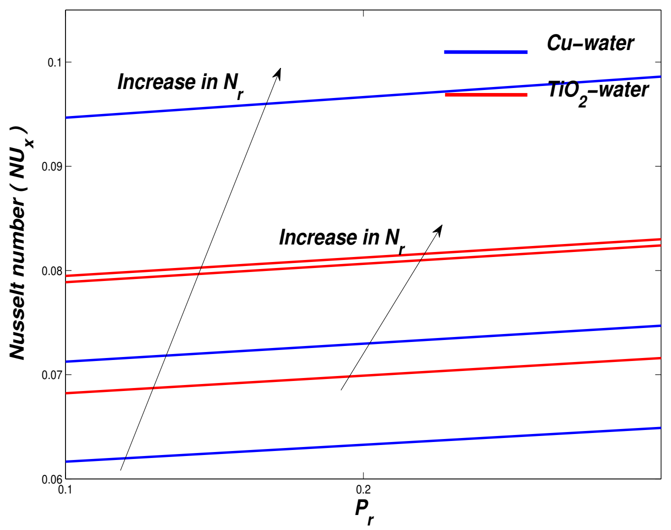

FIGURE 3.23: Nusselt Number Nu_x against the Parameter P_r

γ	A	M	K	ϕ	Λ	ϵ	N_r	B_i	S	$C_fRe_x^{\frac{1}{2}}$ $Cu-water$	$C_fRe_x^{\frac{1}{2}}$ $T_iO_2-water$	$N_uRe_x^{\frac{-1}{2}}$ $Cu-water$	$N_uRe_x^{\frac{-1}{2}}$ $T_iO_2-water$
0.01	0.6	0.6	0.6	0.2	0.1	0.1	0.2	0.1	0.2	2.4702	2.2194	0.0650	0.0718
0.3										2.5859	2.3025	0.0649	0.0716
0.5										2.6656	2.3592	0.0648	0.0715
0.3	0.2									2.4713	2.2125	0.0644	0.0711
	0.6									2.5859	2.3025	0.0649	0.0716
	1.6									2.8408	2.5061	0.0657	0.0723
		0.6								2.5859	2.3025	0.0649	0.0716
		1.6								2.8225	2.5862	0.0648	0.0714
		2.6								3.0215	2.8159	0.0647	0.0713
			0.6							2.5859	2.3025	0.0649	0.0716
			1.6							2.8221	2.5858	0.0648	0.0714
			2.6							3.0290	2.8152	0.0647	0.0713
				0.1						2.0461	1.8795	0.0857	0.0901
				0.15						2.2392	2.1081	0.0708	0.0837
				0.2						2.5859	2.3025	0.0649	0.0716
					0.0					3.7682	3.1669	0.0652	0.0718
					0.1					2.5859	2.3025	0.0649	0.0716
					0.2					1.9998	1.8309	0.0647	0.0713
						0.1				2.5859	2.3025	0.0649	0.0716
						1.0				2.5859	2.3025	0.0648	0.0715
						2.0				2.5859	2.3025	0.0647	0.0714
							0.2			2.5859	2.3025	0.0649	0.0716
							0.5			2.5859	2.3025	0.0796	0.0877
							0.8			2.5859	2.3025	0.0939	0.1035

γ	A	M	K	ϕ	Λ	ϵ	N_r	B_i	S	$C_f Re_x^{\frac{1}{2}}$ $Cu-water$	$C_f Re_x^{\frac{1}{2}}$ $T_iO_2-water$	$N_u Re_x^{\frac{-1}{2}}$ $Cu-water$	$N_u Re_x^{\frac{-1}{2}}$ $T_iO_2-water$
								0.1		2.5859	2.3025	0.0649	0.0716
								0.2		2.5859	2.3025	0.1230	0.1359
								0.6		2.5859	2.3025	0.3041	0.3385
									0.2	2.5859	2.3025	0.0649	0.0716
									0.5	3.0447	2.5977	0.0655	0.0722
									0.6	3.2456	2.7177	0.0656	0.0724

TABLE 3.2: Values of Skin Friction $= C_f Re_x^{\frac{1}{2}}$ and Nusselt Number $= N_u Re_x^{\frac{-1}{2}}$ for $P_r = 6.2$

3.7 Conclusions

The numerical results presented in this chapter focus on heat transfer and entropy generation of non-Newtonian Maxwell nanofluid in the existence of slip and convective boundary conditions. Thermal radiation and the temperature dependent thermal conductivity are also considered in the present model along with the effects of uniform magnetic field. The main findings of the present research are:

- A stronger magnetic field has a negative impact on the motion of the fluid particles in the boundary layer and the velocity of the fluid decreases with increasing strength of magnetic field.

- The key parameters such as Maxwell fluid parameter, permeability parameter, nanoparticle volumetric concentration parameter, thermal conductivity parameter, velocity slip parameter and thermal radiation parameter increases the temperature distribution and thickness of thermal boundary layer and reduces the rate of heat transfer at the surface.

- The unsteadiness parameter and the suction parameter reduces the thickness of the thermal boundary layer and increases the rate of heat transfer at the surface.

- It is well known fact that the inclusion of solid nanoparticles in the ordinary fluids increases the overall thermal conductivity of the mixture. Therefore the increase in ϕ decrease in thickness of momentum and increase the thickness of thermal boundary layer respectively.

- Entropy is found to be rising with the Reynolds number R_e, Brinkman number B_r, unsteadiness parameter A, magnetic parameter M, permeability parameter K, nanoparticle volume fraction parameter ϕ and suction parameter $S > 0$ but reduce with increase in the values of injection parameter $S < 0$ and velocity slip parameter Λ.

- For the present study, Cu-water based nanofluid is observed as a better thermal conductor than TiO_2-water based nanofluid.

Chapter 4

Flow, Heat Transfer and Entropy Analysis of Powell-Eyring Nanofluid with nanoparticle shape factor

4.1 Introduction

Powell-Eyring non-Newtonian fluid is considered for nanofluid in this chapter. The same flow geometry is considered as in previous chapter along with the temperature dependent thermal conductivity. Solutions to governing equations are found using similarity technique along with Keller box method or implicit finite difference approach. Results are discussed to study the effect of governing physical parameters on velocity, temperature and entropy profiles and velocity gradient (skin friction coefficient) and the strength of convective heat exchange (Nusselt number) of nanofluid. In addition to this, empirical values of five different nanoparticle shapes have been utilize to look at their impact on the heat transfer rate as well as the temperature distribution in the boundary layer.

4.2 Mathematical Formulation

Assume an incompressible, electrically conducting, two-dimensional laminar slip flow of non-Newtonian Powell-Eyring nanofluid which covers the space over an infinite stretching flat porous plat. The surface of the plate is insulated and velocity slip conditions has been invoked at the boundary. Thermal conductivity of fluid-solid mixture is assumed to vary linearly with temperature θ. The radiative heat transfer is taken into account and Rosseland approximation is utilized for the radiation effects. The flow is produced due to the stretching of surface with non-uniform velocity $U_w(x,t)$ given in equation (3.1).
The schematic diagram of the mathematical model under consideration is presented in Figure 4.1.

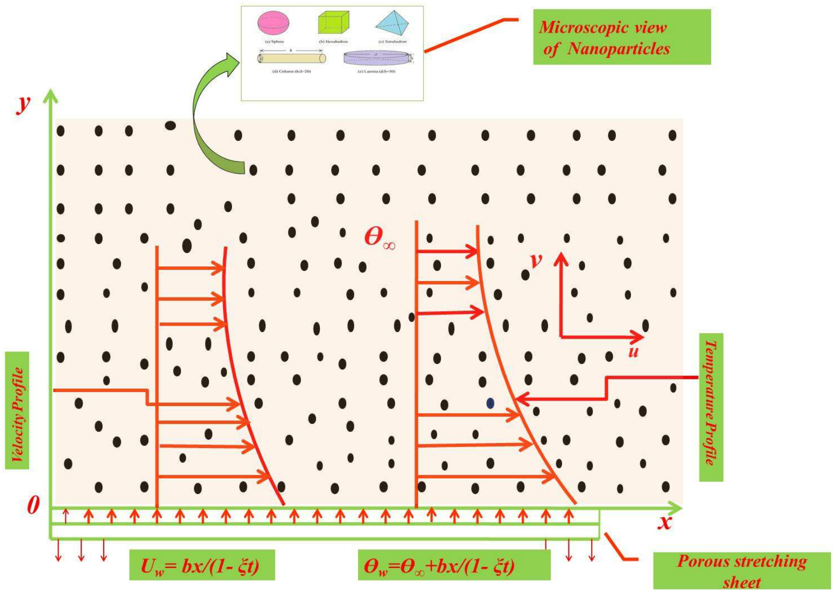

FIGURE 4.1: Schematic Diagram of the Fluid Flow

For suitability the principal edge of the plate is assumed at $x = 0$ and is considered along the x-axis. The temperature of the convective surface is assumed as $\Theta_w(x,t) = \Theta_\infty + \frac{bx}{1-\xi t}$, where Θ_∞ is the temperature outside of the boundary layer. The Cauchy stress tensor for the Power-Eyring fluid is given in equation (2.39).

The equation (2.39) for the present nanofluid model becomes

$$\tau_{ij} = \mu_{nf}\left(\frac{\partial u_i}{\partial x_j}\right) + \frac{1}{\tilde{\beta}}\sinh^{-1}\left(\frac{1}{\varsigma^*}\frac{\partial u_i}{\partial x_j}\right). \tag{4.1}$$

where $\tilde{\beta}$ and ς^* are the material constants.

The governing equations of two-dimensional boundary layer flow and heat transfer of Powell-Eyring fluid are given in equations (2.56) and (2.85). These equations for the Powell-Eyring nanofluid reduced to the form (see for example, Hayat *et al.* [192])

$$\frac{\partial u}{\partial t} + u\frac{\partial u}{\partial x} + v\frac{\partial u}{\partial y} = \left(\nu_{nf} + \frac{1}{\rho_{nf}\tilde{\beta}\varsigma^*}\right)\frac{\partial^2 u}{\partial y^2} - \frac{1}{2\tilde{\beta}{\varsigma^*}^3\rho_{nf}}\left(\frac{\partial u}{\partial y}\right)^2\frac{\partial^2 u}{\partial y^2}, \tag{4.2}$$

$$\frac{\partial \Theta}{\partial t} + u\frac{\partial \Theta}{\partial x} + v\frac{\partial \Theta}{\partial y} = \frac{1}{(\rho C_p)_{nf}}\left[\frac{\partial}{\partial y}\left(\kappa^*_{nf}(\Theta)\frac{\partial \Theta}{\partial y}\right)\right] - \frac{1}{(\rho C_p)_{nf}}\left(\frac{\partial q_r}{\partial y}\right). \tag{4.3}$$

The BCs for the modeled problem are

$$u(x,0) = U_w + \mu_{nf}\left(\frac{\partial u}{\partial y}\right), \quad v(x,0) = V_w, \quad -k_0\left(\frac{\partial \Theta}{\partial y}\right) = h_f(\Theta_w - \Theta), \tag{4.4}$$

$$u \to 0, \quad \Theta \to \Theta_\infty \quad \text{as} \quad y \to \infty. \tag{4.5}$$

The shape factor m is explained in Table 4.1, (for details see for example, Hamilton and Crosser [193])

ParticleShapes	*Sphere*	*Hexahedron*	*Tetrahedron*	*Column*	*Lamina*
m	3	3.7221	4.0613	6.3698	16.1576

TABLE 4.1: Values of the Empirical Shape Factor for Different Particle Shapes

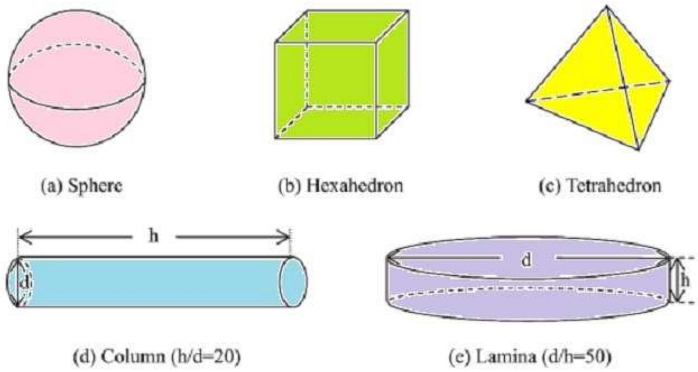

FIGURE 4.2: Different Shapes of Nanoparticles

4.3 Solution of the Problem

To solve the governing system of partial differential equations (4.2) and (4.3). The similarity variables are defined as (see for example, Hayat *et al.* [184])

$$u = \frac{\partial \psi}{\partial y}, \qquad v = -\frac{\partial \psi}{\partial x}. \tag{4.6}$$

$$\psi(x,y) = \sqrt{\frac{\nu_f b}{(1-\xi t)}}\, x f(\eta) \quad \text{and} \quad \eta(x,y) = \sqrt{\frac{b}{\nu_f(1-\xi t)}}\, y, \qquad \theta(\eta) = \frac{\Theta - \Theta_\infty}{\Theta_w - \Theta_\infty}. \tag{4.7}$$

Using equations (4.7) in (4.6),

$$u = \frac{bx}{(1-\xi t)} f'(\eta), \tag{4.8}$$

$$v = -\sqrt{\frac{\nu_f b}{(1-\xi t)}}\, f(\eta). \tag{4.9}$$

Now using appropriate equations from (3.16 - 3.34) into (4.2)-(4.3). we get the following ODEs

$$\left(\frac{1}{\phi_1\phi_2} + \frac{\omega}{\phi_1}\right) f''' + f f'' - f'^2 - A\left(f' + \frac{\eta}{2} f''\right) - \frac{\omega\Delta}{\phi_2} f''^2 f''' = 0, \tag{4.10}$$

$$\theta''\left(1+\epsilon\theta+\frac{1}{\phi_5}P_rN_r\right)+\epsilon\theta'^2+P_r\frac{\phi_3}{\phi_5}\left[f\theta'-f'\theta-A(\theta+\frac{\eta}{2}\theta')\right]=0. \tag{4.11}$$

The transformed boundary conditions from equations (3.43), (3.46), (3.56), (3.58) and (3.60)) are

$$f(0)=S, \qquad f'(0)=1+\frac{\Lambda}{\phi_1}f''(0), \qquad \theta'(0)=-B_i(1-\theta(0)), \tag{4.12}$$

$$f'(\eta)\to 0, \qquad \theta(\eta)\to 0, \quad \text{as} \quad \eta\to\infty. \tag{4.13}$$

In the above equations primes stand for the differentiation of the function with respect to η. $A=\frac{\xi}{b}$ is the unsteady flow parameter, $\omega=\frac{1}{\mu_f\tilde{\beta}\varsigma^*}$ and $\Delta=\frac{{U_w}^3}{2{\varsigma^*}^2\nu_f x}$ are the material parameters, $P_r=\frac{\nu_f}{\alpha_f}$ is the Prandtl number, $\alpha_f=\frac{\kappa_f}{(\rho C_p)_f}$ is the thermal diffusivity parameter, $N_r=\frac{16}{3}\frac{\sigma^*\Theta_\infty^3}{\kappa^*\nu_f(\rho C_p)_f}$ is the thermal radiation parameter, $S=-V_w\sqrt{\frac{1-\xi t}{\nu_f\ b}}$ is the mass transfer parameter, $\Lambda=\sqrt{\frac{b}{\nu_f(1-\xi t)}}\mu_f$ is the velocity slip parameter and $B_i=\frac{h_f}{k_0}\sqrt{\frac{\nu_f(1-\xi t)}{b}}$ is the sheet convection parameter or so-called Biot number. It is observed some parameters depend on ξ and is time dependent. Therefore to obtain non-similar solutions for the proposed problem numerical results are computed for locally similar parameters.

4.4 Entropy Generation Analysis

The entropy generation for the present thermal system is given by (see for example, Das *et al.* [167])

$$E_G=\frac{k_{nf}}{\Theta_\infty^2}\left\{\left(\frac{\partial\Theta}{\partial y}\right)^2+\frac{16}{3}\frac{\sigma^*\Theta_\infty^3}{\kappa^*\nu_f(\rho C_p)_f}\left(\frac{\partial\Theta}{\partial y}\right)^2\right\}+\frac{\mu_{nf}}{\Theta_\infty}\left(\frac{\partial u}{\partial y}\right)^2. \tag{4.14}$$

The first term in entropy equation represents the heat transfer irreversibility, second term is the fluid friction. The entropy generation is represented by N_G and is given in equation (3.104). Now putting (4.14) in (3.104), we get

$$N_G = \frac{\Theta_\infty^2 b^2}{k_f\left(\Theta_w - \Theta_\infty\right)^2}\frac{k_{nf}}{\Theta_\infty^2}\left\{\left(\frac{\partial\Theta}{\partial y}\right)^2 + \frac{16}{3}\frac{\sigma^*\Theta_\infty^3}{\kappa^*\nu_f(\rho C_p)_f}\left(\frac{\partial\Theta}{\partial y}\right)^2\right\} + \frac{\mu_{nf}}{\Theta_\infty}\left(\frac{\partial u}{\partial y}\right)^2. \tag{4.15}$$

Consider first term of equation (4.15),

$$\frac{\Theta_\infty^2 b^2}{k_f\left(\Theta_w - \Theta_\infty\right)^2}\frac{k_{nf}}{\Theta_\infty^2}\left\{(1+N_r)\left(\frac{\partial\Theta}{\partial y}\right)^2\right\}, \tag{4.16}$$

using equation (3.33) and (3.62), we get

$$= \frac{\Theta_\infty^2 b^2}{k_f\left(\Theta_w - \Theta_\infty\right)^2}\frac{k_f\phi_5}{\Theta_\infty^2}\left\{(1+N_r)\left(\frac{(bx)^2}{(1-\xi t)}^2\theta'(\eta)^2\frac{b}{\nu_f(1-\xi t)}\right)\right\}, \tag{4.17}$$

$$\frac{\Theta_\infty^2 b^2}{k_f\left(\Theta_w - \Theta_\infty\right)^2}\frac{k_{nf}}{\Theta_\infty^2}\left\{(1+N_r)\left(\frac{\partial\Theta}{\partial y}\right)^2\right\} = \frac{b^2}{k_f x}\left(\frac{bx}{(1-\xi t)}\right)\frac{\theta'^2}{\nu_f}\phi_5, \tag{4.18}$$

$$\frac{\Theta_\infty^2 b^2}{k_f\left(\Theta_w - \Theta_\infty\right)^2}\frac{k_{nf}}{\Theta_\infty^2}\left\{(1+N_r)\left(\frac{\partial\Theta}{\partial y}\right)^2\right\} = \frac{b^2}{\nu_f x}U_w\left(1+N_r\right)\frac{\theta'^2}{\phi_5}, \tag{4.19}$$

$$\frac{\Theta_\infty^2 b^2}{k_f\left(\Theta_w - \Theta_\infty\right)^2}\frac{k_{nf}}{\Theta_\infty^2}\left\{(1+N_r)\left(\frac{\partial\Theta}{\partial y}\right)^2\right\} = R_e\left(1+Nr\right)\frac{\theta'^2}{\phi_5}. \tag{4.20}$$

Consider second term of equation (4.15),

$$\frac{\mu_{nf}}{\Theta_\infty}\left(\frac{\partial u}{\partial y}\right)^2, \tag{4.21}$$

using equation (3.19) and (3.61), we get

$$\frac{\mu_{nf}}{\Theta_\infty}\left(\frac{\partial u}{\partial y}\right)^2 = \frac{\mu_{nf}}{\Theta_\infty}\left(\frac{bxf''(\eta)}{(1-\xi t)}\sqrt{\frac{b}{\nu_f(1-\xi t)}}\right)^2, \tag{4.22}$$

$$\frac{\mu_{nf}}{\Theta_\infty}\left(\frac{\partial u}{\partial y}\right)^2 = R_e\left(\frac{Br}{\Omega\phi_1}\right)f''^2. \tag{4.23}$$

Substituting the equation (4.20) and (4.23) in (4.15), we get

$$N_G = R_e \left(1 + N_r\right) \frac{\theta'^2}{\phi_{\ 5}} + R_e \left(\frac{B_r}{\Omega \phi_1}\right) f''^2, \tag{4.24}$$

$$N_G = R_e \left[\phi_5 (1 + N_r)\theta'^2 + \frac{1}{\phi_1} \frac{B_r}{\Omega} \left(f''^2\right)\right], \tag{4.25}$$

here Re represents the Reynolds number, B_r represents the Brinkman number and the dimensional less temperature gradient that can represented by Ω, which is defined by

$$R_e = \frac{U_w b^2}{\nu_f x}, \qquad B_r = \frac{\mu_f U_w^2}{k_f \left(\Theta_w - \Theta_\infty\right)}, \qquad \Omega = \frac{\Theta_w - \Theta_\infty}{\Theta_\infty}. \tag{4.26}$$

4.5 Code Validation

To check the validity of our numerical results comparison is made with the already published results of [167, 190, 191, 194] as the special cases for our study. The test case is the natural convection boundary layer flow of fluid over a flat plate in the presence of Newtonian slip. Results have been obtained for $A = 0$, $\phi = 0$, $\Lambda = 0$, $\epsilon = 0$, $S = 0$, $Nr = 0$, $m = 3$ and $B_i = 0$. In Table 4.2 the comparison is presented with acceptable level of accuracy.Therefore it is assumed that the results presented through present numerical scheme are very much accurate.

Pr	*Ishak* [190]	*Nazar* [191]	*Abolbashari* [194]	*Das* [167]	*Present* Results
0.72	0.8086	0.8086	0.80863135	0.80876122	0.80876181
1.0	1.0000	1.0000	1.00000000	1.00000000	1.00000000
3.0	1.9237	1.9236	1.92368259	1.92357431	1.92357420
7.0	3.0723	3.0722	3.07225021	3.07314679	3.07314651
10	3.7207	3.7006	3.72067390	3.72055436	3.72055429

TABLE 4.2: Numerical Results of Nusselt Number for Various Values of Prandtl Number

4.6 Numerical Results and Discussion

The Keller box numerical scheme is adopted in this section to solve the system of equations (4.10)-(4.11) along with the entropy equation (4.25). The boundary conditions are given in equations (3.43), (3.46), (3.56), (3.58) and (3.60). The initial step of Keller box scheme is to reduce the higher order ODEs into a system of first order ODEs that is,

$$z_1 = f', \tag{4.27}$$

$$z_2 = z_1', \tag{4.28}$$

$$z_3 = \theta', \tag{4.29}$$

$$\left(\frac{1}{\phi_1\phi_2} + \frac{\omega}{\phi_1}\right) z_2' + f z_2 - z_1^2 - A(z_1 + \frac{\eta}{2} z_2) - \frac{\omega\Delta}{\phi_2} z_2^2 z_2' = 0, \tag{4.30}$$

$$z_3' \left(1 + \epsilon\theta + \frac{1}{\phi_5} P_r N_r\right) + \epsilon z_3^2 + P_r \frac{\phi_3}{\phi_5} \left[f z_3 - z_1\theta - A(\theta + \frac{\eta}{2} z_3)\right] = 0. \tag{4.31}$$

The boundary conditions are reduced to the form

$$f(0) = S, z_1(0) = 1 + \frac{\Lambda}{\phi_1} z_2(0), z_3(0) = -B_i(1 - \theta(0)), z_1(\infty) \to 0, \theta(\infty) \to 0. \tag{4.32}$$

The derivatives appeared in the above system are then approximated by the central differences and averages are centered at the midpoints of the mesh and are expressed by

$$\eta_0 = 0, \quad \eta_j = \eta_{j-1} + h, \quad j = 1, 2, 3, ..., J-1, \quad \eta_J = \eta_\infty. \tag{4.33}$$

The ODEs (4.27)-(4.31) are then reduced to the following set of nonlinear algebraic equations.

$$\frac{(z_1)_j + (z_1)_{j-1}}{2} = \frac{f_j - f_{j-1}}{h}, \tag{4.34}$$

$$\frac{(z_2)_j + (z_2)_{j-1}}{2} = \frac{(z_1)_j - (z_1)_{j-1}}{h}, \tag{4.35}$$

$$\frac{(z_3)_j + (z_3)_{j-1}}{2} = \frac{\theta_j - \theta_{j-1}}{h}, \tag{4.36}$$

$$\begin{aligned}\left(\frac{1}{\phi_1\phi_2}+\frac{\omega}{\phi_1}\right)\left(\frac{(z_2)_j-(z_2)_{j-1}}{h}\right)+\left(\frac{f_j+f_{j-1}}{2}\right)\left(\frac{(z_2)_j+(z_2)_{j-1}}{2}\right)\\ -A\left\{\left(\frac{(z_1)_j+(z_1)_{j-1}}{2}\right)+\frac{\eta}{2}\left(\frac{(z_2)_j+(z_2)_{j-1}}{2}\right)\right\}\\ -\left(\frac{(z_1)_j+(z_1)_{j-1}}{2}\right)^2-\frac{\omega\Delta}{\phi_2}\left(\frac{v_j+v_{j-1}}{2}\right)^2\left(\frac{v_j+v_{j-1}}{h}\right)=0,\end{aligned} \tag{4.37}$$

$$\begin{aligned}\left(\frac{(z_3)_j-(z_3)_{j-1}}{h}\right)\left(1+\epsilon\left(\frac{\theta_j+\theta_{j-1}}{2}\right)+\frac{1}{\phi_5}P_rN_r\right)\\ +\epsilon\left(\frac{(z_3)_j+(z_3)_{j-1}}{2}\right)^2+P_r\frac{\phi_3}{\phi_5}\left[\left(\frac{f_j+f_{j-1}}{2}\right)\left(\frac{(z_3)_j+(z_3)_{j-1}}{2}\right)\right]\\ -P_r\frac{\phi_3}{\phi_5}\left[\left(\frac{(z_1)_j+(z_1)_{j-1}}{2}\right)\left(\frac{\theta_j+\theta_{j-1}}{2}\right)\right]\\ -P_r\frac{\phi_3}{\phi_5}\left[A\left\{\left(\frac{\theta_j+\theta_{j-1}}{2}\right)+\frac{\eta}{2}\left(\frac{(z_3)_j+(z_3)_{j-1}}{2}\right)\right\}\right]=0.\end{aligned} \tag{4.38}$$

In the above discussion, we write for the $(i+1)-th$ iterate as

$$()_j^{(i+1)}=()_j^{(i)}+\varepsilon()_j^{(i)}. \tag{4.39}$$

Substitution of above equation in equations (4.34)-(4.38) and neglecting the quadratic and higher terms of ε_j^i, a linear tri-diagonal system is achieved

$$\varepsilon f_j-\varepsilon f_{j-1}-\frac{1}{2}h(\varepsilon(z_1)_j+\varepsilon(z_1)_{j-1})=(r_1)_{j-\frac{1}{2}}, \tag{4.40}$$

$$\varepsilon(z_1)_j-\varepsilon(z_1)_{j-1}-\frac{1}{2}h(\varepsilon(z_2)_j+\varepsilon(z_2)_{j-1})=(r_2)_{j-\frac{1}{2}}, \tag{4.41}$$

$$\varepsilon\theta_j-\varepsilon\theta_{j-1}-\frac{1}{2}h(\varepsilon(z_3)_j+\varepsilon(z_3)_{j-1})=(r_3)_{j-\frac{1}{2}}, \tag{4.42}$$

$$\begin{aligned}(a_1)_j\varepsilon f_j+(a_2)_j\varepsilon f_{j-1}+(a_3)_j\varepsilon(z_1)_j+(a_4)_j\varepsilon(z_1)_{j-1}+(a_4)_j\varepsilon(z_1)_{j-1}\\ +(a_5)_j\varepsilon(z_2)_j+(a_6)_j\varepsilon(z_2)_{j-1}+(a_7)_j\varepsilon\theta_j+(a_8)_j\varepsilon\theta_{j-1}+(a_9)_j\varepsilon(z_3)_j\\ +(a_{10})_j\varepsilon(z_3)_{j-1}=(r_4)_{j-\frac{1}{2}},\end{aligned} \tag{4.43}$$

$$\begin{aligned}(b_1)_j\varepsilon f_j+(b_2)_j\varepsilon f_{j-1}+(b_3)_j\varepsilon(z_1)_j+(b_4)_j\varepsilon(z_1)_{j-1}+(b_4)_j\varepsilon(z_1)_{j-1}\\ +(b_5)_j\varepsilon(z_2)_j+(b_6)_j\varepsilon(z_2)_{j-1}+(b_7)_j\varepsilon\theta_j+(b_8)_j\varepsilon\theta_{j-1}+(b_9)_j\varepsilon(z_3)_j\\ +(b_{10})_j\varepsilon(z_3)_{j-1}=(r_5)_{j-\frac{1}{2}}.\end{aligned} \tag{4.44}$$

Where

$$(r_1)_{j-\frac{1}{2}} = -f_j + f_{j-1} + \frac{h}{2}((z_1)_j + (z_1)_{j-1}), \tag{4.45}$$

$$(r_2)_{j-\frac{1}{2}} = -(z_1)_j + (z_1)_{j-1} + \frac{h}{2}((z_2)_j + (z_2)_{j-1}), \tag{4.46}$$

$$(r_3)_{j-\frac{1}{2}} = -\theta_j + \theta_{j-1} + \frac{h}{2}((z_3)_j + (z_3)_{j-1}), \tag{4.47}$$

$$\begin{aligned}
(r_4)_{j-\frac{1}{2}} = h &\left[\left(\frac{1}{\phi_1\phi_2} + \frac{\omega}{\phi_1}\right)\left(\frac{((z_2)_j - (z_2)_{j-1})}{h}\right)\right] \\
&+ h\left[\left(\frac{(f_j + f_{j-1})((z_2)_j + (z_2)_{j-1})}{4}\right)\right] \\
&- h\left[\left(\frac{(z_1)_j + (z_1)_{j-1}}{2}\right)^2\right] \\
&- h\left[A\left(\frac{(z_1)_j + (z_1)_{j-1}}{2} + \eta\frac{(z_2)_j + (z_2)_{j-1}}{2}\right)\right] \\
&- h\left[\frac{\omega\Delta}{\phi_2}\left(\frac{(z_2)_j + (z_2)_{j-1}}{2}\right)^2\left(\frac{(z_2)_j + (z_2)_{j-1}}{h}\right)\right],
\end{aligned} \tag{4.48}$$

$$\begin{aligned}
(r_5)_{j-\frac{1}{2}} = -h &\left[\frac{\left((z_3)_j - (z_3)_{j-1}\right)\left(1 + \epsilon\left(\frac{\theta_j + \theta_{j-1}}{2}\right) + \frac{1}{\phi_5}P_r N_r\right)}{h}\right] \\
&- h\left[\epsilon\left(\frac{(z_3)_j + (z_3)_{j-1}}{2}\right)^2\right] \\
&- h\frac{\phi_3}{\phi_5}P_r A\left[\left(\frac{\theta_j + \theta_{j-1}}{2} + \eta\frac{(z_3)_j + (z_3)_{j-1}}{2}\right)\right] \\
&- h\frac{\phi_3}{\phi_5}P_r A\left[\left(\frac{(f_j + f_{j-1})(t_j + t_{j-1})}{4}\right)\right] \\
&+ h\frac{\phi_3}{\phi_5}P_r\left[\left(\frac{(\theta_j + \theta_{j-1})((z_1)_j + (z_1)_{j-1})}{4}\right)\right].
\end{aligned} \tag{4.49}$$

Similarly, the boundary conditions becomes

$$\varepsilon f_0 = 0, \varepsilon(z_1)_0 = 0, \varepsilon(z_3)_0 = 0, \varepsilon(z_1)_J = 0, \varepsilon\theta_J = 0. \tag{4.50}$$

The system of linear equations (4.40)-(4.44) can be written in the matrix form

$$R\varepsilon = p, \tag{4.51}$$

$$R = \begin{bmatrix} A_1 & C_1 & & & & \\ B_2 & A_2 & C_2 & & & \\ & \ddots & \ddots & \ddots & & \\ & & \ddots & \ddots & \ddots & \\ & & & B_{J-1} & A_{J-1} & C_{J-1} \\ & & & & B_J & A_J \end{bmatrix}, \varepsilon = \begin{bmatrix} \varepsilon_1 \\ \varepsilon_2 \\ \vdots \\ \varepsilon_{j-1} \\ \varepsilon_j \end{bmatrix}, p = \begin{bmatrix} (r_1)_{j-\frac{1}{2}} \\ (r_2)_{j-\frac{1}{2}} \\ \vdots \\ (r_{J-1})_{j-\frac{1}{2}} \\ (r_J)_{j-\frac{1}{2}} \end{bmatrix}. \tag{4.52}$$

In the above equation R represents the $J \times J$ block tridiagonal matrix with each block size of 5×5 and ε and p are column vectors of order $J \times 1$. The LU factorization method is now applied to find then solution of ε.

In this study, the desired physical quantities are the skin-friction coefficient (C_f) and the local Nusselt number (Nu_x). These quantities are expressed as: (see for example, Khan *et al.* [195])

$$C_f = \frac{\tau_w}{\rho_f U_w^2}, \qquad Nu_x = \frac{x q_w}{k_f(\Theta_w - \Theta_\infty)}, \tag{4.53}$$

The τ_w and q_w are wall shear stress and wall heat flux for the present model are given as (see for example, Khan *et al.* [195])

$$\tau_w = \left(\left(\mu_{nf} + \frac{1}{\tilde{\beta}\varsigma^*} \right) \frac{\partial u}{\partial y} - \frac{1}{6\tilde{\beta}\varsigma^{*3}} \left(\frac{\partial u}{\partial y} \right)^3 \right)_{y=0}, \tag{4.54}$$

$$q_w = -k_{nf} \left(1 + \frac{16}{3} \frac{\sigma^* \Theta_\infty^3}{\kappa^* \nu_f (\rho C_p)_f} \right) \left(\frac{\partial \Theta}{\partial y} \right)_{y=0}. \tag{4.55}$$

using τ_w in (4.53) for C_f,

$$\begin{aligned} C_f = \frac{1}{\rho_f U_w^2} \left(\left(\mu_{nf} + \frac{1}{\tilde{\beta}\varsigma^*} \right) \left(\frac{bxf''(0)}{(1-\xi t)} \sqrt{\frac{b}{\nu_f(1-\xi t)}} \right) \right) - \\ \frac{1}{\rho_f U_w^2} \left(\frac{1}{6\tilde{\beta}\varsigma^{*3}} \left(\left(\frac{bxf''(0)}{(1-\xi t)} \sqrt{\frac{b}{\nu_f(1-\xi t)}} \right) \right)^3 \right), \end{aligned} \tag{4.56}$$

$$C_f = \left(\frac{1}{\phi_1} + \omega \right) \left(\frac{U_w x}{\nu_f}^{-1/2} f''(0) \right) - \frac{\Delta\omega}{3} \left(\frac{U_w x}{\nu_f}^{-1/2} (f''(0))^3 \right), \tag{4.57}$$

$$C_f = \left(\frac{1}{\phi_1} + \omega\right)\left(\frac{1}{\sqrt{Re_x}} f''(0)\right) - \frac{\Delta\omega}{3}\left(\frac{1}{\sqrt{Re_x}} (f''(0))^3\right), \tag{4.58}$$

$$C_f\sqrt{Re_x} = \left(\frac{1}{\phi_1} + \omega\right) f''(0) - \left(\frac{\Delta\omega}{3}\right)(f''(0))^3, \tag{4.59}$$

$$C_f Re_x^{\frac{1}{2}} = \left[\left(\frac{1}{(1-\phi)^{2.5}} + \omega\right) f''(0) - \frac{\omega\Delta}{3}(f''(0))^3\right]. \tag{4.60}$$

Using q_w in (4.53) for Nu_x,

$$Nu_x = \frac{x}{k_f(\Theta_w - \Theta_\infty)}\left(-k_{nf}\left(1 + \frac{16}{3}\frac{\sigma^*\Theta_\infty^3}{\kappa^*\nu_f(\rho C_p)_f}\right)\left(\frac{\partial\Theta}{\partial y}\right)_{y=0}\right), \tag{4.61}$$

using (3.33) in (4.61), we obtain

$$Nu_x = -\frac{k_{nf}}{k_f}(1 + N_r)\left(\frac{bx}{(1-\xi t)}\theta'(0)\sqrt{\frac{b}{\nu_f(1-\xi t)}}\right), \tag{4.62}$$

$$Nu_x = -\frac{k_{nf}}{k_f}(1 + N_r)\left(\sqrt{Re_x}\right)\theta'(0), \tag{4.63}$$

$$Nu_x Re_x^{-\frac{1}{2}} = -\frac{k_{nf}}{k_f}(1 + N_r)\,\theta'(0). \tag{4.64}$$

4.6.1 Effect of Nanoparticle Volume Fraction Parameter ϕ

Figures 4.3-4.5 displayed the nature of fluid motion, temperature distribution and entropy generation

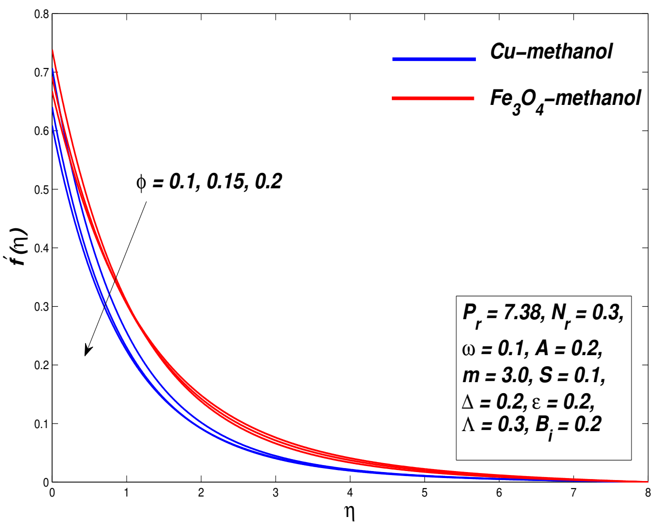

FIGURE 4.3: Velocity Distribution against the Parameter ϕ

within boundary layer for Powell-Eyring nanofluids due to variation in nanoparticle volume concentration parameter ϕ. The parameter ϕ correspond to volume of solid particles in the basefluid.

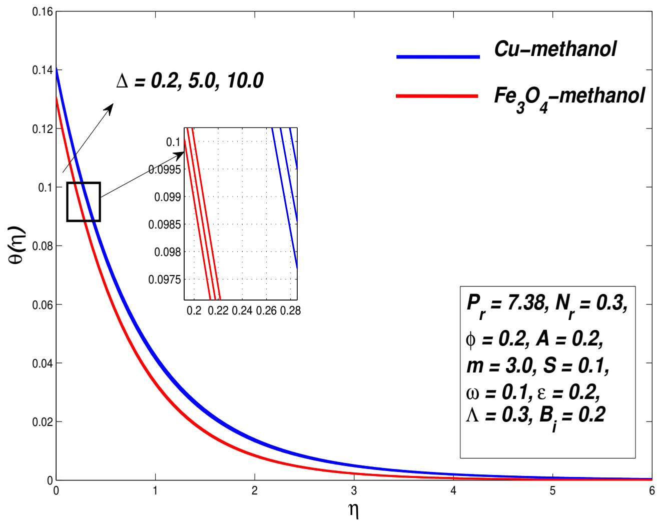

FIGURE 4.4: Temperature Distribution against the Parameter ϕ

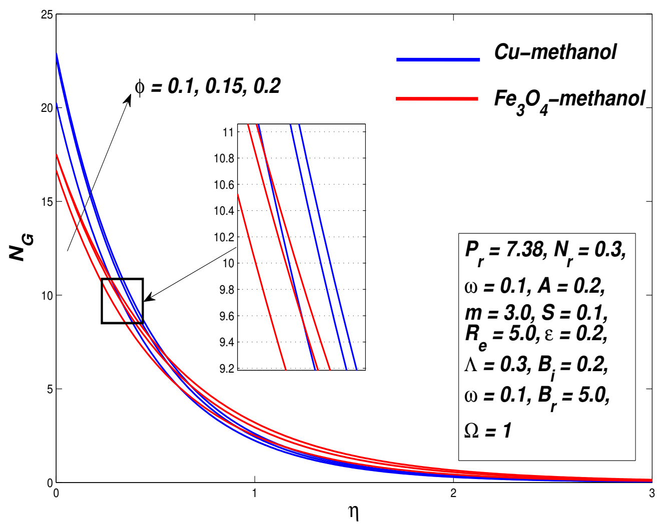

FIGURE 4.5: Entropy Generation Distribution against the Parameter ϕ

It is well known solid particles have higher thermal conductivity than fluids, therefore increase in ϕ reduces fluid velocity as observed from Figure 4.3 and enhances its temperature in the boundary layer region. Whereas, this fact is very much evident in Figure 4.4

that the increase in the total thermal conductivity of nanofluids increases the temperature and the thickness of thermal boundary layer. The increasing and decreasing trend of the velocity gradient and Nusselt number is observed with the increase of parameter ϕ see Table 4.3. Figure 4.5 illustrates that the entropy profile increases with the increasing nanoparticle volume fraction parameter. The entropy generation rate is higher for Cu-methanol(MeOH) nanofluids as compared to Fe_3O_4-methanol(MeOH) nanofluids.

4.6.2 Effect of Material Fluid Parameter ω

The effects of material fluid parameter ω on velocity, temperature and entropy generation profiles of Cu-methanol and Fe_3O_4-methanol non-Newtonian Powell-Eyring nanofluids are presented in Figures 4.6-4.8. Computations are performed for $\omega = 0.1, 0.3, 0.5$ at uniform nanoparticle concentration of 0.2. The velocity profiles in Figure 4.6 rise with raising values of ω and hence increases the thickening level of momentum boundary layer. Moreover, for the fixed value of $\omega = 0.1$ the boundary layer thickness of Fe_3O_4-methanol nanofluid is relatively more than the Cu-methanol nanofluid. The increasing trend in velocity profiles is due to fall of resistance in fluid. This also corresponds to increase in skin friction coefficient (velocity gradient) at the boundary.

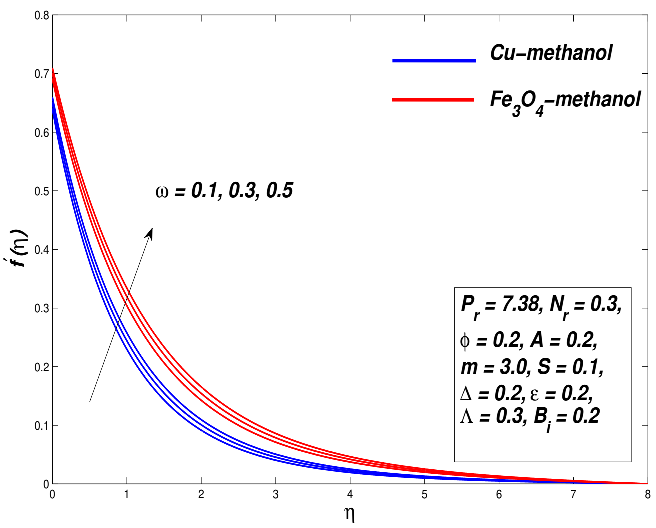

FIGURE 4.6: Velocity Distribution against the Parameter ω

From Figure 4.7 it can be observed that the temperature of nanofluids reduces with the increasing values of parameter ω. This decreasing trend indicates the reduction in the thickness thermal boundary layer and enhancement in the rate of heat transfer. The reason behind this behaviour of temperature profiles is the decrease in the elasticity stress parameter. The heat transfer rate (Nusselt number) increases for both Cu and Fe_3O_4 methanol based nanofluids Table 4.3.

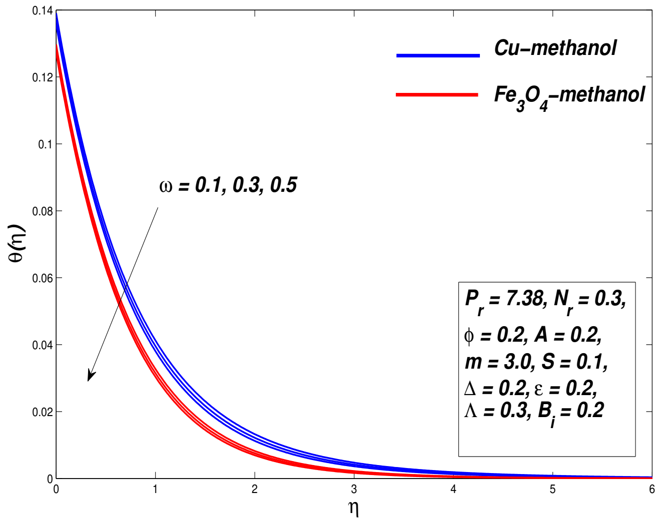

FIGURE 4.7: Temperature Distribution against the Parameter ω

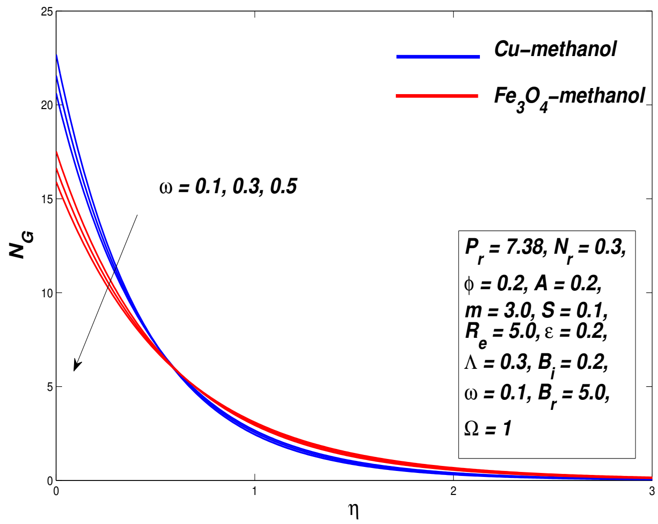

FIGURE 4.8: Entropy Generation Distribution against the Parameter ω

Finally, Figure 4.8 presented the impact of material parameter ω on the entropy of the system. It is noticed that growing material parameter decreases the entropy of the system. The irreversibility of the system is maximum near the surface of the plate and decreases to zero far away from the surface. Moreover the irreversibility of Cu-methanol nanofluids is more than the Fe_3O_4-methanol nanofluids.

4.6.3 Effect of Material Fluid Parameter Δ

Figures 4.9 to 4.11 demonstrated the behaviour of nanofluid motion, temperature distribution

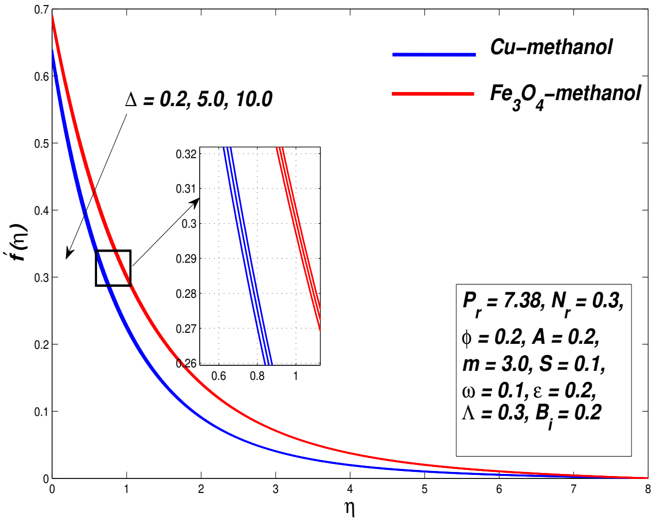

FIGURE 4.9: Velocity Distribution against the Parameter Δ

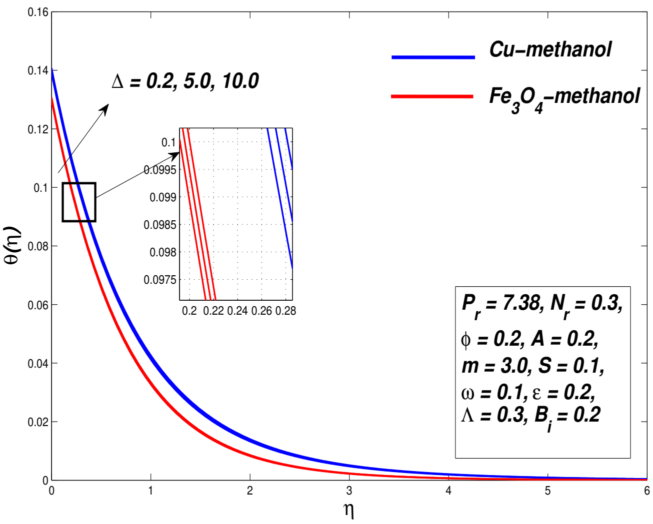

FIGURE 4.10: Temperature Distribution against the Parameter Δ

and entropy generation with increasing material fluid parameter Δ. The impact of Δ on the fluid motion and thickening level of boundary layer is opposite to that of ω. The velocity profiles in Figure 4.9 decreases with the raising values of Δ and hence decreases the thickness of momentum boundary layer. It can be observe from Figure 4.10 that the temperature of nanofluids rises with the increasing values of fluid parameter Δ. This increasing trend indicate the boost in the thickness of thermal boundary layer and reduction in the rate of heat transfer. Furthermore, Figure 4.11 depicts the effect of fluid parameter Δ on the entropy of the system. It is noticed that raising fluid parameter increases the entropy of the system. Lastly, it is detected from Table 4.3, skin friction coefficient (velocity gradient) reduces with growing values of Δ.

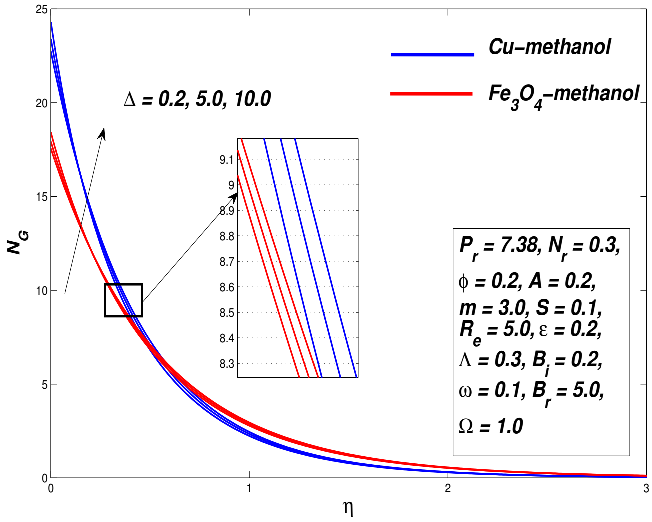

FIGURE 4.11: Entropy Generation Distribution against the Parameter Δ

4.6.4 Effect of Nanoparticle Shape Parameter m

Figure 4.12 depicted the effect of different nanoparticles shapes (sphere, hexahedron, tetrahedron, column, and lamina) on the heat transfer characteristics of the boundary layer flow in the Cu-methanol and Fe_3O_4-methanol nanofluids at nanoparticle concentration $\phi = 0.2$. The graphical view shows that non-dimensional temperature of the nanofluid rises as the shape factor m increases. Dimensionless temperature at the boundary is lowest for spherical shape nanoparticles followed by hexahedron, tetrahedron, column and lamina. The spherical shaped particle tends to drag more heat from the boundary layer due to its greater surface area while this effect is less evident for

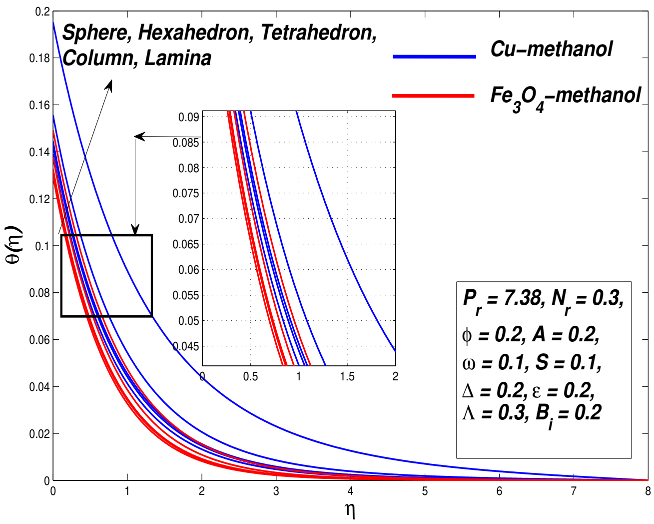

FIGURE 4.12: Temperature Distribution against the Parameter m

other shapes thus the temperature fall in the boundary layer in witnessed most for the spherical particles. This is the very reason for greatest heat transfer observed in the case of spherical shaped particle as we have observed the variation in Nusselt number. Moreover, Figure 4.13 showed the entropy of the system increases and the lowest rate of entropy generation is seen for the spherical shape particles.

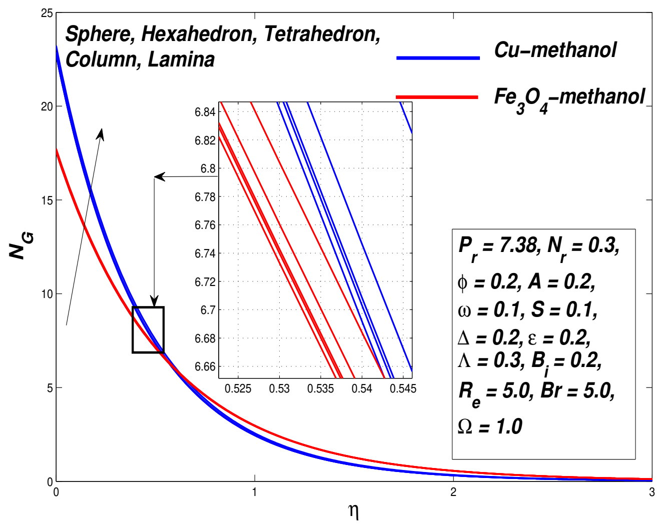

FIGURE 4.13: Entropy Generation Distribution against the Parameter m

4.6.5 Effect of Variable Thermal Conductivity Parameter ϵ, Thermal Radiation Parameter N_r and Biot Number B_i

Figures 4.14-4.19 displayed plots of temperature distribution for methanol based nanofluids with variation in thermal conductivity parameter ϵ, thermal radiation parameter N_r and Biot number B_i, respectively.

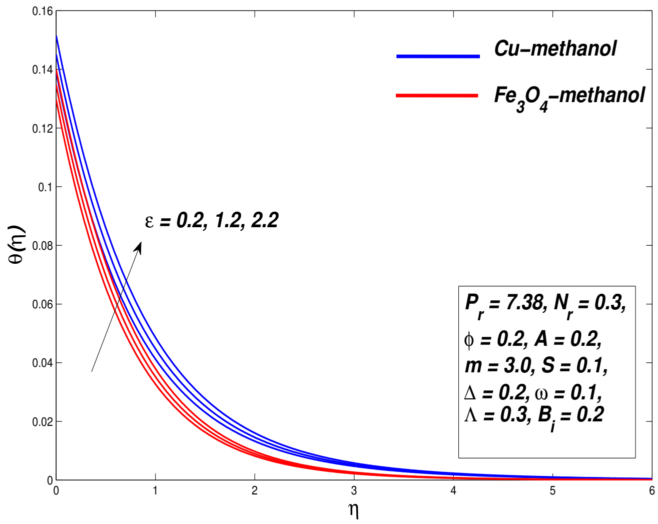

FIGURE 4.14: Temperature Distribution against the Parameter ϵ

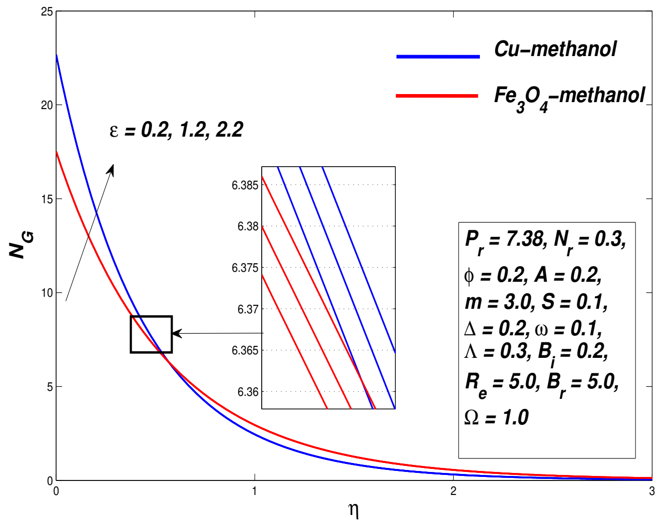

FIGURE 4.15: Entropy Generation Distribution against the Parameter ϵ

The positive values of parameter ϵ resulted in, $\kappa^*_{nf} > \kappa_{nf}$, therefore fluid temperature increases across the boundary layer see Figure 4.14. The thickening level of thermal boundary layer also boost with rise in temperature.

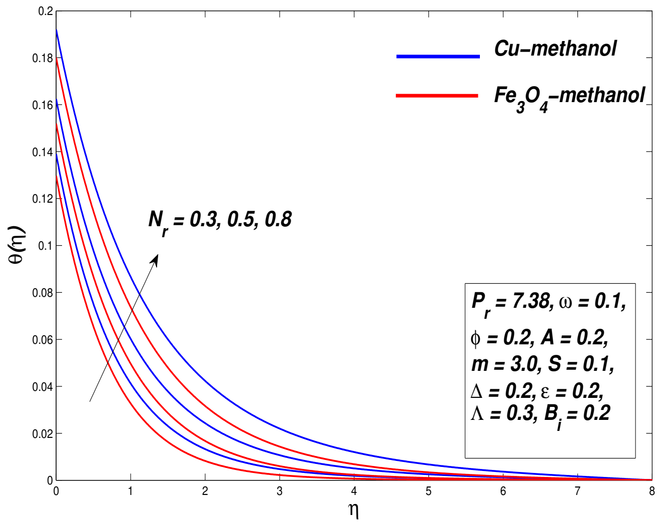

FIGURE 4.16: Temperature Distribution against the Parameter N_r

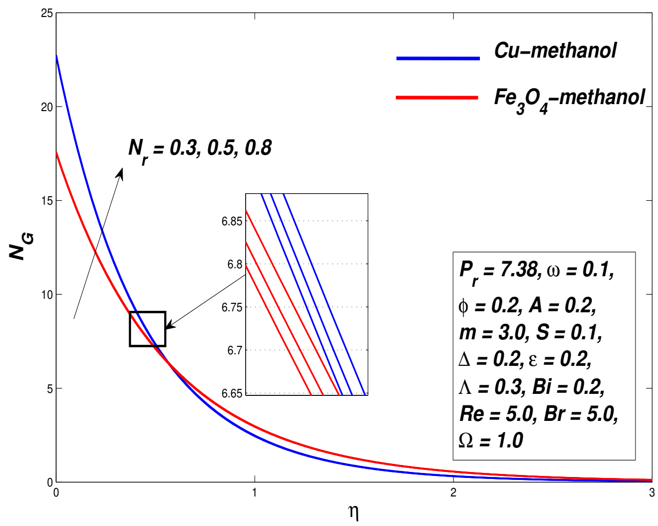

FIGURE 4.17: Entropy Generation Distribution against the Parameter N_r

Physically speaking, the strengthening of parameter N_r transfer more heat into the fluid and raise the thickening level of thermal boundary layer. The Biot number or the sheet convection parameter showed the ratio of conduction inside the fluid to the convection at its surface. Increasing sheet convection parameter means that the heat transfer through conduction dominates the convection coefficient at the surface of the fluid The increase in B_i showed that the hot fluid within boundary layer heat the stretching surface and raise the temperature of the thermal system.

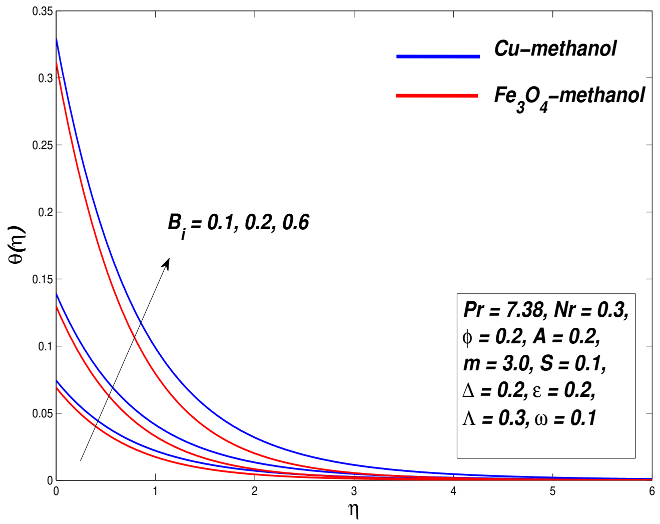

FIGURE 4.18: Temperature Distribution against the Parameter B_i

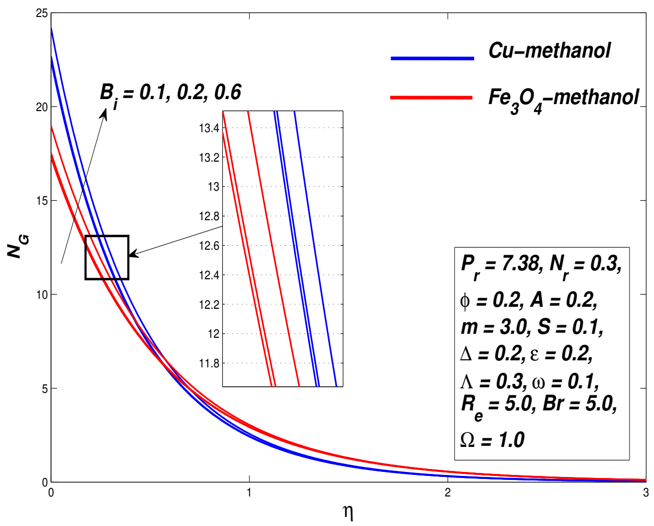

FIGURE 4.19: Entropy Generation Distribution against the Parameter B_i

Thus, increase in parameters ϵ, N_r and B_i is directly related to boost in the Nusselt number at the boundary. Figures 4.15, 4.17 and 4.19 depicted the increase in entropy with raise in variable thermal conductivity parameter ϵ, thermal radiation parameter N_r and Biot number B_i, respectively. In Figures 4.15, 4.17 and 4.19 the crossover point for the entropy profile is estimated at about $\eta = 0.3$. Before this behaviour the entropy is enhanced and then it begins to fall. In other words the thermal process is converging towards the case of reversible process.

4.6.6 Effect of Reynolds Number R_e and the Brinkman Number B_r

The influence of Reynolds number R_e and Brinkman number B_r on entropy generation

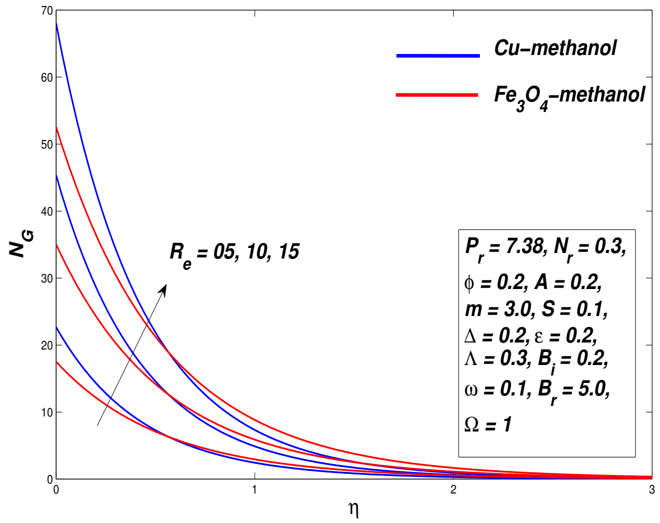

FIGURE 4.20: Entropy Generation Distribution against the Parameter R_e

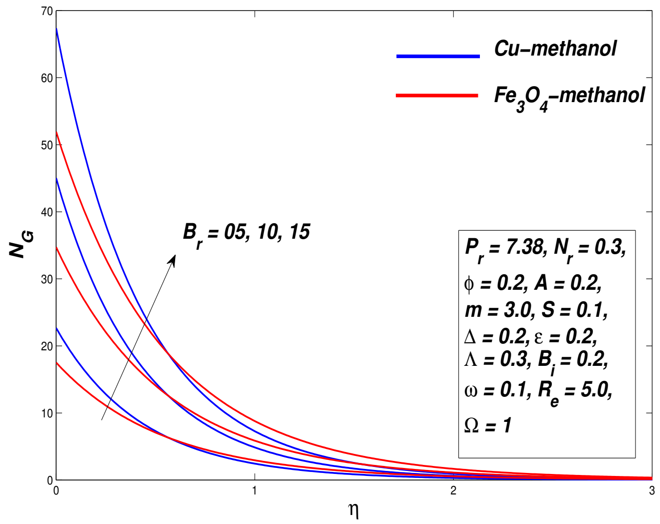

FIGURE 4.21: Entropy Generation Distribution against the Parameter B_r

profiles are presented in this section. Numerical computations showed the higher values of R_e increases entropy which physically means that the inertial forces dominate the viscous effects see Figure 4.20. Figure 4.21 discussed the influence of B_r on the entropy. It is found that the Brinkman number augmentation increases the entropy generation. This is due to the fact that Brinkman number is the ratio of heat dissipation to the conduction at the surface so increasing the values of B_r means more heat is dissipated compared with the conduction of heat at the surface, which results in an increase in the entropy.

4.6.7 Effect of Material Parameter Δ and Radiation Parameter N_r on Skin Friction C_f and the Nusselt Number Nu_x, Respectively

The effects of material parameter Δ and radiation parameter N_r on Skin friction coefficient C_f and Nusselt number Nu_x profiles of Cu- methanol and Fe_3O_4-methanol non-Newtonian nanofluids are presented in Figures 4.22-4.23, respectively.

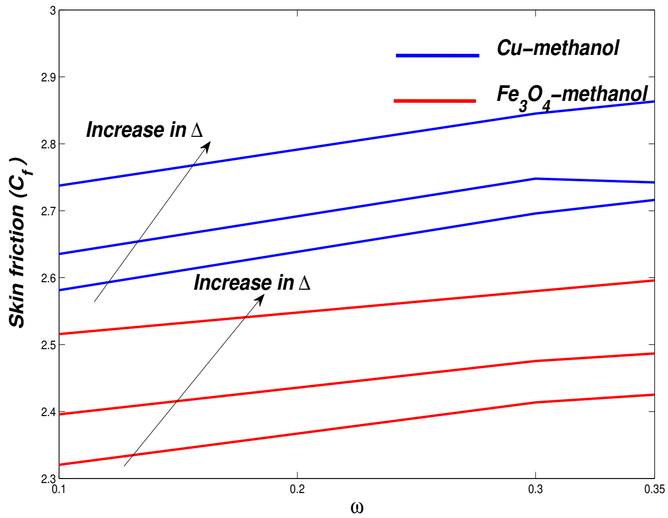

FIGURE 4.22: Skin Friction C_f against the Parameter ω

In 4.22 computations are performed for $\Delta = 0.2, 0.3, 0.9$ whereas the parameter ω takes the values $0.1, 0.3, 0.5$. It is noted when we increase the material parameter Δ the skin friction coefficient C_f increases. The physical reason behind this is that the resistance in fluid is responsible for the decreased fluid motion, as a result skin friction increases. In 4.23 computations are performed for $N_r = 0.2, 0.4, 0.9$ whereas the Prandtl number P_r is fixed on $1.0, 6.2, 7.38$. It is observed when we increase the radiation parameter N_r the rate of convective heat transfer (Nusselt number) increases. This is due to the fact that a greater heat flux is generated, which results in a greater heat transfer rate.

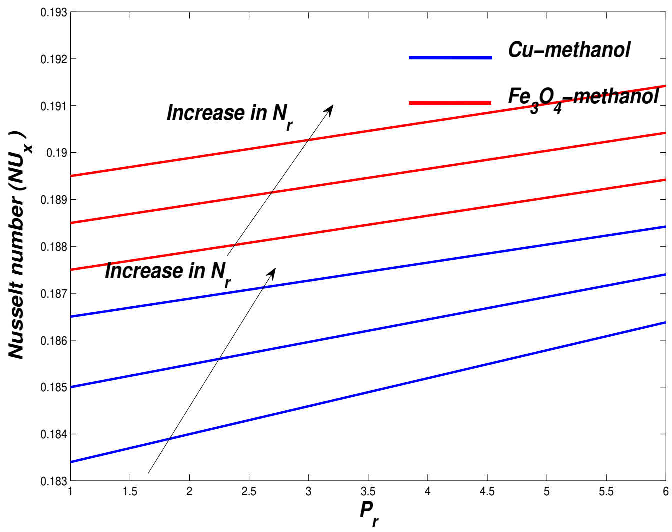

FIGURE 4.23: Nusselt Number Nu_x against the Parameter P_r

ω	Δ	A	ϕ	Λ	ϵ	N_r	B_i	S	$C_f Re_x^{\frac{1}{2}}$ $Cu-MeOH$	$C_f Re_x^{\frac{1}{2}}$ Fe_3O_4-MeOH	$N_u Re_x^{\frac{-1}{2}}$ $Cu-MeOH$	$N_u Re_x^{\frac{-1}{2}}$ Fe_3O_4-MeOH
0.1	0.2	0.2	0.2	0.3	0.2	0.3	0.2	0.1	1.3590	1.2192	0.1300	0.1353
0.3									1.4593	1.3060	0.1303	0.1355
0.5									1.5567	1.3927	0.1305	0.1357
	0.2								1.3590	1.2192	0.1300	0.1353
	5.0								1.3187	1.1905	0.1299	0.1352
	10.0								1.2719	1.1593	0.1297	0.1350
		0.2							1.3590	1.2192	0.1300	0.1353
		0.6							1.4205	1.2754	0.1311	0.1362
		1.0							1.4768	1.3298	0.1320	0.1370
			0.1						1.1214	1.0278	0.1724	0.1760
			0.15						1.2411	1.1523	0.1403	0.1492
			0.2						1.3590	1.2192	0.1300	0.1353
				0.0					2.6847	2.2094	0.1330	0.1379
				0.1					1.9992	1.7192	0.1317	0.1368
				0.3					1.3590	1.2192	0.1300	0.1353
					0.2				1.3590	1.2192	0.1300	0.1353
					1.2				1.3590	1.2192	0.1293	0.1346
					2.2				1.3590	1.2192	0.1289	0.1340
						0.3			1.3590	1.2192	0.1300	0.1353
						0.5			1.3590	1.2192	0.1460	0.1522
						0.8			1.3590	1.2192	0.1692	0.1767
							0.1		1.3590	1.2192	0.0694	0.0719
							0.2		1.3590	1.2192	0.1300	0.1353
							0.6		1.3590	1.2192	0.3107	0.1767

TABLE 4.3: Values of Skin Friction $= C_f Re_x^{\frac{1}{2}}$ and Nusselt Number $= N_u Re_x^{\frac{-1}{2}}$ for $P_r = 7.38$, $m = 3$

4.7 Conclusions

Entropy generation and heat transfer capabilities of the non-Newtonian Powell-Eyring nanofluid in the existence of velocity slip and convective boundary conditions. Furthermore the temperature dependent thermal conductivity are numerically investigated in this chapter. The results are summarized on the basis of variation in nanofluid's motion, temperature distribution and entropy generation within the boundary layer. The core findings of the present study are:

- Spherical shaped nanoparticles has the lowest rate of entropy generation when compared with different shaped of nanoparticles. The increase in nanoparticle volume fraction parameter ϕ in the base fluid increases the overall entropy of the thermal system. Moreover ist is well known fact that the inclusion of solid nanoparticles in the ordinary fluids increases the overall thermal conductivity of the mixture. Therefore the increase in ϕ decrease in thickness of momentum and increase the thickness of thermal boundary layer respectively.

- The spherical shaped particle tends to drag more heat from the boundary layer due to its greater surface area while this effect is less evident for other shapes thus the temperature fall in the boundary layer is witnessed most for the spherical particles. This is the very reason for greatest rate of heat transfer at the surface for the spherical shaped particle.

- For the fixed value of material parameter $\Delta = 0.2$ the momentum boundary layer thickness of Fe_3O_4-methanol nanofluid is relatively more than the Cu-methanol nanofluid. This decreasing trend in velocity profiles is caused by an increase in fluid resistance and also by an increase in the skin friction coefficient at the boundary surface.

- On the basis of numerical results, Cu-methanol based nanofluid is observed as a better thermal conductor than Fe_3O_4-methanol based nanofluid. The entropy is found to be rising with the increase in Reynolds number Re, Brinkman number Br, thermal radiation Nr and sheet convection parameter Bi.

Chapter 5

Entropy and Heat Transfer Analysis Using Cattaneo-Christov Heat Flux Model for a Boundary Layer Flow of Casson Nanofluid

5.1 Introduction

In this chapter, a numerical investigation of Casson nanofluid flow, heat transfer and entropy generation over a horizontal porous stretching surface is carried out. The simplified flow model includes the effect of Lorentz forces, Cattaneo-Christov heat flux model, thermal radiation and non-uniform stretching of porous surface. An appropriate similarity transformations is employed to convert the governing nonlinear PDEs to a set of nonlinear ODEs. A numerical technique based on the finite difference method is applied to approximate the solutions for the velocity, temperature and the entropy profiles. Furthermore, the velocity gradient and the heat exchange rate at the boundary have been computed and explored graphically. The numerical simulations are performed for $Cu - H_2O$ and $TiO_2 - H_2O$ nanofluids.

5.2 Mathematical Formulation

Consider the numerical investigation of MHD boundary layer flow of an incompressible Casson nanofluid. The flow is produced due to the stretching of surface with non-uniform velocity $U_w(x,t)$ given in equation (3.1). Figure 5.1 shows the geometry of the flow model.

.

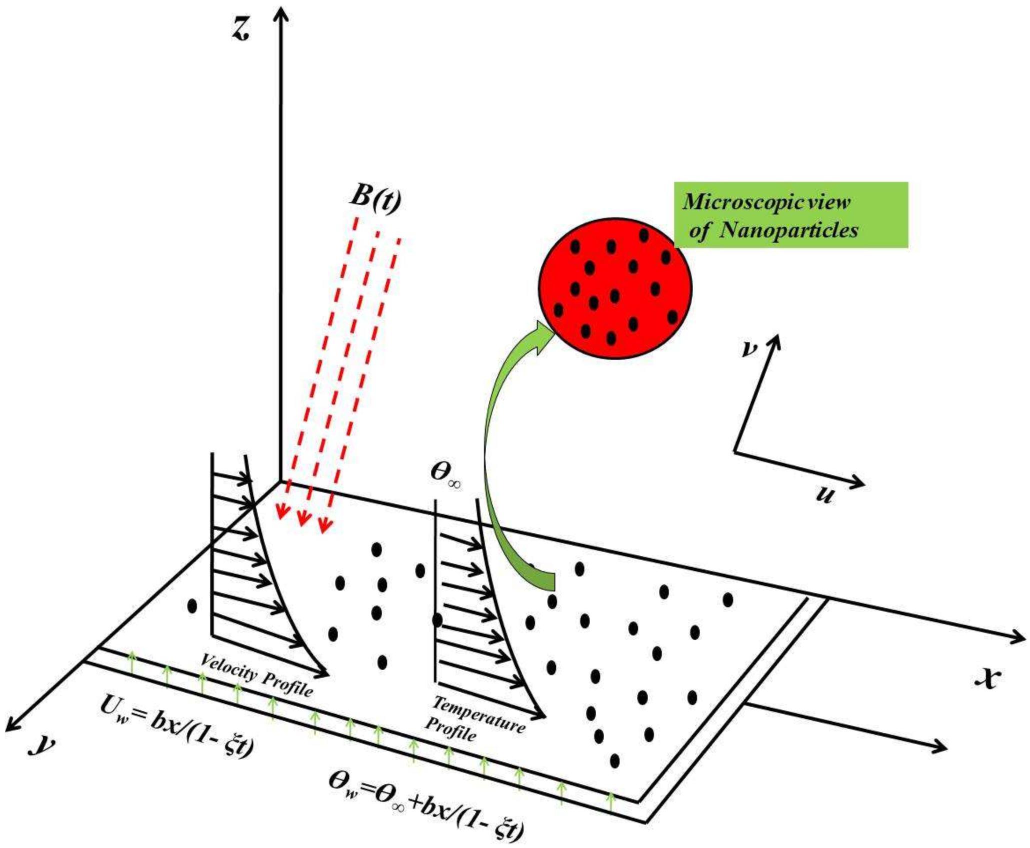

Figure 5.1: Schematic Representation of the Fluid Flow

An electrically conducting Casson nanofluid occupies the space over a surface stretching in the horizontal direction along the positive x-axis. A uniformly distributed transverse magnetic field of strength $B(t) = \frac{B_0}{\sqrt{1-\xi t}}$ is assumed in the present model. The temperature of the convective surface is $\Theta_w(x,t) = \Theta_\infty + \frac{bx}{1-\xi t}$. The stretching sheet is assumed to be porous in nature with the slip and convective boundary conditions considered at the fluid-surface boundary. The equations representing the basic form of incompressible Casson fluid with isotropic properties are given in equation (2.57). For Casson nanofluid μ_B in equation (2.57) is replaced by μ_{nfB} that is,

$$\tau_{ij} = \begin{cases} 2\left(\mu_{nfB} + \dfrac{p_y}{\sqrt{2\pi}}\right) e_{ij}, & \pi > \pi_c, \\ \\ 2\left(\mu_{nfB} + \dfrac{p_y}{\sqrt{2\pi_c}}\right) e_{ij}, & \pi < \pi_c. \end{cases} \tag{5.1}$$

The governing equations of two-dimensional boundary layer flow and heat transfer of Casson fluid are given in equations (2.74) and (2.85). These equations for the Casson nanofluid are reduced to the form (see for example, Ali and Sandeep [196])

$$\frac{\partial u}{\partial t} + u\frac{\partial u}{\partial x} + v\frac{\partial u}{\partial y} = \nu_{nf}\left(1 + \frac{1}{\beta}\right)\frac{\partial^2 u}{\partial y^2} - \frac{\sigma_{nf} B^2(t)}{\rho_{nf}} u, \tag{5.2}$$

$$\frac{\partial \Theta}{\partial t} + u\frac{\partial \Theta}{\partial x} + v\frac{\partial \Theta}{\partial y} = \frac{k_{nf}}{(\rho C_p)_{nf}}\left[\frac{\partial^2 \Theta}{\partial x^2} + \frac{\partial^2 \Theta}{\partial y^2}\right] - \frac{1}{(\rho C_p)_{nf}}\left[\frac{\partial q_r}{\partial y}\right]$$
$$-\lambda^*\left[u\frac{\partial u}{\partial x}\frac{\partial \Theta}{\partial x} + v\frac{\partial v}{\partial y}\frac{\partial \Theta}{\partial y} + u\frac{\partial v}{\partial x}\frac{\partial \Theta}{\partial y} + v\frac{\partial u}{\partial y}\frac{\partial \Theta}{\partial x} + u^2\frac{\partial^2 \Theta}{\partial x^2} + v^2\frac{\partial^2 \Theta}{\partial y^2} + 2uv\frac{\partial^2 \Theta}{\partial x \partial y}\right]. \tag{5.3}$$

The associated BCs for the modeled problem are

$$u(x,0) = U_w + \mu_{nf}\left(\frac{\partial u}{\partial y}\right), \quad v(x,0) = V_w, \quad -k_0\left(\frac{\partial \Theta}{\partial y}\right) = h_f(\Theta_w - \Theta), \tag{5.4}$$

$$u \to 0, \quad \Theta \to \Theta_\infty \ \text{ as } \ y \to \infty. \tag{5.5}$$

5.3 Solution of the Problem

In this section first we use similarity transformation to reduce the governing system of PDEs (5.2)-(5.5) into a system of ODEs.

$$u = \frac{\partial \psi}{\partial y}, \qquad v = -\frac{\partial \psi}{\partial x}. \tag{5.6}$$

Here the similarity variables of ψ and θ are introduced (see for example, Hayat *et al.* [184])

$$\eta(x,y)=\sqrt{\frac{b}{\nu_f(1-\xi t)}}y,\quad \psi(x,y)=\sqrt{\frac{\nu_f b}{(1-\xi t)}}xf(\eta),\quad \theta(\eta)=\frac{\Theta-\Theta_\infty}{\Theta_w-\Theta_\infty}. \tag{5.7}$$

From equations (3.14) and (3.15),

$$u=\frac{bx}{(1-\xi t)}f'(\eta), \tag{5.8}$$

$$v=-\sqrt{\frac{\nu_f b}{(1-\xi t)}}f(\eta). \tag{5.9}$$

In order to utilize (3.14)-(3.15) in (5.3), we require

$$\frac{\partial^2\Theta}{\partial x^2}=0. \tag{5.10}$$

$$\frac{\partial^2\Theta}{\partial y^2}=\frac{bx}{(1-\xi t)}\theta''(\eta)\frac{b}{\nu_f(1-\xi t)}. \tag{5.11}$$

$$\frac{\partial^2\Theta}{\partial xy^2}=\frac{bx}{(1-\xi t)}\theta''(\eta)\sqrt{\frac{b}{\nu_f(1-\xi t)}}. \tag{5.12}$$

Equation (3.35) has satisfied the continuity equation. Now using appropriate equations from (3.16 - 3.34) and (5.10- 5.12) into (5.2) and (5.3). we get the following ODEs

$$\frac{1}{\phi_1\phi_2}\left(1+\frac{1}{\beta}\right)f'''+ff''-f'^2-A\left(f'+\frac{\eta}{2}f''\right)-\frac{\phi_4}{\phi_2}Mf'=0. \tag{5.13}$$

$$\begin{aligned}\theta''\left(1+\frac{1}{\phi_5}P_rN_r\right)+P_r\frac{\phi_3}{\phi_5}\left[f\theta'-f'\theta-A\left(\theta+\frac{\eta}{2}\theta'\right)\right]\\ -P_r\vartheta\frac{\phi_3}{\phi_5}\left[\left(f'^2\theta-f''\theta-f^2\theta^2-ff'\theta''\right)\right]=0.\end{aligned} \tag{5.14}$$

The transformed boundary conditions from equations (3.43), (3.46), (3.56), s(3.58) and (3.60)) are

$$f(0)=S,\qquad f'(0)=1+\frac{\Lambda}{\phi_1}f''(0),\qquad \theta'(0)=-B_i(1-\theta(0)), \tag{5.15}$$

$$f'(\eta)\to 0,\qquad \theta(\eta)\to 0,\quad \text{as}\quad \eta\to\infty. \tag{5.16}$$

In the above equations primes stand for the differentiation of the function with respect to η. $A = \frac{\xi}{b}$ is the unsteady flow parameter, $M = \frac{\sigma_f B_0^2}{b\rho_f}$ is the magnetic parameter, $\vartheta = b\lambda_0^*$ is the thermal relaxation time parameter, $P_r = \frac{\nu_f}{\alpha_f}$ is the Prandtl number, $\alpha_f = \frac{\kappa_f}{(\rho C_p)_f}$ is the thermal diffusivity parameter, $N_r = \frac{16}{3}\frac{\sigma^*\Theta_\infty^3}{\kappa^*\nu_f(\rho C_p)_f}$ is the radiation parameter, $S = -V_w\sqrt{\frac{1-\xi t}{\nu_f\ b}}$ is the mass transfer parameter, $\Lambda = \sqrt{\frac{b}{\nu_f(1-\xi t)}}\mu_f$ is the velocity slip parameter and $B_i = \frac{h_f}{k_0}\sqrt{\frac{\nu_f(1-\xi t)}{b}}$ is the Biot number. It is observed some parameters depend on ξ and is time dependent. Therefore to obtain non-similar solutions for the proposed problem numerical results are computed for locally similar parameters.

The nonlinear system of ODEs (5.13)-(5.14) is difficult to solve analytically. Therefore finite difference numerical scheme is implemented to find the approximate solutions. The numerical scheme is inherently stable and is second order convergent. The methodology of finite difference method (FDM) is given in the following steps to obtain the solution:

i. Convert equations (5.13)-(5.14) to a system of first ODEs.

ii. Convert them to difference equations by replacing functions with mean averages and their derivatives by central differences.

iii. Linearize the resulting algebraic equations by applying Newton's scheme and then write them in matrix form.

iv. Solve the matrix using block-tri-diagonal elimination scheme.

The desired physical quantities for the present model are the skin-friction coefficient (C_f) and the local Nusselt number (Nu_x) are defined in (2.106) and (2.103). The τ_w and q_w are wall shear stress and wall heat flux for the present model are given as (see for example, Shit and Mandal [197])

$$\tau_w = \mu_{nf}\left(1+\frac{1}{\beta}\right)\left(\frac{\partial u}{\partial y}\right)_{y=0}, \qquad q_w = -k_{nf}\left(1+\frac{16}{3}\frac{\sigma^*\Theta_\infty^3}{\kappa^*\nu_f(\rho C_p)_f}\right)\left(\frac{\partial \Theta}{\partial y}\right)_{y=0}, \tag{5.17}$$

using τ_w in (3.90) for C_f,

$$C_f = \frac{\mu_{nf}\left(1+\frac{1}{\beta}\right)\left(\frac{\partial u}{\partial y}\right)_{y=0}}{\rho_f U_w^2}, \tag{5.18}$$

using (3.19) in (5.18)

$$C_f = \frac{\mu_f}{\rho_f\phi_1}\frac{x f''(0) b^{3/2}}{\nu_f(1-\xi t)^{3/2}}\left(1+\frac{1}{\beta}\right)\left(\frac{(1-\xi t)^{3/2}}{bx}^2\right), \tag{5.19}$$

$$C_f = \left(1 + \frac{1}{\beta}\right) \frac{\sqrt{\nu_f}}{\phi_1} \sqrt{\frac{1}{U_w x}} f''(0), \tag{5.20}$$

$$C_f = \left(1 + \frac{1}{\beta}\right) \frac{1}{\sqrt{Re_x}} f''(0) \frac{1}{\phi_1}, \tag{5.21}$$

$$C_f \sqrt{Re_x} = \left(1 + \frac{1}{\beta}\right) \frac{f''(0)}{\phi_1}, \tag{5.22}$$

$$C_f Re_x^{\frac{1}{2}} = \left(1 + \frac{1}{\beta}\right) \frac{f''(0)}{(1-\phi)^{2.5}}. \tag{5.23}$$

Using q_w in (3.90) for Nu_x,

$$Nu_x = \frac{x}{k_f(\Theta_w - \Theta_\infty)} \left(-k_{nf} \left(1 + \frac{16}{3} \frac{\sigma^* \Theta_\infty^3}{\kappa^* \nu_f (\rho C_p)_f}\right) \left(\frac{\partial \Theta}{\partial y}\right)_{y=0} \right), \tag{5.24}$$

using (3.33) in (5.24)

$$Nu_x = -\frac{k_{nf}}{k_f}(1 + N_r) \left(\frac{bx}{(1-\xi t)} \theta'(0) \sqrt{\frac{b}{\nu_f (1-\xi t)}} \right), \tag{5.25}$$

$$Nu_x = -\frac{k_{nf}}{k_f}(1 + N_r) \left(\sqrt{Re_x}\right) \theta'(0), \tag{5.26}$$

$$Nu_x Re_x^{-\frac{1}{2}} = -\frac{k_{nf}}{k_f}(1 + N_r)\theta'(0). \tag{5.27}$$

5.4 Entropy Generation Analysis

The entropy generation for Casson nanofluids is defined as follows (see for example, Das *et al.* [167])

$$E_G = \frac{k_{nf}}{\Theta_\infty^2} \left\{ \left(\frac{\partial \Theta}{\partial y}\right)^2 + \frac{16}{3} \frac{\sigma^* \Theta_\infty^3}{\kappa^* \nu_f (\rho C_p)_f} \left(\frac{\partial \Theta}{\partial y}\right)^2 \right\} + \frac{\mu_{nf}}{\Theta_\infty} \left(\frac{\partial u}{\partial y}\right)^2 \left(1 + \frac{1}{\beta}\right) + \frac{\sigma_{nf} B^2(t) u^2}{\Theta_\infty}. \tag{5.28}$$

The first term in entropy equation represents the heat transfer irreversibility, second term is the fluid friction and the third term is represents the magnetohydrodynamic effects. The entropy generation is represented by N_G and is given in equation (3.104).

Now putting (5.28) in (3.104), we get

$$N_G = \frac{\Theta_\infty^2 b^2}{k_f\left(\Theta_w-\Theta_\infty\right)^2}\frac{k_{nf}}{\Theta_\infty^2}\left\{\left(\frac{\partial \Theta}{\partial y}\right)^2+\frac{16}{3}\frac{\sigma^*\Theta_\infty^3}{\kappa^*\nu_f(\rho C_p)_f}\left(\frac{\partial \Theta}{\partial y}\right)^2\right\}+ \frac{\mu_{nf}}{\Theta_\infty}\left(\frac{\partial u}{\partial y}\right)^2\left(1+\frac{1}{\beta}\right)+\frac{\sigma_{nf}B^2(t)u^2}{\Theta_\infty}. \tag{5.29}$$

Consider first term of equation (5.29),

$$\frac{\Theta_\infty^2 b^2}{k_f\left(\Theta_w-\Theta_\infty\right)^2}\frac{k_{nf}}{\Theta_\infty^2}\left\{(1+N_r)\left(\frac{\partial \Theta}{\partial y}\right)^2\right\}, \tag{5.30}$$

using equation (3.33) and (3.62), we get

$$= \frac{\Theta_\infty^2 b^2}{k_f\left(\Theta_w-\Theta_\infty\right)^2}\frac{k_f\phi_5}{\Theta_\infty^2}\left\{(1+N_r)\left(\frac{(bx)^2}{(1-\xi t)}^2\theta'(\eta)^2\frac{b}{\nu_f(1-\xi t)}\right)\right\}, \tag{5.31}$$

$$\frac{\Theta_\infty^2 b^2}{k_f\left(\Theta_w-\Theta_\infty\right)^2}\frac{k_{nf}}{\Theta_\infty^2}\left\{(1+N_r)\left(\frac{\partial \Theta}{\partial y}\right)^2\right\} = \frac{b^2}{k_f x}\left(\frac{bx}{(1-\xi t)}\right)\frac{\theta'^2}{\nu_f}\phi_5, \tag{5.32}$$

$$\frac{\Theta_\infty^2 b^2}{k_f\left(\Theta_w-\Theta_\infty\right)^2}\frac{k_{nf}}{\Theta_\infty^2}\left\{(1+N_r)\left(\frac{\partial \Theta}{\partial y}\right)^2\right\} = \frac{b^2}{\nu_f x}U_w\left(1+N_r\right)\frac{\theta'^2}{\nu_f}\phi_5, \tag{5.33}$$

$$\frac{\Theta_\infty^2 b^2}{k_f\left(\Theta_w-\Theta_\infty\right)^2}\frac{k_{nf}}{\Theta_\infty^2}\left\{(1+N_r)\left(\frac{\partial \Theta}{\partial y}\right)^2\right\} = R_e\left(1+N_r\right)\frac{\theta'^2}{\nu_f}\phi_5. \tag{5.34}$$

Consider second term of equation (5.29),

$$\frac{\mu_{nf}}{\Theta_\infty}\left(\frac{\partial u}{\partial y}\right)^2\left(1+\frac{1}{\beta}\right), \tag{5.35}$$

using equation (3.19) and (3.61), we get

$$\frac{\mu_{nf}}{\Theta_\infty}\left(\frac{\partial u}{\partial y}\right)^2\left(1+\frac{1}{\beta}\right) = \frac{\mu_{nf}}{\Theta_\infty}\left(\frac{bxf''(\eta)}{(1-\xi t)}\sqrt{\frac{b}{\nu_f(1-\xi t)}}\right)^2\left(1+\frac{1}{\beta}\right), \tag{5.36}$$

$$\frac{\mu_{nf}}{\Theta_\infty}\left(\frac{\partial u}{\partial y}\right)^2\left(1+\frac{1}{\beta}\right) = R_e\left(\frac{Br}{\Omega\phi_1}\right)f''^2\left(1+\frac{1}{\beta}\right). \tag{5.37}$$

Consider third term of equation (5.29),

$$\frac{\sigma_{nf}B^2(t)u^2}{\Theta_\infty}, \tag{5.38}$$

$$\frac{\sigma_{nf}B^2(t)u^2}{\Theta_\infty} = \frac{\Theta_\infty^2 b^2}{k_f\left(\Theta_w-\Theta_\infty\right)^2}\left(\frac{\sigma_{nf}B^2(t)u^2}{\Theta_\infty}\right), \tag{5.39}$$

using equation (3.14) and (3.62), we get

$$\frac{\sigma_{nf}B^2(t)u^2}{\Theta_\infty} = \frac{\Theta_\infty^2 b^2}{k_f\left(\Theta_w-\Theta_\infty\right)^2}\left(\left(\frac{\sigma_f\phi_4}{\Theta_\infty}\right)\left(\frac{B_o^2}{1-\xi t}\right)\left(\frac{bx}{1-\xi t}\right)^2 f'^2\right), \tag{5.40}$$

$$\frac{\sigma_{nf}B^2(t)u^2}{\Theta_\infty} = \frac{\phi_4 B_r}{\Omega}M^2R_e f'^2. \tag{5.41}$$

Substituting the equation (5.34), (5.37) and (5.41) in (5.29), we get

$$N_G = R_e\left(1+N_r\right)\frac{\theta'^2}{\nu_f}\phi_5 + R_e\left(\frac{B_r}{\Omega\phi_1}\right)\left(1+\frac{1}{\beta}\right)f''^2 + R_e\frac{\phi_4 B_r}{\Omega}M^2 f'^2, \tag{5.42}$$

$$N_G = R_e\left[\phi_5(1+N_r)\theta'^2 + \frac{1}{\phi_1}\frac{B_r}{\Omega}\left\{\left(1+\frac{1}{\beta}\right)f''^2 + \phi_1\phi_4 M f'^2\right\}\right], \tag{5.43}$$

where

$$R_e = \frac{U_w b^2}{\nu_f x}, \qquad B_r = \frac{\mu_f U_w^2}{k_f\left(\Theta_w-\Theta_\infty\right)}, \qquad \Omega = \frac{\Theta_w-\Theta_\infty}{\Theta_\infty}. \tag{5.44}$$

5.5 Numerical Results and Discussion

The numerical results of the current mathematical model are graphically presented in this section. The calculations have been made for different estimations includes Casson fluid model parameter β, Hartman number M, nanoparticle volume concentration parameter ϕ, time relaxation parameter ϑ, radiation parameter N_r, Biot number B_i, velocity slip parameter Λ, nanoparticle shapes parameter m, Reynolds number Re and the Brinkman number B_r. The results are produced for the $Cu-H_2O$ and TiO_2-H_2O Casson nanofluids. In addition to these Table 5.3 showed the velocity gradient and heat transfer rate at the surface of the boundary.

5.5.1 Effect of Casson Parameter β

The impact of Casson parameter β on velocity, temperature and entropy generation profiles of $Cu-H_2O$ and TiO_2-H_2O non-Newtonian Casson nanofluids are displayed in

Figures 5.2-5.4. Computations are performed for $\beta = 1.0, 5.0, 10.0$ at uniform nanoparticle volume concentration of $\phi = 0.2$.

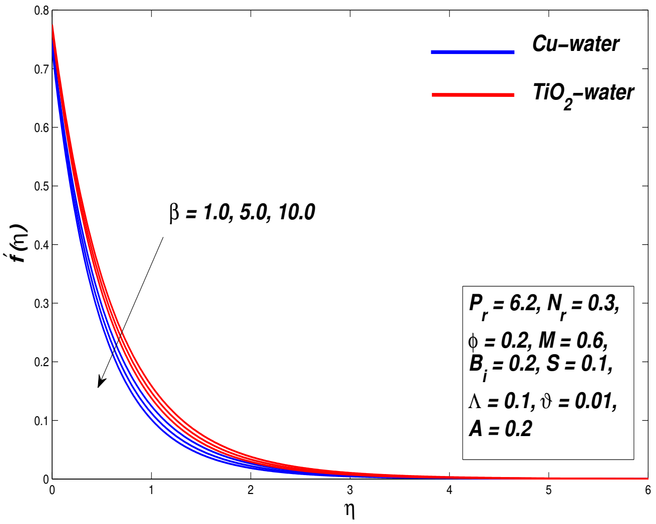

FIGURE 5.2: Velocity Distribution against the Parameter β

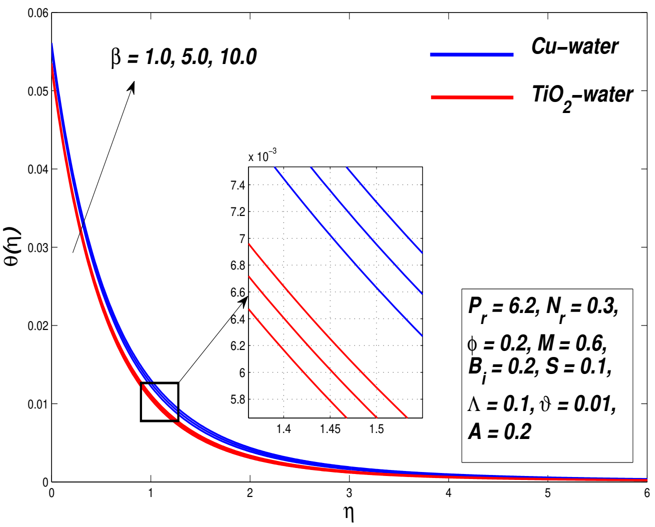

FIGURE 5.3: Temperature Distribution against the Parameter β

The velocity profiles in Figure 5.2 decreases with growing values of β and hence declines the thickening level of momentum boundary layer. In other words, fluid motion reduces to a region near the fluid-surface boundary as an increase in the Casson parameter. Physically there is a decrease in the fluid yield stress by rising values of β, which results in the reduction in the velocity profile and a rise in the velocity gradient at the boundary.

Moreover, for the constant value of $\beta = 1.0$, the thickness of the boundary layer of $TiO_2 - H_2O$ nanofluid is comparatively higher than the $Cu - H_2O$ nanofluid. Figure 5.3 showed that the temperature of nanofluids rises with the raising values of the parameter β. This increasing trend indicate the boost in the thickness of thermal boundary layer and reduction in the rate of heat transfer. This behaviour of temperature profiles is due to rise in the elasticity stress parameter. Furthermore, Figure 5.4 depicted the effect of Casson parameter β on the entropy of the system. It is noticed that raising fluid parameter increases the entropy of the system. Finally, it is detected from Table 5.2 that the local Nusselt number decreases for both $Cu - H_2O$ and $TiO_2 - H_2O$ nanofluids.

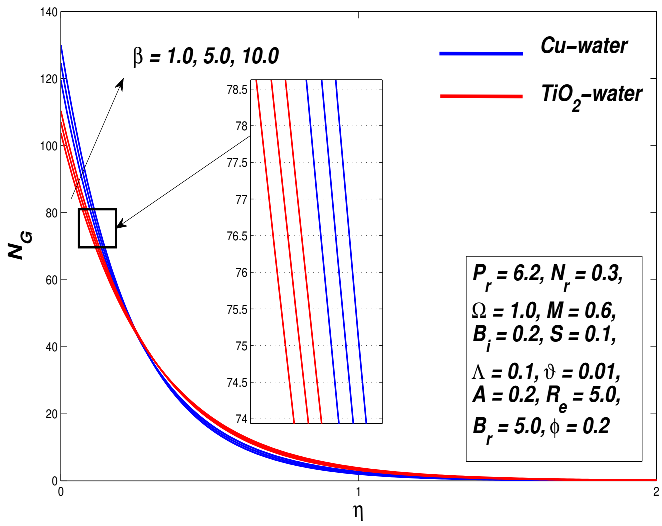

FIGURE 5.4: Entropy Generation Distribution against the Parameter β

5.5.2 Effect of Magnetic parameter M

Figures 5.5-5.7 presented the effect of magnetic parameter M on velocity, temperature and entropy profiles against similarity variable η. The velocity of nanofluids reduces with increasing strength of magnetic parameter M. The interaction of electrically conducting nanofluids with the applied transverse magnetic field generates a resistive force known as Lorentz force. Moreover, the strength of Lorentz force rises with raising strength of applied magnetic field and counteracts the fluid motion within the boundary layer and reduces the thickening level of momentum boundary layer. The decreasing trend in fluid velocity is observed for both $Cu - H_2O$ and $TiO_2 - H_2O$ nanofluids. In Figure 5.6, the temperature of nanofluids rises with increasing strength of parameter M and thus increases the thickening level of the thermal boundary layer. It is observed that the parameter M is inversely proportional to the density of nanofluid, therefore the increase in M reduces the density and, as a result the temperature of the fluid rises.

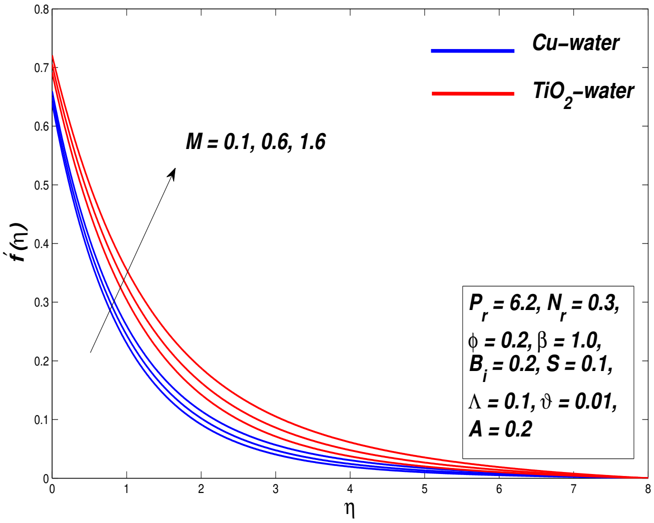

FIGURE 5.5: Velocity Distribution against the Parameter M

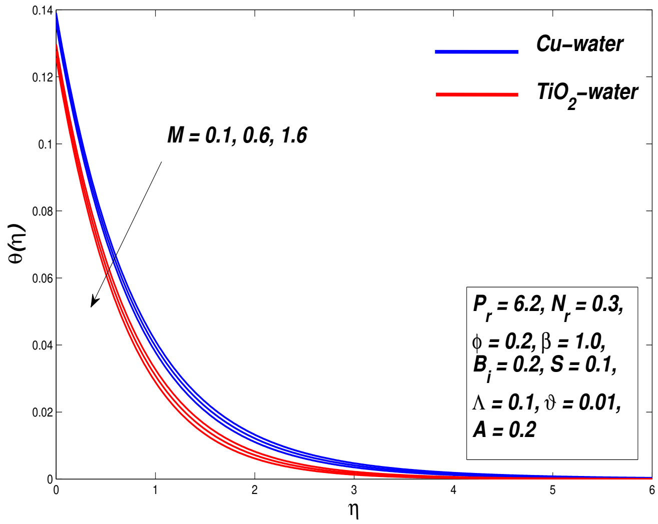

FIGURE 5.6: Temperature Distribution against the Parameter M

The increase in nanofluid temperature within the boundary layer decreases the rate of heat transfer at the boundary. The influence of the Lorentz force at the boundary is presented in Table 5.2. The velocity gradient raises but the Nusselt number reduces with growing strength of the applied magnetic field. The effect of M on the entropy profile is discussed in Figure 5.7. It is noted that a more traverse magnetic field tends to increase the entropy of the system.

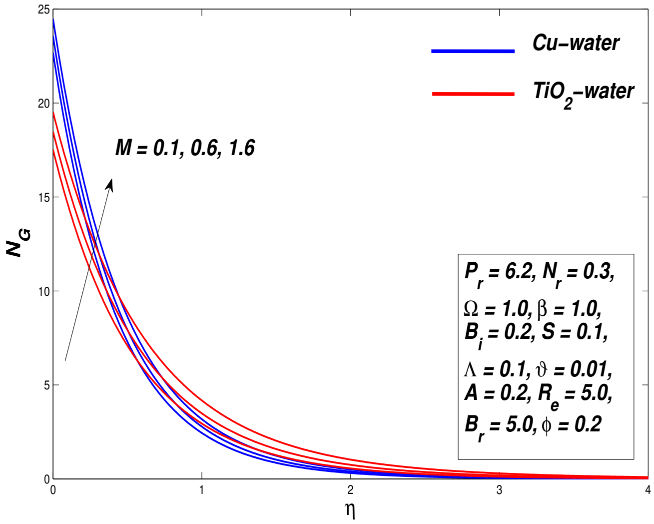

FIGURE 5.7: Entropy Generation Distribution against the Parameter M

5.5.3 Effect of Nanoparticle Volume Fraction Parameter ϕ

Figures 5.8-5.10 presented the nature of fluid motion, temperature distribution and entropy generation within boundary layer for Casson nanofluids due to variation in nanoparticle volume concentration parameter ϕ.

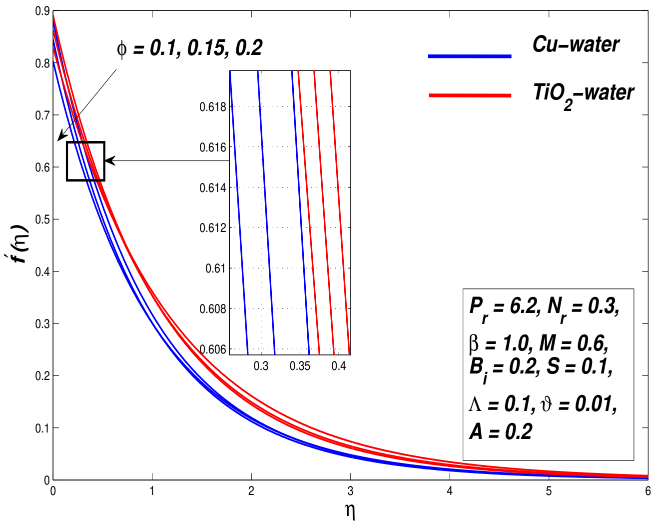

FIGURE 5.8: Velocity Distribution against the Parameter ϕ

The parameter ϕ correspond to volume of solid particles in the basefluid. It is well known solid particles have higher thermal conductivity than fluids, therefore increase in ϕ reduces fluid velocity as observed from Figure 5.8 and enhances its temperature in the boundary layer region.

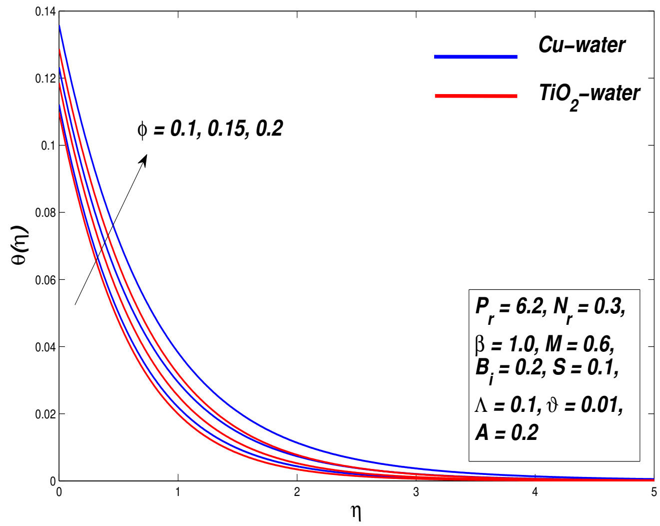

FIGURE 5.9: Temperature Distribution against the Parameter ϕ

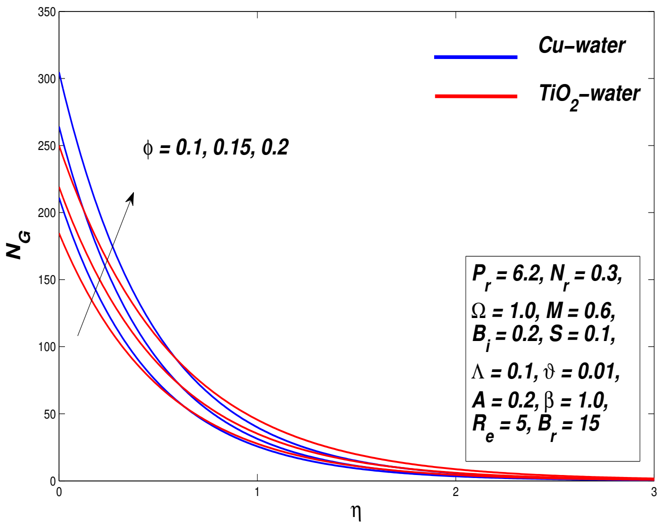

FIGURE 5.10: Entropy Generation Distribution against the Parameter ϕ

Whereas, this fact is very much evident in Figure 5.9 that the increase in the total thermal conductivity of nanofluids increases the temperature and the thickness of thermal boundary layer. The increasing and decreasing trend of the velocity gradient and heat transfer rate is detected with the increase of parameter ϕ (see Table 5.2). Figure 5.10 illustrates that the entropy profile increases with the increasing nanoparticle volume fraction parameter. The entropy generation rate is higher for Cu-water nanofluids as compared to TiO_2-water nanofluids.

5.5.4 Effect of Velocity Slip Parameter Λ

Figures 5.11-5.13 illustrated that the positive values of slip parameter Λ reduces fluid

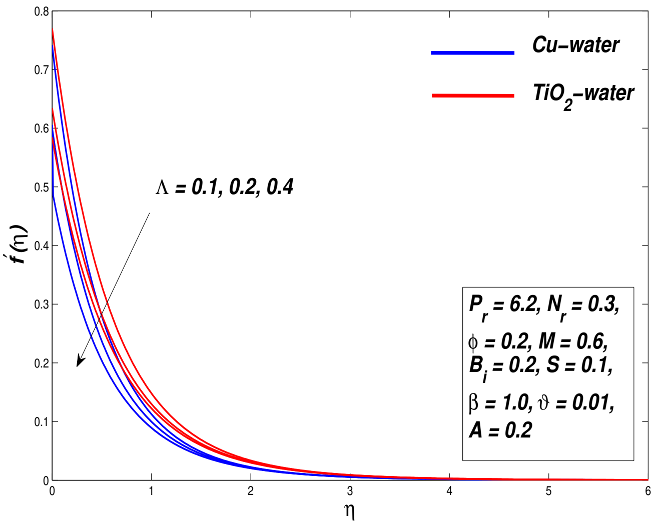

FIGURE 5.11: Velocity Distribution against the Parameter Λ

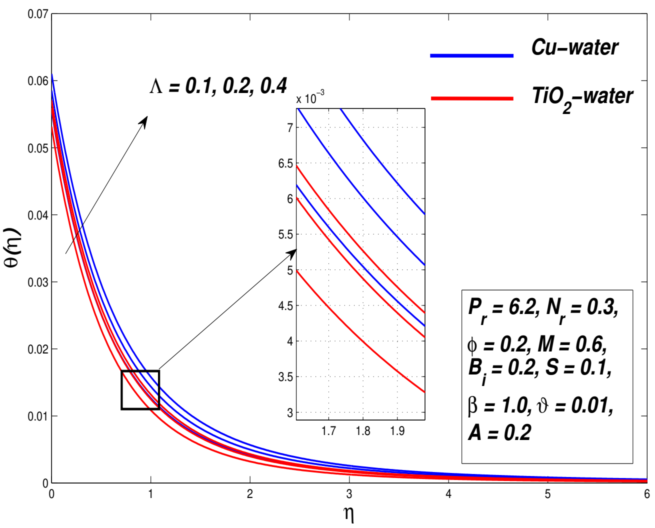

FIGURE 5.12: Temperature Distribution against the Parameter Λ

movement and entropy generation of Casson nanofluids. Whereas the temperature of Casson nanofluids increases with increasing values of parameter Λ. In Figure 5.11 the decrease in velocity is consistent with the fact that slip velocity retards the motion of the boundary surface. In other words, velocity slip act opposite to stretching pull of the surface and resists its transmission to the fluid. As a result, momentum boundary layer decreases with rise in parameter Λ. Figure 5.12 showed the temperature distribution within the boundary layer against the parameter Λ. The velocity slip is inversely proportional to the temperature distribution and an increase in the parameter Λ increases the thermal boundary layer thickness and reduces the Nusselt number. Table 5.2 shows that positive increase in velocity slip leads to decrease in velocity gradient and heat transfer rate for both $Cu - H_2O$ and $TiO_2 - H_2O$ nanofluids. This expected behaviour is due to the fact that the boundary slip reduces the friction at the solid-fluid interface and consequently the rate of heat transfer.

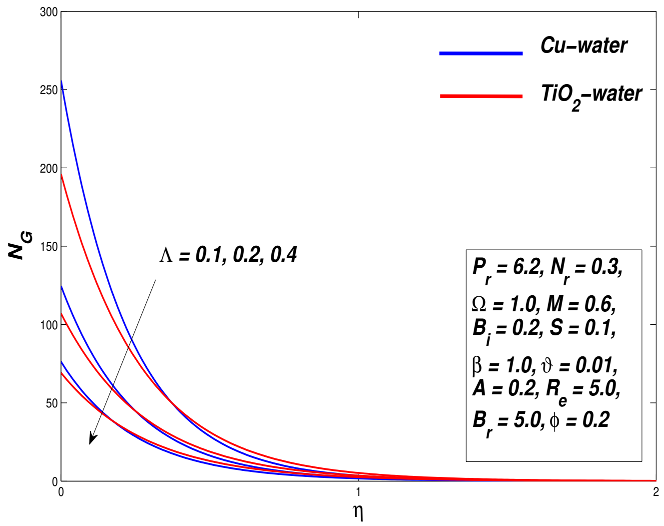

FIGURE 5.13: Entropy Generation Distribution against the Parameter Λ

From Figure 5.13 it can be observed easily that the entropy decreases with increasing values of Λ. Greater Λ values result in a reduce velocity in the boundary layer. This reduce velocity in return reduces the frictional forces inside the fluid reduce friction means that the frictional irreversibilities will also reduce. Thus its contribution towards the entropy becomes less pronounced in the entropy, so the entropy of the system decreases.

5.5.5 Effect of the Relaxation Time Parameter ϑ, Radiation Parameter N_r and Biot Number B_i

There is no effect of relaxation time parameter ϑ, thermal radiation parameter $N(r)$ and Biot number B_i/sheet convection parameter on the velocity profile of Casson nanofluids. Figures 5.14-5.19 exhibit the graphs of temperature profiles for $Cu - H_2O$ and $TiO_2 - H_2O$ nanofluids with variation in relaxation time parameter ϑ, thermal radiation parameter N_r and Biot number B_i/ sheet convection parameter, respectively.

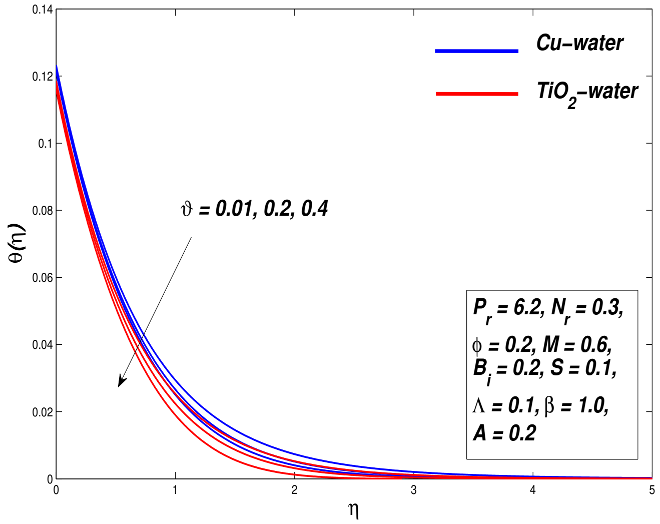

FIGURE 5.14: Temperature Distribution against the Parameter ϑ

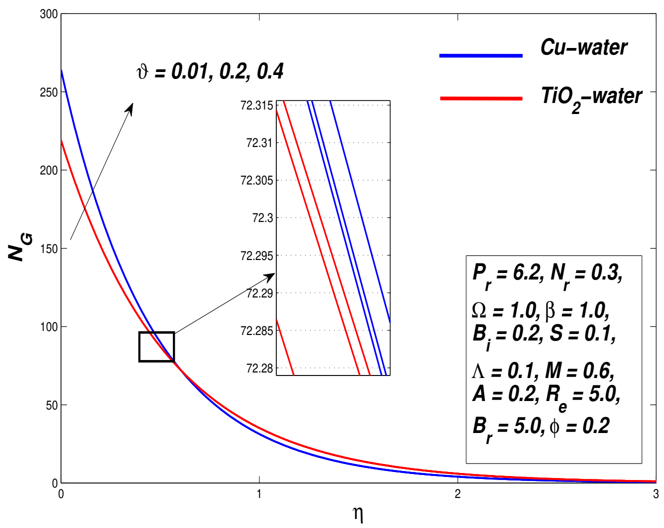

FIGURE 5.15: Entropy Generation Distribution against the Parameter ϑ

Figure 5.14 demonstrates that the temperature profile and the thickening level of thermal boundary layer are less for greater relaxation time parameter ϑ. In addition, radiation parameter N_r is illustrated in Figure 5.16. An increase in radiation parameter N_r exposed the significant improvement in the fluid temperature distribution for $Cu - H_2O$ and $TiO_2 - H_2O$ nanofluids.

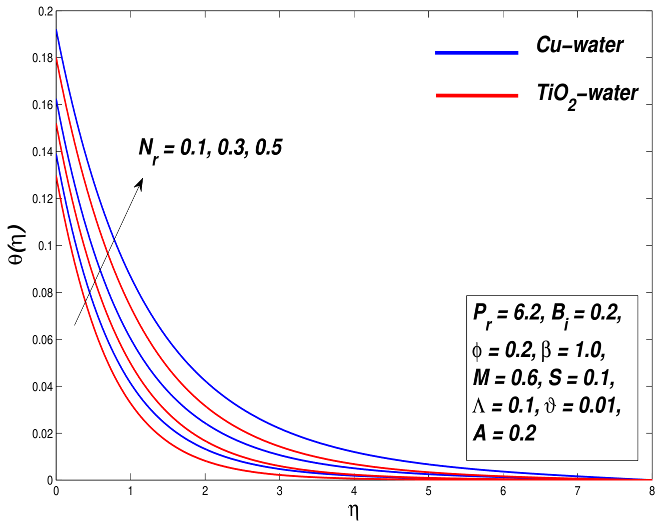

Figure 5.16: Temperature Distribution against the Parameter N_r

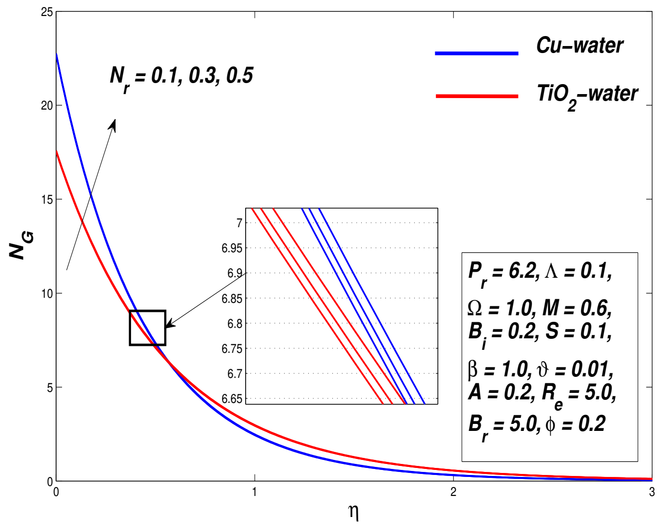

Figure 5.17: Entropy Generation Distribution against the Parameter N_r

Physically speaking strengthening N_r leads to more heat into the fluid as a result of which the thickness level of associated thermal boundary layer increases. Thus, N_r

impact plays a significant role in magnifying the heat transfer rate. In Figure 5.18, Biot number or the sheet convection parameter shows the ratio of conduction inside the fluid to the convection at its surface.

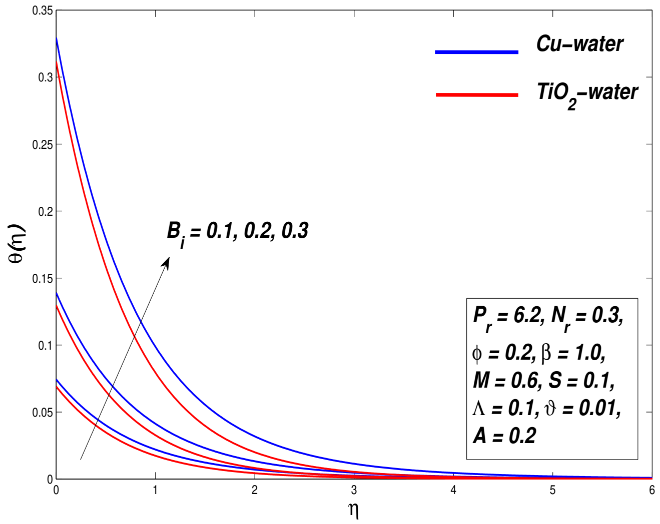

FIGURE 5.18: Temperature Distribution against the Parameter B_i

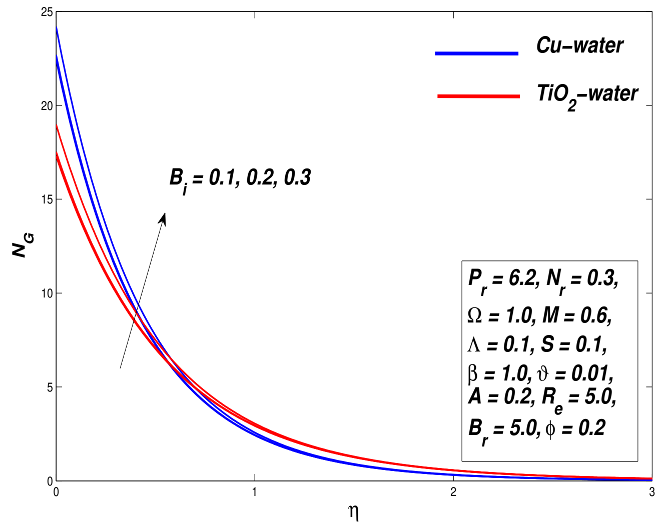

FIGURE 5.19: Entropy Generation Distribution against the Parameter B_i

Increasing sheet convection parameter means that the heat transfer through conduction dominates the convection coefficient at the surface of the fluid. The increase in B_i showed that the hot fluid within boundary layer heats the stretching surface and raises the temperature of the thermal system. Figures 5.15, 5.17 and 5.19 exhibited influence of ϑ, N_r and B_i parameters on the entropy profile, respectively. The changeover point for the entropy profile is estimated at nearby $\eta = 0.3$. Before this behaviour the entropy is enhanced and then it begins to fall. In other words the thermal process is converging towards the case of reversible process. Table 5.2 showed that the temperature rises with the raising relaxation time, radiation and convection parameters.

5.5.6 Effect of Reynolds Number R_e and the Brinkman Number B_r

The effects of Reynolds number R_e and Brinkman number B_r on entropy generation profiles are presented in this section. Numerical computations showed the higher values of R_e increases entropy which physically means that the inertial forces dominate the

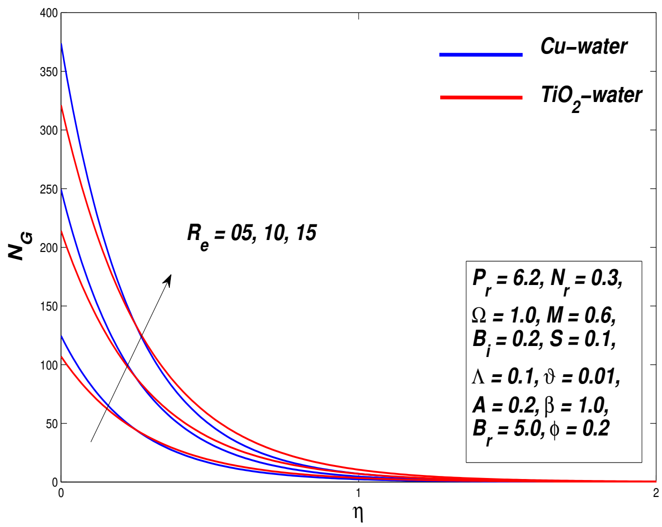

FIGURE 5.20: Entropy Generation Distribution against the Parameter R_e

viscous effects see Figure 5.20. Figure 5.21 discussed the influence of B_r on the entropy. It is found that the Brinkman number augmentation increases the entropy generation. This is due to the fact that Brinkman number is the ratio of heat dissipation to the conduction at the surface so increasing the values of B_r means more heat is dissipated compared with the conduction of heat at the surface, which results in an increase in the entropy.

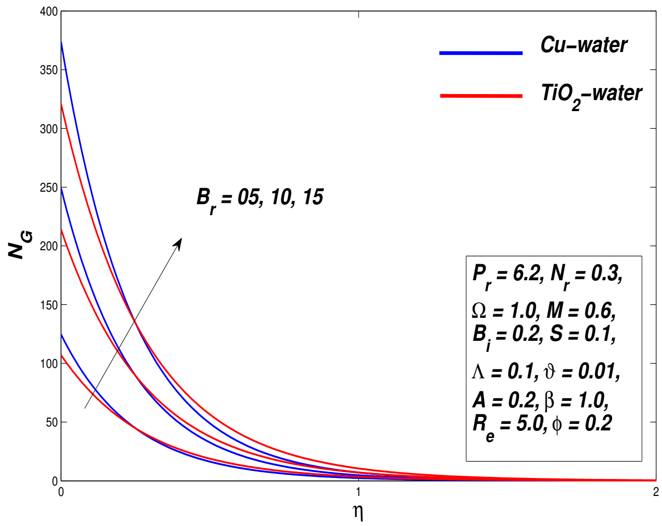

FIGURE 5.21: Entropy Generation Distribution against the Parameter B_r

5.5.7 Effect of Magnetic Parameter M and Radiation Parameter N_r on Skin Friction C_f and the Nusselt Number Nu_x, Respectively

The influence of magnetic parameter M and radiation parameter N_r on skin friction

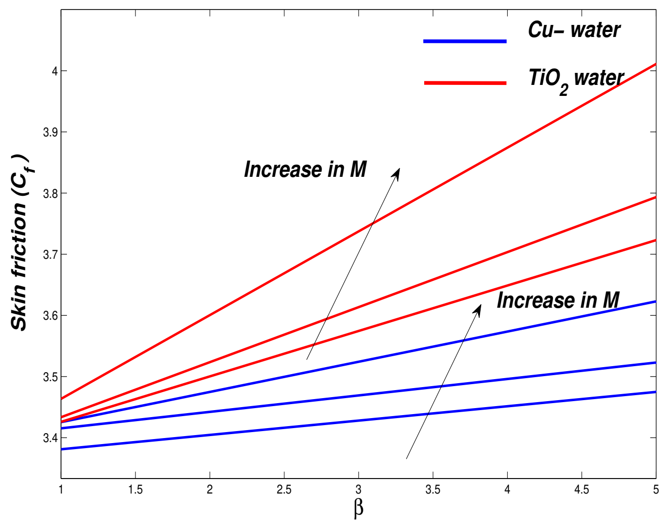

FIGURE 5.22: Skin Friction C_f against the Parameter β

coefficient C_f and Nusselt number Nu_x profiles of Cu-water and TiO_2-water non-Newtonian nanofluids are presented in Figures 5.22-5.23, respectively. In 5.22 computations are performed for $M = 0.6, 0.8, 1.2$ whereas the parameter β takes the values $1.0, 5.0, 10.0$. It is noted when we increase the magnetic parameter M the skin friction coefficient C_f increases. The physical reason behind this is that greater M is responsible for greater friction between the surface and the fluid as a result skin friction increases. In 5.23 computations are performed for $Nr = 0.2, 0.4, 0.9$ whereas the prandtle number P_r is fixed on $1.0, 6.2, 7.38$. It is observed when we increase the radiation parameter Nr the rate of convective heat transfer (Nusselt number) increases. This is due to the fact that a greater heat flux is generated, which results in a greater heat transfer rate.

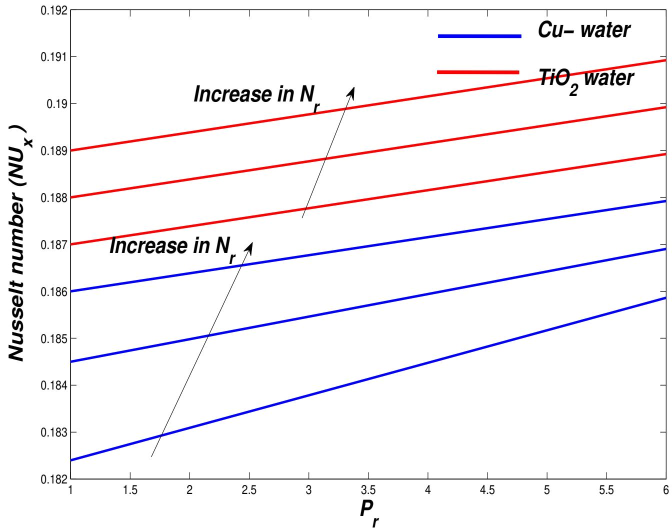

FIGURE 5.23: Nusselt Number Nu_x against the Parameter P_r

β	A	M	ϕ	Λ	ϑ	N_r	B_i	S	$C_f Re_x^{\frac{1}{2}}$ $Cu-water$	$C_f Re_x^{\frac{1}{2}}$ $T_iO_2-water$	$N_u Re_x^{\frac{-1}{2}}$ $Cu-water$	$N_u Re_x^{\frac{-1}{2}}$ $T_iO_2-water$
1.0	0.2	0.6	0.2	0.1	0.01	0.3	0.2	0.1	3.1100	2.7307	0.1306	0.1443
5.0									2.3002	2.0315	0.1295	0.1433
10.0									2.1831	1.9300	0.1293	0.1431
	0.2								3.1100	2.7307	0.1306	0.1443
	0.6								3.3511	2.9203	0.1322	0.1459
	1.6								3.8712	3.3385	0.1350	0.1488
		0.1							2.7898	2.3307	0.1310	0.1449
		0.6							3.1100	2.7307	0.1306	0.1443
		1.6							3.6288	3.3420	0.1298	0.1434
			0.1						2.3877	2.1783	0.1734	0.1826
			0.15						2.9264	2.6102	0.1419	0.1525
			0.2						3.1100	2.7307	0.1306	0.1443
				0.1					3.1100	2.7307	0.1306	0.1443
				0.2					2.6164	2.3497	0.1296	0.1434
				0.4					2.0063	1.8492	0.1281	0.1419
					0.01				3.1100	2.7307	0.1306	0.1443
					0.2				3.1100	2.7307	0.1308	0.1445
					0.4				3.1100	2.7307	0.1310	0.1447
						0.1			3.1100	2.7307	0.1137	0.1256
						0.3			3.1100	2.7307	0.1306	0.1443
						0.5			3.1100	2.7307	0.1470	0.1626
							0.1		3.1100	2.7307	0.0696	0.0767
							0.2		3.1100	2.7307	0.1306	0.1443
							0.3		3.1100	2.7307	0.1845	0.2043
								0.1	3.1100	2.7307	0.1306	0.1443
								0.2	3.2012	2.7921	0.1316	0.1454
								0.5	3.4868	2.9814	0.1343	0.1482

TABLE 5.1: Values of Skin Friction $= C_f Re_x^{\frac{1}{2}}$ and Nusselt Number $= N_u Re_x^{\frac{-1}{2}}$ for $P_r = 6.2$.

5.6 Conclusions

In this research, a simplified mathematical model is studied numerically to investigate the flow and heat transfer characteristics of water based Casson nanofluids. The governing equations are modeled by including the Cattaneo-Christov heat flux model, Lorentz forces, thermal radiation and the velocity slip at the boundary. The implicit finite difference scheme is utilized to approximate solutions for the velocity, temperature and entropy profiles of $Cu - H_2O$ and $TiO_2 - H_2O$ nanofluids. The observations made can be summed as follows:

- The temperature profiles are observed as an increasing function of the Casson parameter, the magnetic parameter, the nanoparticle volumetric concentration parameter, the velocity slip parameter, the thermal radiation parameter and the sheet convection parameter. Whereas it is a decreasing function of the unsteadiness parameter, the relaxation time parameter and the suction parameter.

- It is well known fact that the inclusion of solid nanoparticles in the ordinary fluids increases the overall thermal conductivity of the mixture. Therefore the increase in ϕ decrease in thickness of momentum and increase the thickness of thermal boundary layer respectively.

- For the present study, $Cu - H_2O$ nanofluid is detected as a superior thermal conductor than $TiO_2 - H_2O$ nanofluid.

- Entropy of the thermal system is found to be rising with the unsteadiness parameter, the magnetic parameter, the nanoparticle volumetric concentration parameter, the relaxation time parameter, the thermal radiation parameter, the suction parameter, the Reynolds number and the Brinkman number but decreases with the rise of the Casson parameter, velocity slip parameter and injection parameter.

- The velocity profile increases for the injection parameter because more fluid is injected when the heated fluid is pushed further away from the wall and it is accelerated due to less viscosity.

- The stronger traverse magnetic field has a negative impact on the movement of the fluid particles in the boundary layer. The interaction of electrically conducting nanofluids with uniformly distributed transverse magnetic field of strength generates a resistive force known as Lorentz force. The Lorentz force impact is presented in the form of decreasing trend in velocity profiles.

Chapter 6

Casson Hybrid Nanofluid Flow, Heat Transfer and Entropy Generation Analysis

6.1 Introduction

In this chapter, hybridity of nanofluids is analyzed considering its flow over a permeable stretching surface. Volumetric total entropy generation is studied in the presence of uniform, transverse magnetic field along with Cattaneo-Christov model. The mathematical results are presented for considering velocity slip at the boundary and inducing the effect of thermal radiation for optically thick hybrind nanofluid. Similarity transformations simplifications are carried to reduce governing PDEs to ODEs and then numerical simulations are performed using Keller box technique. Results are depicted in the form of graphs and computations are carried for conventional Copper oxide-Ethylene glycol ($CuO - EG$) and hybrid Titanium-Copper oxide/Ethylene glycol ($TiO_2 - CuO/EG$) nanofluids. Moreover nanoparticles of common geometrical shapes are considered in this work and conclusions are also drawn on the basis of nanoparticles shape.

6.2 Mathematical Formulation

Consider the hybrid nanofluid flow over a horizontal surface moving with a non-uniform stretching velocity $U_w(x,t)$ given in equation (3.1). The hybrid nanofluid is manufactured by first adding Copper oxide (CuO) nanoparticles in the Ethylene glycol base fluid at a contact volume fraction (ϕ_w). Titanium-Copper/water $(TiO_2 - CuO)$ nanoparticles are then dispersed into the mixture to make it a hybrid nanofluid at the volume fraction (ϕ_z). The surface of the plate is insulated and velocity slip and convective conditions have been invoked at the boundary. The leading edge of the plate is assumed at $x = 0$ and is considered along the x-axis. Figure 6.1 shows the geometry of the flow model.

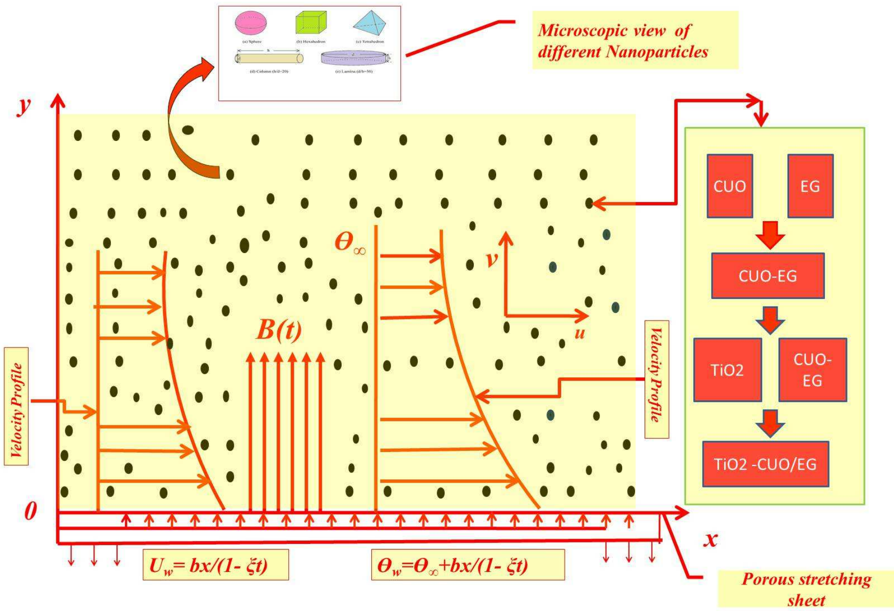

FIGURE 6.1: Physical Model of Schematic Diagram

A uniformly distributed transverse magnetic field of strength $B(t) = \frac{B_0}{\sqrt{1-\xi t}}$ is assumed in the present model. The temperature of the convective surface is $\Theta_w(x,t) = \Theta_\infty + \frac{bx}{1-\xi t}$. This assumption is valid because thermal properties of nanofluid changes significantly with rise in temperature, type of nanoparticles, pressure etc. The Casson hybrid nanofluid is considered optically thick so that the radiations only travel a short distance and the Rosseland approximation is utilized for the radiation effects. The equations representing the basic form of incompressible Casson fluid with isotropic properties are given in equation (2.57). For Casson nanofluid μ_B in equation (2.57) is replaced by

μ_{hnfB} that is,

$$\tau_{ij} = \begin{cases} 2\left(\mu_{hnfB} + \dfrac{p_y}{\sqrt{2\pi}}\right) e_{ij}, & \pi > \pi_c, \\ \\ 2\left(\mu_{hnfB} + \dfrac{p_y}{\sqrt{2\pi_c}}\right) e_{ij}, & \pi < \pi_c. \end{cases} \tag{6.1}$$

The constitutive equations for conservation of mass, momentum and energy under boundary layer assumptions along with suitable boundary conditions for the Maxwell nanofluid are given in equations (2.74) and (2.85). These equations for the Casson hybrid nanofluid are reduced to the form (see for example, Mustafa and Junaid [198])

$$\frac{\partial u}{\partial t} + u\frac{\partial u}{\partial x} + v\frac{\partial u}{\partial y} = \nu_{hnf}\left(1 + \frac{1}{\beta}\right)\frac{\partial^2 u}{\partial y^2} - \frac{\sigma_{hnf}B^2(t)}{\rho_{hnf}}u, \tag{6.2}$$

$$\begin{aligned} \frac{\partial \Theta}{\partial t} + u\frac{\partial \Theta}{\partial x} + v\frac{\partial \Theta}{\partial y} = \frac{k_{hnf}}{(\rho C_p)_{hnf}}\left[\frac{\partial^2 \Theta}{\partial y^2}\right] - \frac{1}{(\rho C_p)_{hnf}}\left[\frac{\partial q_r}{\partial y}\right] \\ -\lambda^*\left[u\frac{\partial u}{\partial x}\frac{\partial \Theta}{\partial x} + v\frac{\partial v}{\partial y}\frac{\partial \Theta}{\partial y} + u\frac{\partial v}{\partial x}\frac{\partial \Theta}{\partial y} + v\frac{\partial u}{\partial y}\frac{\partial \Theta}{\partial x} + u^2\frac{\partial^2 \Theta}{\partial x^2} + v^2\frac{\partial^2 \Theta}{\partial y^2} + 2uv\frac{\partial^2 \Theta}{\partial x \partial y}\right]. \end{aligned} \tag{6.3}$$

The BCs are assumed as

$$\begin{aligned} &u(x,0) = U_w + \left(1 + \frac{1}{\beta}\right)\mu_{hnf}\left(\frac{\partial u}{\partial y}\right), \quad v(x,0) = V_w, \\ &-k_0\left(\frac{\partial \Theta}{\partial y}\right) = h_f(\Theta_w - \Theta), \end{aligned} \tag{6.4}$$

$$u \to 0, \quad \Theta \to \Theta_\infty \ \text{ as } \ y \to \infty. \tag{6.5}$$

Moreover, the thermal radiation q_r and nanoparticles shape factor m are given in equation (3.8) and Table 2.1 (for details see for example, [88, 186, 193]).

6.3 Solution of the Problem

To solve the governing system of PDEs (6.2)-(6.5), we introduce similarity variables which are given in equation (3.13). The substitution of equations (3.12)-(3.13) the governing boundary value problem (6.2)-(6.5) reduced into a system of ODEs.

From equations (3.14) and (3.15),

$$u = \frac{bx}{(1-\xi t)} f'(\eta), \tag{6.6}$$

$$v = -\sqrt{\frac{\nu_f b}{(1-\xi t)}} f(\eta). \tag{6.7}$$

Equation (3.35) has satisfied the continuity equation. Now using appropriate equations from (3.16 - 3.34) and (5.10 - 5.12) into (6.2) and (6.3). we get the following ODEs

$$\begin{aligned}
&\frac{(1-\phi_w)^{-2.5}(1-\phi_z)^{-2.5}}{[(1-\phi_z)\{(1-\phi_w)+\phi_w \frac{\rho_{p_1}}{\rho_f}\}]+\phi_z \frac{\rho_{p2}}{\rho_f}} \left(1+\frac{1}{\beta}\right) f''' + ff'' - f'^2 \\
&-A\left(f'+\frac{\eta}{2}f''\right) - \frac{\left[1+\frac{3(\frac{\phi_w\sigma_{p_1}+\phi_z\sigma_{p_2}}{\sigma_f}-(\phi_w+\phi_z))}{(\frac{\phi_w\sigma_{p_1}+\phi_2\sigma_{p_2}}{(\phi_w+\phi_z)\sigma_f}+2)-(\frac{\phi_w\sigma_{p_1}+\phi_z\sigma_{p_2}}{\sigma_f}-(\phi_w+\phi_z))}\right]}{[(1-\phi_z)\{(1-\phi_w)+\phi_w \frac{\rho_{p_1}}{\rho_f}\}]+\phi_z \frac{\rho_{p2}}{\rho_f}} M f' = 0.
\end{aligned} \tag{6.8}$$

$$\begin{aligned}
&\theta''\left(1+\frac{\kappa_f}{\kappa_{hnf}}PrNr\right) + Pr\frac{\kappa_f}{\kappa_{hnf}}\left((1-\phi_z)\{(1-\phi_w)+\phi_w\frac{(\rho C_p)_{p_1}}{(\rho C_p)_f}\} + \frac{\phi_z(\rho C_p)_{p_2}}{(\rho C_p)_f}\right) \\
&\left[f\theta' - f'\theta - A\left(\theta+\frac{\eta}{2}\theta'\right) - \vartheta\left(f'^2\theta - f''\theta - f^2\theta^2 - ff'\theta''\right)\right] = 0.
\end{aligned} \tag{6.9}$$

The associated boundary conditions get the form, from equation (3.38)

$$u(x,0) = U_w + \left(1+\frac{1}{\beta}\right)\mu_{hnf}\left(\frac{\partial u}{\partial y}\right), \tag{6.10}$$

Using (3.1) and (3.19) in (6.10),

$$u(x,0) = \frac{bx}{1-\xi t} + \left(1+\frac{1}{\beta}\right)\frac{\mu_f}{\phi_a}\left(\frac{bxf''(0)}{(1-\xi t)}\sqrt{\frac{b}{\nu_f(1-\xi t)}}\right), \tag{6.11}$$

using equation (3.14) in equation (6.11)

$$\frac{bx}{(1-\xi t)}f'(0) = \frac{bx}{1-\xi t} + \left(1+\frac{1}{\beta}\right)\frac{\mu_f}{\phi_a}\left(\frac{bxf''(0)}{(1-\xi t)}\sqrt{\frac{b}{\nu_f(1-\xi t)}}\right), \tag{6.12}$$

$$\frac{bx}{(1-\xi t)}f'(0) = \frac{bx}{1-\xi t}\left(1+\left(1+\frac{1}{\beta}\right)\frac{\mu_f}{\phi_a}f''(0)\sqrt{\frac{b}{\nu_f(1-\xi t)}}\right), \tag{6.13}$$

$$f'(0) = 1 + \left(1+\frac{1}{\beta}\right)\frac{\mu_f}{\phi_a}f''(0)\sqrt{\frac{b}{\nu_f(1-\xi t)}}, \tag{6.14}$$

$$f'(0) = 1 + \left(1 + \frac{1}{\beta}\right)\frac{\Lambda}{\phi_a} f''(0), \tag{6.15}$$

where,

$$\phi_a = \left[(1-\phi_w)^{2.5}(1-\phi_z)^{2.5}\right], \tag{6.16}$$

$$f'(0) = 1 + \left(1 + \frac{1}{\beta}\right)\frac{\Lambda}{(1-\phi_w)^{2.5}(1-\phi_z)^{2.5}} f''(0). \tag{6.17}$$

From equation (5.15) and (5.16), we have

$$\begin{aligned} f(0) &= S, \\ \theta'(0) &= -B_i(1-\theta(0)), \end{aligned} \tag{6.18}$$

$$f'(\eta) \to 0, \qquad \theta(\eta) \to 0, \quad \text{as} \quad \eta \to \infty. \tag{6.19}$$

In the above equations primes stand for the differentiation of the function with respect to η. $A = \frac{\xi}{b}$ is the unsteady flow parameter, $M = \frac{\sigma_f B_0^2}{b\rho_f}$ is the magnetic parameter, $\vartheta = b\lambda_0^*$ is the thermal relaxation time parameter, $P_r = \frac{\nu_f}{\alpha_f}$ is the Prandtl number, $\alpha_f = \frac{\kappa_f}{(\rho C_p)_f}$ is the thermal diffusivity parameter, $N_r = \frac{16}{3}\frac{\sigma^*\Theta_\infty^3}{\kappa^*\nu_f(\rho C_p)_f}$ is the thermal radiation parameter, $S = -V_w\sqrt{\frac{1-\xi t}{\nu_f\ b}}$ is the mass transfer parameter, $\Lambda = \sqrt{\frac{b}{\nu_f(1-\xi t)}}\mu_f$ is the velocity slip parameter and $B_i = \frac{h_f}{k_0}\sqrt{\frac{\nu_f(1-\xi t)}{b}}$ is the sheet convection parameter or so-called Biot number. It is observed some parameters depend on ξ and is time dependent. Therefore to obtain non-similar solutions for the proposed problem numerical results are computed for locally similar parameters.

The nonlinear system of ODEs (6.8)-(6.9) arising from mathematical modeling of physical system of nanofluid flow is difficult to solve analytically. Therefore, Keller box [182] numerical scheme is employed to find the approximate solutions. The numerical scheme is inherently stable and is second order convergent. The initial step of this scheme is to reduce the equations (6.8)-(6.9) into a system of five first ODEs, that is

$$z_1 = f', \tag{6.20}$$

$$z_2 = z_1', \tag{6.21}$$

$$z_3 = \theta', \tag{6.22}$$

$$\frac{(1-\phi_w)^{-2.5}(1-\phi_z)^{-2.5}}{[(1-\phi_z)\{(1-\phi_w)+\phi_w\frac{\rho_{p1}}{\rho_f}\}]+\phi_z\frac{\rho_{p2}}{\rho_f}}\left(1+\frac{1}{\beta}\right)z_2'+fz_2-z_1^2$$

$$-A(z_1+\frac{\eta}{2}z_2)-\frac{\left[1+\frac{3(\frac{\phi_w\sigma_{p1}+\phi_z\sigma_{p2}}{\sigma_f}-(\phi_w+\phi_z))}{(\frac{\phi_w\sigma_{p1}+\phi_2\sigma_{p2}}{(\phi_w+\phi_z)\sigma_f}+2)-(\frac{\phi_w\sigma_{p1}+\phi_z\sigma_{p2}}{\sigma_f}-(\phi_w+\phi_z))}\right]}{[(1-\phi_z)\{(1-\phi_w)+\phi_w\frac{\rho_{p1}}{\rho_f}\}]+\phi_z\frac{\rho_{p2}}{\rho_f}}Mz_1=0, \tag{6.23}$$

$$z_3'\left(1+\frac{\kappa_f}{\kappa_{hnf}}P_rN_r\right)+P_r\frac{\kappa_f}{\kappa_{hnf}}\left((1-\phi_z)\{(1-\phi_w)+\phi_w\frac{(\rho C_p)_{p1}}{(\rho C_p)_f}\}+\frac{\phi_z(\rho C_p)_{p2}}{(\rho C_p)_f}\right)$$
$$\left[fz_3-z_1\theta-A\left(\theta+\frac{\eta}{2}z_3\right)-\vartheta(z_1^2\theta-z_1'\theta-f^2\theta^2-fz_1z_3')\right]=0, \tag{6.24}$$

The boundary conditions (6.17)-(6.19) are similarly transformed into

$$f(0)=S, \quad z_1(0)=1+\left(1+\frac{1}{\beta}\right)\frac{\Lambda}{(1-\phi_w)^{2.5}(1-\phi_z)^{2.5}}z_2(0),$$
$$z_3(0)=-B_i(1-\theta(0)), \tag{6.25}$$

$$z_1(\infty)\to 0, \qquad \theta(\infty)\to 0. \tag{6.26}$$

The derivatives appeared in the above system are then approximated by the central differences and averages are centered at the midpoints of the mesh and are expressed by

$$\eta_0=0, \quad \eta_j=\eta_{j-1}+h, \quad j=1,2,3,...,J-1, \quad \eta_J=\eta_\infty. \tag{6.27}$$

The system of first order ODEs (6.20)-(6.24) is then reduced to the following set of nonlinear algebraic equations.

$$\frac{(z_1)_j+(z_1)_{j-1}}{2}=\frac{f_j-f_{j-1}}{h}, \tag{6.28}$$

$$\frac{(z_2)_j+(z_2)_{j-1}}{2}=\frac{(z_1)_j-(z_1)_{j-1}}{h}, \tag{6.29}$$

$$\frac{(z_3)_j+(z_3)_{j-1}}{2}=\frac{\theta_j-\theta_{j-1}}{h}, \tag{6.30}$$

$$\frac{(1-\phi_w)^{-2.5}(1-\phi_z)^{-2.5}}{[(1-\phi_z)\{(1-\phi_w)+\phi_w\frac{\rho_{p_1}}{\rho_f}\}]+\phi_z\frac{\rho_{p_2}}{\rho_f}}\left(1+\frac{1}{\beta}\right)\left(\frac{(z_2)_j-(z_2)_{j-1}}{h}\right)$$
$$+\left(\frac{f_j+f_{j-1}}{2}\right)\left(\frac{(z_2)_j+(z_2)_{j-1}}{2}\right)-\left(\frac{(z_1)_j+(z_1)_{j-1}}{2}\right)^2$$
$$-A\left\{\left(\frac{(z_1)_j+(z_1)_{j-1}}{2}\right)+\frac{\eta}{2}\left(\frac{(z_2)_j+(z_2)_{j-1}}{2}\right)\right\}$$
$$-\frac{\left[1+\frac{3(\frac{\phi_w\sigma_{p1}+\phi_z\sigma_{p2}}{\sigma_f}-(\phi_w+\phi_z))}{(\frac{\phi_w\sigma_{p1}+\phi_2\sigma_{p2}}{(\phi_w+\phi_z)\sigma_f}+2)-(\frac{\phi_w\sigma_{p1}+\phi_z\sigma_{p2}}{\sigma_f}-(\phi_w+\phi_z))}\right]}{[(1-\phi_z)\{(1-\phi_w)+\phi_w\frac{\rho_{p_1}}{\rho_f}\}]+\phi_z\frac{\rho_{p_2}}{\rho_f}}M\left(\frac{(z_1)_j+(z_1)_{j-1}}{2}\right)=0, \tag{6.31}$$

$$\left(\frac{(z_3)_j-(z_3)_{j-1}}{h}\right)\left(1+\frac{\kappa_f}{\kappa_{hnf}}P_rN_r\right)+P_r\frac{\kappa_f}{\kappa_{hnf}}$$
$$\left((1-\phi_z)\{(1-\phi_w)+\phi_w\frac{(\rho C_p)_{p_1}}{(\rho C_p)_f}\}+\frac{\phi_z(\rho C_p)_{p_2}}{(\rho C_p)_f}\right)(\left(\frac{f_j+f_{j-1}}{2}\right)\left(\frac{(z_3)_j+(z_3)_{j-1}}{2}\right)$$
$$-\left(\frac{(z_1)_j+(z_1)_{j-1}}{2}\right)\left(\frac{\theta_j+\theta_{j-1}}{2}\right)-A\left\{\left(\frac{\theta_j+\theta_{j-1}}{2}\right)+\frac{\eta}{2}\left(\frac{(z_3)_j+(z_3)_{j-1}}{2}\right)\right\}$$
$$-\vartheta\left(\left(\frac{f_j+f_{j-1}}{2}\right)^2\left(\frac{(z_3)_j-(z_3)_{j-1}}{h}\right)\right)$$
$$-\vartheta\left(\left(\frac{f_j+f_{j-1}}{2}\right)\left(\frac{(z_1)_j+(z_1)_{j-1}}{2}\right)\left(\frac{t_j+t_{j-1}}{2}\right)\right))=0. \tag{6.32}$$

Linearize the resulting algebraic equations by using Newton's method i.e.

$$()_j^{(i+1)}=()_j^{(i)}+\varepsilon()_j^{(i)}, \tag{6.33}$$

$$\varepsilon f_j-\varepsilon f_{j-1}-\frac{1}{2}h(\varepsilon(z_1)_j+\varepsilon(z_1)_{j-1})=(r_1)_{j-\frac{1}{2}}, \tag{6.34}$$

$$\varepsilon(z_1)_j-\varepsilon(z_1)_{j-1}-\frac{1}{2}h(\varepsilon(z_2)_j+\varepsilon(z_2)_{j-1})=(r_2)_{j-\frac{1}{2}}, \tag{6.35}$$

$$\varepsilon\theta_j-\varepsilon\theta_{j-1}-\frac{1}{2}h(\varepsilon(z_3)_j+\varepsilon(z_3)_{j-1})=(r_3)_{j-\frac{1}{2}}, \tag{6.36}$$

$$\begin{aligned}(a_1)_j\varepsilon f_j+(a_2)_j\varepsilon f_{j-1}+(a_3)_j\varepsilon(z_1)_j+(a_4)_j\varepsilon(z_1)_{j-1}+(a_4)_j\varepsilon(z_1)_{j-1}\\+(a_5)_j\varepsilon(z_2)_j+(a_6)_j\varepsilon(z_2)_{j-1}(a_7)_j\varepsilon\theta_j+(a_8)_j\theta_{j-1}+(a_9)_j\varepsilon(z_3)_j\\+(a_{10})_j\varepsilon(z_3)_{j-1}=(r_4)_{j-\frac{1}{2}},\end{aligned} \tag{6.37}$$

$$\begin{aligned}(b_1)_j\varepsilon f_j+(b_2)_j\varepsilon f_{j-1}+(b_3)_j\varepsilon(z_1)_j+(b_4)_j\varepsilon(z_1)_{j-1}+(b_4)_j\varepsilon(z_1)_{j-1}\\+(b_5)_j\varepsilon(z_2)_j+(b_6)_j\varepsilon(z_2)_{j-1}(b_7)_j\varepsilon\theta_j+(b_8)_j\varepsilon\theta_{j-1}+(b_9)_j\varepsilon(z_3)_j\\+(b_{10})_j\varepsilon(z_3)_{j-1}=(r_5)_{j-\frac{1}{2}},\end{aligned} \tag{6.38}$$

where

$$(r_1)_{j-\frac{1}{2}} = -f_j + f_{j-1} + \frac{h}{2}((z_1)_j + (z_1)_{j-1}), \tag{6.39}$$

$$(r_2)_{j-\frac{1}{2}} = -(z_1)_j + (z_1)_{j-1} + \frac{h}{2}((z_2)_j + (z_2)_{j-1}), \tag{6.40}$$

$$(r_3)_{j-\frac{1}{2}} = -\theta_j + \theta_{j-1} + \frac{h}{2}((z_3)_j + (z_3)_{j-1}), \tag{6.41}$$

$$\begin{aligned}
(r_4)_{j-\frac{1}{2}} = -h &\left[\frac{(1-\phi_w)^{-2.5}(1-\phi_z)^{-2.5}}{[(1-\phi_z)\{(1-\phi_w)+\phi_w \frac{\rho_{p_1}}{\rho_f}\}]+\phi_z \frac{\rho_{p_2}}{\rho_f}} \left(1+\frac{1}{\beta}\right) \left(\frac{(z_2)_j-(z_2)_{j-1}}{h}\right) \right] \\
&- h \left[\left(\frac{(f_j + f_{j-1})((z_2)_j + (z_2)_{j-1})}{4} \right) \right] \\
&- h \left[A \left(\frac{\left((z_1)_j + (z_1)_{j-1}\right)}{4} \right)^2 \right] \\
&+ h \left[A \left(\eta \frac{((z_2)_j + (z_2)_{j-1})}{4} \right) \right] \\
&+ h \left[\frac{\phi_4}{\phi_z} M \left(\frac{(z_1)_j + (z_1)_{j-1}}{2} \right) \right],
\end{aligned} \tag{6.42}$$

$$\begin{aligned}
(r_5)_{j-\frac{1}{2}} = -h &\left[\left(\frac{((z_3)_j - (z_3)_{j-1})}{h} \right) \left(1 + \frac{1}{\phi_5} P_r N_r \right) \right] \\
&- h P_r \frac{\kappa_f}{\kappa_{hnf}} \left((1-\phi_z)\{(1-\phi_w) + \phi_w \frac{(\rho C_p)_{p_1}}{(\rho C_p)_f}\} + \frac{\phi_z (\rho C_p)_{p_2}}{(\rho C_p)_f} \right) \\
&\left[\left(\frac{(f_j + f_{j-1})((z_3)_j + (z_3)_{j-1})}{4} \right) \right] \\
&+ h P_r \frac{\kappa_f}{\kappa_{hnf}} \left((1-\phi_z)\{(1-\phi_w) + \phi_w \frac{(\rho C_p)_{p_1}}{(\rho C_p)_f}\} + \frac{\phi_z (\rho C_p)_{p_2}}{(\rho C_p)_f} \right) \\
&\left[\left(\frac{((z_3)_j + (z_3)_{j-1})(u_j + u_{j-1})}{4} \right) \right] \\
&+ A h P_r \frac{\kappa_f}{\kappa_{hnf}} \left((1-\phi_z)\{(1-\phi_w) + \phi_w \frac{(\rho C_p)_{p_1}}{(\rho C_p)_f}\} + \frac{\phi_z (\rho C_p)_{p_2}}{(\rho C_p)_f} \right) \\
&\left[\left(\frac{\theta_j + \theta_{j-1}}{2} \right) \right]
\end{aligned} \tag{6.43}$$

$$+AhP_r\frac{\kappa_f}{\kappa_{hnf}}\left((1-\phi_z)\{(1-\phi_w)+\phi_w\frac{(\rho C_p)_{p1}}{(\rho C_p)_f}\}+\frac{\phi_z(\rho C_p)_{p2}}{(\rho C_p)_f}\right)$$
$$\eta\left[\left(\frac{(z_3)_j+(z_3)_{j-1}}{4}\right)\right]$$
$$+\vartheta hP_r\frac{\kappa_f}{\kappa_{hnf}}\left((1-\phi_z)\{(1-\phi_w)+\phi_w\frac{(\rho C_p)_{p1}}{(\rho C_p)_f}\}+\frac{\phi_z(\rho C_p)_{p2}}{(\rho C_p)_f}\right)$$
$$\left[\left(\frac{f_j+f_{j-1}}{2}\right)^2\left(\frac{(z_3)_j-(z_3)_{j-1}}{h}\right)\right]$$
$$+\vartheta hP_r\frac{\kappa_f}{\kappa_{hnf}}\left((1-\phi_z)\{(1-\phi_w)+\phi_w\frac{(\rho C_p)_{p1}}{(\rho C_p)_f}\}+\frac{\phi_z(\rho C_p)_{p2}}{(\rho C_p)_f}\right)$$
$$\left[\left(\frac{f_j+f_{j-1}}{2}\right)\left(\frac{(z_1)_j+(z_1)_{j-1}}{2}\right)\left(\frac{(z_3)_j+(z_3)_{j-1}}{2}\right)\right]. \tag{6.44}$$

Using the similarity process the boundary conditions becomes

$$\varepsilon f_0=0,\quad \varepsilon(z_1)_0=0,\quad \varepsilon(z_3)_0=0,\quad \varepsilon(z_1)_J=0,\quad \varepsilon\theta_J=0. \tag{6.45}$$

The system of linear equations in (6.34)-(6.38) can be written in the matrix form

$$R\varepsilon=p, \tag{6.46}$$

where

$$R=\begin{bmatrix} A_1 & C_1 & & & & \\ B_2 & A_2 & C_2 & & & \\ & \ddots & \ddots & \ddots & & \\ & & \ddots & \ddots & \ddots & \\ & & & B_{J-1} & A_{J-1} & C_{J-1} \\ & & & & B_J & A_J \end{bmatrix},\quad \varepsilon=\begin{bmatrix}\varepsilon_1\\ \varepsilon_2\\ \vdots\\ \varepsilon_{j-1}\\ \varepsilon_j\end{bmatrix},\quad p=\begin{bmatrix}(r_1)_{j-\frac{1}{2}}\\ (r_2)_{j-\frac{1}{2}}\\ \vdots\\ (r_{J-1})_{j-\frac{1}{2}}\\ (r_J)_{j-\frac{1}{2}}\end{bmatrix}. \tag{6.47}$$

Here R represents the $J\times J$ block tridiagonal matrix with block size of 5×5 and ε and p are column vectors of order $J\times 1$. In order to solve a linear system for ε the LU factorization technique can be utilized.

The desired physical quantities for the present model are the skin-friction coefficient (C_f) and the local Nusselt number (Nu_x) which are defined in equations (2.106) and (2.103). The τ_w and q_w are wall shear stress and wall heat flux for the present model are given as (see for example, Shit and Mandal [197])

$$\tau_w = \mu_{hnf}\left(1+\frac{1}{\beta}\right)\left(\frac{\partial u}{\partial y}\right)_{y=0}, \quad q_w = -k_{hnf}\left(1+\frac{16}{3}\frac{\sigma^*\Theta_\infty^3}{\kappa^*\nu_f(\rho C_p)_f}\right)\left(\frac{\partial \Theta}{\partial y}\right)_{y=0}, \tag{6.48}$$

using τ_w in (3.90) for C_f,

$$C_f = \frac{\mu_{hnf}\left(1+\frac{1}{\beta}\right)\left(\frac{\partial u}{\partial y}\right)_{y=0}}{\rho_f U_w^2}, \tag{6.49}$$

using (3.19) in (6.49)

$$C_f = \frac{\mu_f}{\rho_f \phi_a}\frac{x f''(0) b^{3/2}}{\nu_f(1-\xi t)^{3/2}}\left(1+\frac{1}{\beta}\right)\left(\frac{(1-\xi t)^{3/2}}{bx}^2\right), \tag{6.50}$$

$$C_f = \left(1+\frac{1}{\beta}\right)\frac{\sqrt{\nu_f}}{\phi_a}\sqrt{\frac{1}{U_w x}}f''(0), \tag{6.51}$$

$$C_f = \left(1+\frac{1}{\beta}\right)\frac{1}{\sqrt{Re_x}}f''(0)\frac{1}{\phi_a}, \tag{6.52}$$

$$C_f\sqrt{Re_x} = \left(1+\frac{1}{\beta}\right)\frac{f''(0)}{\phi_a}, \tag{6.53}$$

using equation (6.75) in (6.53), we get

$$C_f Re_x^{\frac{1}{2}} = \left(1+\frac{1}{\beta}\right)\frac{f''(0)}{(1-\phi_w)^{2.5}(1-\phi_z)^{2.5}}. \tag{6.54}$$

Using q_w in (3.90) for Nu_x,

$$Nu_x = \frac{x}{k_f(\Theta_w-\Theta_\infty)}\left(-k_{hnf}\left(1+\frac{16}{3}\frac{\sigma^*\Theta_\infty^3}{\kappa^*\nu_f(\rho C_p)_f}\right)\left(\frac{\partial \Theta}{\partial y}\right)_{y=0}\right), \tag{6.55}$$

using (3.33) in (6.55)

$$Nu_x = -\frac{k_{hnf}}{k_f}(1+N_r)\left(\frac{bx}{(1-\xi t)}\theta'(0)\sqrt{\frac{b}{\nu_f(1-\xi t)}}\right), \tag{6.56}$$

$$Nu_x = -\frac{k_{hnf}}{k_f}(1+N_r)\left(\sqrt{Re_x}\right)\theta'(0), \tag{6.57}$$

$$Nu_x Re_x^{-\frac{1}{2}} = -\frac{k_{hnf}}{k_f}(1+N_r)\,\theta'(0). \tag{6.58}$$

6.4 Entropy Generation Analysis

The entropy generation for the present mathematical model is given by (see for example Das *et al.* [167])

$$\begin{aligned} E_G = \frac{k_{hnf}}{\Theta_\infty^2}\left\{\left(\frac{\partial \Theta}{\partial y}\right)^2 + \frac{16}{3}\frac{\sigma^*\Theta_\infty^3}{\kappa^*\nu_f(\rho C_p)_f}\left(\frac{\partial \Theta}{\partial y}\right)^2\right\} + \frac{\mu_{hnf}}{\Theta_\infty}\left(\frac{\partial u}{\partial y}\right)^2\left(1+\frac{1}{\beta}\right) \\ + \frac{\sigma_{hnf}B^2(t)u^2}{\Theta_\infty}. \end{aligned} \tag{6.59}$$

The first term in entropy equation represents the heat transfer irreversibility, second term is the fluid friction and the third term is represents the magnetohydrodynamic effects. The entropy generation is represented by N_G and is given in equation (3.104). Further using equations (3.12)-(3.13), we can obtain the non-dimensional equation of entropy as follows Now putting (6.59) in (3.104), we get

$$\begin{aligned} N_G = \frac{\Theta_\infty^2 b^2}{k_f\left(\Theta_w - \Theta_\infty\right)^2}\frac{k_{hnf}}{\Theta_\infty^2}\left\{\left(\frac{\partial \Theta}{\partial y}\right)^2 + \frac{16}{3}\frac{\sigma^*\Theta_\infty^3}{\kappa^*\nu_f(\rho C_p)_f}\left(\frac{\partial \Theta}{\partial y}\right)^2\right\} + \\ \frac{\mu_{hnf}}{\Theta_\infty}\left(\frac{\partial u}{\partial y}\right)^2\left(1+\frac{1}{\beta}\right) + \frac{\sigma_{hnf}B^2(t)u^2}{\Theta_\infty}. \end{aligned} \tag{6.60}$$

Consider first term of equation (6.60),

$$\frac{\Theta_\infty^2 b^2}{k_f\left(\Theta_w - \Theta_\infty\right)^2}\frac{k_{hnf}}{\Theta_\infty^2}\left\{(1+N_r)\left(\frac{\partial \Theta}{\partial y}\right)^2\right\}, \tag{6.61}$$

using equation (3.33), we get

$$= \frac{\Theta_\infty^2 b^2}{k_f\left(\Theta_w - \Theta_\infty\right)^2}\frac{k_f\phi_e}{\Theta_\infty^2}\left\{(1+N_r)\left(\frac{(bx)^2}{(1-\xi t)}^2\theta'(\eta)^2\frac{b}{\nu_f(1-\xi t)}\right)\right\}, \tag{6.62}$$

$$\frac{\Theta_\infty^2 b^2}{k_f\left(\Theta_w - \Theta_\infty\right)^2}\frac{k_{hnf}}{\Theta_\infty^2}\left\{(1+N_r)\left(\frac{\partial \Theta}{\partial y}\right)^2\right\} = \frac{b^2}{k_f x}\left(\frac{bx}{(1-\xi t)}\right)\frac{\theta'^2}{\nu_f}\phi_e, \tag{6.63}$$

$$\frac{\Theta_\infty^2 b^2}{k_f\left(\Theta_w-\Theta_\infty\right)^2}\frac{k_{hnf}}{\Theta_\infty^2}\left\{(1+N_r)\left(\frac{\partial\Theta}{\partial y}\right)^2\right\}=\frac{b^2}{\nu_f x}U_w\left(1+N_r\right)\frac{\theta'^2}{\phi_e}, \tag{6.64}$$

$$\frac{\Theta_\infty^2 b^2}{k_f\left(\Theta_w-\Theta_\infty\right)^2}\frac{k_{hnf}}{\Theta_\infty^2}\left\{(1+N_r)\left(\frac{\partial\Theta}{\partial y}\right)^2\right\}=R_e\left(1+N_r\right)\frac{\theta'^2}{\phi_e}. \tag{6.65}$$

Consider second term of equation (6.60),

$$\frac{\mu_{hnf}}{\Theta_\infty}\left(\frac{\partial u}{\partial y}\right)^2\left(1+\frac{1}{\beta}\right), \tag{6.66}$$

using equation (3.19), we get

$$\frac{\mu_{hnf}}{\Theta_\infty}\left(\frac{\partial u}{\partial y}\right)^2\left(1+\frac{1}{\beta}\right)=\frac{\mu_{hnf}}{\Theta_\infty}\left(\frac{bxf''(\eta)}{(1-\xi t)}\sqrt{\frac{b}{\nu_f(1-\xi t)}}\right)^2\left(1+\frac{1}{\beta}\right), \tag{6.67}$$

$$\frac{\mu_{hnf}}{\Theta_\infty}\left(\frac{\partial u}{\partial y}\right)^2\left(1+\frac{1}{\beta}\right)=R_e\left(\frac{Br}{\Omega\phi_a}\right)f''^2\left(1+\frac{1}{\beta}\right). \tag{6.68}$$

Consider third term of equation (6.60),

$$\frac{\sigma_{hnf}B^2(t)u^2}{\Theta_\infty}, \tag{6.69}$$

$$\frac{\sigma_{hnf}B^2(t)u^2}{\Theta_\infty}=\frac{\Theta_\infty^2 b^2}{k_f\left(\Theta_w-\Theta_\infty\right)^2}\left(\frac{\sigma_{hnf}B^2(t)u^2}{\Theta_\infty}\right), \tag{6.70}$$

using equation (3.14), we get

$$\frac{\sigma_{hnf}B^2(t)u^2}{\Theta_\infty}=\frac{\Theta_\infty^2 b^2}{k_f\left(\Theta_w-\Theta_\infty\right)^2}\left(\left(\frac{\sigma_f\phi_d}{\Theta_\infty}\right)\left(\frac{B_o^2}{1-\xi t}\right)\left(\frac{bx}{1-\xi t}\right)^2 f'^2\right), \tag{6.71}$$

$$\frac{\sigma_{hnf}B^2(t)u^2}{\Theta_\infty}=\frac{\phi_d B_r}{\Omega}M^2 R_e f'^2. \tag{6.72}$$

Substituting the equation (6.65), (6.68) and (6.72) in (6.60), we get

$$N_G=R_e\left(1+N_r\right)\theta'^2\phi_e+R_e\left(\frac{B_r}{\Omega\phi_a}\right)\left(1+\frac{1}{\beta}\right)f''^2+R_e\frac{\phi_d B_r}{\Omega}M^2 f'^2, \tag{6.73}$$

$$N_G=R_e\left[\phi_e(1+N_r)\theta'^2+\frac{1}{\phi_a}\frac{B_r}{\Omega}\left\{(f''^2)\left(1+\frac{1}{\beta}\right)+\phi_a\phi_d M f'^2\right\}\right], \tag{6.74}$$

where

$$\phi_a=\left[(1-\phi_w)^{2.5}(1-\phi_z)^{2.5}\right], \tag{6.75}$$

$$\phi_c = \left[(1-\phi_z)\{(1-\phi_w)+\phi_w\frac{(\rho C_p)_{p_1}}{(\rho C_p)_f}\}+\phi_z\frac{(\rho C_p)_{p_2}}{(\rho C_p)_f}\right], \tag{6.76}$$

$$\phi_d = \left[1+\frac{3(\frac{\phi_w\sigma_{p_1}+\phi_z\sigma_{p_2}}{\sigma_f}-(\phi_w+\phi_z))}{(\frac{\phi_w\sigma_{p_1}+\phi_2\sigma_{p_2}}{(\phi_w+\phi_z)\sigma_f}+2)-(\frac{\phi_w\sigma_{p_1}+\phi_z\sigma_{p_2}}{\sigma_f}-(\phi_w+\phi_z))}\right]. \tag{6.77}$$

$$\begin{aligned}\phi_e = &\left[\frac{(\kappa_{p_2}+(m-1)\kappa_{nf})-(m-1)\phi_z(\kappa_{nf}-\kappa_{p_2})}{(\kappa_{p_2}+(m-1)\kappa_{nf})+\phi_z(\kappa_{nf}-\kappa_{p_2})}\right]\\ &\left[\frac{(\kappa_{p_1}+(m-1)\kappa_f)+\phi_w(\kappa_f-\kappa_{p_1})}{(\kappa_{p_1}+(m-1)\kappa_f)-(m-1)\phi_w(\kappa_f-\kappa_{p_1})}\right].\end{aligned} \tag{6.78}$$

$$\begin{aligned}N_G = &R_e\left(\frac{\kappa_{hnf}}{\kappa_f}(1+N_r)\theta'^2\right)+\frac{1}{(1-\phi_w)^{2.5}(1-\phi_z)^{2.5}}\frac{B_rR_e}{\Omega}\left(f''^2\left(1+\frac{1}{\beta}\right)\right)+\\ &\frac{B_rR_e}{\Omega}\left(\left[1+\frac{3(\frac{\phi_w\sigma_{p_1}+\phi_z\sigma_{p_2}}{\sigma_f}-(\phi_w+\phi_z))}{(\frac{\phi_w\sigma_{p_1}+\phi_2\sigma_{p_2}}{(\phi_w+\phi_z)\sigma_f}+2)-(\frac{\phi_w\sigma_{p_1}+\phi_z\sigma_{p_2}}{\sigma_f}-(\phi_w+\phi_z))}\right]Mf'^2\right),\end{aligned} \tag{6.79}$$

where

$$R_e = \frac{U_wb^2}{\nu_f x}, \qquad B_r = \frac{\mu_f U_w^2}{k_f\left(\Theta_w-\Theta_\infty\right)}, \qquad \Omega = \frac{\Theta_w-\Theta_\infty}{\Theta_\infty}. \tag{6.80}$$

are the Reynolds number, Brinkman number and the dimensional less temperature gradient, respectively.

6.5 Numerical Results and Discussion

The numerical results are obtained for the Copper oxide-Ethylene glycol (CuO-EG) conventional Casson nanofluid and the Titanium-Copper oxide/Ethylene glycol (TiO_2-CuO/EG) Casson hybrid nanofluid. Results are presented graphically with focus on the main features of the mathematical model. In addition to these Table 6.2 showed the velocity gradient and heat transfer rate at the surface of the boundary. The discussion is based on the fluid motion and temperature variation in the boundary layer and comparison is also drawn on the behavior of conventional and hybrid nanofluids.

6.5.1 Effect of Magnetic Parameter M

The magnetic effects on the fluids motion, temperature distribution and entropy generation are depicted in Figures 6.2-6.4. The graphs present the numerical results for both conventional and hybrid nanofluids. The velocity of nanofluids reduced with increasing uniformly distributed transverse magnetic field of strength. The interaction of electrically conducting nanofluids with the applied transverse magnetic field generates a resistive force known as Lorentz force.

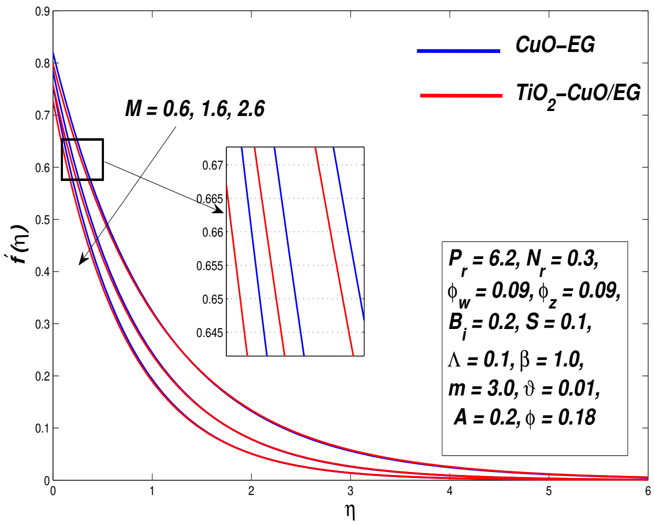

FIGURE 6.2: Velocity Distribution against the Parameter M

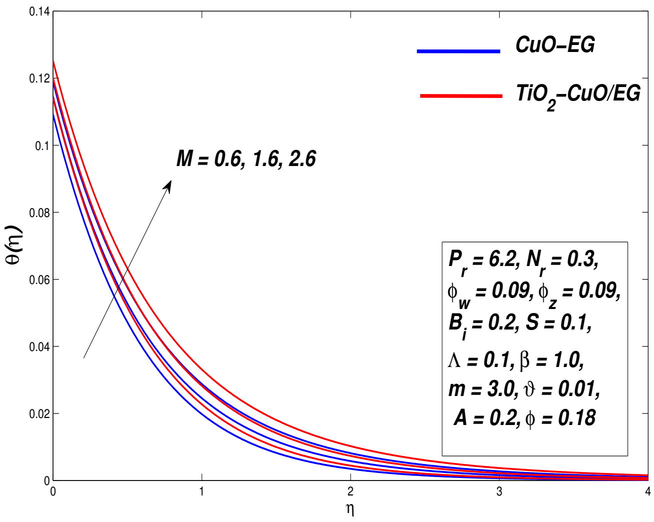

FIGURE 6.3: Temperature Distribution against the Parameter M

Moreover, the strength of Lorentz force rises with raising strength of applied magnetic field and counteracts the fluid motion within the boundary layer and reduces the thickening level of momentum boundary layer. The decreasing trend in fluid velocity is observed for both conventional and hybrid nanofluids. In Figure 6.3, the temperature of nanofluids rises with increasing strength of parameter M and therefore increases the thickening level of thermal boundary layer. It is observed that the parameter M is inversely proportional to the density of nanofluid, therefore the increase in M decrease the density and, as a result the temperature of the fluid rises. The increase in nanofluid temperature within the boundary layer decreases the heat transfer rate at the boundary. The influence of Lorentz force at the boundary is presented in Table 6.2. The skin friction coefficient increases but the heat transfer rate decreases with increasing magnetic field. Figure 6.4 demonstrated the entropy distribution of thermal system increases with increasing strength of magnetic parameter M. The increase in entropy increases the irreversibility of the thermal process and less energy is available to do work.

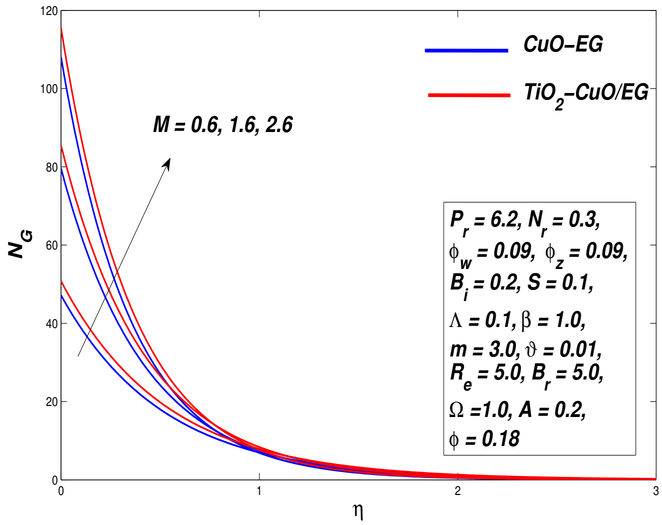

FIGURE 6.4: Entropy Generation Distribution against the Parameter M

6.5.2 Effect of Nanoparticle Volume Fraction Parameters ϕ and ϕ_{hnf}

The effects of nanoparticle volume fraction parameter ϕ of conventional Casson nanofluid and ϕ_{hnf} of hybrid Casson nanofluid are plotted in Figures 6.5-6.7. In Figures 6.5-6.7 ϕ_w is fixed at 0.09 and analysis is carried out by assuming different values of volume fraction parameter ϕ_z. It is observed that nanofluids velocity decreases and the temperature increases with increasing values of parameter ϕ and ϕ_{hnf}, respectively. The parameter

ϕ and ϕ_{hnf} correspond to volume of solid particles in the basefluid. It is well known solid particles have higher thermal conductivity than fluids, therefore increase in ϕ and ϕ_{hnf} reduces fluid velocity as observed from Figure 6.5 and enhances its temperature in the boundary layer region.

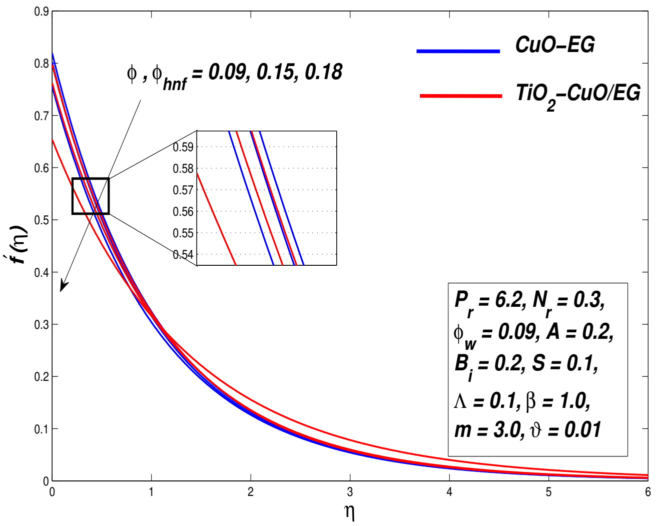

FIGURE 6.5: Velocity Distribution against the Parameter ϕ, ϕ_{hnf}

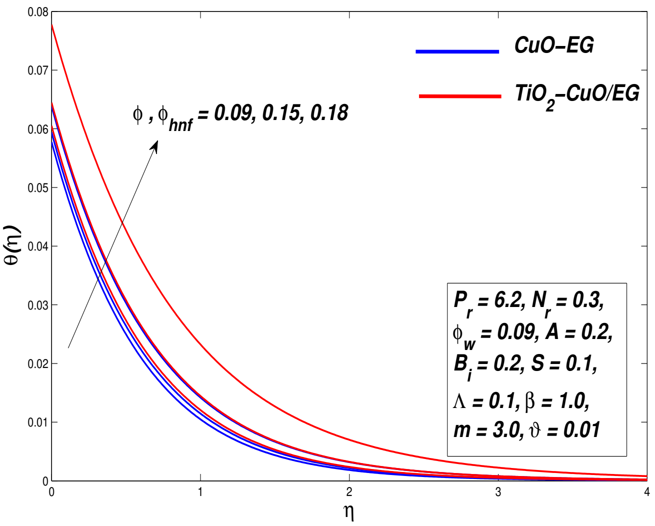

FIGURE 6.6: Temp Distribution against the Parameter ϕ, ϕ_{hnf}

Whereas, this fact is very much evident in Figure 6.6 that the increase in the total thermal conductivity of nanofluids increases the temperature and the thickening level of thermal boundary layer. Moreover, the collision among nanoparticles dissipate heat energy in the system and increases the overall temperature. It is visualized the temperature of hybrid nanofluid rises at a faster rate when compared with conventional nanofluids. Figure 6.7 illustrated the entropy increases for lager values of nanoparticle volume fraction parameters.

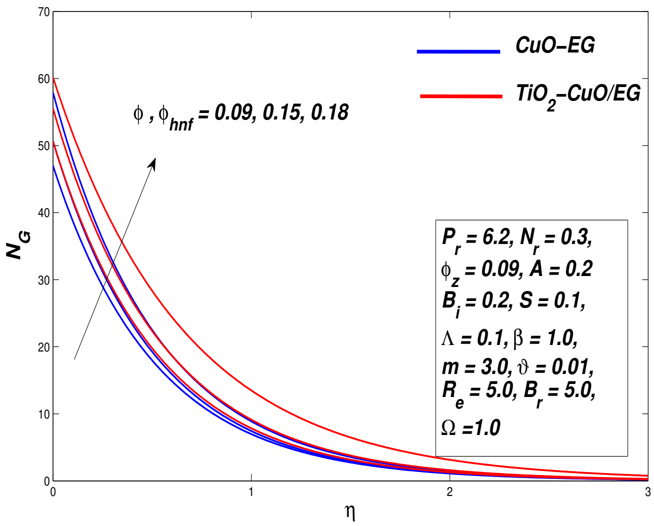

FIGURE 6.7: Entropy Generation Distribution against the Parameter ϕ, ϕ_{hnf}

6.5.3 Effect of Velocity Slip Parameter Λ

Figures 6.8-6.10 demonstrated that the positive values of slip parameter Λ reduces fluid

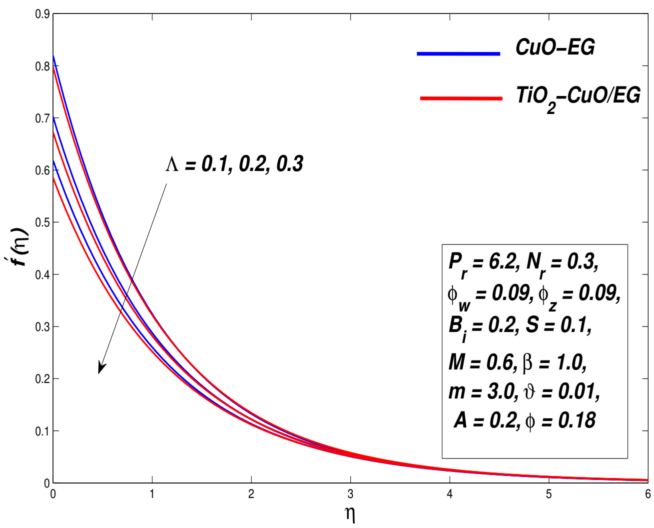

FIGURE 6.8: Velocity Distribution against the Parameter Λ

movement and entropy generation of Casson hybrid nanofluids. Whereas the temperature of Casson hybrid nanofluids increases with increasing values of parameter Λ. In Figure 6.8 the decrease in velocity is consistent with the fact that slip velocity retards the motion of the boundary surface.

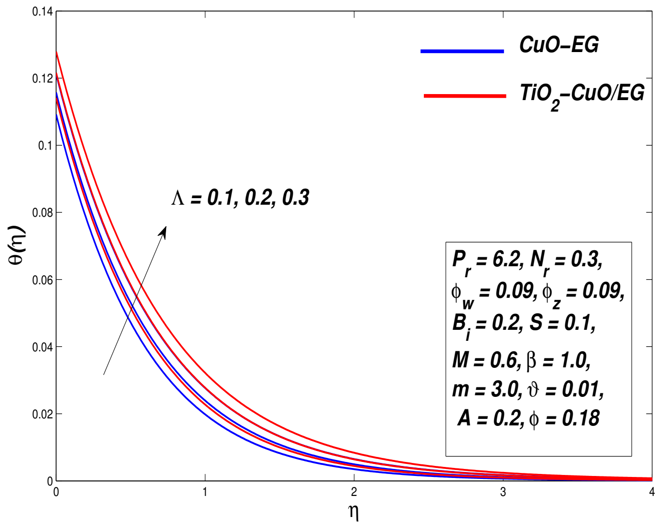

FIGURE 6.9: Temperature Distribution against the Parameter Λ

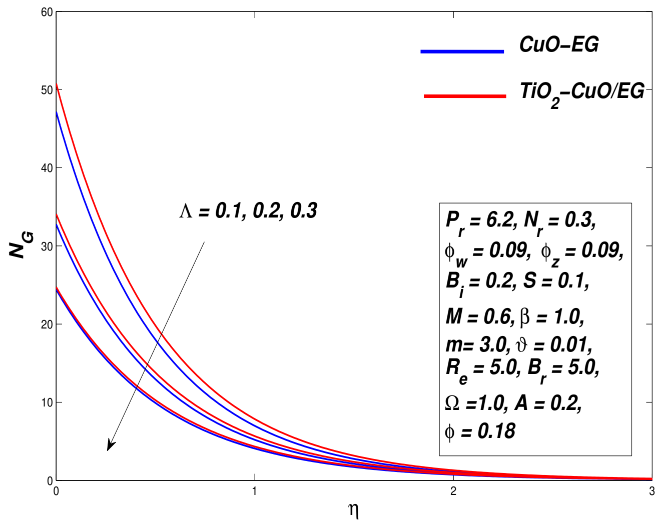

FIGURE 6.10: Entropy Generation Distribution against the Parameter Λ

In other words, velocity slip act opposite to stretching pull of the surface and resists its transmission to the fluid. As a result, momentum boundary layer decreases with rise in parameter Λ. Figure 6.9 depicted the temperature distribution within the boundary layer against the parameter Λ. The velocity slip is inversely proportional to the temperature distribution and an increase in the parameter Λ increases the thermal boundary layer thickness and reduces the Nusselt number. Table 6.2 shows that positive increase in velocity slip leads to decrease in velocity gradient and heat transfer rate for both CuO-EG and TiO_2-CuO/EG nanofluids. This expected behaviour is due to the fact that the boundary slip reduces the friction at the solid-fluid interface and consequently the rate of heat transfer. From Figure 6.10 it can be observed easily that the entropy decreases with increasing values of Λ. The decrease in entropy indicates that the system is cooling down. If the entropy in the boundary layer decreases, it must increase by the same amount outside the boundary layer.

6.5.4 Effect of the Thermal Radiation Parameter N_r and Biot Number B_i

There are no effects of thermal radiation parameter N_r and Biot number B_i on velocity profiles of conventional and hybrid Casson nanofluids. Figures 6.11-6.14 displayed plots for nanofluids temperature and entropy distribution within boundary layer with variation in thermal radiation parameter N_r and Biot number B_i, respectively. The temperature of both conventional and hybrid nanofluids increases with increasing values of thermal radiation parameter N_r and Biot number B_i see Figures 6.11 and 6.13.

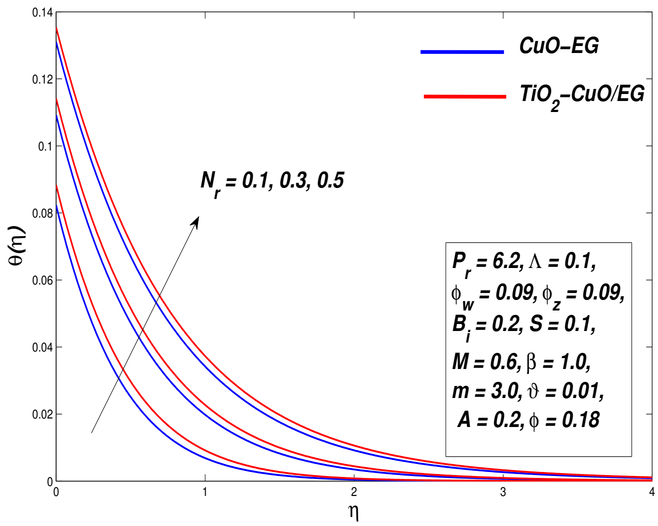

FIGURE 6.11: Temperature Distribution against the Parameter N_r

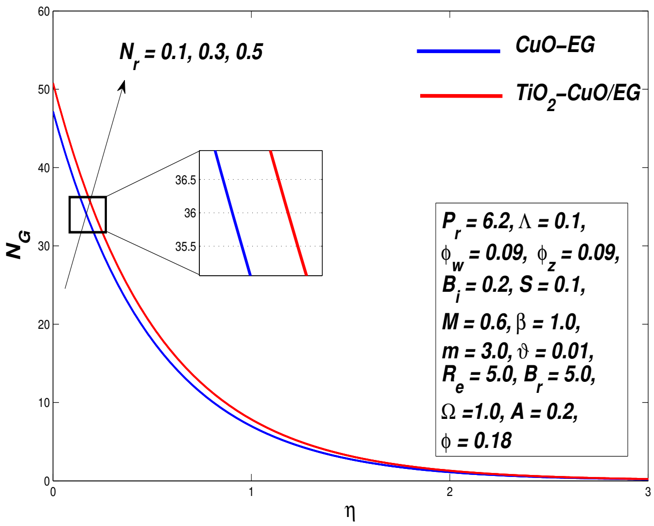

FIGURE 6.12: Entropy Generation Distribution against the Parameter N_r

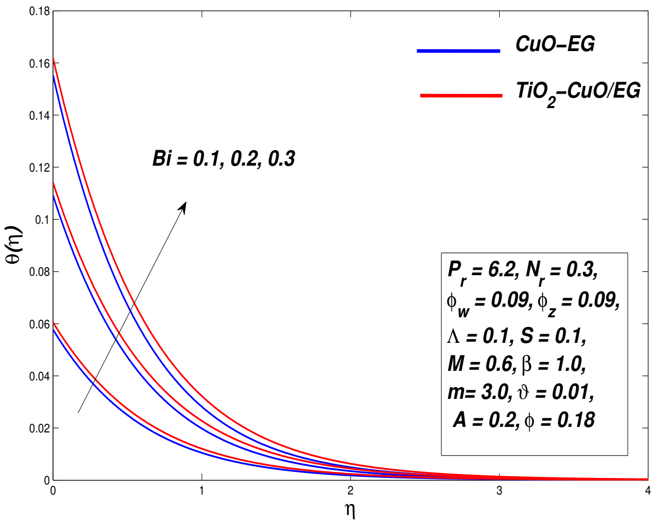

FIGURE 6.13: Temperature Distribution against the Parameter B_i

Physically speaking, the strengthening of parameter N_r transfer more heat into the fluid and raise the thickening level of thermal boundary layer. The Biot number or the sheet convection parameter showed the ratio of conduction inside the fluid to the convection at its surface. Increasing sheet convection parameter means that the heat transfer through conduction dominates the convection coefficient at the surface of the fluid The increase in B_i showed that the hot fluid within boundary layer heat the stretching surface and raise the temperature of the thermal system. Thus, increase in parameters N_r and B_i is directly related to boost in the Nusselt number at the boundary. Figures 6.12 and 6.14 depicted the increase in entropy with raise in thermal radiation parameter N_r and Biot number B_i, respectively. In Figures 6.12 and 6.14 the crossover point for the entropy profile is estimated at about $\eta = 0.3$. Before this behaviour the entropy is enhanced and then it begins to fall. In other words the thermal process is converging towards the case of reversible process.

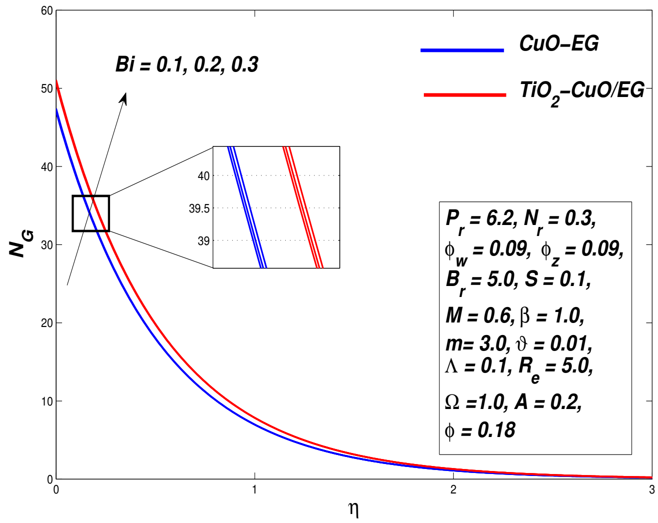

FIGURE 6.14: Entropy Generation Distribution against the Parameter B_i

6.5.5 Effect of Nanoparticle Shapes Parameter m

Figure 6.15 depicted the effect of different nanoparticles shapes (sphere, hexahedron, tetrahedron, cylinder, and lamina) on the heat transfer characteristics of CuO-EG conventional Casson nanofluid and $TiO_2 - CuO/EG$ hybrid Casson nanofluids at nanoparticle concentration $\phi_w = 0.09$ and $\phi_z = 0.09$, respectively. The Figure 6.15 showed the non-dimensional temperature of nanofluids rises with increase in shape factor parameter m. Dimensionless temperature at the boundary is lowest for the spherical shaped nanoparticles followed by hexahedron, tetrahedron, cylinder and lamina shapes. The spherical shaped nanoparticles tend to drag more heat from the boundary due to its greatest surface area while this effect is less evident for other nanoparticles. This is the main reason for the greatest heat exchange rate at the boundary for the nanofluids with spherical shaped nanoparticles. This fact is also observed from the variation in Nusselt number given in Table 6.2. Figure 6.16 showed the entropy of the system increases with increase in parameter m. The entropy of the system increases at slowest rate for the spherical shaped nanoparticles.

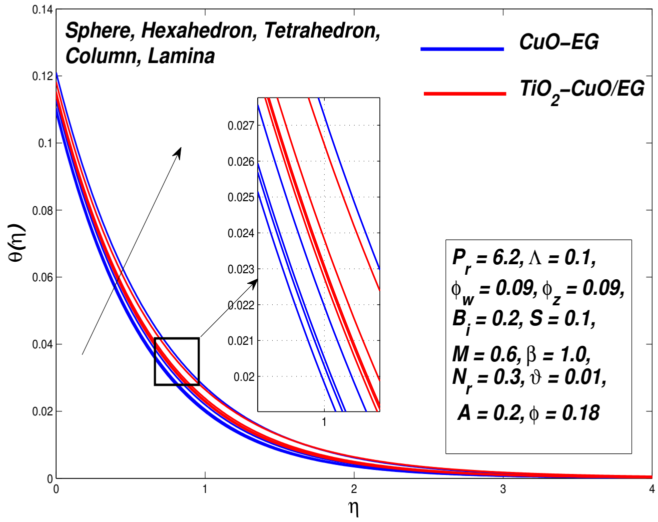

FIGURE 6.15: Temperature Distribution against the Parameter m

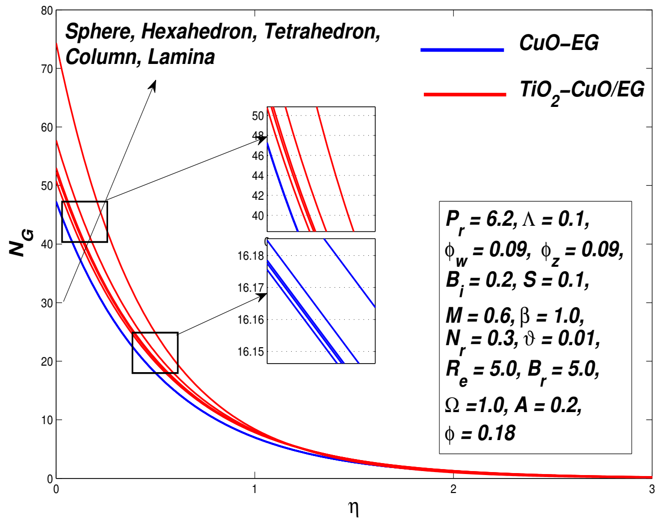

FIGURE 6.16: Entropy Generation Distribution against the Parameter m

6.5.6 Effect of Reynolds Number R_e and the Brinkman Number B_r

The impact of Reynolds number R_e and Brinkman number B_r on entropy generation profiles are presented in this section. Numerical computations showed the higher values of R_e increases entropy which physically means that the inertial forces dominate the viscous effects see Figure 6.17. Figure 6.18 discussed the influence of B_r on the entropy. It is found that the Brinkman number augmentation increases the entropy generation.

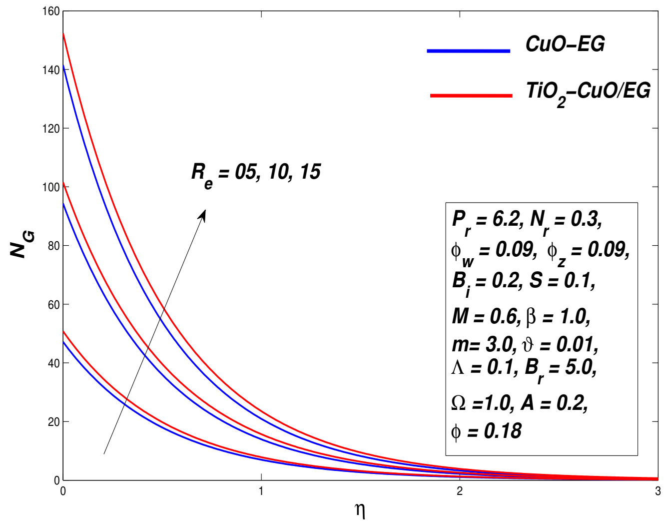

FIGURE 6.17: Entropy Generation Distribution against the Parameter R_e

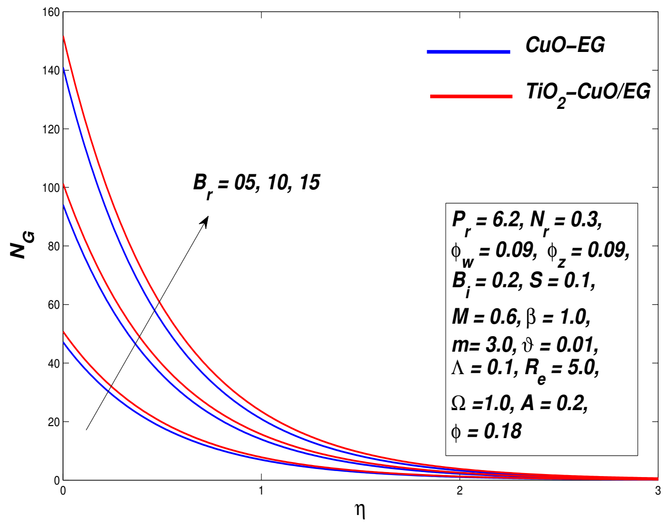

FIGURE 6.18: Entropy Generation Distribution against the Parameter B_r

This is due to the fact that Brinkman number is the ratio of heat dissipation to the conduction at the surface so increasing the values of B_r means more heat is dissipated compared with the conduction of heat at the surface, which results in an increase in the entropy.

6.5.7 Effect of Magnetic Parameter M and Radiation Parameter N_r on Skin Friction C_f and the Nusselt Number Nu_x, Respectively

The effects of magnetic parameter M and radiation parameter N_r on skin friction coefficient C_f and Nusselt number Nu_x profiles of CuO-EG and $CuO - TiO_2$/EG non-Newtonian hybrid nanofluids are presented in Figures 6.19-6.20, respectively.

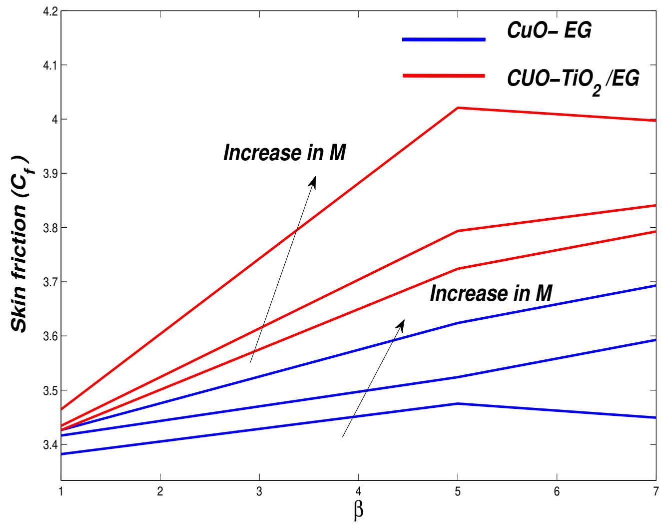

FIGURE 6.19: Skin Friction C_f against the Parameter β

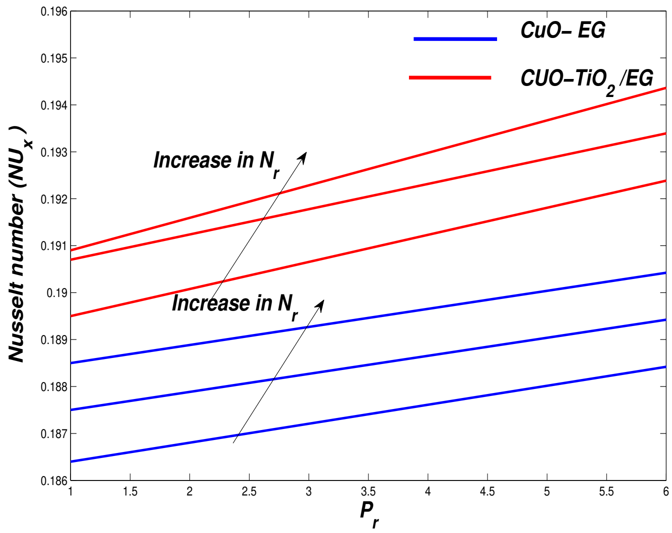

FIGURE 6.20: Nusselt Number Nu_x against the Parameter P_r

In 6.19 computations are performed for $M = 0.6, 0.8, 1.2$ whereas the parameter β takes the values $1.0, 5.0, 10.0$. It is noted when we increase the magnetic parameter M the skin friction coefficient C_f increases. The physical reason behind this is that greater M is responsible for greater friction between the surface and the fluid as a result skin friction increases. In 6.19 computations are performed for $N_r = 0.2, 0.4, 0.9$ whereas the prandtle number P_r is fixed on $1.0, 6.2, 7.38$. It is observed when we increase the radiation parameter N_r the rate of convective heat transfer (Nusselt number) increases. This is due to the fact that a greater heat flux is generated, which results in a greater heat transfer rate.

β	A	M	ϕ	ϕ_z	Λ	ξ	N_r	B_i	$C_f Re_x^{\frac{1}{2}}$ CuO-EG	$C_f Re_x^{\frac{1}{2}}$ TiO_2- CuO/EG	$N_u Re_x^{\frac{-1}{2}}$ CuO-EG	$N_u Re_x^{\frac{-1}{2}}$ TiO_2- CuO/EG
1.0	0.2	0.6	0.18	0.09	0.1	0.01	0.3	0.2	1.1719	1.2564	0.1307	0.1312
5.0									0.9460	1.0157	0.1292	0.1299
10.0									0.9118	0.9791	0.1289	0.1296
	0.2								1.1719	1.2564	0.1307	0.1312
	0.6								1.2386	1.4910	0.1340	0.1382
	1.6								1.3896	1.6321	0.1384	0.1409
		0.6							1.1719	1.2564	0.1307	0.1312
		1.6							1.5055	1.6088	0.1283	0.1290
		2.6							1.7526	1.8692	0.1267	0.1273
			0.09						0.1953	-	1.0857	-
			0.15						1.0328	-	1.1163	-
			0.18						1.1719	-	1.2564	-
				0.0					-	0.1039	-	0.1098
				0.06					-	0.1221	-	0.1289
				0.09					-	0.1307	-	0.1312
					0.1				1.1719	1.2564	0.1307	0.1312
					0.2				1.0314	1.0964	0.1297	0.1301
					0.3				0.9235	0.9751	0.1288	0.1292
						0.01			1.1719	1.2564	0.1307	0.1312
						0.2			1.1719	1.2564	0.1309	0.1314
						0.4			1.1719	1.2564	0.1310	0.1316
							0.1		1.1719	1.3907	0.1154	0.1157
							0.3		1.1719	1.3907	0.1307	0.1312
							0.5		1.1719	1.3907	0.1454	0.1157
								0.1	1.1719	1.2564	0.0713	0.0714
								0.2	1.1719	1.2564	0.1307	0.1312
								0.3	1.1719	1.2564	0.1810	0.1820

TABLE 6.1: Values of Skin Friction $= C_f Re_x^{\frac{1}{2}}$ and Nusselt Number $= N_u Re_x^{\frac{-1}{2}}$ for $P_r = 6.2$ and $m = 3$.

6.6 Conclusions

A computational analysis of heat transfer and entropy generation for boundary layer flow of conventional and hybrid Casson nanofluids in the presence of Cattaneo-Christov heat flux model is carried out in the present research. The electrically conducting nanofluid occupies the space over a porous non-uniform stretching surface with uniformly distributed transverse magnetic field of strength applied normal to the flow. The Keller box numerical technique is utilized to approximate the solutions for the velocity, temperature and the entropy distributions, velocity gradient and the rate of heat exchange of the $CuO-EG$ and TiO_2-CuO/EG nanofluids. The main findings of the present research are:

- The temperature of hybrid Casson nanofluid TiO_2-CuO/EG rises at the faster rate when compared with the conventional Casson nanofluid *CuO-EG*.

- On the basis of numerical results, the hybrid Casson nanofluid TiO_2-CuO/EG is observed to be a better thermal conductor than the conventional Casson nanofluid *CuO-EG*.

- A stronger magnetic field has a negative impact on the motion of the fluid particles in the boundary layer and the velocity of the fluid reduces with growing strength of magnetic field.

- It is well known fact that the inclusion of solid nanoparticles in the ordinary fluids increases the overall thermal conductivity of hybrid and conventional nanofluids. Therefore the increase in ϕ and ϕ_{hnf} decrease in thickness of momentum and increase the thickness of thermal boundary layer respectively.

- The heat transfer rate is greater for the smaller number of shape factor m in the boundary layer.

- Lamina-shaped particles result in the greatest temperature in the boundary layer while the lowest temperature are observed in case of spherical shaped nanoparticles.

- Entropy of the thermal system is seen to rise with rise in Casson parameter, unsteadiness parameter, magnetic parameter, nanoparticle volumetric concentration parameter, thermal radiation parameter, Brinkman number and Reynolds number but reduces with the rise in velocity slip parameter.

Chapter 7

Conclusion and Future Work

7.1 Conclusion

In this thesis, we studied the flow, heat transfer and entropy generation for thermal system containing non-Newtonian nanofluids. Nanofluids have countless applications in fields like biomedical devices, tumor treatment, solar collectors, nuclear reactor, crystal growth, heat exchangers and cooling radiators etc. Extensive research on the flow and heat transfer characteristics of nanofluids is undertaken considering different flow geometries, boundary conditions, external effects and surface motion. In general the addition of nanoparticles in the Newtonian base fluid changes the behavior of the fluids to non-Newtonian. However, it depend on the concentration of nanoparticles in the base fluid, nanoparticles shape, nanoparticles size and the interaction between them. Therefore non-Newtonian models will lead to superior understanding of flow and heat transfer of nanofluids. Keeping above in view this thesis aims to understand the non-Newtonian nanofluids flow, heat transfer and entropy generation along with variable thermophyiscal properties. The physical model considered in the present research includes the flat porous surface. The nanofluid occupies the space over the surface. The flow is generated by the non-uniform stretching of the surface. Three non-Newtonian models namely i.e. Maxwell fluid model, Powell-Eyring fluid model and Casson fluid model are considered for the nanofluids. The main fundamental equations are attained from the law of conservation of mass, momentum and energy are then transformed into the system of coupled nonlinear ODEs by means of appropriate similarity transformation. The ODEs are then solved by an efficient numerical finite difference technique known as Keller box method. Numerical results are also presented in the form of graphs and tables showing the effects of physical parameters such as non-Newtonian parameters, porous medium parameter, nanoparticle volume concentration parameter, velocity slip parameter, thermal radiation parameter, mass transfer parameter, Biot number, Reynolds number and Brinkman number on the physical behaviour of the non-dimensional quantities such as velocity, temperature and entropy generation. The entire study can be concluded with the following observations.

- The velocity profiles decreases with an increasing values of non-Newtonian parameter and declines the thickness of momentum boundary layer. The decreasing trend in velocity profiles is due to increase of resistance in fluid and also corresponds to increase in skin friction coefficient (velocity gradient) at the boundary.

- A stronger magnetic field has a negative impact on the motion of the fluid particles in the boundary layer and the velocity of the fluid reduces with growing strength of magnetic field.

- It is well known fact that the inclusion of solid nanoparticles in the ordinary fluids increases the overall thermal conductivity of hybrid and conventional nanofluids. Therefore the increase in ϕ and ϕ_{hnf} decrease in thickness of momentum and increase the thickness of thermal boundary layer respectively.

- The heat transfer rate is greater for the smaller number of shape factor in the boundary layer.

- Lamina-shaped particles results in the greatest temperature in the boundary layer while the lowest temperature are observed in case of spherical shaped nanoparticles.

- The cross over point is observed in the entropy profile for increase in Biot number, variable thermal conductivity and thermal radiation parameter. Whereas the opposite behavior in entropy profiles are observed for increases Reynolds number and velocity slip parameter.

- The material parameters presented opposite behaviour on entropy generation profile. The irreversibility of the system is maximum at the boundary and reduces to zero far away from the boundary of the surface.

- Spherical shaped nanoparticles have the lowest rate of entropy generation.

- For the present study, $Cu - H_2O$ nanofluid is detected as a superior thermal conductor than $TiO_2 - H_2O$ nanofluid.

- The Cu-methanol based nanofluid is observed as a better thermal conductor than Fe_3O_4-methanol based nanofluid.

- On the basis of numerical results, the hybrid Casson nanofluid $TiO_2 - CuO/EG$ is observed to be a better thermal conductor than the conventional Casson nanofluid *CuO-EG*.

- The temperature of hybrid Casson nanofluid $TiO_2 - CuO/EG$ rises at the faster rate when compared with the conventional Casson nanofluid *CuO-EG*.

7.1.1 Future Work

The study of heat transfer characteristics of nanofluids including effects of variable thermophyiscal properties and non-Newtonian fluids models is still in its initial phase. There is a lot of work to be done in this area, for example, the comparison among different non-Newtonian fluid models to find the most efficient nanofluids for thermal systems (in particular for the thermal solar systems). In future, mathematical models presented in this thesis can be extended in direction focusing on the areas:-

- The flow geometry can be considered in the form of a disk or cylinder to further increase the applications of the present research.

- The temperature dependent viscosity and density can be added to analyze the flow, heat and mass transfer characteristics.

- Second grade, Williamson, Carreau and Micropolar nanofluids models can be explored for MHD, porous medium, thermal radiation, Joule heating, buoyancy, Soret-Dufour, chemical reactions, internal heat generation, ion-slip, Hall and induced magnetic field effects etc.

Bibliography

[1] J. Dick, "Rubber technology compounding and testing for performance," *Hanser Publications Cincinnati, Edition 2*, USA, 2009.

[2] F. Wallenberger and P. Bingham, "Fiberglass and glass technology," *Springer-Verlag US, Edition 1*, USA, 2010.

[3] Hossein and A. Makhlouf, "Industrial applications for intelligent polymers and coatings," *Springer, International Publishing, Edition 1*, Switzerland, 2016.

[4] L. Prandtl, "On fluid motions with very small friction," *International Mathathematics Kongr Heidelberg, Auch*, vol. 6, pp. 484–491, 1904.

[5] O. Makinde and O. Onyejekwe, "A numerical study of MHD generalized Couette flow and heat transfer with variable viscosity and electrical conductivity," *Journal of Magnetism and Magnetic Materials*, vol. 323, pp. 2757–2763, 2011.

[6] S. Ibrahim and O. Makinde, "Chemically reacting magnetohydrodynamics MHD boundary layer flow of heat and mass transfer past a low-heat-resistant sheet moving vertically downwards," *Scientific Research and Essays*, vol. 22, pp. 4762–4775, 2011.

[7] O. Makinde, "Entropy analysis for MHD boundary layer flow and heat transfer over a flat plate with a convective surface boundary condition," *International Journal of Exergy*, vol. 10, pp. 142–154, 2012.

[8] O. Makinde, K. Zimba, and O. Beg, "Numerical study of chemically-reacting hydromagnetic boundary layer flow with soret/dufour effects and a convective surface boundary condition," *International Journal of Thermal and Environmental Engineering*, vol. 4, pp. 89–98, 2012.

[9] S. Liao, "On the analytic solution of magnetohydrodynamic flows of non-Newtonian fluids over a stretching sheet," *Journal of Fluid Mechanics*, vol. 488, pp. 189–212, 2003.

[10] S. Liao and H. Xu, "Series solutions of unsteady magnetohydrodynamic flows of non-Newtonian fluids caused by an impulsively stretching plate," *Journal of Non-Newtonian Fluid Mechanics*, vol. 129, pp. 46–55, 2005.

[11] S. Liao, "A new branch of solutions of boundary layer flows over an impermeable stretched plate," *International Journal of Heat and Mass Transfer*, vol. 48, pp. 2529–2539, 2005.

[12] M. Guedda and H. Zakia, "Similarity flow solutions of a non-Newtonian Power-law fluid," *International Journal of Nonlinear Science*, vol. 35, pp. 255–264, 2008.

[13] M. Abel, P. Siddheshwar, and M. Nandeppanavar, "Heat transfer in a viscoelastic boundary layer flow over a stretching sheet with viscous dissipation and non-uniform heat source," *International Journal of Heat and Mass Transfer*, vol. 50, pp. 960–966, 2007.

[14] M. Sajid and T. Hayat, "Influence of thermal radiation on the boundary layer flow due to an exponentially stretching sheet," *International Communications in Heat and Mass Transfer*, vol. 35, pp. 347–356, 2008.

[15] R. Cortell, "Effects of viscous dissipation and radiation on the thermal boundary layer over a nonlinearly stretching sheet," *Physics Letters A*, vol. 28, pp. 631–636, 2008.

[16] C. Chen, "Effects of magnetic field and suction/injection on convection heat transfer of non-Newtonian Power-law fluids past a Power-law stretched sheet with surface heat flux," *International Journal of Thermal Sciences*, vol. 47, pp. 954–961, 2008.

[17] A. Postelnicu and I. Pop, "Falkner–Skan boundary layer flow of a Power-law fluid past a stretching wedge," *Applied Mathematics and Computation*, vol. 217, pp. 4359–4368, 2011.

[18] T. Hayat, R. saif, R. Ellahi, T. Muhammad, and A. Alsaedi, "Simultaneous effects of melting heat and internal heat generation in stagnation point flow of Jeffrey

fluid towards a nonlinear stretching surface with variable thickness," *International Journal of Thermal Sciences*, vol. 132, pp. 344–354, 2018.

[19] R. Kumar, G. Kumar, C. Raju, S. Shehzad, and S. Varma, "Analysis of arrhenius activation energy in magnetohydrodynamic Carreau fluid flow through improved theory of heat diffusion and binary chemical reaction," *Journal of Physics Communications*, vol. 2, 2018.

[20] E. Elbashbeshy, "Heat transfer over an exponentially stretching continuous surface with suction," *Archives of Mechanics*, vol. 53, pp. 643–651, 2001.

[21] E. Sanjayanand and K. Khan, "On heat and mass transfer in a viscoelastic boundary layer flow over an exponentially stretching sheet," *International Journal of Thermal Sciences*, vol. 45, pp. 819–828, 2006.

[22] E. Magyari and B. Keller, "Heat and mass transfer in the boundary layers on an exponentially stretching continuous surface," *Journal of Physics*, vol. 32, pp. 577–585, 1999.

[23] P. Carragher and L. Crane, "Heat transfer on a continuous stretching sheet," *ZAMM - Journal of Applied Mathematics and Mechanics*, vol. 62, pp. 564–565, 1982.

[24] H. Anderssonl, J. Aarseth, and B. Dandapat, "Heat transfer in MHD viscoelastic fluid flow over a stretching sheet with variable thermal conductivity, non-uniform heat source and radiation," *International Journal of Heat and Mass Transfer*, vol. 43, pp. 69–74, 2000.

[25] M. Abel, K. Khan, and V. Prasada, "Study of visco-elastic fluid flow and heat transfer over a stretching sheet with variable viscosity," *International Journal of Non-Linear Mechanics*, vol. 37, pp. 81–88, 2002.

[26] P. Siddheshwar and U. Mahabaleswar, "Effects of radiation and heat source on MHD flow of a viscoelastic liquid and heat transfer over a stretching sheet," *International Journal of Non-Linear Mechanics*, vol. 40, pp. 807–820, 2005.

[27] R. Cortell, "A note on flow and heat transfer of a viscoelastic fluid over a stretching sheet," *International Journal of Non-Linear Mechanics*, vol. 41, pp. 78–85, 2006.

[28] M. Abel and N. Mahesha, “Heat transfer in MHD viscoelastic fluid flow over a stretching sheet with variable thermal conductivity, non-uniform heat source and radiation,” *Applied Mathematical Modelling*, vol. 32, pp. 1965–1983, 2008.

[29] Y. Lin, L. Zheng, X. Zhang, and G. Chen, “MHD pseudo-plastic nanofluid unsteady flow and heat transfer in a finite thin film over stretching surface with internal heat generation,” *International Journal of Heat and Mass Transfer*, vol. 84, pp. 903–911, 2015.

[30] N. Akbar, A. Ebaid, and Z. Khan, “Numerical analysis of magnetic field effects on Eyring-Powell fluid flow towards a stretching sheet,” *Journal of Magnetism and Magnetic Materials*, vol. 382, pp. 355–358, 2015.

[31] M. Waqas, M. Farooq, M. Khan, A. Alsaedi, T. Hayat, and T. Yasmeen, “Magnetohydrodynamic (MHD) mixed convection flow of micropolar liquid due to nonlinear stretched sheet with convective condition,” *International Journal of Heat and Mass Transfer*, vol. 102, pp. 766–772, 2016.

[32] A. Majeed, A. Zeeshan, S. Almari, and R. Ellahi, “Heat transfer analysis in ferromagnetic viscoelastic fluid flow over a stretching sheet with suction,” *Neural Computing and Applicationsr*, vol. 6, pp. 1947–1955, 2018.

[33] S. Ghadikolaei, K. Hosseinzadeh, M. Yassari, H. Sadeghi, and D. Ganji, “Analytical and numerical solution of non-Newtonian second-grade fluid flow on a stretching sheet,” *Thermal Science and Engineering Progress*, vol. 5, pp. 309–316, 2018.

[34] S. Choi, “Enhancing thermal conductivity of fluids with nanoparticles,” *ASME International Mechanical Engineering Congress and Exposition*, vol. 66, pp. 99–105, 1995.

[35] N. Kumar and V. Devadas, “A household-based analysis of domestic energy consumption for lighting in jaipur city,” *International journal of built environment and sustainability*, 2016.

[36] H. Gupta, G. Agrawal, and M. J, “A new media towards green environment,” *International Journal of Environmental Sciences*, vol. 3, 2012.

[37] K. Sreelakshmy, S. Aswathy, K. Vidhya, T. Saranya, and S. CN, "An overview of recent nanofluid research," *International Research Journal of Pharmacy*, vol. 128, pp. 49–56, 2013.

[38] W. Chamsa, S. Brundavanam, C. Fung, D. Fawcett, and G. Poinern, "Nanofluid types, their synthesis, properties and incorporation in direct solar thermal collectors: a review," *Nanomaterials*, vol. 07, 2017.

[39] J. Eastman, S. Choi, S. Li, W. Yu, and L. Thompson, "Anomalously increases effective thermal conductvities of ethylene glycol-bases nanofluids containing copper nanoparticles," *Applied Physics Letters*, vol. 78, 2001.

[40] X. Wang, X. Xu, and S. Choi, "Thermal conductivity of nanoparticles-fluid mixture," *Journal of Thermophysics and Heat Transfer*, vol. 13, 1999.

[41] P. Keblinski, S. Phillpot, S. Choi, and J. Eastman, "Mechanisms of heat flow in suspensions of nano-sized particles (nanofluids)," *International Journal of Heat and Mass Transfer*, vol. 45, pp. 855–863, 2002.

[42] J. Buongiorno, "Convective transport in nanofluids," *Journal of Heat Transfer*, vol. 28, pp. 240–250, 2006.

[43] A. Rahmati, O. Akbari, A. Marzban, R. karimi, and F. Pourfattah, "Simultaneous investigations the effects of non-Newtonian nanofluid flow in different volume fractions of solid nanoparticles with slip and no-slip boundary conditions," *Thermal Science and Engineering Progress*, vol. 5, pp. 263–277, 2018.

[44] A. Arabpour, D. Toghraie, and O. Akbari, "Investigation into the effects of slip boundary condition on nanofluid flow in a double-layer microchannel," *Journal of Thermal Analysis and Calorimetry*, vol. 131, pp. 2975–2991, 2018.

[45] O. Koriko, I. Animasaun, M. Reddy, and N. Sandeep, "Scrutinization of thermal stratification, nonlinear thermal radiation and quartic autocatalytic chemical reaction effects on the flow of three-dimensional Eyring-Powell Alumina-water nanofluid," *Multidiscipline Modeling in Materials and Structures*, vol. 14, pp. 261–283, 2018.

[46] I. Tlili, W. Khan, and I. Khan, "Multiple slips effects on MHD $SA - Al_2O_3$ and $SA - Cu$ non-Newtonian nanofluids flow over a stretching cylinder in porous

medium with radiation and chemical reaction," *Results in Physics*, vol. 08, pp. 213–222, 2018.

[47] P. Barnoon and D. Toghraie, "Numerical investigation of laminar flow and heat transfer of non-Newtonian nanofluid within a porous medium," *Powder Technology*, vol. 325, pp. 78–91, 2018.

[48] M. Sheikholeslami, "CuO-water nanofluid flow due to magnetic field inside a porous media considering Brownian motion," *Journal of Molecular Liquids*, vol. 249, pp. 921–929, 2018.

[49] M. Sheikholeslami, A. Zeeshan, and A. Majeed, "Control volume based finite element simulation of magnetic nanofluid flow and heat transport in non-Darcy medium," *Journal of Molecular Liquids*, vol. 268, pp. 354–364, 2018.

[50] P. Nagarajan, J. Subramani, S. Suyambazhahan, and R. Sathyamurthy, "Nanofluids for solar collector applications: A Review," *The 6th International Conference on Applied Energy ICAE, Energy Procedia*, vol. 61, pp. 2416–2434, 2004.

[51] S. Kalogirou, "Solar thermal collectors and applications," *Progress in Energy and Combustion Science*, vol. 30, pp. 231–295, 2004.

[52] E. Bellos, C. Tzivanidis, K. Antonopoulos, and G. Gkinis, "Thermal enhancement of solar parabolic trough collectors by using nanofluids and converging-diverging absorber tube," *Renewable Energy*, vol. 94, pp. 213–222, 2016.

[53] H. Chaji, Y. Ajabshirchi, E. Esmaeilzadeh, S. Heris, M. Hedayatizadeh, and M. Kahani, "Experimental study on thermal efficiency of flat plate solar collector using TiO_2-water nanofluid," *Modern Applied Science*, vol. 7, 2013.

[54] S. Ghasemi and G. Ahangar, "Numerical analysis of performance of solar parabolic trough collector with Cu-water nanofluid," *International Journal of Nano Dimension*, vol. 05, pp. 233–240, 2014.

[55] K. Sharma and L. Kundan, "Nanofluid based concentrating parabolic solar collector (NBCPSC): A new alternative," *International Journal of Research in Mechanical Engineering and Technology*, vol. 04, pp. 2249–5762, 2014.

[56] Y. Tong, J. Kim, and H. Cho, "Effects of thermal performance of enclosed-type evacuated U-tube solar collector with multi-walled carbon nanotube/water nanofluid," *Renewable Energy*, vol. 83, pp. 463–473, 2015.

[57] H. Kim, J. Ham, C. Park, and H. Cho, "Theoretical investigation of the efficiency of a U-tube solar collector using various nanofluids," *Energy*, vol. 94, pp. 497–507, 2016.

[58] M. Muhammad, I. Muhammad, N. Sidik, and A. Yazid, "Thermal performance enhancement of flat-plate and evacuated tube solar collectors using nanofluid: A review," *International Communications in Heat and Mass Transfer*, vol. 76, pp. 06–15, 2016.

[59] J. Subramani, P. Nagarajan, S. Wongwises, S. El-Agouz, and R. Sathyamurthya, "Experimental study on the thermal performance and heat transfer characteristics of solar parabolic trough collector using Al_2O_3 nanofluids," *Environmental Progress and Sustainable Energy*, 2017.

[60] A. Allouhi, M. Amine, R. Saidu, T. Kousksou, and A. Jamila, "Energy and exergy analyses of a parabolic trough collector operated with nanofluids for medium and high temperature applications," *Energy Conversion and Management*, vol. 155, pp. 201–217, 2018.

[61] P. Salazar, K. Nigam, and C. Solorio, "Heat transfer model for thermal performance analysis of parabolic trough solar collectors using nanofluids," *Renewable Energy*, vol. 125, pp. 334–343, 2018.

[62] A. Kasaiean, M. Sameti, R. Daneshazarian, Z. Noori, A. Adamian, and T. Ming, "Heat transfer network for a parabolic trough collector as a heat collecting element using nanofluid," *Renewable Energy*, vol. 123, pp. 439–449, 2018.

[63] G. Keeffe, S. Mitchell, T. Myers, and V. Cregan, "Modelling the efficiency of a nanofluid-based direct absorption parabolic trough solar collector," *Solar Energy*, vol. 159, pp. 44–54, 2018.

[64] M. Sheremet, I. Pop, and O. Mahiand, "Natural convection in an inclined cavity with time-periodic temperature boundary conditions using nanofluids: Application

in solar collectors," *International Journal of Heat and Mass Transfer*, vol. 116, pp. 751–761, 2018.

[65] J. Pakhare, H. Pandey, M. Selvam, and C. Jawahar, "Experimental performance evaluation of a parabolic solar dish collector with nanofluid," *Concentrated Solar Thermal Energy Technologies*, pp. 115–123, 2018.

[66] M. Siavashi, K. Ghasemi, R. Yousofvand, and S. Derakhshan, "Computational analysis of SWCNH nanofluid-based direct absorption solar collector with a metal sheet," *Solar Energy*, vol. 170, pp. 252–262, 2018.

[67] Y. Gan, H. Ong, T. Ling, N. Zulkifli, C. Wang, and Y. Yang, "Thermal conductivity optimization and entropy generation analysis of titanium dioxide nanofluid in evacuated tube solar collector," *Applied Thermal Engineering*, vol. 145, pp. 155–164, 2018.

[68] A. Sharafeldin and G. Grf, "Evacuated tube solar collector performance using CeO_2/water nanofluid," *Journal of Cleaner Production*, vol. 185, pp. 347–356, 2018.

[69] H. Alfven, "Flow past a stretching plate," *Existence of electromagnetic-hydrodynamic waves*, vol. 150, pp. 405–406, 1942.

[70] A. Hakeem, N. Ganesh, and B. Ganga, "Magnetic field effect on second order slip flow of nanofluid over a stretching/shrinking sheet with thermal radiation effect," *Journal of Magnetism and Magnetic Materials*, vol. 381, 2015.

[71] K. Hsiao, "Micropolar nanofluid flow with MHD and viscous dissipation effects towards a stretching sheet with multimedia feature," *International Journal of Heat and Mass Transfer*, vol. 112, pp. 983–990, 2017.

[72] S. Qayyum, T. Hayat, and A. Alsaedi, "Thermal radiation and heat generation/absorption aspects in third grade magnetonanofluid over a slendering stretching sheet with Newtonian conditions," *Physica B: Physics of Condensed Matter*, 2018.

[73] M. Khan, M. Malik, T. Salahuddin, and A. Hussian, "Heat and mass transfer of Williamson nanofluid flow yield by an inclined Lorentz force over a nonlinear stretching sheet," *Results in Physics*, vol. 08, pp. 862–868, 2018.

[74] M. Eid, K. Mahny, T. Muhammad, and M. Sheifleslami, "Numerical treatment for Carreau nanofluid flow over a porous nonlinear stretching surface," *Results in Physics*, vol. 08, pp. 1185–1139, 2018.

[75] Y. Kho, A. Hussanan, N. Sarif, Z. Ismail, and M. Salleh, "Thermal radiation effects on MHD with flow heat and mass transfer in Casson nanofluid over a stretching sheet," *MATEC Web of Conferences*, vol. 150, 2018.

[76] M. Sheikholeslami, H. Ashorynejad, D. Ganji, and A. Kolahdooz, "Investigation of rotating MHD viscous flow and heat transfer between stretching and porous surfaces using analytical method," *Mathematical Problems in Engineering*, 2011.

[77] P. Kundu, T. Chakraborty, and K. Das, "Framing the Cattaneo–Christov heat flux phenomena on CNT- based Maxwell nanofluid along stretching sheet with multiple slips," *Arabian Journal for Science and Engineering*, vol. 43, pp. 1177–1188, 2017.

[78] N. Balazadeh, M. Sheikholeslamia, D. Ganji, and Z. Li, "Mathematical model for thermal and entropy analysis of thermal solar collectors by using Maxwell nanofluids with slip conditions, thermal radiation and variable thermal conductivity," *Journal of Molecular Liquids*, vol. 260, pp. 130–136, 2018.

[79] Hashim, M. Khan, and A. Hamid, "Numerical investigation on time-dependent flow of Williamson nanofluid along with heat and mass transfer characteristics past a wedge geometry," *International Journal of Heat and Mass Transfer*, vol. 118, pp. 480–491, 2018.

[80] S. Ghadikolaei, K. Hosseinzadeh, D. Ganji, and M. Hatami, "Fe_3O_4–$(CH_2OH)_2$ nanofluid analysis in a porous medium under MHD radiative boundary layer and dusty fluid," *Journal of Molecular Liquids*, vol. 258, pp. 172–185, 2018.

[81] F. Selimefendigil and H. Ztop, "MHD natural convection and entropy generation in a nanofluid-filled cavity with a conductive partition," *Exergetic, Energetic and Environmental Dimensions*, vol. 01, pp. 763–778, 2018.

[82] S. Qayyum, T. Hayat, S. Shezad, and A. Alsaedi, "Mixed convection and heat generation/absorption aspects in MHD flow of tangent-hyperbolic nanoliquid with Newtonian heat/mass transfer," *Radiation Physics and Chemistry*, vol. 144, pp. 396–404, 2018.

[83] H. Sajjadi, A. Delouei, M. Atashafrooz, and M. Sheikholeslami, "Double MRT Lattice Boltzman simulation of 3-D MHD natural convection in a cubic cavity with sinusoidal temperature distribution utilizing nanofluid," *International Journal of Heat and Mass Transfer*, vol. 126, pp. 489–503, 2018.

[84] M. Elias, M. Miqdad, I. Mahbubul, R. Saidur, Kamalisarvestani, M. Sohel, A. Hepbasli, N. Rahima, and M. Amalina, "Effect of nanoparticle shape on the heat transfer and thermodynamic performance of a shell and tube heat exchanger," *International Journal of Heat and Mass Transfer*, vol. 44, pp. 93–99, 2013.

[85] O. Mahian, A. Kianifar, S. Heris, and Wongwises, "First and second laws analysis of a minichannel-based solar collector using boehmite alumina nanofluids: Effects of nanoparticle shape and tube materials," *International Journal of Heat and Mass Transfer*, vol. 78, pp. 1166–1176, 2014.

[86] R. Ellahi, M. Hassan, A. Zeeshan, and A. Khan, "The shape effects of nanoparticles suspended in HFE-7100 over wedge with entropy generation and mixed convection," *Applied Nanoscience*, vol. 06, pp. 641–651, 2016.

[87] M. Sheikholeslami and M. Bhatti, "Forced convection of nanofluid in presence of constant magnetic field considering shape effects of nanoparticles," *International Journal of Heat and Mass Transfer*, vol. 11, pp. 1039–1049, 2017.

[88] X. Xu and S. Chen, "Cattaneo-Christov heat flux model for heat transfer of marangoni boundary layer flow in a copper-water nanofluid," *WILEY*, vol. 7, 2017.

[89] M. Sheikholeslami, "Magnetic field influence on $Cu - H_2O$ nanofluid convective flow in a permeable cavity considering various shapes for nanoparticles," *International Journal of Hydrogen Energy*, 2017.

[90] M. Tausif, D. Das, and P. kundu, "Presence of different shapes of Z_rO_2 nanoparticles in the melting heat transfer of a casson flow," *The European Physical Journal Plus*, vol. 132, 2017.

[91] M. Shen, S. Chen, and F. Liu, "Unsteady MHD flow and heat transfer of fractional Maxwell viscoelastic nanofluid with Cattaneo heat flux and different particle shapes," *Chinese Journal of Physics*, vol. 56, pp. 1199–1211, 2018.

[92] M. Hatami, M. Jafaryar, and D. Jing, "Investigation of engines radiator heat recovery using different shapes of nanoparticles in $H_2O/(CH_2OH)_2$ based nanofluids," *International Journal of Hydrogen Energy*, vol. 42, pp. 10 891–10 900, 2017.

[93] U. Khan, N. Ahmed, and T. Din, "Analysis of magnetohydrodynamic flow and heat transfer of Cu–water nanofluid between parallel plates for different shapes of nanoparticles," *Neural Computing and Applications*, vol. 29, pp. 695–703, 2018.

[94] M. Sheikholeslami and D. Ganji, "Influence of electric field on Fe_3O_4- water nanofluid radiative and convective heat transfer in a permeable enclosure," *Journal of Molecular Liquids*, vol. 250, pp. 404–412, 2018.

[95] V. Mikkola, S. Puupponen, H. Granbohm, K. Saari, T. Nissila, and A. Seppl, "Influence of particle properties on convective heat transfer of nanofluids," *International Journal of Thermal Sciences*, vol. 124, pp. 187–195, 2018.

[96] F. Selimefendigil, "Natural convection in a trapezoidal cavity with an inner conductive object of different shapes and filled with nanofluids of different nanoparticle shapes," *Iranian Journal of Science and Technology*, vol. 42, pp. 169–184, 2018.

[97] A. Dogonchil, F. Selimefendigil, and D. Ganji, "Magneto-hydrodynamic natural convection of CuO-water nanofluid in complex shaped enclosure considering various nanoparticle shapes," *International Journal of Numerical Methods for Heat and Fluid Flow*, 2018.

[98] S. Suresh, K. Venkitaraj, P. Selvakumar, and M. Chandrasekar, "Experimental investigation of mixed convection with synthesis of $Al_2O_3 - water$ hybrid nanofluids using two step method and its thermo physical properties," *Colloids Surface*, vol. 08, pp. 41–48, 2011.

[99] S. Devi and S. Devi, "Numerical investigation on three dimensional hybrid $Cu - Al_2O_3/water$ nanofluid flow over a stretching sheet with effecting Lorentz force subject to Newtonian heatings," *Canadian Journal of Physics*, vol. 94, pp. 490–496, 2016.

[100] M. Afrand, D. Toghraie, and B. Ruhani, "Effects of temperature and nanoparticles concentration on rheological behavior of $Fe_3O_4 - Ag/EG$ hybrid nanofluid: An

experimental study." *Experimental Thermal and Fluid Science*, vol. 77, pp. 38–44, 2016.

[101] T. Hayat and S. Nadeem, "Heat transfer enhancement with Ag-CuO/water hybrid nanofluid," *Results in Physics*, vol. 7, pp. 2317–2324, 2017.

[102] S. Ghadikolaei, M. Yassari, k. Hosseinzadeh, and D. Ganji, "Investigation on thermophysical properties of $TiO_2 - Cu/H_2O$ hybrid nanofluid transport dependent on shape factor in MHD stagnation point flow," *Powder Technolgy*, vol. 322, pp. 428–438, 2017.

[103] S. Hussain, S. Ahmed, and T. Akbar, "Investigation on thermophysical properties of $TiO_2 - Cu/H_2O$ hybrid nanofluid transport dependent on shape factor in MHD stagnation point flow," *International Journal of Heat and Mass Transfer*, vol. 114, pp. 1054–1066, 2017.

[104] S. Suresh, K. Venkitaraj, P. Selvakumar, and M. Chandrasekar, "Effect of $Al_2O_3 - water$ hybrid nanofluid in heat transfer," *Experimental Thermal and Fluid Science*, vol. 08, pp. 54–60, 2012.

[105] G. Momin, "Experimental investigation of mixed convection with $Al_2O_3 - water$ and hybrid nanofluid in inclined tube for laminar flow," *International Journal of Scientific Research in Science*, 2013.

[106] M. Prakash and S. Devi, "Hydromagnetic hybrid $Al_2O_3 - Cu$ / water nanofluid flow over a slendering stretching sheet with prescribed surface temperature," *Asian Journal of Humanities and Social Sciences*, vol. 06, pp. 1921–1936, 2016.

[107] M. Bahiraei and N. Mazaheri, "Application of a novel hybrid nanofluid containing grapheme-platinum nanoparticles in a chaotic twisted geometry for utilization in miniature devices thermal and energy efficiency considerations," *International Journal of Mechanical Sciences*, vol. 138, pp. 337–349, 2018.

[108] A. Akhgar and D. Toghraie, "An experimental study on the stability and thermal conductivity of water-ethylene glycol/TiO_2-MWCNTs hybrid nanofluid: Developing a new correlation," *Powder Technology*, vol. 338, pp. 806–818, 2018.

[109] G. Moldoveanu, GM andHuminic, A. Minea, and A. Huminic, "Experimental study on thermal conductivity of stabilized Al_2O_3 and SiO_2 nanofluids and their

hybrid," *International Journal of Heat and Mass Transfer*, vol. 127, pp. 450–457, 2018.

[110] A. Bejan, "The method of thermodynamic optimization of finite-size systems and finite-time processes," *CRC Press: Boca Raton, FL, USA*, 1995.

[111] J. Qing, M. Bhatti, M. Abbas, M. Rashidi, and M. Ali, "Entropy generation on MHD Casson nanofluid flow over a porous stretching/shrinking surface," *Entropy*, vol. 18, 2016.

[112] M. Bhatti, T. Abbas, M. Rashidi, M. Ali, and Z. Yang, "Entropy generation on MHD Eyring-Powell nanofluid through a permeable stretching surface," *Entropy*, vol. 18, 2017.

[113] A. Shahzad, R. Ali, M. Hussian, and M. Kamran, "Unsteady axisymmetric flow and heat transfer over time dependent radially stretching sheet," *Alexandria Engineering Journal*, vol. 56, pp. 35–41, 2017.

[114] M. Mehrali, E. Sadeghinezhad, A. Akhiani, S. Latibari, H. Metselaar, A. Kherbeet, and M. Mehrali, "Heat transfer and entropy generation analysis of hybrid graphene/Fe_3O_4 ferro-nanofluid flow under the influence of a magnetic field," *Powder Technology*, vol. 308, pp. 149–157, 2017.

[115] H. Sithole, H. Mondal, and P. Sibanda, "Entropy generation in a second grade magnetohydrodynamic nanofluid flow over a convectively heated stretching sheet with nonlinear thermal radiation and viscous dissipation," *Results in Physics*, vol. 09, pp. 1077–1085, 2018.

[116] N. Akbar, M. Raza, and R. Ellahi, "Peristaltic flow with thermal conductivity of $H_2O + Cu$ nanofluid and entropy generation," *Results in Physics*, vol. 5, pp. 115–124, 2015.

[117] N. Akbar and A. Butt, "Entropy generation analysis for the peristaltic flow of $Cu - water$ nanofluid in a tube with viscous dissipation," *Journal of Molecular Liquids*, vol. 29, pp. 135–143, 2017.

[118] M. Rashidi, S. Bagheri, E. Momoniat, and N. Freidoonimehr, "Entropy analysis of convective MHD flow of third grade non-Newtonian fluid over a stretching sheet," *Ain Shams Engineering Journal*, vol. 8, pp. 77–85, 2017.

[119] A. Chamkha, M. Rashad, T. Armaghani, and M. Mansour, "Effects of partial slip on entropy generation and MHD combined convection in a lid-driven porous enclosure saturated with a $Cu--water$ nanofluid," *Journal of Thermal Analysis and Calorimetry*, vol. 132, pp. 1291–1306, 2017.

[120] A. Butt, A. Ali, R. Masood, and Z. Hussian, "Parametric study of entropy generation effects in magnetohydrodynamic radiative flow of second grade nanofluid past a linearly convective stretching surface embedded in a porous medium," *Journal of Nanofluids*, vol. 7, pp. 1004–1023, 2018.

[121] D. Nouri, M. Fard, M. Oboodi, O. Mahia, and A. Sahin, "Entropy generation analysis of nanofluid flow over a spherical heat source inside a channel with sudden expansion and contraction," *International Journal of Heat and Mass Transfer*, vol. 116, pp. 1036–1043, 2018.

[122] G. Huminic and A. Huminic, "The heat transfer performances and entropy generation analysis of hybrid nanofluids in a flattened tube," *International Journal of Heat and Mass Transfer*, vol. 119, pp. 813–827, 2018.

[123] N. Gibanov, M. Sheremet, H. Oztop, and N. Hamdeh, "Mixed convection with entropy generation of nanofluid in a lid-driven cavity under the effects of a heat-conducting solid wall and vertical temperature gradient," *European Journal of Mechanics - B/Fluids*, vol. 70, pp. 148–159, 2018.

[124] Z. Li, M. Sheikholeslami, M. Jafaryar, and A. Chamkha, "Investigation of nanofluid entropy generation in a heat exchanger with helical twisted tapes," *Journal of Molecular Liquids*, vol. 266, pp. 797–805, 2018.

[125] J. Fourier, "The orie Analytique," *De La Chaleur, Paris*, 1822.

[126] C. Cattaneo, "Conduzione del calore," *Atti del Seminario Matematico e Fisico dell' Universita di Modena e Reggio Emilia*, vol. 3, pp. 83–101, 1948.

[127] C. Christov, "On frame indifferent formulation of the MaxwellCattaneo model of finite-speed heat conduction," *Mechanics Research Communications*, vol. 36, pp. 481–486, 2009.

[128] T. Hayat, A. Muhammad, T Alsaedi, and B. Ahmad, "Three-dimensional flow of nanofluid with Cattaneo-Christov double diffusion," *Results in Physics*, vol. 6, pp. 897–903, 2016.

[129] M. Upadhay, Mahesha, and C. Raju, "Three-dimensional flow of nanofluid with Cattaneo-Christov double diffusion," *Informatics in Medicine Unlocked*, vol. 9, pp. 76–85, 2017.

[130] A. Dogonchi, A. Chamkha, S. Seyyedi, and D. Ganji, "Radiative nanofluid flow and heat transfer between parallel disks with penetrable and stretchable walls considering Cattaneo-Christov heat flux model," *Heat TransferAsian*, pp. 01–19, 2018.

[131] V. Nagendramma, C. Raju, B. Mallikarjuna, S. Shezad, and A. Leelarathnam, "3D Casson nanofluid flow over slendering surface in a suspension of gyrotactic microorganisms with Cattaneo-Christov heat flux," *Applied Mathematics and Mechanics*, vol. 39, pp. 623–638, 2018.

[132] A. Dogonchi and D. Ganji, "Effect of Cattaneo-Christov heat flux on buoyancy MHD nanofluid flow and heat transfer over a stretching sheet in the presence of Joule heating and thermal radiation impacts," *Indian Journal of Physics*, vol. 92, pp. 757–766, 2018.

[133] T. Hayat, S. Qayyum, S. Shezad, and A. Alsaedi, "Cattaneo-Christov double-diffusion theory for three-dimensional flow of viscoelastic nanofluid with the effect of heat generation/absorption," *Results in Physics*, vol. 08, pp. 489–495, 2018.

[134] K. Prasad, Vaidya, Hanumesh, K. Vajravelu, and V. Ramanjini, "Analytical study of Cattaneo-Christov heat flux model for Williamson-nanofluid flow over a slender elastic sheet with variable thickness," *Journal of Nanofluids*, vol. 12, pp. 583–594, 2018.

[135] A. Naseem, A. Shafiq, L. Zhao, and M. Farooq, "Analytical investigation of third grade nanofluidic flow over a riga plate using Cattaneo-Christov model," *Results in Physics*, vol. 09, pp. 961–969, 2018.

[136] R. Ellahi, M. Hassan, and A. Zeeshan, "A study of heat transfer in Power law nanofluid," *Thermal Science*, vol. 20, pp. 2015–2026, 2016.

[137] M. Eid, K. Mahny, T. Muhammad, and M. Sheikholeslami, "Numerical treatment for Carreau nanofluid flow over a porous nonlinear stretching surface," *Results in Physics*, vol. 8, pp. 1185–1139, 2018.

[138] C. Sravanthi and R. Gorla, "Effects of heat source/sink and chemical reaction on MHD Maxwell nanofluid flow over a convectively heated exponentially stretching sheet using homotopy analysis method," *International Journal of Applied Mechanics and Engineering*, vol. 23, pp. 137–159, 2018.

[139] Y. Kho, A. A. Hussanan, N. Sarif, Z. Ismail, and M. Salleh, "Thermal radiation effects on MHD with flow heat and mass transfer in Casson nanofluid over a stretching sheet," *MATEC Web of Conferences*, vol. 150, 2018.

[140] I. Khan, S. Fatima, M. Malik, and T. Salahuddin, "Exponentially varying viscosity of magnetohydrodynamic mixed convection Eyring-Powell nanofluid flow over an inclined surface," *Results in Physics*, vol. 08, pp. 1194–1203, 2018.

[141] M. Khan, M. Irfan, W. Khan, and A. Alshomrani, "A new modeling for 3D Carreau fluid flow considering nonlinear thermal radiation," *Results in Physics*, vol. 07, pp. 2692–2704, 2017.

[142] C. Reddy, N. Kishan, and M. Madh, "Finite element analysis of Eyring–Powell nano fluid over an exponential stretching sheet," *International Journal of Applied Mathematics and Computer Science*, 2017.

[143] S. Hussain, A. Aziz, C. Khalique, and T. Aziz, "Numerical investigation of magnetohydrodynamic slip flow of Power-law nanofluid with temperature dependent viscosity and thermal conductivity over a permeable," *Open Physics*, vol. 01, pp. 867–876, 2018.

[144] M. Khan, A. Shahid, M. Malik, and T. Salahuddin, "Thermal and concentration diffusion in Jeffery nanofluid flow over an inclined stretching sheet: A generalized Fouriers and Ficks perspective," *Journal of Molecular Liquids*, vol. 251, pp. 7–14, 2018.

[145] K. Kuma, G. Ramesh, and B. Gireesha, "Thermal analysis of generalized Burgers nanofluid over a stretching sheet with nonlinear radiation and non uniform heat source/sink," *Archives of Thermodynamics*, vol. 39, pp. 97–122, 2018.

[146] A. Alshomrani, M. Ullah, W. Khan, and M. Khan, "Interpretation of chemical reactions and activation energy for unsteady 3D flow of EyringPowell magneto-nanofluid," *Arabian Journal for Science and Engineering*, pp. 01–11, 2018.

[147] T. Hayat, F. Shah, Z. Hussian, and A. Alsaedi, "Outcomes of double stratification in DarcyForchheimer MHD flow of viscoelastic nanofluid," *Journal of the Brazilian Society of Mechanical Sciences and Engineering*, vol. 40, 2018.

[148] M. Ansari, S. Motsa, and M. Trivedi, "A new numerical approach to MHD Maxwellian nanofluid flow past an impulsively stretching sheet," *Journal of the Brazilian Society of Mechanical Sciences and Engineering*, vol. 11, pp. 449–459, 2018.

[149] M. Irfan, M. Khan, and W. Khan, "Numerical analysis of unsteady 3D flow of Carreau nanofluid with variable thermal conductivity and heat source/sink," *Results in Physics*, vol. 07, pp. 3315–3324, 2017.

[150] S. Reddy, K. Naikoti, and M. Rashidi, "MHD flow and heat transfer characteristics of Williamson nanofluid over a stretching sheet with variable thickness and variable thermal conductivity," *Transactions of A. Razmadze Mathematical Institute*, vol. 171, pp. 195–211, 2017.

[151] M. Khan, L. Ahmad, and M. Gulzar, "Unsteady Sisko magneto-nanofluid flow with heat absorption and temperature dependent thermal conductivity: A 3D numerical study," *Results in Physics*, vol. 08, pp. 1092–1103, 2018.

[152] S. Motsa and M. Ansari, "Unsteady boundary layer flow and heat transfer of Oldroyd-B nanofluid towards a stretching sheet with variable thermal conductivity," *Thermal Science*, vol. 19, pp. 239–248, 2015.

[153] M. Ramzan, M. Bilal, J. Chung, and U. Farooq, "Impact of generalized Fouriers and Ficks laws on MHD 3D second grade nanofluid flow with variable thermal conductivity and convective heat and mass conditions," *Physics of Fluids*, vol. 29, 2017.

[154] M. Ramzan, M. Bilal, S. Kanwal, and J. Chung, "Effects of variable thermal conductivity and non-linear thermal radiation past an Eyring Powell nanofluid

flow with chemical reaction," *Communications in Theoretical Physics*, vol. 67, 2017.

[155] H. Hamid, L. Khan, Masood, and M. Gulzar, "Unsteady mixed convective flow of Williamson nanofluid with heat transfer in the presence of variable thermal conductivity and magnetic field," *Journal of Molecular Liquids*, vol. 260, pp. 436–446, 2018.

[156] R. Tivari and M. Das, "Heat transfer augmentation in a two-sided lid-driven differentially heated square cavity utilizing nanofluids," *International Journal of Heat and Mass Transfer*, vol. 50, pp. 2002–2018, 2007.

[157] H. George and F. Qureshi, "Newtons law of viscosity, Newtonian and non-Newtonian fluids," *Encyclopedia of Tribology, Springer*, USA, 2013.

[158] F. Incropera, T. Lavine AS, Bergman, and D. Dewitt, "Fundamentals of heat and mass transfer," *Wiley*, USA, 2007.

[159] J. Harris, "Rheology and non-Newtonian flow," *Longman, London*, 1977.

[160] S. Mukhopadhyay, "Heat transfer analysis of unsteady flow of a Maxwell fluid over a stretching surface in the presence of a heat source/sink," *Chinese Physics Letters*, vol. 29, 2012.

[161] T. Papanastasiou, G. Georgiou, and A. Alexandrou, "Viscous fluid flow," *CRC Press Boca Raton*, USA, 2000.

[162] A. Ruban and G. JSB, "Classical fluid dynamics," *Oxford University Press*, UK, 2014.

[163] R. Powell and H. Eyring, "Mechanism for relaxation theory of viscosity," *Nature*, vol. 154, pp. 427–428, 1944.

[164] S. Mukhopadhyay, K. Vajravelu, and R. Gorder, "Casson fluid flow and heat transfer at an exponentially stretching permeable surface," *Journal of Applied Mechanics*, vol. 80, 2013.

[165] I. Oyelakin, M. Sabyasachi, and P. Sibanda, "Unsteady Casson nanofluid flow over a stretching sheet with thermal radiation, convective and slip boundary conditions," *Alexandria Engineering Journal*, vol. 55, pp. 1025–1035, 2016.

[166] J. Shiner, "Entropy and entropy generation," *Kluwer Academic Publisher*, USA, 2001.

[167] S. Das, S. Chakraborty, R. Jana, and O. Makinde, "Entropy analysis of unsteady magneto-nanofluid flow past accelerating stretching sheet with convective boundary condition," *Advances in Applied Mathematics and Mechanics*, vol. 36, pp. 1593–1610, 2015.

[168] J. Ligere, "Analytical solutions of magnetohydrodynamical problems on a flow of conducting fluid in the entrance region of channels in a strong magnetic field," *Ph.D. Thesis Riga Technical University, Latvia*, 2014.

[169] S. Asghar, K. Hanif, and T. Hayat, "MHD non-Newtonian flow due to non-coaxial rotations of an accelerated disk and a fluid at infinity," *Communication non-Linear Scinence Numerical Simulation*, vol. 12, pp. 465–485, 2007.

[170] A. Das, A. Choi, W. Yu, and T. Pradeep, "Nanofluids," *Kluwer Academic Publisher*, USA, 2007.

[171] J. Maxwell, "A treatise on electricity and magneism (second edition)," *Clarendon Press, Oxford, UK*, 1881.

[172] N. Reddy, T. Poornima, and P. Sreenivasulu, "Influence of variable thermal conductivity on MHD boundary layar slip flow of ethylene-glycol based Cu nanofluids over a stretching sheet with convective boundary condition," *International Journal of Engineering Mathematics*, pp. 01–10, 2014.

[173] R. Sharma, A. Ishak, and I. Pop, "Entropy analysis of unsteady magneto-nanofluid flow past accelerating stretching sheet with convective boundary condition," *Mathematical Problems in Engineering*, 2013.

[174] W. Mutuku, "Ethylene glycol (EG)based nanofluids as a coolant for automotive radiator," *International Journal of Computer and Electrical Engineering*, 2016.

[175] M. AA, "A review on the thermophysical properties of water-based nanofluids and their hybrids," *The Annals of "Dunarea de Jos" University of Galati Fascicle IX Metallurgy and Materials Science*, 2016.

[176] H. Alkasasbeh, M. Swalmeh, A. Hussanan, and M. Mamat, "Effects of mixed convection on methanol and kerosene oil based micropolar nanofluid containing oxide nanoparticles," *CFD Letters*, vol. 11, pp. 70–83, 2019.

[177] H. Ali, "Hybrid nanofluids for convection heat transfer," *Academic Press, Elsevier*, USA, 2020.

[178] M. Favre and M. Tardu, "Convective heat transfer," *Wiley*, USA, 2010.

[179] H. Abolbashari, N. Freidoonimehr, F. Nazari, and M. Rashidi, "Analytical modeling of entropy generation for Casson nanofluid flow induced by a stretching surface," *Advanced Powder Technology*, vol. 26, pp. 542–552, 2015.

[180] A. Kamran, S. Hussain, M. Sagheer, and N. Akmal, "A numerical study of magnetohydrodynamics flow in Casson nanofluid combined with joule heating and slip boundary conditions," *Result in Physics*, vol. 7, pp. 3037–3048, 2017.

[181] Z. Abbas, J. Hasnain, and M. Sajid, "Effects of slip on MHD flow of a Dusty fluid over a stretching sheet through porous space," *Journal of Engineering Thermophysics*, vol. 28, pp. 84–102, 2019.

[182] H. Keller, "A new difference scheme for parabolic problems. in: Hubbard, b., ed., numerical solutions of partial differential equations," *Academic Press, New York*, vol. 02, pp. 327–350, 1971.

[183] K. Vajravelu and K. Prasad, "Keller-box method and its application," *De Gruyter*, 2014.

[184] T. Hayat, M. Qasim, and S. Mesloub, "MHD flow and heat transfer over permeable stretching sheet with slip conditionst," *International Journal for Numerical Methods in Fluids*, vol. 66, pp. 963–975, 2011.

[185] M. Arunachalam and N. Rajappa, "Forced convection in liquid metals with variable thermal conductivity and capacity," *Acta Mechanica*, vol. 31, 1978.

[186] M. Q. Brewster, "Thermal radiative transfer and properties, numerical solutions of partial differential equations," *John Wiley and Sons*, 1992.

[187] M. Abel, J. Tawade, and M. Nandeppanavar, "MHD flow and heat transfer for the upper-convected Maxwell fluid over a stretching sheet," *Meccanica*, vol. 47, pp. 385–393, 2012.

[188] L. Grubka and K. Bobba, "Heat transfer characteristics of a continuous, stretching surface with variable temperature," *Journal of Heat Transfer ASME*, vol. 107, pp. 248–250, 1985.

[189] A. ME, "Heat transfer characteristics of a continuous stretching surface," *Journal of Heat Transfer ASME*, vol. 29, pp. 227–234, 1994.

[190] A. Ishak, R. Nazar, and I. Pop, "Mixed convection on the stagnation point flow towards a vertical, continuously stretching sheet," *Journal of Heat Transfer*, vol. 129, pp. 1087–1090, 2009.

[191] A. Ishak, R. Nazaar, and I. Pop, "Boundary layer flow and heat transfer over an unsteady stretching vertical surface," *Meccanica*, vol. 44, pp. 369–375, 2009.

[192] T. Hayat, R. Sajjad, T. Muhammad, A. Alsaedi, and R. Ellahi, "On MHD nonlinear stretching flow of Powell–Eyring nanomaterial," *Results in Physics*, vol. 07, pp. 535–543, 2017.

[193] R. Hamilton and O. Crosser, "Thermal conductivity of heterogeneous two-component systems," *Industrial and Engineering Chemistry Fundamentals*, vol. 13, pp. 27–40, 1962.

[194] M. Abolbashari, N. Freidoonimehr, F. Nazari, and M. Rashidi, "Entropy analysis for an unsteady MHD flow past a stretching permeable surface in nano-fluid," *Powder Technology*, vol. 267, pp. 256–267, 2014.

[195] I. Khan, M. Malik, T. Salahuddin, M. Khan, and K. Rehman, "Homogenous–heterogeneous reactions in MHD flow of Powell–Eyring fluid over a stretching sheet with Newtonian heating," *Neural Computing and Applications*, pp. 1–8, 2017.

[196] M. Ali and N. Sandeep, "Cattaneo-Christov model for radiative heat transfer of magnetohydrodynamic Casson-ferrofluid: A numerical study," *Result in Physics*, vol. 7, pp. 21–30, 2017.

[197] G. Shit and S. Mandal, “Entropy analysis on unsteady mhd flow of Casson nanofluid over a stretching vertical plate with thermal radiation effect,” *International Journal of Applied and Computational Mathematics*, 2019.

[198] M. Mustafa and J. Khan, “Model for flow of Casson nanofluid past a non-linearly stretching sheet considering magnetic field effects,” *AIP Advances*, vol. 5, 2015.